NASA/TM—2016-218864

Viscoplastic Characterization of Ti-6-4: Experiments

Bradley A. Lerch and Steven M. Arnold
Glenn Research Center, Cleveland, Ohio

July 2016

NASA STI Program . . . in Profile

Since its founding, NASA has been dedicated to the advancement of aeronautics and space science. The NASA Scientific and Technical Information (STI) Program plays a key part in helping NASA maintain this important role.

The NASA STI Program operates under the auspices of the Agency Chief Information Officer. It collects, organizes, provides for archiving, and disseminates NASA's STI. The NASA STI Program provides access to the NASA Technical Report Server—Registered (NTRS Reg) and NASA Technical Report Server—Public (NTRS) thus providing one of the largest collections of aeronautical and space science STI in the world. Results are published in both non-NASA channels and by NASA in the NASA STI Report Series, which includes the following report types:

- TECHNICAL PUBLICATION. Reports of completed research or a major significant phase of research that present the results of NASA programs and include extensive data or theoretical analysis. Includes compilations of significant scientific and technical data and information deemed to be of continuing reference value. NASA counter-part of peer-reviewed formal professional papers, but has less stringent limitations on manuscript length and extent of graphic presentations.

- TECHNICAL MEMORANDUM. Scientific and technical findings that are preliminary or of specialized interest, e.g., "quick-release" reports, working papers, and bibliographies that contain minimal annotation. Does not contain extensive analysis.

- CONTRACTOR REPORT. Scientific and technical findings by NASA-sponsored contractors and grantees.

- CONFERENCE PUBLICATION. Collected papers from scientific and technical conferences, symposia, seminars, or other meetings sponsored or co-sponsored by NASA.

- SPECIAL PUBLICATION. Scientific, technical, or historical information from NASA programs, projects, and missions, often concerned with subjects having substantial public interest.

- TECHNICAL TRANSLATION. English-language translations of foreign scientific and technical material pertinent to NASA's mission.

For more information about the NASA STI program, see the following:

- Access the NASA STI program home page at http://www.sti.nasa.gov

- E-mail your question to help@sti.nasa.gov

- Fax your question to the NASA STI Information Desk at 757-864-6500

- Telephone the NASA STI Information Desk at 757-864-9658

- Write to:
  NASA STI Program
  Mail Stop 148
  NASA Langley Research Center
  Hampton, VA 23681-2199

NASA/TM—2016-218864

Viscoplastic Characterization of Ti-6-4: Experiments

Bradley A. Lerch and Steven M. Arnold
Glenn Research Center, Cleveland, Ohio

National Aeronautics and
Space Administration

Glenn Research Center
Cleveland, Ohio 44135

July 2016

Acknowledgments

This work was supported by NASA programs IVHM (Integrated Vehicle and Health Management) and SSAT (System-wide Safety and Assurance Technologies). The authors appreciate the efforts of William Brown of Sierra Lobo, Inc., in preparing the test rig and samples. They also appreciate the time invested by the editor, Laura Becker of Alcyon Technical Services, and the Publishing Services team at NASA Glenn Research Center. The authors also thank Dr. Ivan Locci of the University of Toledo for his technical review of this manuscript.

Level of Review: This material has been technically reviewed by technical management.

Available from

NASA STI Program
Mail Stop 148
NASA Langley Research Center
Hampton, VA 23681-2199

National Technical Information Service
5285 Port Royal Road
Springfield, VA 22161
703-605-6000

This report is available in electronic form at http://www.sti.nasa.gov/ and http://ntrs.nasa.gov/

Viscoplastic Characterization of Ti-6-4: Experiments

Bradley A. Lerch and Steven M. Arnold
National Aeronautics and Space Administration
Glenn Research Center
Cleveland, Ohio 44135

Summary

As part of a continued effort to improve the understanding of material time-dependent response, a series of mechanical tests have been conducted on the titanium alloy, Ti-6Al-4V. Tensile, creep, and stress relaxation tests were performed over a wide range of temperatures and strain rates to engage various amounts of time-dependent behavior. Additional tests were conducted that involved loading steps, overloads, dwell periods, and block loading segments to characterize the interaction between plasticity and time-dependent behavior. These data will be used to characterize a recently developed, viscoelastoplastic constitutive model with a goal toward better estimates of aerospace component behavior, resulting in improved safety.

Introduction

As part of a prognostics program at NASA, the titanium alloy Ti-6Al-4V (Ti-6-4) has been characterized. This widely used aeronautics material is often used at elevated temperatures and therefore is prone to experiencing time-dependent behavior. Understanding the mechanical response of the alloy as a function of time is key to predicting deformation and life of the structure. Diagnosing the damage state of the component along with an accurate lifing methodology enables condition-based maintenance and allows the correct action to be taken on the component to ensure maximum part usage and safe system operation. As part of the prognostics process, an advanced viscoelastoplastic deformation model is being characterized. It is intended that the model will provide improved descriptions of the deformation state, particularly as related to time-dependent, high-temperature behavior.

Previous experimental work (Lerch and Arnold, 2014) showed that Ti-6-4 exhibited viscoelastic behavior over the temperature range 20 to 538 °C. There, a series of tests were conducted predominantly at low stress levels within the proportional stress-strain domain. It was experimentally shown that there was a temperature-dependent threshold value (Y) that delineated the boundary between fully reversible and nonreversible deformation. Below this threshold, all deformation should be completely recovered given sufficient time (typically on the order of a day or two). Above the threshold, some amounts of deformation could still be recovered; however, once the viscoelastic process dissipated (often described as anelastic behavior in the literature), permanent deformation still remained. The threshold stress was nearly equivalent to the apparent proportional limit *PL* at low temperatures irrespective of loading rate, and at higher temperature it was equal to or less than the *PL* at a very slow rate of loading (e.g., $<10^{-6}$ s^{-1}). Viscoelasticity also was exhibited through the significant rate dependence of the modulus at elevated temperatures. The rate deformation of the modulus was shown to be very small at low temperatures, but became significant above 316 °C. At 538 °C the modulus was 84 GPa for a strain rate of 10^{-3} s^{-1} and 30 GPa for an infinitely slow rate (termed "E_S" or "time-independent stiffness" in the model), a difference of 67 percent. Figure 1 illustrates the variation of threshold stress, apparent *PL*, and modulus as a function of temperature for the titanium alloy, Ti-6-4.

Viscoelastic behavior has been shown to occur in various materials including titanium, nickel, copper, and ice, to name a few. Saleeb and Arnold (2001) and Arnold, Saleeb, and Castelli (2001) showed that viscoelastic behavior occurs in Timetal 21S (a β titanium alloy). Research at the NASA Glenn Research Center also showed viscoelastic behavior in GRCop-84 (a high-conductivity, high-temperature copper alloy) and ME3 (a nickel-base turbine disc material; Arnold et al., 2014). Sinha has shown "delayed elastic strains" (his term for viscoelasticity) in Ti-6Al-2Sn-4Zr-6Mo (2003); In-738 (2001), Waspaloy (2005b), and CMSX–10 (2005a) (all Ni-base superalloys with CMSX being a single-crystalline material); and ice (1979). While Sinha originally attributed viscoelasticity to grain boundary sliding, the suggested mechanism was enlarged to include sliding of any interface, including γ/γ', in his work on the single crystal. It should be noted that all of Sinha's experiments were conducted at load levels above the suspected threshold stress since none of his tests completely recovered to zero stress and strain. This indicates that the deformation response included irreversible behavior and thus was performed in the viscoplastic regime. Moreover, the sliding mechanisms suggested by Sinha are believed to be more irreversible mechanisms, which would be consistent with permanent viscoplastic behavior.

Viscoelastic recovery can account for reversible strains up to 300 microstrain in Ti-6-4, representing approximately 70 percent of the maximum strain in this regime under load at elevated temperature. These values decrease with decreasing temperature. The recoverable strain can be an order of magnitude higher in the nonreversible regime. Sinha (2005b) showed recoverable strains with similar orders of magnitude. During fatigue of metallic materials, cyclic strains of this size can result in fatigue failures. It has not been shown definitively that cyclic strains contain any recoverable portion, however, so it is unknown whether or not time-dependent reversible deformation is a significant issue in component lifing. Traditionally, fatigue life is associated with irreversible (inelastic) strains.

The various deformation mechanisms for Ti-6-4 and for a given stress-temperature regime can be easily identified in Figure 1, a deformation modeling map. As the stress exceeds the threshold, total deformation includes both reversible and irreversible (permanent) portions; thus viscoplasticity becomes even more important as the stress increases. This is the regime in which most conventional mechanical testing is conducted for determining material properties, especially those containing time dependency. Note, however, that significant time dependency can occur below the traditional "yield point" (often defined by either 0.02 or 0.2 percent offset strain, $\sigma_{0.02}$ or $\sigma_{0.2}$) as well as below the *PL*; see Figure 1 for how the *PL* for a 10^{-3}-s^{-1} strain rate is significantly higher than the measured threshold surface for Ti-6-4. This will be further discussed later in this report. The above observations are consistent with the GVIPS (generalized viscoplasticity with potential structure) model capabilities put forth by Arnold, Saleeb, and Castelli (2001); Arnold et al. (2009); Sellers (2009); Saleeb et al. (2001); and Saleeb and Arnold (2004). The current work extends our previous viscoelastic experimental work (see Lerch and Arnold (2014)) on Ti-6-4 into higher stress regimes for the purpose of fully characterizing the viscoplastic portion of the GVIPS model. A succinct description of this viscoelastoplastic GVIPS model can be found in Arnold et al. (2009).

Three types of experiments are necessary to support the rational formulation of constitutive equations:

(1) **Exploratory tests**. These illuminate the salient material response (e.g., time dependence or time independence, sensitivity to hydrostatic stress field, material symmetry and/or anisotropy, etc.), identify fundamental deformation and damage mechanisms, and guide the mathematical structure of the model.

(2) **Characterization tests**. These provide the required database for determining the material specific functional forms and associated parameters to represent a particular material over a given range of conditions.

(3) **Validation tests**. These are often structural (multiaxial) in nature and provide the prototypical response data that enables validation of a constitutive model through comparison of structural response with predictions based on the model.

Results from validation tests ideally provide feedback for subsequent developmental and/or refinement efforts. This report describes the results from a recent characterization experimental program on Ti-6-4 performed under NASA safety programs. Monotonic tension, creep, stress relaxation, and history-dependent tests were conducted over wide ranges of stress, time, and temperature (e.g., 20 to 538 °C). Various loading rates were employed to engage varying degrees of time-dependent deformation. Load history effects were studied by combining multiple test types. Step tests, both in creep and stress relaxation, were used as well as blocks of cyclic loading tests. Dwell times and stress overloads were also employed to characterize interaction effects. Finally the author-generated data are combined with other applicable data from the literature in an attempt to provide a more comprehensive set of data on Ti-6-4 to aid in the characterization and validation of any constitutive model (e.g., unified or nonunified viscoplastic deformation model) of interest. The actual characterization of a unified, fully associative, viscoplastic model (i.e., the GVIPS model) will be described in a companion publication. To aid the reader, Appendix A lists the symbols used in this report and Appendix B gives definitions of terms found throughout.

Experimental Procedure

Coupon tests were performed on samples machined from one 0.625-in.-thick, mill-annealed Ti-6-4 plate purchased to AMS specification 4911. A detailed description of the pedigree of the plate was documented in the viscoelastic study (Lerch and Arnold, 2014). Only a few salient features will be repeated here.

The material was found to have a moderate transverse texture (texture index of 1.55) as a result of the rolling process. The material was found to be orthotropic as a result of this texture, which influenced both its elastic and flow properties. Since all samples were taken out of the plate in the same direction (i.e., the loading axis was parallel to the final rolling direction), texture is only of minor concern in this report. However, this texture clearly influences the response in other directions other than the primary loading direction (see App. C on transverse strain). Furthermore, it should always be remembered that this Ti-6-4 plate has been shown (see Lerch and Arnold, 2014) to possess initial anisotropy (e.g., at least orthotropy), and therefore one needs to use judgment when interpreting the results assuming an isotropic model formulation.

A three-dimensional view of the α-β microstructure is shown in Figure 2. The grain structure is inhomogeneous, with the grains being elongated in the rolling direction. The length of the alpha grains can be as high as 100 μm with an average thickness of 6 μm.

Coupon test samples were excised from the plate. Samples were machined into cylindrical dogbones 150 mm in length and having a 6.4-mm-gage diameter. The gauge section had a final hand polish parallel to the sample's axis.

All samples were tested in the same hydraulically actuated load frame. Heating was performed using direct induction with the temperature measured using type-K thermocouples spot-welded onto the samples' gauge section. The temperature gradient within the gauge section was within ±1 percent of the test temperature. A 12.7-mm gage, high-temperature extensometer was used to measure the axial strains. All tests also included measurement of transverse strains using an optical micrometer. Additional details on the experimental setup can be found in Lerch and Arnold (2014).

Tests were conducted in air, under either load or strain control, depending on the specific test type. The discrete temperatures examined in this study were 20, 200, 316, 371, 427, 482, and 538 °C with a focus on the temperatures of 316, 427, and 538 °C. The rate of load application covered a range of strain rates from 6×10^{-7} to 10^{-3} s^{-1}. When conducting tests under load control, an elastically equivalent load

(stress) rate was used (i.e., $\dot{\sigma} = E(\dot{e})\ \dot{e}$), where $E(\dot{e})$ is the rate-dependent modulus and $\dot{e}$ is the loading strain rate. Load-controlled tests were primarily used for creep tests. All creep tests were performed at constant load. The maximum creep time, as well as relaxation time, for any given load segment used in this study was 24 h. This time restriction was long enough to develop characterization data, but short enough to keep testing times realistic. After reaching the 24-h limit, the majority of the tests were unloaded to zero load and held under load control for another 24-h period. This was assumed to be sufficient to permit complete recovery of any viscoelastic strains generated during the loading portion of the test. In every test, the unloading rates were equivalent to the loading rates. More complicated tests will be described in the report as their data are introduced. A complete test matrix description of all tests conducted is given in Table I.

Results

Data collected from the various experiments are plotted and discussed: tensile, creep, and stress relaxation test results, including results from samples with prior deformation histories.

Tensile

The tensile behavior for Ti-6-4 at various strain rates and temperatures is given in Figures 3 through 11. The data are only shown for strains up to 0.02 to enable comparison with the loadup portions of other test types (e.g., creep and relaxation). This greatly increases the number of replicates and better documents the degree of sample-to-sample scatter within a set of test conditions, thereby enabling statistically meaningful tensile properties. These strains are also sufficient for the material to exhibit a pseudosaturation behavior needed for characterization of the model. The range of viscoelastic threshold values and the *PL* values are also shown in each figure for comparison.

The stress-strain behavior at 20 °C is shown in Figure 3. There are three curves representing three different strain rates. The stress levels achieved are similar to those quoted in various handbooks (Metallic Materials Properties Development and Standardization (MMPDS) Handbook, 2012, and Aerospace Structural Metals Handbook, 1997). The variation in the peak stress (due to rate dependence) is only 100 MPa (i.e., 10 percent) for the three curves. Although each curve was tested at a different strain rate, the data followed the expected rate dependency with the fastest rates giving the highest stresses. This suggests that while small, there is a weak dependence on loading (i.e., strain) rate even at room temperature. There is also a Ti-6-4 sample plotted (dotted line) that was taken from a hot isostatic pressed (HIPped) foil material (neat matrix) used in a previous SiC/Ti composites program (Castelli, Lerch, and Keller, 1999). Its data fall reasonably in line with the others. A similar, small rate dependence is also observed at 200 °C (Fig. 4). By comparing the curves in Figure 4 to those in Figure 3, it can be observed that an increase in the test temperature by only 180 °C causes a drop in the peak stress of approximately 250 MPa. Furthermore, Figures 3 and 4 clearly indicate that the *PL* as well as either 0.02 percent or 0.2 percent yield points ($\sigma_{0.02}$ or $\sigma_{0.2}$, respectively) are rate dependent, even at room temperature.

In Figure 5 the tensile curves are plotted for a test temperature of 316 °C. There are 10 virgin samples shown in this figure. While there is still a weak rate dependence on the behavior, the additional scatter from the replicates partially obscures the trend. Also included are the data from the HIPped foil material. The two upper most curves (dashed lines) are from samples that had prior loading histories. In both of these cases, a series of viscoelastic and viscoplastic tests were conducted prior to running the final tensile tests. The prior history had the expected effect of work hardening the material. Moreover, both of these samples evidenced an upper yield point that was absent on the virgin samples. With increased strains, the

stress-strain response from these two samples converged on the others, albeit they were still marginally higher.

For the few tests conducted at 371 °C, there was little difference between curves from the fast and slow strain rates (Fig. 6). The largest difference occurred at small strains where the sample tested at the slow strain rate had a lower modulus, *PL*, and apparent yield points. This difference is reduced as work hardening continued. There is also a dashed curve shown from a sample with prior viscoelastoplastic history. Its values are slightly higher than the virgin samples, and this difference remains through termination of the curves at 0.018 strain. Similar to the samples with prior deformation history tested at 316 °C, the sample at 371 °C has a distinct upper yield point, but less evident than at the lower temperature. Also very good sample-to-sample repeatability is exhibited for the 10^{-3} strain rate.

Figure 7 shows data from various samples tested at 427 °C. At this temperature there is more separation between curves as a function of strain rate, indicating more significance from time-dependent flow. There is a discernable, slight ordering of the curves at rates of 10^{-5} s^{-1} and above. However, testing at a slower rate of 6×10^{-7} s^{-1} yields curves that have much lower stress levels. It can be observed that the modulus, yield, and final stress are all significantly lower than those at the faster strain rates. The two samples having prior load histories are once again hardened and lie slightly above the other data. A distinct upper yield was not observed in these two samples, unlike those at 316 and 371 °C.

Tensile curves for samples tested at 482 °C are given in Figure 8. At this temperature there is significant rate dependence with the final stress at a strain rate of 10^{-3} s^{-1} being 70 percent higher than at 6.1×10^{-7} s^{-1}, thus indicating activation of a substantial amount of rate-dependent deformation mechanisms. The sample with a prior load history shows again slightly stronger behavior than the virgin sample. Finally, note that no upper "yield" behavior is exhibited at this temperature.

Tests at 538 °C exhibit the most time-dependent behavior (Fig. 9). Whereas data for the strain rates of 5×10^{-4} and 10^{-3} s^{-1} show no difference within scatter, data at all other lower strain rates depict distinctive rate dependence. The sample from the HIPped foil material (dotted line) tested at a rate of 10^{-4} s^{-1} shows a significant reduction in properties compared with those at the two higher strain rates. Even though this sample was from a different batch of Ti-6-4, earlier tests on this batch (Figs. 3, 5, and 7) showed that its tensile properties were comparable to those observed in the current study. The samples tested at 10^{-5} and 6×10^{-7} s^{-1} show large reductions of 30 and 70 percent, respectively, in their saturated stress levels (stress values at 0.018 strain, $\sigma_{1.8}$). Similar to the lower test temperatures, samples having prior load histories had the highest strengths, although small enough at this temperature that the data could have been just grouped within the scatter of the fast-strain-rate tests.

The temperature dependence of the tension behavior is shown as a function of strain rate in Figures 10 and 11. Figure 10 shows the relationship at the fastest strain rate of 10^{-3} s^{-1}. The maximum stress (i.e., strength) of the material decreases with increasing temperature, with a substantial drop occurring between 20 and 200 °C. It can also be observed that the stiffness of the material decreases significantly with increasing temperature. Similar trends are exhibited when testing at the slowest strain rate of 6×10^{-7} s^{-1} (Fig. 11). Clearly at slow rates one observes significantly larger temperature dependence on modulus, apparent yield, and maximum stress.

A summary of the tensile properties as a function of temperature and strain rate is shown in Figures 12 through 16, and in Table II. Figure 12 depicts the drop in axial modulus with increasing temperature. Representing the dynamic modulus is a line with data points taken every 5 °C. These tests (documented in Lerch and Arnold, 2014) were conducted using an impulse excitation method (ASTM Standard E1876–09, 2009), which yielded resonant frequencies of approximately 10 kHz. This equates to a strain rate of approximately 1 s^{-1}. All other values were taken from static tests. The error bars represent ±1 standard deviation or half the range if only two data points were available. The number of data points

per test condition is given in Table II. The modulus E for the fast-strain-rate tests (10^{-3} s^{-1}) coincides with the dynamic modulus E_D up until 427 °C, where there begins a slight deviation from the curve. Similar behavior is observed for the rates of 10^{-4} and 10^{-5} s^{-1} with the deviations becoming greater with decreasing strain rate. At the slowest rate of 6×10^{-7} s^{-1} the modulus begins to deviate from the dynamic results at 316 °C and varies substantially from E_D at 538 °C. The difference between the dynamic value and the slowest static rate modulus at 538 °C is 32 percent. Finally, data points for the infinitely slow modulus E_S calculated from the viscoelastic study are shown and show a large deviation from the static moduli. All of these data show that the modulus is highly rate dependent above a temperature of approximately 316 °C.

Temperature dependence is also observed with respect to the flow behavior as traditionally represented by the PL, $\sigma_{0.02}$, $\sigma_{0.2}$, and $\sigma_{1.8}$ (see Figs. 13 to 16, respectively). The $\sigma_{1.8}$ is nearly the highest strain value attainable in the highest resolution strain range on the test machine, allowing the most accurate calculations of modulus and yield and in most cases is a reasonable approximation of the ultimate tensile strength (UTS). The strain of 0.018 was also used as a common stress relaxation target value for relaxation tests, thus giving additional data for analysis. The lines in these figures represent visual trends. All of these figures show that the associated stress values (for a given yield criteria) for a strain rate of 6.0×10^{-7} s^{-1} are lower than for the faster rate of 10^{-3} s^{-1}. This is even true at room temperature where strain rate effects are typically ignored or do not occur in metals. With increasing temperature the stress values drop as expected. Both the PL and $\sigma_{0.02}$ drop suddenly at 316 °C for the slower strain rates and tend to plateau at 427 °C and above, whereas $\sigma_{0.2}$ and $\sigma_{1.8}$ tend to have a more gradual drop with a concave downward curvature at the higher temperatures. Large strain rate-temperature effects on stress begin at 316 °C for the PL and $\sigma_{0.02}$. For $\sigma_{0.2}$ and $\sigma_{1.8}$, the curves collapse over the temperature range of approximately 200 to 400 °C. This is due to a slight stress dip during the fast rates and a slight increase in the slow-rate stresses, presumably a result of strain aging. Cheng and Nemat-Nasser (2000) showed that dynamic strain aging manifests in titanium through an increase in flow stress with increasing temperature, with the increase in flow stress shifting to higher temperatures as the rate increases. Strain aging has been observed in Ti-6-4 by others during high-rate compression testing between 300 and 500 °C (Srinivasan and Venugopal, 2008), low-cycle fatigue (LCF) at temperatures between 350 and 450 °C (Lin et al., 2011), and compression tests between the temperatures of 227 and 527 °C (Nemat-Nasser et al., 2001). The current data would indicate that the strain-aging range is approximately in the temperature range of 200 to 372 °C.

Creep

Creep tests were conducted at each temperature with the focus temperatures being 316, 427, and 538 °C. Various applied stress levels $\bar{\sigma}$ were imposed at each temperature; maintaining identical $\bar{\sigma}$ values across adjacent temperatures was attempted. This aided in characterizing the temperature dependence of the various model parameters. The creep test matrix is given in Table III. Here, X indicates tests that were conducted. Unfilled cells are tests on samples that had prior history, usually for viscoelastic evaluation. Creep test results for virgin samples are represented as are the approximate ranges of the viscoelastic threshold (Y) as given in Lerch and Arnold (2014). There were tests run at elastic equivalent strain rates of both 10^{-3} and 6×10^{-7} s^{-1}; the majority of the tests were loaded at the fast rate. Although the creep hold time in these tests never exceeded 24 h (86 400 s), the full time history is not always shown, particularly at higher stress levels, because of the onset of significant tertiary creep. Since deformation models typically only represent the primary and secondary creep regimes, these regimes are

usually the only ones shown. Occasionally the tertiary creep regime (or part of it) may be shown. Full creep curves will be presented in a future paper on damage.

The 24-h history from creep at 316 °C is shown in Figure 17, where part (a) presents the stress versus total axial strain *e* behavior and part (b) shows the strain behavior over time. Figure 17(a) depicts the stress-strain response for these tests showing the near-linear loading. The test at the highest creep stress of 587 MPa is above its $\sigma_{0.2}$ and obviously experienced more inelastic flow during loading. All of these tests were loaded, in load control, at the fast, equivalent elastic strain rate of 10^{-3} s^{-1}. In Figure 17(b) the vertical axis is associated with the total axial strain (which includes the loadup strains). The lowest curve is from a test at 482 MPa and is below the uniaxial threshold stress *Y* for this particular sample, whereas the curve immediately above it is from a test at 479 MPa, which is above its threshold value. Both have prior viscoelastic history and lie below the range of maximum reversible strains[1] $\varepsilon^{R}_{\max}$ $(=Y/E_s)$ achievable associated with the average threshold stress at 316 °C. All other curves are for virgin samples (i.e., no prior history) tested above the threshold and above their *PL* values. The curves exhibit minimal creep (less than 0.02 inelastic strain compared to a failure strain of 0.20 at this temperature). The sample tested at the highest stress of 587 MPa, which is also the $\sigma_{0.2}$ at 316 °C, shows slightly more inelastic strain. There are two samples tested at or near 517 MPa, and these indicate excellent reproducibility in the strain response.

Creep tests at 427 °C are shown in Figure 18 with their stress-strain curves in Figure 18(a) and their corresponding strain-time curves in Figure 18(b). In general the creep strain, and therefore the creep rates, increase with increasing creep load. The lowest stress level (239 MPa) is near the threshold stress at this temperature. Samples at the two lowest levels (239 and 375 MPa) are below their *PL* values since the stress-strain curves are still linear. Sample 26 has prior deformation history, and this is probably why the curve for 26 is below its *PL* and creeps less than sample 78, which was tested at the same stress level. The samples tested at a creep stress of 445 through 527 MPa lie between $\sigma_{0.02}$ and $\sigma_{0.2}$. The four highest stresses are above their respective $\sigma_{0.2}$ values. Note there is a large difference between the two samples (45 and 87) tested at the highest stresses of 591 and 596 MPa. Sample 87 has the higher creep rate, and sample 45 has the lower. This is consistent with the fact that 87 has a lower $\sigma_{0.2}$ (526 MPa) and 45 a higher value of 537 MPa. We suspect that sample 87 creeps more because of the extra inelastic strain incurred during loading.

Creep as a function of applied stress at a temperature of 538 °C is shown in Figure 19. Figure 19(a) shows the stress-strain curves for these tests and indicate that the loading was predominantly linear. All of the tests are at creep stress levels above the threshold (*Y*). Figure 19(b) shows good ordering of the strain-time curves with respect to increasing $\overline{\sigma}$. On the right side of the graph, the ratio between the creep stress and the *PL* is listed. There are three replicates at $\overline{\sigma} \sim 240$ MPa showing the variation in creep behavior. The maximum reversible strain (Y/E_s) at this temperature falls nearly on the x-axis, and all of the creep stress levels in Figure 19 are above the threshold value. Figure 19(c) gives an enlarged view of the creep behavior with the y-axis truncated at a strain of 0.040. Only two of the samples were tested at stresses below their *PL* (34 MPa), and these are samples 28 and 92. The data from these samples overlap. All other tests were above the *PL*. Three samples (1, 76, and 94) were below the $\sigma_{0.02}$, and the remaining samples were below the $\sigma_{0.2}$. Hence, none of these tests experienced much large-scale yielding during loading. At a creep stress of 240 MPa sample 3 had the lowest creep behavior of the three replicates. Its *PL* (77 MPa) was higher than that for sample 34. Sample 85, with the highest creep behavior of the three tests, had an intermediate *PL*, but its applied stress did exceed its $\sigma_{0.02}$, suggesting that this sample flowed more easily than the other two; this is borne out with the higher creep response. Three of the samples

[1]This is the equivalent of plotting the threshold stresses in strain space.

(3, 34, and 88) fractured, and another (85) was severely necked and near failure. Most of the creep tests (at $\bar{\sigma} > 101$ MPa) exhibited some tertiary creep within the 24-h hold time. Clearly, given the extensive creep shown in the above results, 538 °C exceeds the useful temperature of Ti-6-4.

The next several charts show the temperature behavior of creep at various applied stress levels. Figure 20(a) depicts stress-strain behavior for an applied creep stress of 241 MPa. For tests at 427 °C there is very little creep elongation observed (Fig. 20(b)). Both of these samples were tested at stresses above their thresholds *Y*, but under their *PL*. At 538 °C the creep data fall into two groups even though they were all tested at the same creep load. The higher creep curves (samples 85 and 89) both have exceeded their $\sigma_{0.02}$ values, whereas the two lower creep curves (samples 3 and 34) have only exceeded their *PL*s. Additionally the two lower curves had a slightly higher modulus (86 GPa) than the other two samples (82 GPa). Within these two groups, the reproducibility is very good.

Creep at a stress level of 379 MPa (Fig. 21) incorporates four test temperatures. There is a large difference in creep among three of the temperatures at this stress level (Fig. 21(a)). The sample tested at 316 °C is below its threshold and therefore in the viscoelastic regime (Fig. 21(b)). At 427 °C the samples show minimal creep. Curves from two samples are shown, and they overlap one another even though sample 57 was conducted at its *PL*, and sample 49, under its *PL*. At the two higher temperatures, the applied load is above both *PL*s and above the $\sigma_{0.02}$, and these samples depict extensive creep. Note that the failure strain in tension at 538 °C is approximately 0.10 and the creep sample reached an equivalent strain.

At an applied creep stress level of 517 MPa three temperatures are again represented: 316, 371, and 427 °C. For a temperature of 316 °C, two curves are presented in Figure 22, and they overlap. At this low temperature very little creep is observed, and the stress-strain curves are nearly linear (Fig. 22(a)). The load for both of these samples (9 and 41) was close to, but still below, the $\sigma_{0.02}$. At 371 °C the test is at a stress level between the $\sigma_{0.02}$ and $\sigma_{0.2}$ and experiences more creep than at 316 °C (Fig. 22(b)). The two samples at 427 °C were tested slightly below their $\sigma_{0.2}$. Sample 52 with the higher creep behavior had a slightly lower $\sigma_{0.02}$ than the other sample (72) tested at 427 °C, again suggesting that the relationship between the applied load and the sample yield points highly affects the creep behavior.

Figure 23 illustrates the creep behavior of three samples at a stress of ~550 MPa, two at 316 °C and one at 427 °C. At 316 °C sample 86 (which was tested at a level between its $\sigma_{0.02}$ and $\sigma_{0.2}$) experienced more creep (upper curve) than did sample 54 (Fig. 23(a)). The lower curve (sample 54) had significant viscoelastoplastic history and therefore had been work hardened, yielding a lower creep response and a limited primary creep response regime. In spite of the prior work hardening, sample 54 is not too different from the virgin sample. The sample tested at 427 °C has a stress level above the $\sigma_{0.2}$ and thus generates a large amount of creep including a large primary creep regime (Fig. 23(b)).

At a creep stress level of 586 MPa, tests from the same two temperatures (316 and 427 °C) are represented in Figure 24. All three samples were tested above their $\sigma_{0.2}$ (Fig. 24(a)). The 316 °C sample (loaded only 5 MPa above its $\sigma_{0.2}$) exhibited limited creep as shown in Figure 24(b). The tests at 427 °C (both loaded 50 MPa above their $\sigma_{0.2}$) exhibited extensive creep, including the initiation of a tertiary regime for the lower curve. The data for the second test probably would have shown a tertiary regime as well, had it been continued past 20 000 s.

Figures 25 and 26 depict the influence of loading rate on the creep behavior. Figure 25 shows the behavior at a temperature of 538 °C and a load of 103 MPa. The sample with the faster strain rate was tested at a stress slightly above its rate-dependent *PL* (Fig. 25(a)). For the slower rate sample, the applied stress level was slightly below its rate-dependent $\sigma_{0.2}$. In spite of this much higher stress ratio (applied/yield stress), the slower strain rate sample had a lower creep behavior (Fig. 25(b)). It also has

less of a primary regime than the faster rate test as shown in Figure 25(c) as one might suspect since during loading more time is provided for competition between the hardening and recovery mechanisms.

The effect of loading rate at 427 °C is plotted in Figure 26 for two stress levels, 379 and 517 MPa. For the higher stress level two curves are shown in Figure 26(a) for samples having relatively high loading rates (10^{-3} and 2.4×10^{-3} s^{-1}). In the fast-rate test, the sample exhibits higher creep strains (Figs. 26(b) and (c)) because more primary hardening (evolution of back stress, α) occurs during loading. Both of these samples were tested slightly below their $\sigma_{0.2}$. For the samples tested at 375 MPa, curves for three samples are shown. The two lowest curves overlap and are tested slightly below the *PL* (sample 57). The sample (93) at the slow loading rate reaches steady state sooner and creeps more than the faster rate samples. The slow-rate sample had an applied stress between its rate-dependent $\sigma_{0.02}$ and $\sigma_{0.2}$, thus indicating a "softer" sample, showing more creep. Since this sample is tested at a significantly higher stress ratio than the other two samples, one would expect its creep rate to be higher than the other two samples in spite of its slow loading rate.

For comparison as well as completeness, creep data on annealed Ti-6-4 from the literature were plotted with those obtained from the current study in Figures 27 to 29 for a comparison under closely related conditions. Zerwekh (1978) performed short-term creep tests followed by an unloading and recovery (note that this is termed "relaxation" in his paper). The goal of Zerwekh's work was to characterize the primary creep regime of several metallic systems using the thermodynamic constitutive theory of deformation. Zerwekh's creep test times were less than 4000 s and at a variety of stress levels between 124 and 303 MPa. A number of test temperatures were used: 440, 470, 485, 500, 515, and 530 °C. The data from tests conducted at 427 °C compares favorably with those from Zerwekh in Figure 27. For near-equivalent stresses, the data tested at 440 °C lie slightly higher than those tested at 427 °C. A good example is at 241 MPa where the line for 440 °C is only slightly higher than the line representing the 427 °C test. A similar trend occurs for the samples tested at a still higher temperature of 470 °C. The curve for 255 MPa is even higher than the line tested at 440 °C. This is expected since the material should creep more at similar stresses but at higher temperatures. Also in this figure is a band indicating the maximum reversible strain range $\varepsilon^{R}_{\max}$ at 427 °C. Note that the applied creep stresses for all samples in this figure are above the threshold, *Y*, and therefore lie in the viscoplastic regime.

A comparison to the tests conducted at 482 °C is shown in Figure 28. Unfortunately only three tests were available at 482 °C for comparison, and these bound all of Zerwekh's data at 470 and 485 °C, being at either too low or too high of a creep stress. Additionally the sample (47) tested at the lowest stress level is below the threshold stress. Zerwekh's data show that the tests at higher temperatures creep slightly more than for equivalent stress levels at the slightly lower temperature. Even though this temperature difference is only 15 °C, it appears large enough to influence the creep behavior.

Finally the tests at 538 °C are compared in Figure 29 to Zerwekh's data in the 500 °C regime. Again the two data sets are similar, and our 538 °C data appear to fit with Zerwekh's data between the temperatures of 500 and 515 °C. For example, at a stress level of 226 MPa (current data) the curve lies between 228 MPa (500 °C) and the 221 MPa (515 °C) data. Clearly, given all the data (both literature and current program) for the various conditions one can conclude that the current generated data are consistent with literature data for the creep behavior. Next, steady-state creep rates will be compared in an attempt to determine some typical creep model parameters.

The minimum (steady-state) creep rates are plotted in Figure 30 as a function of stress at various temperatures for a loading rate of 10^{-3} s^{-1}. As expected the creep rate increases with increasing temperature and applied stress. In this figure tests that were conducted above *Y* are depicted as well as those with creep stresses below the threshold, which are in the viscoelastic regime. Earlier work (Lerch and Arnold, 2014) demonstrated that the response in this regime is linear viscoelastic in nature (i.e., $n \approx 1$,

where n is the power law creep exponent). It can be observed at all temperatures that at stresses below the threshold, the trend of the data is toward a more horizontal line ($n \leq 1$), whereas at very high stresses (those above Y) the data approach a more vertical line (indicating the onset of tertiary creep). At moderate stress levels the slope is in between these two regimes (indicating a nonlinear viscoplastic regime). Moreover, the creep rates for the tests below the threshold fall in the range of 10^{-10} to 10^{-9} s^{-1}, which is consistent with the creep rates associated with full dissipation of time-dependent mechanisms below the threshold (Lerch and Arnold, 2014). Data from Barboza, Moura Neto, and Silva (2004) conducted on Ti-6-4 at 500 °C are also plotted in Figure 30 and are more comparable with the current data tested at 482 °C. Although they do not give the heat treatment condition, their material is believed to be in the aged state based on their value of a UTS of 638 MPa, which is 1.3 times the UTS at 538 °C from this study. Data on mill-annealed Ti-6-4 tested at 550 °C from Sastry, Pao, and Sankaran (1980) are also plotted, and these data agree with the 538 °C data from this study. Sastry depicted the data as being bilinear on a logarithmic scale, which fits the current data nicely for stress levels above the threshold. The exponent in the creep equation (slope) at 538 °C for the moderate stresses is 3 and is 6.5 at higher stresses.

Three points are also plotted in Figure 30 that represent creep tests loaded at a slow rate (6×10^{-7} s^{-1} equivalent strain rate) at the temperatures of 427 and 538 °C. Both points fall within their respective temperature fields, indicating that although loading rate does affect the response stress, it does not affect the respondent minimum creep rate.

Evans and Harrison (1983) gave the stress dependence on minimum creep rate representing both an α and an α/β Ti-6-4 material that was tested at 400, 450, and 500 °C, and these results are reproduced in Figure 31(a). As described by them, the data are best described by a bilinear line having a shallower slope at higher stresses. Note that this figure is plotted with the axes switched compared to Figure 30 and is done this way since both representations are common in the literature. Evans and Harrison's fits and exponents, n, are also shown in Figure 31(a) and indicate that n decreases with increasing test temperature. As discussed by Evans and Harrison, the microstructure had no influence on the curves as the data from the α and α/β materials are indistinguishable. The line fits for these data are copied onto Figure 31(b), and the data from the current study are superimposed. The data from Evans and Harrison from the 400 °C tests best fit the points from samples tested at 316 °C for the current study. Likewise, their 450 °C points agree with those tested here at 427 °C. Note that the bilinear representation captures the two-slope trend at 427 °C. Evans and Harrison's 500 °C data fall slightly above the 538 °C points and may coincide more with those samples tested at 482 °C. The literature is replete with data indicating different exponents on the power law form depending upon stress range (this is often been termed "power-law breakdown"). Now that linear viscoelastic behavior has been shown to exist below a threshold stress (Y), one should expect at least two distinct slopes during creep deformation that is $n \approx 1$ (viscoelastic stress region) and $n > 1$ (nonlinear viscoplastic region).

Data from tensile tests have also been added (cross-hatched symbols), where their loading strain rate is used for the steady-state creep rate and the stress is taken to be the ultimate strength (essentially this is a constant stress occurring over a range of strains). These points fall within the creep data at the same temperature and at very high rates. This yields a third distinct slope in this graph.

Note that the data from the very low creep rates (stresses below Y: open symbols) and on the left of the graph do not fall on an extension of the higher rate lines. They are on a line that has a steeper slope and would form a three-sloped log-log dependence of creep rate on stress rather than a two-sloped one as described by Evans and Harrison. The creep exponent (slope) for these lower stresses at 482 and 538 °C is approximately 1.6, but appears to increase with decreasing temperatures.

For various stress levels, the minimum creep rate is plotted versus the reciprocal temperature in Figure 32. Data are plotted for 10 stress levels. Additionally, data for Ti-6-4 are plotted from Sastry et al.

(1980). Sastry's data agree reasonably well with the current data, with his 330 MPa data agreeing with the 379 MPa values and his 164 MPa points coinciding with the 117 MPa data. The data are fitted with straight lines for a single stress value and over a range of temperatures. The slopes of these lines yield the activation energy for creep (Sastry et al., 1980). Sastry gives a value of the activation energy as 188 kJ/mol for his 164 MPa data and 276 kJ/mol for his data at 330 MPa. Figure 32 indicates that the activation energy is a function of stress level: being small at low stresses and high temperatures, high at moderate values of temperature and stress, and lowest at low temperatures and high stresses. For example, the activation energy at 34 MPa is 179 kJ/mol, increases to 249 kJ/mol at 379 MPa, and decreases to 96 kJ/mol at 517 MPa. These values are consistent with those given by Palchan and Rosen (1978) for aged Ti-6-4, where the activation energy was found to be 259 kJ/mol at high temperatures and 71 kJ/mol for low-temperature creep. Doner and Conrad (1973) report the activation energy for self-diffusion in α-Ti to be between 242 and 293 kJ/mol. Sargent and Ashby (1982) report a value of 97 kJ/mol for boundary diffusion in alpha titanium. From the few data points available it appears as if the data from the viscoelastic regime (below the threshold stress) are consistent with the viscoplastic data, suggesting that the thermal mechanisms are similar.

Several investigators (Williams and Wilshire, 1973; Evans and Harrison, 1976, 1979, 1983) have proposed a relationship between secondary creep rate and the effective stress $(\sigma - \sigma_o)$ where σ_o is the friction stress that represents microstructural impediments to dislocation flow. We considered a possible interpretation of the friction stress to be equivalent to the threshold since this represents the boundary between reversible and irreversible deformation. Therefore the data from Figure 31(b) were replotted in Figure 33 using this "effective stress" representation, where Y was taken to be the temperature-specific threshold for each sample. These values for uniaxial tensile Y $(=\sqrt{3}\cdot\kappa)$ can be found in Figure 1 (with more information given in Lerch and Arnold, 2014). In the GVIPS model the quantity $(\sigma - Y)$ is actually equal to the back stress, α, and therefore the abscissa is labeled as "back stress." A solid line with a slope of 3.5 is drawn through the data from temperatures at and below 427 °C and fits the data remarkably well. A slope of 3.5 was suggested by Evans and Harrison (1976) to be the universal exponent relating secondary creep rate to effective stress. For higher temperature regimes the data seem to suggest that multiple slopes (each defining a specific effective stress and steady-state strain regime) are once again needed. For example, in Figure 33 a dashed line is also shown with the same slope but translated to predict the higher temperature data (482 and 538 °C) in the high-stress regime. The line is a good approximation of the data at the intermediate stress regime, but overpredicts at both lower and higher stress regimes. Also note that points below the threshold Y do not appear in this figure since the resultant α would be negative. Finally at very high stresses the slope decreases to a value of approximately 0.04. Figure 33 implies that Y is an appropriate variable to use in place of the friction stress in this relationship. Moreover, Y is believed to be a more appropriate value for this approach. The method used in the literature for determining σ_o would contain mostly viscoelastic behavior since the stress changes are small. A full discussion on the modeling implications of this representation will be given in a sequel paper on modeling.

Stress Relaxation

A series of stress relaxation tests were conducted at a target strain of 0.018 and various temperatures. The relaxation time was limited to 86 400 s (24 h). The applied strain rate was 10^{-3} s^{-1} unless otherwise indicated. Examples of typical relaxation tests are shown in Figure 34 for temperatures of 427 and 538 °C. These curves depict the loadup and the relaxation portions of the test in stress-strain space. Duplicates at each temperature are shown and exhibit good reproducibility. As shown previously in the

tensile results, the tests at 538 °C have an overall lower stress response. Although difficult to see in this figure, the stresses relax to a lower stress value at 538 °C than at 427 °C, and both values lie very close to their respective threshold values.

The relaxation behavior at 0.018 strain in the stress-time space is shown as a function of temperature in Figure 35. As temperature increases, the saturation stress decreases as does the initial stress at which relaxation begins due to the less-stiff material's response with elevated temperature. At the three highest temperatures, duplicates are shown and they agree remarkably well with one another. It can be observed in this figure that the saturation stresses (final relaxation stress) are different for each temperature (i.e., they do not relax to the same value). Note also that even at room temperature (20 °C) the material relaxed approximately 150 MPa (or 15 percent of the maximum stress) over the 24-h period.

In an effort to better understand the total amount of relaxation as a function of temperature, the stresses were normalized against the maximum stress (i.e., the last stress value from the tensile loadup) and plotted in Figure 35(b). Although the ordering based on temperature remains the same (with the exception of the two lowest temperatures), the amount of relaxation is shown to increase with increasing temperature from approximately 15 percent at room temperature to 95 percent at 538 °C.

Applied strain rate effects are plotted in Figures 36 to 40 along with rate-dependent *PL* and the threshold. Even at 20 °C the loadup strain rate has an effect on the behavior (Fig. 36). Not only are the overall stresses lower at the slower strain rate, but the amount of relaxation is less than at the fast strain rate. During slow-rate loading more inelastic strain is accumulated, increasing the back stress; hence, the driving force for relaxation is smaller. Similar results can be observed in Figure 37 for a test temperature of 200 °C. At 316 °C (Fig. 38) an inverse behavior occurs: the stresses for the slow-strain-rate test are higher than those for the fast-rate sample. Additionally, the curve for the slow-strain-rate test is not as smooth as for that of the fast-rate test. This noisy curve can also be observed in the slow-strain-rate data at 200 °C. These are all indications of dynamic strain aging. At 316 °C the slow-rate curve still shows less relaxation, which is consistent with that observed at the lower temperatures.

The trends shown at the lower temperatures also apply to tests at 427 and 538 °C as observed in Figures 39 and 40, respectively. The stresses during the loadups are lower, and the relaxation amounts are smaller, for the samples tested at the slower strain rates; clearly a significant rate dependence is occurring at the elevated temperature of 538 °C.

A more convenient view of the amount of relaxation behavior is shown in Figure 41, where the normalized relaxation range is plotted against temperature and applied strain rate. The normalized relaxation range was defined as the maximum stress minus the final, saturation stress divided by the maximum stress ($(\sigma_{max} - \sigma_{sat})/\sigma_{max}$). The normalized relaxation range decreases slightly from 20 to 200 °C and then increases linearly at higher temperatures. It appears as if data from applied strain rates greater than or equal to 1×10^{-4} s^{-1} all fall on one curve. For rates less than 1×10^{-4} s^{-1}, the data appear to fall on a slightly lower, but parallel curve. The minimum value at 200 °C for both curves is suspected to be a result of strain aging. The values represented in the ordinate seem to be a good method of comparing relaxation over various temperatures and strain rates since both the maximum stress and relaxation range are influenced by these variables.

The effect of the relaxation strain level is shown over the next few figures. In Figure 42 the relaxation behavior at 427 °C is plotted for strains of 0.006, 0.012, and 0.018 for a applied strain rate of 10^{-3} s^{-1}. The relaxation time at each strain level is 24 h. The reproducibility on these five tests is excellent. It also is observed that all samples tended to relax to an identical value of 200 MPa. A similar plot, but for slower strain rates (6 and 8×10^{-7} s^{-1}) is shown in Figure 43. It again appears that all samples tended to relax to a constant value of 200 MPa, although there is slightly more scatter in the data; for example, sample 48 at a strain of 0.012 did not relax quite as much. Note a fast-rate tensile response is also shown in Figure 43 to

help elucidate how significantly softer all relaxation response curves are when loaded at slower strain rates. These relaxation curves are also plotted in the stress-time space in Figure 44. Clearly, the fast-rate tests reach a higher initial starting stress and relax at a faster rate to an overall lower saturated stress value compared to the slow-rate tests. Although, if the slow-rate tests had been continued past the standard 24-h hold period, extrapolation of the curves indicate that they would probably converge to the same saturation stress as the fast-strain-rate tests.

Normalization of the curves with respect to the maximum stress (Fig. 45) more clearly shows that the initial relaxation behavior is dependent on applied strain rate with the slower strain rate tests relaxing less than the fast-strain-rate tests over the same time period. Moreover, within a rate group the samples tested at a higher strain appear to relax more, although there is some overlap between strain values. This is not surprising since at higher relaxation strains or slower strain rates the material experiences increased inelastic flow during loadup, and that is the driver for relaxation.

The normalized relaxation range for all three strains, applied strain rates, and temperatures is shown in Figure 46. Again the slower rate tests exhibit lower normalized relaxation ranges as do the samples tested at lower strains. However, the applied strain rate seems to have a larger effect than the strain level. The data for the samples relaxed at the lower strain values (0.006 and 0.012) follow similar trends to those of the highest relaxation values of 0.018.

Relaxation curves as a function of time and temperature are shown in Figure 47(a). The relaxation decreases with increasing temperature although part of this decrease is due to the temperature effects on the maximum stress. At the lower temperature, the stress drops quickly and tends to level out in times less than 10 000 s. Starting at a temperature of 316 °C and above, the stress relaxes over a larger range of times and continues decreasing at a slower rate through the end of the relaxation period (24 h). The final stress values (saturation stress) appear to be approaching the threshold stress, Y, which is plotted as a colored band for each temperature. These values were taken from Lerch and Arnold (2014). Since there were limited data existing for Y, and there is some uncertainty, more information will not be given about this graph. The relaxation curves were normalized by the threshold and plotted in Figure 47(b).

In general, the curves saturate at a normalized stress of 1.0. It can be observed in this figure that relaxation at the higher temperatures would require more time to fully saturate, particularly at 538 °C, where the tests probably need another 12 h to reach saturation.

Effects of Prior History

This section is devoted to describing tests in which some form of prior irreversible deformation was applied to the material before a simple creep, tensile, or stress relaxation test was conducted. The response of the sample with prior history is compared to that of a virgin sample (those without prior history). Understanding history effects is important since often components in service are subjected to complex histories (e.g., overloads) that significantly affect their subsequent behavior and remaining life of the component. Consequently, such behavior must be factored into any rigorous prognostic approach. These history effects are complicated, often synergistic, and difficult to model. Therefore, coupon tests involving important hereditary effects help differentiate between “good” and “bad” models and provide insight into what features must be included in a given model.

Step relaxation tests were performed in which multiple relaxation holds are applied at increasing strain levels. Figure 48 shows relaxation behavior at 427 °C and strain levels of 0.006, 0.012, and 0.018. These tests were conducted at a loading rate of 10^{-3} s^{-1} using 24-h holds for the relaxation period. The loading sequence is shown in Figure 48(a). Sample 82 involved a relaxation at each of the three strain levels. Sample 31 was relaxed at 0.006 and was subsequently loaded to 0.018 strain and again relaxed. Sample 27 incurred relaxation at 0.012 and 0.018. These data are compared with sample 87, which only

experienced relaxation at 0.018 strain. Excellent reproducibility can be observed among the loadups as the two tests at 0.012 strain overlap, as do the two relaxation samples at 0.006 strain. Hence, any deviation between two curves can be attributed solely to the influence of loading history. For the samples relaxed at 0.006, the subsequent loadups to 0.012 strain were identical, but they achieved a lower maximum stress value (fell short) than the other two samples (87 and 27), which had not yet been relaxed. However, given sufficient inelastic strain the prior history effects diminish. For example with continued straining to 0.018 the previously relaxed sample (31) attained identical stresses to the still-virgin sample (87); whereas sample 82 only experiences additional straining steps of 0.006 with relaxations in between and does not achieve the same stress level at either 0.012 or 0.018.

At a relaxation of 0.012 the virgin sample (27) relaxes to a lower stress than sample 82, which experienced prior relaxation at 0.006. A subsequent loading up to 0.018 strain shows that the two sample curves (82 and 27) do not coincide until nearly 0.018 is reached. However, their saturation stress at 0.018 strain is different and both are higher than the virgin curve (87). By plotting the stress versus time response for relaxation at 0.006 (Fig. 48(b)), 0.012 (Fig. 48(c)) and 0.018 (Fig. 48(d)) strain the ranking of the saturation stress can be best observed.

At 0.006 strain (see Fig. 48(b)), the two virgin samples (82 and 31) tested show excellent reproducibility in their relaxation behavior. At 0.012 strain (Fig. 48(c)) the sample having a previous relaxation at 0.006 (sample 82) and subsequent loadup to 0.012 strain exhibits a stiffer relaxation response (smaller initial relaxation rate and higher saturation stress) than does the still-virgin sample, and even after accounting for a difference in the initial starting stress it does not achieve the same limit stress as the virgin sample (27). This illustrates how prior history can provide additional hardening of the material. At a strain of 0.018 (Fig. 48(d)), the samples with prior relaxation history again appear stiffer than the virgin sample (87). All relaxation responses (including two with prior cyclic history) are shown in Figure 48(d); clearly those with prior history show stiffer relaxation behavior than those without. Note that the two samples (tested at 427 °C) that had experienced 50 fatigue cycles at ±0.01 strain prior to relaxation had a slightly stiffer behavior than the virgin sample, but a more compliant behavior than the three monotonically loaded samples with prior relaxations. It should be noted that these samples had a near-constant stress response over the 50-cycle test, indicating that neither experienced significant cyclic hardening or softening. Therefore one might expect relaxation behavior closer to that of the virgin sample.

Normalizing these relaxation curves at 0.018 strain, which eliminates differences in the maximum stress, yields a slightly different result (Fig. 48(e)). The virgin sample (87) and the two samples that were first cycled have the softest behavior. The next stiffest samples were 27 and 31, which only had one previous relaxation, albeit at different strain levels. The stiffest sample (82) was subjected to two prior relaxations.

Additional step relaxation tests at 427 °C are shown in Figure 49 for samples loaded at slow strain rates (i.e., 6 and 8×10^{-7} s^{-1}). Clearly, reproducibility (sample-to-sample variation) is not as good for the slower rate tests as for the faster rate loading tests shown in Figure 48. This is consistent with experience that initial defects, flaws, and residual stresses can influence inelastic behavior response more so than the elastic response. Note that samples 20 and 11 appear to be almost identical (similar responses in Fig. 49(a)), yet the load rates are not exactly the same. By limiting the view to responses up to 0.006 strain, one can get a good feel for the sample-to-sample variation. In Figure 49(b) four samples (24, 44, 58, and 84) were relaxed at 0.006 strain with samples 24 and 58 subsequently loaded to 0.012. Clearly, sample 58 achieves the highest stress of all samples at 0.012 strain. However, sample 58's initial loading response is slightly harder than sample 24 and 84 as well, thus suggesting that this sample was initially harder. This is substantiated by the fact that its yield point is a bit higher than the other two (e.g., $\sigma_{0.2}$ of

272 MPa for sample 58 compared to 246 MPa for sample 24) even though sample 58 was loaded at a bit lower strain rate (6 vs. 8×10^{-7} s^{-1}). In Figure 49(b) the reproducibility of relaxation at a strain of 0.006 is shown in stress-versus-time space. Note that sample 44 was terminated early because of equipment problems. The two tests from the slowest strain rate (58 and 84) have the stiffest relaxation behavior. However, the maximum difference in the saturation stresses is only 17 MPa (maximum stresses differ by 9 MPa), and both of these samples have higher yield points (58 has the highest). Normalization of the relaxation stress against maximum stress (Fig. 49(b)) eliminates the small difference in the maximum stress, but the ranking of the curves remains identical to the nonnormalized versions. At a relaxation strain of 0.012 (Fig. 49(c)) there is essentially no difference between the relaxation behavior of a virgin sample (48) and one with a prior relaxation at 0.006 strain (24). This is in contrast to results at the faster strain rate of 10^{-3} s^{-1}, thus indicating that material memory fades with continued inelastic straining (note at a slow load rate one has more inelastic strain within the same total delta strain). A similar observation can be made for the relaxation response at a total strain of 0.018 as shown in Figure 49(d). Again in contrast to the fast-rate tests, all curves tend to converge regardless of prior history.

The effects of prior cycling on the relaxation behavior at 0.018 strain and 427 °C are shown in Figure 50(a) for two different loading rates. Figure 50(b) is the normalized version of this plot. For fast-rate (10^{-3} s^{-1}) tests, the virgin samples (dashed lines) relax to the lowest values. Directly above them is the curve for a sample cycled 50 times at ±0.01 strain before relaxing. The highest curve is from a sample previously relaxed at 0.018 strain, then cycled 50 times at a strain of ±0.018 and then relaxed again at 0.018 strain. Note that each of these initially cycled samples is harder than the virgin samples, and the sample with previous relaxation and cycling is harder than the sample with cycling alone.

The two samples tested at a loading rate of 1×10^{-5} s^{-1} fall above the faster-rate curves as have been shown previously. There was no significant difference in the relaxation behavior between the virgin sample and the sample, which was first cycled 20 times at a strain rate of 1×10^{-5} s^{-1} and a strain range of ±0.01. The cycled sample exhibits a slight hardening behavior upon loading; however, this small difference disappears as relaxation continues.

History effects as a function of temperature are shown in Figure 51(a) with its normalized version in Figure 51(b). Here the relaxation curves for fast loading rates (10^{-3} s^{-1}) are plotted with dashed lines for virgin samples and with solid lines for samples with prior history. These samples were part of the viscoelastoplastic series and had multiple loadings before the final relaxation at 0.018. Sample 77 was terminated prematurely because of equipment problems. In all cases, the samples with prior deformation history were harder than their virgin equivalents, and this difference appears to become greater as the test temperature decreases since thermal recovery lessens. This is consistent with the fact that at high temperatures thermal recovery mechanisms (e.g., dislocation annihilation) compete with hardening mechanisms (e.g., dislocation pile-ups). In the one instance at 538 °C where the virgin sample (70) is slightly higher than the sample with prior history, the virgin sample was loaded at a slower strain rate of 5×10^{-4} s^{-1}. This behavior is therefore consistent with the previously mentioned observation that lower loading rates cause less relaxation.

One additional relaxation test was performed at a strain of 0.018 and 538 °C. After relaxing for 24 h, the sample was unloaded to zero strain and recovered for 24 h (Fig. 52). This is one of the few tests in this study that was recovered at zero strain (a stress relaxation recovery) rather than zero load (a creep recovery). Consequently, this test gives some limited insight into the material behavior in compression. The relaxation curves shown in Figure 52(b) indicate that most of the stress has relaxed in a 24-h timeframe. Similarly, the sample recovers after unloading to nearly a zero stress state. Neither of these relaxation periods reduces the stress to zero, nor would they, if given longer relaxation periods. It should also be noted that the maximum stress is similar in both the loading and unloading portions of the stress-

strain space, with the compressive maximum stress being 5 percent larger than in tension. The final saturated stress value in both tension and during recovery is also similar: 22 and –29 MPa.

Cyclic Tests

Since the ultimate goal of this experimental program is to improve life prediction, an important aspect of service conditions to consider is fatigue. Therefore, a limited series of fatigue tests were conducted. However, only the deformation portion of these cyclic tests is presented in this report. Failure (N_f, lifetime) will be presented in a future publication.

Fully reversed, strain-controlled tests were conducted at 427 and 538 °C. In Figure 53 hysteresis loops 1, 25, and 50 are plotted for a sample cycled for 50 cycles at 427 °C at a rate of 10^{-3} s^{-1} and between strain limits of ±0.01. Results indicate no cyclic hardening or softening over this number of cycles as shown by the overlapping of the three hysteresis loops. However, cycling another sample at the same temperature of 427 °C and strain limits of ±0.01, yet at a slower strain rate of 1×10^{-5} s^{-1}, a slight cyclic hardening is observed after the first cycle (see Fig. 54). Thereafter and up through 20 cycles, the sample exhibited very little change. For engineering purposes the small amount of hardening in the second cycle can probably be ignored. Note that both of these cyclic tests were subjected to subsequent relaxation tests, and their relaxation behavior was shown in Figure 50. At 538 °C and a rate of 10^{-3} s^{-1}, a sample was cycled between strain limits of ±0.01 for 50 cycles (Fig. 55). There is some slight evidence of cyclic softening over a range of 50 cycles; however, the amount of softening is only 8 percent (i.e., 35 MPa).

An additional strain-controlled cyclic test was performed under zero-tension loading at a strain ratio ($R_\varepsilon = \varepsilon_{min}/\varepsilon_{max}$) of zero. The test was conducted for 20 cycles at 538 °C, a rate of 1×10^{-5} s^{-1}, and between strain limits of 0 and 0.018. Figure 56 shows the hysteresis loops at cycles 1, 7, and 20. The test assumes a fully reversed form on a stress basis already in the first cycle. There is limited hardening and softening throughout the 20 cycles, although there is a slight negative shift (17 MPa) in the mean stress with increasing cycles with an obviously large shift after the first loading.

Two additional tests were conducted under load control rather than strain control, an equivalent elastic strain rate of 10^{-3} s^{-1}, and at 427 °C. Both of these tests were run under zero-tension conditions at a load ratio ($R_\sigma = \sigma_{min}/\sigma_{max}$) of 0. The first test (Fig. 57) was cycled between 0 and 640 MPa until failure occurred at 115 cycles. The maximum stress represents a value close to the ultimate strength under these conditions (compare with Fig. 7). The sample incurs a large strain on the first cycle. Unloading yields a permanent strain offset just short of 0.06. Subsequent cycles show plastic strains (width of the hysteresis loop) that continually decrease with increasing cycle number and a continually increasing mean strain. Moreover, none of the loops are completely reversible; that is, they do not come to complete closure upon unloading to zero stress, although they get closer to this state as cycling continues. This behavior is termed “strain ratcheting” and is typical of load-controlled tests at positive load ratios (Manson and Halford, 2006) and has also been observed in high-cycle-fatigue tests on Ti-6-4 (Morrissey, McDowell, and Nicholas, 1999). Note also that the hysteresis loops are rounded at the maximum load rather than exhibiting a sharp reversal as in the strain-controlled tests (Fig. 53). Similar behavior has also been observed in TiMetal 21S for load-controlled fatigue tests at elevated temperatures (Solimine and Lissenden, 2004).

The second sample (Fig. 58) was tested under similar conditions, but was a lower maximum stress of 600 MPa. This stress is approximately 70 MPa above the $\sigma_{0.2}$ and 55 MPa below the expected UTS. The first cycle yields a permanent strain at 0 load of approximately 0.02, three times less than that attained in the first cycle of the previous test (Fig. 57(a)). Again, subsequent cycling leads toward tighter hysteresis

loops and increasing mean strains. Note that the accumulated strain after 50 cycles is one-third of the previous test at the higher load, which was subjected to only a 40-MPa higher stress.

The creep ratcheting behavior of both of these tests is plotted in Figures 57(b) and 58(b). The maximum and minimum (negative) strains are shown as a function of time and both exhibit a typical three-stage creep deformation behavior. This behavior is less evident for the higher stress test shown in Figure 57(b) and is understandable since the maximum stress is fairly close to the UTS and failure occurs rather rapidly as soon as small amounts of damage are incurred. At the lower stress (Fig. 58(b)) the sample has more time to deform and more normal creep mechanisms rather than tensile overload dominate. In both figures the strain evolution from constant monotonic load creep tests are shown for comparable stresses. For the high-stress test (Fig. 57(b)), the closest creep stress level available was 596 MPa, which is substantially lower than the 640-MPa maximum stress of the fatigue test. Hence the creep behavior is significantly lower and is not a very good comparison to the strain behavior from the fatigue test. However, the strain behavior from three creep tests are shown in Figure 58(b) at stresses between 586 and 596 MPa, which are only a bit lower than the 600-MPa maximum stress for the fatigue test. Note that the peak strain behavior for the fatigue and the 596-MPa monotonic creep test show remarkable agreement. The creep tests at the lower stresses do, however, exhibit a more significant deviation from the fatigue response. The fatigue behavior does appear "shortened" in that the onset of tertiary creep and final failure of the sample occurs at half the time of that observed in the creep response. However, this is not unusual for observed variability in typical creep lives. More tests would have to be conducted to determine if monotonic creep is representative of the ratcheting behavior observed in the fatigue tests, or if the cyclic nature of the fatigue provides added and synergistic mechanisms to the process.

Finally, a cyclic test at 427 °C was performed with tensile and compressive dwells. The purpose of this test was to introduce creep segments into the load spectrum and determine if the cycling altered the basic creep behavior compared to the virgin state. Also, similar holds are experienced in service conditions of many components. This test was conducted under load control between stress limits of ±375 MPa, a stress value just above the *PL* of 364 MPa. An equivalent elastic strain rate of 10^{-3} s^{-1} was employed, and the dwell hold periods were 1 h in length. A total of 20 cycles were conducted on this sample. Hysteresis loops for cycles 1, 2, and 20 are shown in Figure 59(a). There is a slight shift in the loops toward a more fully reversed strain situation (ratchets toward compression) as the cycling increases. It can be observed in the figure that there is significant creep, on the order of 0.002, incurred during each dwell. Note not all of this time-dependent strain is irreversible: up to the threshold, *Y*, all of the strain is viscoelastic and reversible, and above *Y* a portion of the time-dependent strain is still viscoelastic and reversible. Figure 59(b) compares the creep from the tensile holds at the same three cycles to the creep behavior on virgin samples tested under equivalent conditions. Total axial strain is shown in Figure 59(b) and creep strain, in Figure 59(c). The creep behavior in tension from the first cycle compares well (as it should) with the other two virgin samples (all dotted lines). The amount of creep strain during the second cycle is greater, and there is a lower creep rate after 1 h of creep, than what was observed in the first cycle. After 20 cycles, creep is initially similar to that observed in cycle 2, but it quickly becomes less and has a flatter shape, corresponding to a lower creep rate. Ranked from most to least amount of creep are cycles 2, 1, and 20. Hence cycling has a slight hereditary effect on the creep behavior. The amount of creep during the compressive hold increases from cycle 1 to 2 to 20 (Fig. 59(c)). Only the creep in cycle 1 is higher in compression than in tension. For cycles 2 and 20, the reverse is true.

Plasticity-Creep Interactions

The next series of tests investigated the interaction of plasticity and creep by performing histories involving step creep tests and tests with an overload followed by creep. Figure 60(a) shows results for a

series of tests at 316 °C and an equivalent elastic $\left(\dot{\sigma}/E_D\right)$ loading rate of 10^{-3} s^{-1}. Also shown in this figure are the average yield stresses at 316 °C and a loading rate of 10^{-3} s^{-1}. Depicted in Figure 60(a) are three creep tests on virgin samples at stresses of 520, 561, and 587 MPa to show the baseline creep data. There is also a sample (41) that was crept at the same three stress levels in succession with an 8-h creep hold at each stress level. After creeping at the highest stress (586 MPa) for 8 h, the stress on this sample was reduced back to 517 MPa and crept again for 8 h. The final sample (19) experienced an overload in which the sample was loaded to a maximum stress of 586 MPa, unloaded to 553 MPa, and then crept at that stress level for 24 h as shown in Figure 60(b). Note that upon unloading at 586 MPa, the axial strain continued to increase for another 700 με, creating a forward momentum similar to what was observed during load-controlled fatigue (Fig. 57(a)). This was accompanied by an order-of-magnitude increase in the responding strain rate (Fig. 60(c)). Consequently, what appeared to be a linear portion at the end of the unload yielded an unloading modulus of 177 GPa, which is significantly higher than the average modulus of 91 GPa at this temperature and load rate. Hence, forward momentum was still influential during the entire unload. Such rounding in the stress-strain behavior has been observed by Morishita et al. (1988) in 304 stainless steel and was suggested to be a result of the overstress acting in the direction of the applied stress when unloading starts.

Comparison of all creep behaviors (in a total strain representation) for these tests is shown in Figure 60(d). At the lowest stress value the behavior from the step test (sample 41) and the virgin test (sample 9) are similar and have similar creep rates. At the next step the strain increases but not as high as for the virgin sample (86) indicating that hardening occurred during the first creep step. The creep rates at the end of the step (given in parentheses in the plot) are not too different from one another, especially considering that the rate for the virgin sample was calculated after 24 h rather than after 8 h for the step test. The third step shows a significant variation between its creep levels and those of the virgin sample (66), exhibiting a still harder behavior due to the first two creep steps. Its creep rate is half that of the virgin sample tested at the same stress. After unloading the step-test sample back to 517 MPa, the strain is significantly higher than the initial creep strain in the first step—understandably so, since the total accumulated strain is plotted on the ordinate. Also, the final creep rate is nearly an order of magnitude lower than the virgin samples at the same stress level. Here the step process led to work hardening and less creep.

These curves were replotted using creep strain on the ordinate, where the loading strains have been subtracted. In Figure 60(e) both axes have been reset to zero at the beginning of each step. In Figure 60(f) the time has been reset for zero; however, the creep strains have not been and include all accumulated creep strains. Creep in the first step (41) is nearly identical to that observed in sample 9. The second step exhibits more creep than the virgin sample (86) at a similar stress level and has a larger primary regime. At the highest stress level, the third step, the sample experiences a similar creep amount as the virgin sample (86), which was at a slightly lower load. The behavior at the third step can also be compared to a second virgin sample crept at 587 MPa. There are two curves given in the figure for the virgin sample (66). The dotted line represents the complete data and is situated at much higher creep strains than the step test. However, there was an instantaneous jump in the strain at the beginning of the creep process, which could have been due to slippage of the extensometer. It could also have been real behavior and a result of dislocation unlocking, since deformation at this temperature exhibited dynamic strain aging. Hence, the second curve for this sample (dashed line) removes this “jump” in strain and the magnitude of creep strain is more in-line with both the step test and the second virgin sample.

Upon unloading back to 517 MPa, the step test shows negligible creep and is much lower than the initial creep for similar stress levels. The amount of creep and the final creep rate are both significantly less than observed in both the first step (an equivalent load) and the virgin sample (9). Finally, the

overload sample (19) exhibits similar creep amounts and rates as the virgin samples tested at lower stress levels (33 MPa less) implying that the overload caused hardening in sample 19.

A similar series of tests was conducted at a higher temperature of 427 °C and a loading rate of 10^{-3} s^{-1}. The step creep test was conducted for sample 49 at stress steps of 372, 440, 472, and 372 MPa, followed by an unload to zero load and a recovery. Its stress-strain curve is compared in Figure 61(a) with virgin creep tests at the same stress levels, along with an overload creep test (shown in Fig. 61(b)) in which the stress was loaded to 514 MPa, unloaded to 446 MPa, and crept for 24 h. The creep behavior (total strain versus time space) for these tests is given in Figure 61(c), and the creep strain versus time is given in Figure 61(d). The creep curves for the first stress level (375 MPa) show good reproducibility, as they should since at this point all three samples are in the virgin state. With increasing step levels the final creep rate increases (consistent with increment in stress) for each successive step. At the middle stress level (440 MPa) its creep rate is less than that of the virgin sample (78). This is consistent with the fact that the first step work hardened the material and increased its *PL* to 435 MPa, much higher than 378 MPa for the virgin sample. In contrast, at the highest stress level (473 MPa) the step tests exhibit less creep but a higher creep rate than the virgin sample (51). At this point the *PL* of the step test is 472 MPa, the same as the creep load. In contrast the *PL* of the virgin sample is 396 MPa and its $\sigma_{0.02}$ is 452 MPa, both smaller than the applied creep load. However, the creep rate for the virgin sample after only 8 h was equal to 2.3×10^{-7} s^{-1} and is nearly equivalent to the creep rate for the step test. As the step test is unloaded back to the first step of 372 MPa, its creep behavior is linear, exhibiting no primary creep regime. Moreover, the step-tested sample now has accumulated much less creep by nearly a factor of 2 compared to the virgin samples as well as exhibiting half the creep rate. Similar to the step tests at 316 °C, work hardening due to prior steps at 427 °C decrease the amount of creep strain and the creep rate.

The overload creep test (sample 7) exhibits less creep and a lower creep rate than the virgin sample but higher than those from the second step of the step creep test for equivalent stresses (Fig. 61(c)). It also exhibits a similar response during the overload portion as the sample tested at 316 °C, in which the strain rate increases by an order of magnitude and the strain continues increasing even during the initial portions of unloading (Fig. 61(b)). At the end of unloading the modulus is larger than the original loading modulus by only 4 GPa, a minor difference compared to what was observed at 316 °C and indicates only a minor momentum effect. Figure 61(e) shows the cumulative creep strains versus the time with the beginning of each creep period reset to a time of zero.

At a still higher temperature of 538 °C, an overload creep test (Fig. 62(a)) was conducted at a loading rate of 10^{-3} s^{-1}. The sample (64) was loaded to 241 MPa (slightly above its $\sigma_{0.02}$ of 205 MPa), unloaded to 103 MPa, crept for 24 h, unloaded to zero load, and recovered for another 24 h. In Figure 62(a) the stress-strain curve is compared to a virgin creep test (sample 76C) at 101 MPa, and their creep behavior is shown in Figures 62(b) and (c). Although both samples had identical primary creep regimes, the virgin sample experienced less overall creep and had a lower creep rate than the sample that was first overloaded. This is opposite to what occurred at 316 and 427 °C. This is a bit unexpected since the overload did produce a small amount of inelastic strain, although significantly less than what was produced by overloads at the other two lower temperatures. Also, there is more thermal recovery at 538 °C, and this may reduce the small amounts of work hardening that occur during the overload. The lack of plasticity-creep interaction was unexpected at this temperature. However, examining the initial conditions (E_S and Y) of each of these samples it becomes clear that the overloaded sample has a significantly lower threshold and consequently achieved more inelastic strain during loading than the virgin sample, thus explaining why it crept more. The threshold can easily be determined using the viscoelastic subtraction relation (see Arnold, Saleeb and Castelli (2001) and Lerch and Arnold (2014)). Furthermore, it should be noted that the virgin sample (76C) had a *PL* of 93 MPa, whereas the overload

sample had a very low *PL* (51 MPa) and the applied stress even exceeded its $\sigma_{0.02}$ during loading. Hence we would expect more creep in the overload sample than in the virgin since the creep load was so far past its yield: a softer sample. Note that the forward momentum did not occur in this sample during the load reversal nor was there an increase in the strain rate as the maximum load was approached. This was probably because the amount of inelastic strain was so low for this sample compared to that produced at the lower temperatures.

Thermal Recovery Tests

These tests were designed to examine the effects of a recovery period on the creep behavior. Three tests were run, one at two different maximum stress levels at 427 °C and one at 538 °C. An equivalent elastic loading rate of 10^{-3} s^{-1} was used for both loads and unloads. The test sequence is shown in Figure 63(a) for the sample tested at the lower stress of 375 MPa and at 427 °C. The sample is loaded to 375 MPa and crept for 8 h, unloaded to 69 MPa and recovered for 8 h, reloaded to 375 MPa and crept for another 8 h, and unloaded to zero load and recovered for 24 h. The creep behavior for this sample is shown in Figures 63(b) and (c) and compared to two virgin samples, crept also at 375 MPa. At these loads all of the samples were below their *PL*s. The thermal recovery sample appears to be slightly harder (i.e., less creep) than the other two samples, as indicated by the "first creep" curve. After thermal recovery, this sample exhibits less primary creep and exhibits a flatter creep curve. There is less than half the amount of creep for the same 8-h period, and the creep rate is 32 percent less. It can also be observed that during the thermal recovery the sample exhibits negative creep (strains become smaller with time). The recovery portions at zero load are also shown in this figure. Both of the recovery curves are less than those for the virgin sample, indicating a slight amount of hardening during the thermal recovery test.

A second set of thermal recovery tests was conducted at 427 °C for a higher stress of 575 MPa (which is above the sample's $\sigma_{0.2}$) and a rate of 10^{-3} s^{-1}. Its stress-strain curve is shown in Figure 64(a), and its creep behavior shown in Figures 64(b) and (c). Three virgin creep samples at stresses near 575 MPa are also shown in Figures 64(b) and (c). The "first creep" curve from the thermal recovery sample falls between those of the virgin samples tested at 591 and 596 MPa and lies above the virgin sample tested at 549 MPa. During the "second creep" event, the creep response (Figs. 64(b) and (c)) immediately exhibits secondary creep (i.e., creep rate is constant) and is approximately equal to the creep rate just prior to the unloading in the first creep step. This suggests that an insufficient amount of time (or too low of temperature) was allowed for thermal recovery. Finally, after approximately 6 h (21 600 s) of creep a tertiary regime commenced. As observed with the previous sample, the creep during the thermal recovery period was in the negative direction.

The only direct comparison of the creep behavior at a stress level of 575 MPa is for sample 83. However, sample 83 had prior viscoelastoplastic history and therefore exhibited less creep than in the thermal recovery test. Also, the initiation of damage in sample 88 after the thermal recovery probably accelerated its creep behavior. During the thermal recovery at 69 MPa the sample displayed negative creep (total recovered amount of –1600 microstrain). Comparing this to a viscoelastic creep sample tested also at 69 MPa showed it to display positive creep of +250 microstrain after a similar 8 h. Hence the amount and direction of creep is dependent on the prior deformation history.

Thermal recovery at 538 °C is shown in Figure 65(a). This test was loaded at an equivalent elastic strain rate of 10^{-3} s^{-1} (86 MPa/s) to a stress level of 243 MPa (slightly above its $\sigma_{0.02}$ of 231 MPa) and held for 4 h, followed by an 8-h thermal recovery at 69 MPa, and then a final creep at 243 MPa for 2.7 h. Unlike the samples tested at 427 °C, this sample crept in the positive direction during thermal recovery, indicating that the recovery stress of 69 MPa was too high for initiating recovery rather than further creep at this temperature. The creep behavior is shown in Figures 65(b) and (c), and the first creep period for the thermal

recovery sample falls between the behavior of the other two virgin samples tested at 239 and 241 MPa. At this stress level all three samples eventually enter the tertiary creep regime. During the second creep period the total strains are at a higher total strain value and the creep rates are faster. However, the creep behavior prior to the onset of significant tertiary creep agrees with that from the virgin sample 85. The thermal recovery behavior depicts creep in the increasing strain direction, although it is only a small change in strain. In actuality the sample first crept in the negative direction for a strain of 1100 microstrain then reversed and crept in the positive direction for a strain increment of 3300 microstrain. The thermal recovery portion is consistent with a virgin creep sample tested at a slightly higher stress level of 101 MPa, which crept 6000 microstrain over a similar 8-h period. It does not appear that thermal recovery had much of an effect on the creep behavior in this test, but this was probably a result of the accelerating effect of damage (as evidenced by the tertiary regime) on creep behavior.

Discussion

Aeroengine components are subjected to extreme service conditions that often push the capabilities of the materials. Many of them, such as turbine discs, are exposed to very high temperatures, comparatively high loads, and aggressive atmospheres from the gas path. They are pushed into operating regimes where even the smallest of defects can lead to rapid failure and result in catastrophic failure because of the high amounts of released energy. By nature the design considerations on these components are conservative, which results in excessive weight and corresponding increased fuel consumption. To improve this situation, prognostics systems are needed that can account for the complicated load-temperature-time fields that the material experiences, thereby enabling the optimum use of materials. Simplified models often cannot accomplish this task. The model put forth by Saleeb and Arnold (2001) is general enough to cover a wide range of behavior, albeit at the expense of a larger test program and multiple characterization parameters. In theory these parameters represent different deformation mechanisms operational over varied time and temperature domains, which in reality are necessary for the large range of conditions being incorporated. The characterized model should be able to predict any loading condition over the complete set of temperatures and loading (both stress and strain) rates and include elastic, viscoelastic, plastic, and viscoplastic deformation as needed. Hence the characterization and validation test matrix must also include tests evaluating this wide range of conditions. Although the currently investigated material, Ti-6-4, is not a turbine material, it does have applications in the cooler sections of the engine (thus used over a similar range of homologous temperatures) and will experience most of the same deformation behavior that turbine materials do. The selection of Ti-6-4 resulted from its wide use in jet engines and its similarity to previous experimental work on Timetal 21S for this model (Arnold, Saleeb, and Castelli, 2001). Currently, a similar test matrix (to that presented herein) is being conducted for a Ni-based superalloy turbine disk material, ME-3.

Tensile

Uniaxial tensile tests indicate that, like most materials, Ti-6-4 properties are dependent on both temperature and loading rate. Figures 3 to 11 show the decrease in load-carrying capability as test temperature increases and strain rate decreases. Additionally small, rate-dependent “yielding” is even observed at room temperature (Fig. 3). Although, time-dependent behavior is generally not thought of existing at such low homologous temperatures, titanium alloys have been shown to exhibit these characteristics. There have been many studies showing creep (Doner and Conrad, 1973; Savage, Neeraj, and Mills, 2002; Thompson and Odegard, 1973; Hatch, Partridge, and Broadwell, 1967; Wapniarsky, Rotem, and Rosen, 1991; Chakrabarti and Nichols, 1980; Odegard and Thompson, 1974; Katcher, 1968; and Imam and Gilmore, 1979) and stress relaxation (Chiu, Eftis, and Jones 1990; Stephens and Munford, 1988; Evans, 1987; and Dunn, 1991) at ambient conditions. At higher temperatures, loading rate has an increasingly

larger influence on properties, until at 538 °C there is a spread of approximately 400 MPa in the maximum stress between the fastest and slowest strain rates (Fig. 9). More recently, Ti-6-4 was also shown to exhibit a rate dependence of its initial "elastic" modulus (see Fig. 12), which indicates the existence of viscoelasticity. A previous article by Lerch and Arnold (2014) has fully documented the viscoelastic behavior of Ti-6-4 and has shown that a significant difference in elastic modulus occurs at temperatures of 316 °C and above. At 538 °C the maximum difference in modulus between a very fast (e.g., $1\ s^{-1}$) strain rate and an infinitely slow (e.g., $10^{-7}\ s^{-1}$) strain rate (termed "E_D" and "E_S," respectively, in the GVIPS model) was 71 percent. Thus careful thought must be given to the value of the material stiffness used in typical lifing models at the higher temperatures since it can be rate dependent.

The influence of temperature and loading rate on the apparent yield stress as well as the maximum stress achieved at a strain of 0.018 is shown in Figures 13 to 16. All of these values decrease with increasing temperature and decreasing strain rate. However, at temperatures between approximately 200 and 371 °C, there is a convergence of the rate curves, and at certain temperatures within this range even an inverse relationship between strain rate and yield can occur. It is over this temperature range that dynamic strain aging has been observed in Ti-6-4 (Srinivasan and Venugopal, 2008; Lin, et al., 2011; Nemat-Nasser, et al., 2001; and Katcher, 1968), which also produces a jagged loading curve at low strain rates and an enhanced apparent yield point in certain loading curves as shown in Figures 5 and 6.

Creep

Although monotonic tensile tests have indicated rate dependency, they provide relatively little information regarding long-term time-dependent rate and plasticity behavior compared to other test types such as creep and relaxation. Therefore to better document the time dependency of Ti-6-4, many creep tests were conducted (Table III) over a range of temperatures, stress levels, and loading rates. The creep curves are summarized in Figures 17 to 25 and show the standard three-regime creep behavior (i.e., primary, secondary, and tertiary—if the tests were crept long enough). Note that documentation of total strain is extremely important for characterizing unified viscoplastic models since inelastic strain accumulation during loading can greatly impact its subsequent behavior during constant loading. This is why the creep response curves are usually plotted in this manner. There was very little, if any, steady-state creep observed, and the creep rates mentioned in this report usually represent the minimum creep rates. The total strains and the minimum creep rates all increased with increasing temperature and stress, not taking into account the occasional sample-to-sample scatter. In some cases, particularly at the higher temperatures, there was more scatter in the creep curves. For example, during creep at 427 °C (Fig. 18) the highest three stress levels (i.e., 574, 591, and 596 MPa, respectively samples 88, 45, and 87) were nearly the same (within 4 percent) yet exhibited significantly different creep responses (e.g., 100 percent variation in accumulated inelastic strain within 10 000 s). Sample 87, which had the highest applied stress, had—as expected—the highest creep rate. Yet sample 45, which had only a 5 MPa (0.8 percent) lower applied stress than sample 87, had the lowest creep rate among the three samples. Sample 88's (the lowest applied stress, 3.7 percent lower) creep behavior fell in between the other two. One way to explain such scatter is to examine the "yield" property (e.g., consider definition of 0.2 percent) of each of these samples. In this case all three had exceeded their $\sigma_{0.2}$ during loadup. Samples 88, 45, and 87 had $\sigma_{0.02}$ values of 527, 537, and 526 MPa, respectively. This shows that sample 87 with the highest creep had the highest applied stress but the lowest $\sigma_{0.2}$. The sample with the lowest creep (45) had a similar applied stress, but the highest $\sigma_{0.2}$. The remaining sample (88) was in between.

At 538 °C a similar observance was noted (Fig. 19). Three of the higher applied stress tests (241 MPa) showed fairly wide scatter amongst the creep behavior. Sample 85 had the most creep and appeared to be the softest since its $\sigma_{0.02}$ of 31.6 MPa was exceeded during the loadup. This sample also

had the lowest modulus (80 GPa) of the three samples. Both of the two remaining samples were "stronger" since only their *PL* was exceeded during loadup. Of these two samples, sample 3 had the highest *PL* (77 vs. 74 MPa) and this resulted in sample 3 having less creep strain.

Finally in Figure 26, sample 93 loaded at a slow rate of 7×10^{-7} s^{-1} and 427 °C had a higher creep response than that of sample 57, which was tested at a fast rate of 10^{-3} s^{-1}. This is contrary to the behavior that was previously mentioned about slow loading rate leading to less creep. However, sample 93 had its $\sigma_{0.02}$ of 153 MPa exceeded, whereas sample 57 remained elastic during the loadup. The large difference in the yield points (the average *PL* at 427 °C is approximately 401 MPa for a strain rate of 10^{-3} s^{-1} as given in Table II) can easily explain their rate dependence. Therefore, although the slower strain rate test should have a lower creep response, this is countered by the fact that the applied stress level is so much higher than its yield point. These results show that creep is influenced by both the applied stress and its relationship to the yield point of the sample, the latter being both temperature and loading rate dependent. It is possible that an even better predictor of creep behavior may be the threshold, *Y*, which defines the beginning of irreversible flow and is rate independent. However, the threshold is not measured on every sample and cannot be determined by conducting only one creep test.

Figures 25 and 26 clearly illustrate the impact of loading rate on the resulting creep behavior: faster loading rates result in higher creep strains and creep rates than slower loading rates. The reason for this resides in the fact that during faster loading rates there is less inelastic strain accumulated during loadup than for the slower loading rate tests (compare inelastic strains in Figs. 25(c) and 26(c)). Faster loading rates do not enable significant back stress (α) accumulation during loading, thereby producing a higher initial effective stress ($\sigma - \alpha$) within the material and consequently more creep for a given applied load. Observe that the creep rate is also higher for the faster loading rate. However, these tests probably have not quite reached their steady-state (or minimum) creep values during the given test time. If they had, we would expect both the fast and slow loading rate tests to have very similar creep rates. It should also be noted that the slow-rate test should reach steady state quicker than the fast-rate test because of its lower effective stress.

The creep behavior of this material is consistent with that in the literature of annealed Ti-6-4. This is not only shown with the creep curves in Figures 27 to 29 for a comparison with data from Zerwekh (1978), but also with the minimum creep rate as a function of creep stress in Figures 30 and 31. In Figure 30, results from 500 and 550 °C creep tests from Barboza, Moura Neto, and Silva (2004) and Sastry, Pao, and Sankaran (1980), respectively, show good agreement with the current test data at 538 °C. Fits for these data yield a creep exponent of 2.9 at intermediate stresses and 6.5 for higher stresses. There are insufficient points at very low stresses (i.e., below the viscoelastic threshold) to fit, but based on the trends at lower temperatures, the creep exponent should be very low as the fit line should be approximately horizontal at values of a minimum creep rate $\leq1\times10^{-9}$ s^{-1}. This is because shutdown of the viscoelastic response results in no creep.

A similar plot is given in Figure 31(a) with the axes reversed. This plot was taken directly from Evans and Harrison (1983) for Ti-6-4 with both an alpha/beta and primarily an alpha microstructure. Their fits are also reproduced in this figure. They noted no difference between the behaviors of the two different microstructures. The creep exponents from the tests at 500 °C are 4.1 for intermediate stresses and 7.6 for the higher stresses. These are similar to those from the 538 °C data shown in Figure 30. The exponents from Evans and Harrison are slightly higher, and this could be due to the temperature being 38 °C lower since the exponents increase with decreasing temperature. Both sets of data are superimposed in Figure 31(b) where only the fits from the Evans and Harrison data are shown, and they fit the current data for slightly lower temperatures. A fit of the very low stress data was performed at 538 °C, and the creep exponent was 1.6.

The activation energy for creep is given in Figure 32 along with data from two stress levels from Sastry, Pao, and Sankaran (1980). Their 164 MPa data compares reasonably well with ours at 117 MPa, and their 330-MPa data agrees with our 379-MPa data. The Sastry value for activation energy of 188 kJ/mol at 164 MPa lies in between ours for a slightly higher stress level (246 kJ/mol at 241 MPa) and a lower stress level (179 kJ/mol at 34 MPa). It is observed in this figure that the creep rates at stress levels below the viscoelastic threshold (see Fig. 1 for threshold values) seem to fall on an extrapolation of the fits from the samples tested above the threshold in the viscoplastic regime.

Relaxation

A comparably time-dependent test to creep, yet typically much more repeatable, is the relaxation test. Herein a series of single and multistep relaxation tests were conducted. Typically, samples were loaded to a strain of 0.018 and allowed to relax for 24 h. A typical stress-strain response is shown in Figure 34 for temperatures of 427 and 538 °C. For any given temperature, the material typically relaxed to the same saturation stress, with this stress increasing as the temperature decreased. This is shown in Figure 35, where the relaxation behavior is given over the entire temperature range. At the higher temperatures, replicates were run and exhibited excellent reproducibility. As expected the scatter in relaxation is significantly less compared to that of creep, one reason being the equivalence of engineering and true stress since the cross-sectional area does not change during the relaxation. The relaxation behavior consists of the typical three regimes where there is a rapid drop of stress within the first 500 s. The second regime is a more gradual transition and occurs over an order of about 10 000 s. The final regime consists of very little change in stress with saturation (approximate plateau) occurring at a given temperature-dependent stress. This final stress value is termed the “saturation stress.” With increasing temperature, the transition region (stage 2) appears to occur over a longer timeframe. Moreover, at the temperatures of 200 and 316 °C, the transition appears to be more abrupt; this may have to do with the dynamic strain aging occurring over this range of temperatures. It is also important to note that there is significant stress relaxation at room temperature yielding a 150-MPa difference between the maximum stress and the saturation stress (see Fig. 35(a)). Evans (1987) has shown a similar drop in stress for annealed Ti-6-4 when tested at room temperature. This irreversible time dependency is certainly reflected in the observed room-temperature creep, rate-dependent maximum tensile stress, and albeit very small rate-dependent moduli of titanium alloys. Although this affect is small, this room-temperature time dependence could be of issue, particularly over long periods of time. Stephens and Munford (1988) were concerned about the long-term relaxation of threaded joints, although they found that the amount of relaxation was not a significant amount for their application. Nonetheless, it is a behavior that may need to be considered when designing structures made of titanium.

Since the tension behavior of Ti-6-4 is loading rate dependent, one would expect the relaxation behavior to be rate dependent as well. Figures 36 to 40 document the relaxation behavior at a strain of 0.018 for various temperatures and loading rates. Although difficult to see the trend in these figures, the saturation stress seems to be unaffected by loading rate. However, the range of relaxation definitely appears reduced for lower loading strain rates. This is clearly shown in Figure 41, where the relaxation range is normalized with respect to the maximum stress and plotted versus temperature. The normalized range is slightly smaller for slower strain rates, but this dependence is dwarfed by the temperature dependence of the normalized relaxation range. The magnitude of the normalized range reaches a minimum at 200 °C, probably a result of strain aging, and then increases at higher temperatures.

The target relaxation strain appears to be of minimal importance in determining the saturation stress. Figures 42 and 43 show the 24-h relaxation behavior at 427 °C and strains of 0.006, 0.012, and 0.018 for both a fast and a slow loading rate. In neither case is the dissipation stress significantly different, having a value of approximately 200 MPa; however, more variability clearly exists when the loading rate is slower. Note again in these figures that there is excellent reproducibility in the data for repeat tests. The similarity of the relaxation behavior is better shown in Figure 44, where all the samples from the previous two figures would converge in the limit on the stress level of 200 MPa. The slower rate tests are a bit higher, which suggests that the amount of time necessary for full dissipation to occur is longer than for the fast-rate tests. This is consistent with the previous observation that slower loading rates produce less driving force for deformation mechanisms. The relaxation behavior is simply driven by the maximum stress (i.e., effective stress) attained during loadup, which is temperature and strain rate dependent. To help sort this out, the data were normalized in Figure 45 with respect to their maximum stresses. It can be observed that the slower rate tests again have a lower relaxation range (since a larger back stress α is achieved during loadup) than for the fast-rate tests. There also appears to be no clear differentiation in range based on the strain level. This can also be seen in Figure 46.

We conclude that the saturation stress is independent of strain level, but is a function of temperature and has a slight strain rate dependency. Moreover, the saturation stress appears to agree with the threshold stress value, Y, as indicated by comparing Figures 1 and 47(a). Considering that the exact value for Y was unknown for each of these samples, and an average had to be calculated from other samples, the stress threshold between reversible and irreversible behavior appears to be the lower limit for relaxation. This is further shown in Figure 47(b), where the instantaneous stress is normalized by the average value of Y. Given sufficient time to fully relax, all samples at all temperatures asymptotically reach a normalized value of 1. However, it can be seen in this figure that the 24-h relaxation time was insufficient to permit complete dissipation of the viscous mechanism. The higher the temperature, the more time was needed to reach full saturation, and it was estimated to require 48 h at 538 °C rather than the 24 h used in this study.

History and Cyclic Effects

The introduction of irreversible (e.g., plastic) deformation often leads to work hardening of an alloy, and this could in turn lead to changes in the subsequent deformation behavior; that is, a higher postdeformation strength (maximum stress) and less time-dependent behavior. However, it is not as clear what will happen if the load reverses or other more complicated deformations occur. Therefore it was important to conduct a series of tests that involved a deformation "history." The first set involved multistep relaxation tests, with steps encompassing previously used strains of 0.006, 0.012, and 0.018 for easy comparison to the virgin state. In Figure 48 tests are shown that have various sequences of these target strains. Both samples relaxed at the strain of 0.006 (Fig. 48(b)) show excellent reproducibility due mainly to the fact that they are both virgin samples for this step. Both samples also fall short of the maximum stress when reloaded to a strain of 0.012 (Fig. 48(a)) compared to the other two virgin tests at a strain value of 0.012. This difference (between virgin and prior-history tests) apparently disappears when the sample (31) is further strained to 0.018 (Fig. 48(a)). Note that the sample with history relaxed at 0.012 (82) does not relax as much as the virgin sample relaxed at 0.012. This is due to the additional hardening (increase in back stress α) incurred during relaxation and reloading. However, both of these samples converge to the same saturation stress level after further straining to 0.018; albeit both are still lower than a virgin test and the sample (31) that was first relaxed at a low strain (0.006). The relaxation behavior at a strain of 0.018 is shown in Figure 48(d). The sample that relaxed the most was the virgin sample (87). All other samples shown in this figure relaxed less, thus indicating a hardened state (higher back stress) as compared to the relaxed virgin sample (87). The hardest sample was 82, which had relaxations at all three levels, and this hardening would be expected since

it had the most prior history. However, sample 31 only had a relaxation at the strain of 0.006, which is barely beyond the elastic range; and with another 0.012 plastic strain increment one might expect the prior history to be erased, yet this is not the case. This indicates that the effects of history are not that straightforward. This complexity necessitates additional mechanisms in the model, such as those representing hardening interacting with those describing recovery.

Finally, in Figure 48(d) are curves from two fatigue samples (5 and 87B) that were subjected to 50 cycles at ±0.01 strain before relaxing at 0.018. These two curves illustrate their relaxation behavior to be slightly harder than the virgin sample's, but softer than the step relaxation test samples' behavior. Note that neither of the cycled samples displayed much if any cyclic hardening or softening over the 50 cycles, suggesting that there was minimal change in the deformation state during the fatigue process. It is interesting to note that the fatigue samples were monotonically strained to a strain of 0.01 during their first (and subsequent) cycles and yet they behave more like virgin samples than they do samples relaxed at monotonic strains of 0.006 and 0.012.

When tested at slower strain rates, history affects the relaxation behavior less as shown in Figure 49. Although there seems to be a small rate effect for very small rate differences (6 vs. 8×10^{-7} s^{-1}) at a strain of 0.006 as shown in Figure 49(b), at the other two strain levels (Fig. 49(c) and (d)), prior history does not seem that significant. Presumably the lower loading rates give the samples sufficient time to adjust their internal deformation structure and reduce the effects of previous deformation.

The effects of previous cycling on the relaxation behavior at 427 °C and 0.018 are shown in Figure 50. In this figure the dashed lines depict the virgin relaxation response, and the solid curves have prior history. Strain rates of 10^{-3} s^{-1} and 1×10^{-5} s^{-1} are represented in this plot. This figure indicates that the strain rate has a larger effect on the subsequent relaxation behavior than does the number of prior cycles. The rate of cycling also appears to have a minimal effect.

Tests in load control often exhibit a rounding of the stress-strain curve at the point of load reversal. This can be observed in Figures 57(a) and 58(a) for fatigue and in Figures 60(a) and 61(a) for overload creep. The behavior, in which the inelastic strain continues in the direction of the original applied load, has been observed in type 304 stainless steel by Morishita et al. (1988) and attributed to an overstress as described by Krempl (1979). The overstress (or as many others call it, "effective stress") is the difference between the applied stress and the back stress. Hence even upon unloading, if the applied stress is still larger than the back stress, the material will continue to flow in the same direction.

Another possible explanation is that there is an inertial effect based on the rapid reversal at the peak. Examination of the stress-time curve (Fig. 60(b)) for the overload creep samples shows clean, crisp peaks indicative of a well-controlled test rig. However, the strain response is nonlinear because of the inelastic strain. Moreover, calculations of the strain rate show that it increases from the elastic regime up to the point of load reversal. This increase spans approximately one order of magnitude. It is possible that this is fast enough that the extensometer cannot keep up with the expected decrease in strain. Although, the data from Figure 60(c) indicate that the strain continued in the forward direction for 0.4 s after the load was reversed and this would seem to be sufficient time for the extensometer to catch up with the stress. Nonetheless, the dynamic response of the extensometer is near its upper reactivity limit at these rates.

Note that this behavior does not appear in the overload-creep test at 538 °C (Fig. 62(a)). This is probably because the loading curve is nominally linear and very little inelastic strain has been incurred. The strain rate was also noticed to remain constant up to the load reversal at which point the rate decreased into the negative regime. It is suspected that with higher overload stresses, the forward-going behavior would return. In fact the fatigue test in Figure 57(a) and 427 °C shows rounded peaks and was loaded to a higher stress well past its $\sigma_{0.2}$.

Summary of Results

The time and loading-rate dependence of deformation in the reversible regime was investigated and documented for annealed Ti-6Al-4V. Tensile, creep, and stress relaxation tests were performed over a wide range of temperatures and strain rates to be able to observe various amounts of time-dependent behavior. Additional tests were conducted that involved loading steps, overloads, dwell periods, and block-loading segments to characterize the interaction between plasticity and time-dependent behavior. These tests are in support of characterization of the GVIPS (generalized viscoplasticity with potential structure) viscoelastoplastic constitutive model, which will be used in life prognosis for aircraft engines. The salient features of this work are as follows:

- The tensile behavior was found to be both temperature and loading rate dependent over the entire temperature regime of 20 to 538 °C, with larger contributions of time-dependent deformation occurring above 316 °C.
- The time-dependent deformation was irreversible with a smaller fraction of deformation being caused by reversible mechanisms. The stress threshold delineating the boundary between reversible and irreversible regimes is referred to in the model as "*Y*," and this value (or its strain equivalent) is referenced to the various load levels in these tests.
- Creep amounts and creep rates were dependent on both the temperature and loading rate as well as the proximity of the creep stress to the yield points. The scatter in the yield points led to significant scatter in the creep responses.
- Stress relaxation tests were performed over the entire range of temperatures at various strain rates and strain limits.
    - Temperature and strain rate affected the maximum stress and the amount of relaxation. Higher temperatures resulted in lower maximum stresses and more relaxation. Slower strain rates resulted in lower maximum stresses and less relaxation.
    - Given sufficient time, the stress tended to relax to the threshold stress, *Y*.
    - The material exhibits significant relaxation (150 MPa) even at 20 °C.
- Cyclic loading under strain limits showed very minimal hardening or softening. A test conducted between zero and a maximum load exhibited extensive strain ratcheting in the tensile direction. This ratcheting appeared to be very similar to the deformation observed in monotonic creep tests under similar conditions.
- Prior deformation tended to harden the material. In creep, prior deformation resulted in less creep and the minimalization or elimination of the primary regime. The creep rates were usually less for samples with prior deformation.
- Thermal recovery resulted in an alteration of the subsequent creep behavior, with the effect being dependent on the stress level of recovery. If the recovery stress was sufficiently low, recovery would occur and result in less creep in the subsequent step with a minimal primary regime. If the recovery stress was too high, the sample would continue to creep during recovery and result in more creep during the subsequent step.

Conclusions

This study shows that Ti-6Al-4V experiences a significant amount of time-dependent deformation when subjected to loads. This is true even at low temperatures, although to a lesser amount than when tested above 316 °C. The deformation behavior is highly dependent not only on temperature, but also loading rate and prior deformation history. Deformation behavior at high temperatures is determined by

the interplay between hardening and recovery. Additionally, all of the deformation occurring at stresses above the threshold, *Y*, contain both reversible and irreversible behavior. Attempts at modeling the complex, time-dependent behavior can only be accomplished with a large number of modeling mechanisms that address the various regimes in which they are active. Consequently this requires a large number of tests to characterize such a model and multiple ways of examining the data. This study has accomplished this goal by conducting various mechanical tests over a very wide range of conditions and has generated a large and thorough database. These data will be used to characterize the GVIPS model, and can also be employed to characterize or verify any other constitutive model of interest. A future, final publication in this experimental study on Ti-6-4 will address damage and failure.

TABLE I.—TEST SAMPLE MATRIX

Sample	Test type[a]	Strain rate, s^{-1}	Loadup mode	Strain level[b]	Stress level,[b] MPa	Comments[c]
20 °C						
89A	Relaxation	6×10^{-7}	Strain	0.018	862	Unload, with 12-h recovery
89B	Relaxation	10^{-3}	Strain			Step relaxation every 0.02 to 0.12 strain; sample tested previously
10	Relaxation	10^{-3}	Strain	0.018	941	With two load reversals to 0 strain
200 °C						
56	Relaxation	6×10^{-7}	Strain	0.018	659	Unload, with 14-h recovery
50	Relaxation	10^{-3}	Strain	0.018	705	With two load reversals to 0 strain
316 °C						
55	Relaxation	6×10^{-7}	Strain	0.018	629	Unload, with recovery
42	Tension	10^{-5}	Strain			Tension to 0.198 strain; unload, with recovery
33	Relaxation	10^{-3}	Strain	0.018	601	Unload, with 19-h recovery
41	Creep	10^{-3}	Stress		517, 552, 586, 517	Step creep (8-h holds); unload, with recovery
19	Creep	10^{-3}	Stress		553	Overload to 586 MPa, then creep at 553 MPa
79	Tension	10^{-3}	Strain			Tension to 0.199 strain; unload, with recovery
9	Creep	10^{-3}	Stress	0.006	520	Unload, with 20-h recovery
86	Creep	10^{-3}	Stress	0.006	561	Unload, with 22-h recovery
66	Creep	10^{-3}	Stress	0.009	587	Unload, with recovery
371 °C						
80	Relaxation	6×10^{-7}	Strain	0.018	584	Unload, with recovery
29	Relaxation	10^{-3}	Strain	0.018	590	Unload, with 42-h recovery
53	Creep	10^{-3}	Stress	0.006	513	Unload, with recovery
427 °C						
84	Relaxation	6×10^{-7}	Strain	0.006, 0.008	379	No unload or recovery
58	Relaxation	6×10^{-7}	Strain	0.006	390	Relaxation with subsequent loadup; reload to 0.012 and stop
20	Relaxation	6×10^{-7}	Strain	0.018	481	No unload or recovery
93	Creep	7×10^{-7}	Stress	0.006	374	Unload, with 42-h recovery
44	Relaxation	8×10^{-7}	Strain	0.006	375	6-h relaxation; no unload

TABLE I.—Continued.

Sample	Test type[a]	Strain rate, s^{-1}	Loadup mode	Strain level[b]	Stress level,[b] MPa	Comments[c]
24	Relaxation	8×10^{-7}	Strain	0.006, 0.012, 0.018	372, 463, 484	Unload, with recovery
67	Relaxation	8×10^{-7}	Strain	0.006, 0.018	287, 356	No unload or recovery
48	Relaxation	8×10^{-7}	Strain	0.012, 0.018	461, 485	Unload, with recovery
11	Relaxation	8×10^{-7}	Strain	0.018	503	Unload, with 20-h recovery
32	Relaxation	10^{-5}	Strain	0.018	472	Unload, with recovery
46	Relaxation	10^{-4}	Strain	0.018	549	Unload, with recovery
40	Relaxation	10^{-4}	Strain	0.018	570	Apply 20 cycles at ±0.01 strain before relaxation
69	Tension	10^{-4}	Strain			Tension to 0.198 strain; unload, with recovery
91	Relaxation	10^{-4}	Strain	0.018	530	Unload, with 42-h recovery
5	Relaxation	10^{-3}	Strain	0.018	591	Apply 50 cycles at ±0.01 strain before relaxation
61	Relaxation	10^{-4}	Strain	0.018	572	Unload, with 59-h recovery
51	Creep	10^{-3}	Stress	0.005	471	Unload, with recovery
27A	Relaxation	10^{-3}	Strain	0.012, 0.018	549, 540	Unload, with recovery
27B	Relaxation	10^{-3}	Strain			Step relaxation at 0.03 and 0.049 strain
27C	Tension	10^{-3}	Strain			Test interrupted at 0.11 strain
27D	Relaxation	10^{-3}	Strain			Relaxation at 0.13 strain; failed at 0.139 on subsequent loadup
31	Relaxation	10^{-3}	Strain	0.006, 0.018	491, 574	Unload, with recovery
87A	Relaxation	10^{-3}	Strain	0.018	577	Unload, with recovery
87B	Relaxation	10^{-3}	Strain	0.018	605	Prior deformation + 50 cycles at ±0.01 strain before relaxation
43	Relaxation	10^{-3}	Strain	0.018	590	Unload, with 21-h recovery
82	Relaxation	10^{-3}	Strain	0.006, 0.012, 0.018	485, 523, 541	Unload, with recovery
63	Creep	10^{-3}	Stress	0.002	139	Unload, with recovery
49	Creep	10^{-3}	Stress		372, 441, 476, 372	Step creep (8-h holds); unload, with recovery
7	Creep	10^{-3}	Stress		446	Overload to 514 MPa, then creep at 446 MPa
72	Creep	10^{-3}	Stress	0.007	527	Unload, with 4-h recovery
7*	Creep	10^{-3}	Stress	0.010	550	Unload, with 4-h recovery
45	Creep	10^{-3}	Stress	0.018	591	Unload, with 4-h recovery
35	Creep	10^{-3}	Stress	0.018	585	Unload every 0.02 to 0.14 strain; unload, with recovery
87	Creep	10^{-3}	Stress	0.025	596	Creep to failure (0.204 strain) with periodic unloads
88	Creep	10^{-3}	Stress	0.016	574	Creep to 0.19 strain with periodic unloads
36	Creep	10^{-3}	Stress	0.004	374	Creep (thermal recovery); unload with recovery
96	Cyclic creep	10^{-3}	Stress		379	$R_\sigma = -120$ cycles with 1-h creep holds at max. and min. stresses
95	Tension	10^{-3}	Strain			Tension with unloads every 0.01 to 0.20 strain
23	Tension	10^{-3}	Strain			Tension to failure (0.196 strain)
98	LCF	10^{-3}	Stress		547	$R_\sigma = 0$; failure at 130 683 cycles
58	LCF	10^{-3}	Stress		643	$R_\sigma = 0$, failure at 115 cycles
78	Creep	10^{-3}	Stress	0.005	441	Unload, with recovery
57	Creep	10^{-3}	Stress	0.004	375	Unload, with 29-h recovery
52	Creep	2.4×10^{-3}	Stress	0.006	508	No unload or recovery
59	LCF	10^{-3}	Stress		595	$R_\sigma = 0$; failure at 9735 cycles
57	LCF	10^{-2}	Stress		534	$R_\sigma = 0$; interrupt at 580 948 cycles
56	LCF	10^{-2}	Stress		582	$R_\sigma = 0$; failure at 22 134 cycles

TABLE I.—Concluded.

Sample	Test type[a]	Strain rate, s^{-1}	Loadup mode	Strain level[b]	Stress level,[b] MPa	Comments[c]
482 °C						
22	Relaxation	6×10^{-7}	Strain	0.018	350	Unload, with recovery
14	Relaxation	10^{-3}	Strain	0.018	530	Unload, with 45-h recovery
81	Creep	10^{-3}	Stress	0.005	376	Failure at 0.104 strain
538 °C						
38	Relaxation	6×10^{-7}	Strain	0.006	137	39-h relaxation; no unload
2	Relaxation	6×10^{-7}	Strain	0.006	134	600-s relaxation; no unload
90	Relaxation	6×10^{-7}	Strain	0.018	151	Unload, with recovery
65	Tensile	10^{-5}	Strain			With unloads every 0.02 to 0.16 strain
15	Tensile	10^{-5}	Strain			With unloads at 0.002, 0.02, 0.04, 0.06, and 0.08 strain
75	Relaxation	10^{-5}	Strain	0.018	321	12-h relaxation; no unload
13	Relaxation	10^{-5}	Strain	0.018	324	11-h relaxation; no unload
73A	LCF	10^{-5}	Strain	0.018		$R_\varepsilon = 0$; run to 176 cycles
73B	Relaxation	10^{-5}	Strain	0		Recover for 42 h at 0 strain
73C	Tensile	10^{-5}	Strain			Tension to failure (0.142 strain)
71	Tensile	10^{-5}	Strain			Interrupt at 0.0094 strain
97	Tensile	10^{-5}	Strain			Tension to failure (0.128 strain)
37	Tensile	5×10^{-4}	Strain	0.014		Tension to 0.014 strain; reload to failure (0.10 strain)
70A	Relaxation	5×10^{-4}	Strain	0.018	501	No unload
70B	Tensile	5×10^{-4}	Strain			Tension to failure (0.177 strain)
77A	Relaxation	10^{-3}	Strain	0.018	438	8-h relaxation; no unload
77B	Relaxation	10^{-3}	Strain	Various		Step relaxation 0.04, 0.08, 0.12, and 0.16 strain; failure at 0.183 strain
12	Relaxation	10^{-3}	Strain	0.018	473	Unload to 0 strain and recover
94	Creep	10^{-3}	Stress	0.002	205	Unload, with recovery
1	Creep	10^{-3}	Stress	0.003	226	Unload, with recovery
3	Creep	10^{-3}	Stress	0.003	241	Failure at top radius (0.114 strain)
34	Creep	10^{-3}	Stress	0.003	241	Creep with unloads every 0.02 to 0.12 strain; failure at upper radius
89	Creep	10^{-3}	Stress		243	Creep, with unloads to 0.16 strain
64	Creep	10^{-3}	Stress		103	Overload to 241 MPa then creep at 103 MPa
39	Tensile	10^{-3}	Strain			Tension to failure (0.069 strain)
21	Tensile	10^{-3}	Strain			Tension to failure (0.133 strain)
89	Tensile	10^{-3}	Strain			Tension with unloads every 0.01 up to 20 strain
74	LCF	10^{-3}	Strain			$R_\varepsilon = -1$; strain range = ±0.01; $N_f = 900$
76	Creep	10^{-3}	Stress	0.001	101	Unload, with 19-h recovery
88	Creep	10^{-3}	Stress	0.005	376	Failure at top radius (0.13 strain)
85	Creep	10^{-3}	Stress	0.003	239	Necking at top radius (0.097 strain)

[a]LCF is low-cycle fatigue.

[b]Values for response signal taken at end of loadup.

[c]R_σ is load ratio, R_ε is strain ratio, and N_f is fatigue life.

TABLE II.—TENSILE PROPERTIES AS FUNCTION OF TEMPERATURE AND STRAIN RATE

[Property values given with (standard deviation/number of tests).]

Temperature, °C	Strain rate, s^{-1}			
	10^{-3}	10^{-4}	10^{-5}	6×10^{-7}
(a) Modulus, *E*, GPa				
20	115.1 (2.21/102)			
200	103.8 (0/1)			102.1 (0/1)
316	97.4 (1.29/10)	99.2 (0/1)		94.7 (0/1)
371	93.6 (0.41/3)			90.0 (0/1)
427	91.0 (1.50/35)	89.9 (0/1)	86.8 (3.58/3)	86.0 (3.21/10)
482	86.1 (1.07/3)			72.1 (0/1)
538	83.0 (2.71/22)	78.9 (3.18/3)	80.1 (2.23/5)	66.3 (7.65/5)
(b) Proportional limit, *PL*, MPa				
20	781.6 (54.8/2)			762.2 (0/1)
200	587.0 (0/1)			533.9 (0/1)
316	490.1 (61.9/10)			423.8 (0/1)
371	445.4 (49.2/3)			244.8 (0/1)
427	401.4 (35.2/26)	183.5 (87.5/2)	150.9 (68.7/4)	54.7 (9.0/10)
482	245.3 (63.2/3)			45.7 (0/1)
538	94.3 (23.2/19)		30.9 (4.2/7)	19.0 (2.6/4)
(c) 0.02% offset yield, $\sigma_{0.02}$, MPa				
20	881.1 (1.5/2)			802.3 (0/1)
200	640.1 (0/1)			570.2 (0/1)
316	519.2 (10.5/5)	492.3 (0/1)		481.0 (0/1)
371	507.2 (21.5/2)			426.3 (48.7/2)
427	454.5 (10.2/23)	326.1 (71.7/2)	300.5 (89.7/4)	150.5 (7.9/5)
482	403.0 (49.1/2)			127.1 (23.2/2)
538	229.9 (26.5/14)		89.6 (5.4/7)	39.6 (1.9/3)
(d) 0.2% offset yield, $\sigma_{0.2}$, MPa				
20	925.5 (0/1)			836.8 (0/1)
200	676.8 (0/1)			604.6 (0/1)
316	586.5 (27.2/6)	569.5 (0/1)		562.4 (0/1)
371	544.7 (8.1/2)			512.4 (0/1)
427	530.5 (7.6/17)	499.0 (16.7/2)	471.4 (47.2/4)	402.2 (9.1/3)
482	498.9 (14.5/2)			281.1 (0/1)
538	433.1 (23.8/10)		258.2 (8.7/6)	110.3 (0.8/3)
(e) Stress at 1.8% strain, $\sigma_{1.8}$, MPa				
20	941.3 (0/1)			862.0 (0/1)
200	704.5 (0/1)			659.2 (0/1)
316	627.4 (20.4/4)		628.7 (0/1)	634.9 (0/1)
371	603.3 (13.2/2)			585.9 (0/1)
427	580.6 (13.2/12)	550.9 (21.0/2)	545.7 (52.4/4)	488.4 (1.0/4)
482	541.4 (11.4/2)			349.9 (0/1)
538	475.4 (26.7/9)		339.2 (16.9/5)	150.7 (0/1)

TABLE III.—CONSTANT LOAD CREEP TEST MATRIX[a,b]
[Equivalent strain rate of 10^{-3} s^{-1}.]

Stress level, MPa	Temperature, °C						
	20	200	316	371	427	482	538
<34					X	X	X
34					X	X	X
69					X	X	
103			X		X		X
138					X		
207				X	X		X
241			X		X		X
310			X	X	X		
379			X	X	X	X	X
448			X		X		
483			X		X		
517			X	X	X		
552	X		X		X		
586			X		X		
690	X						
896	X						
	Virgin samples.						
	Viscoelastic threshold (Lerch and Arnold, 2014).						
	Test also run at equivalent strain rate of 6×10^{-7} s^{-1}.						

[a]An "X" indicates tests that have been run.

[b]Unfilled cells with "X" are tests of samples with prior history.

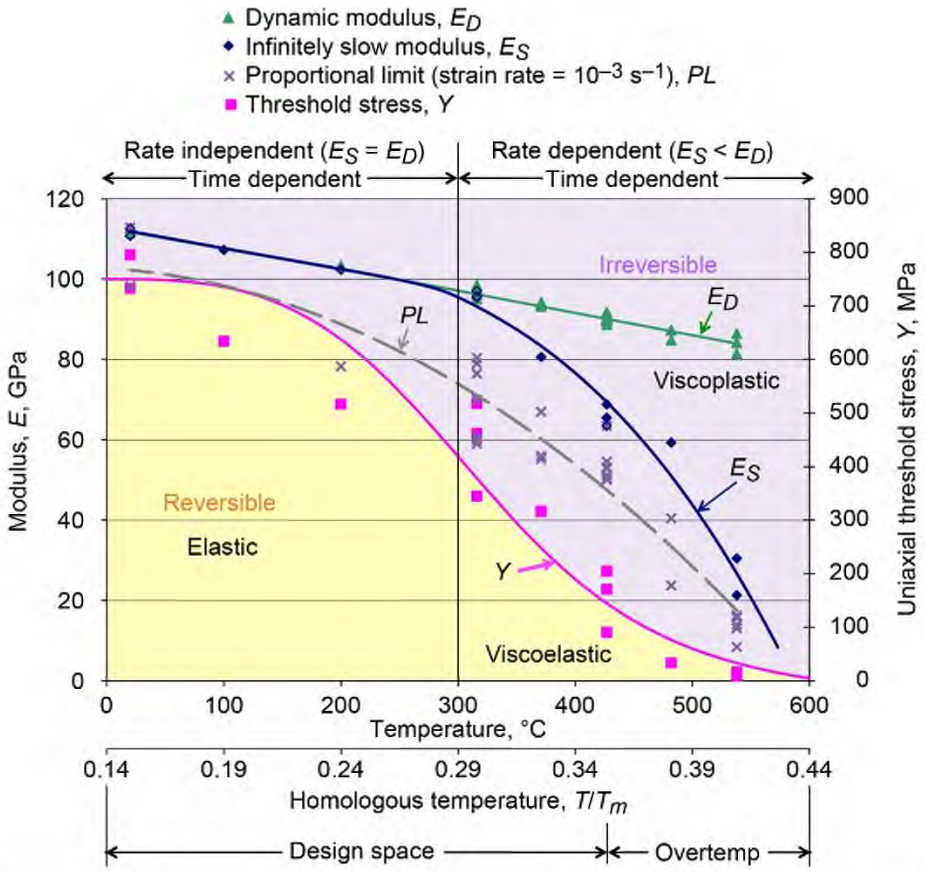

Figure 1.—Ti-6Al-4V time-dependent deformation modeling map (from Lerch and Arnold, 2014).

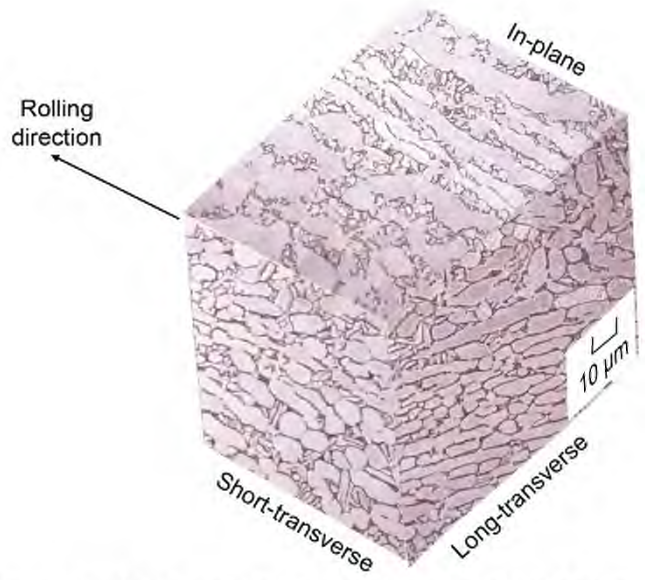

Figure 2.—Three-dimensional microstructure of Ti-6-4 plate.

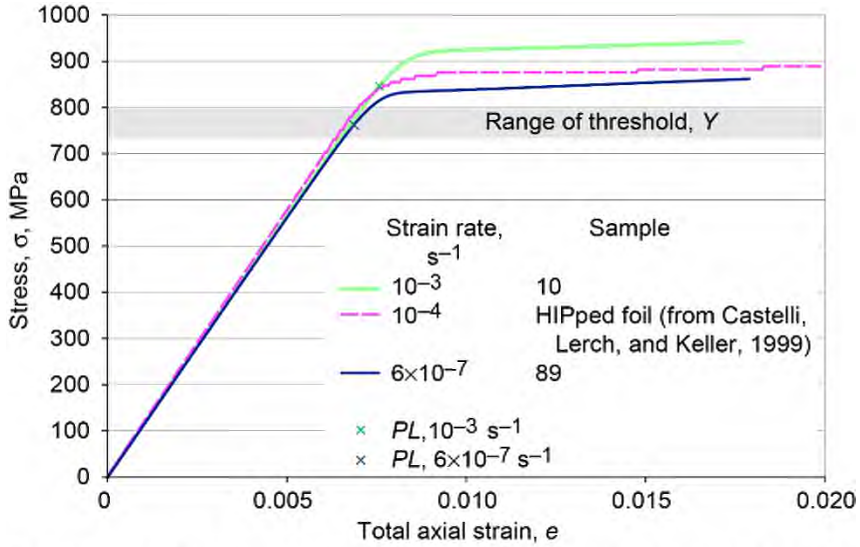

Figure 3.—Tensile behavior of Ti-6-4 at 20 °C as function of strain rate, showing proportional limits *PL* and threshold stress *Y*.

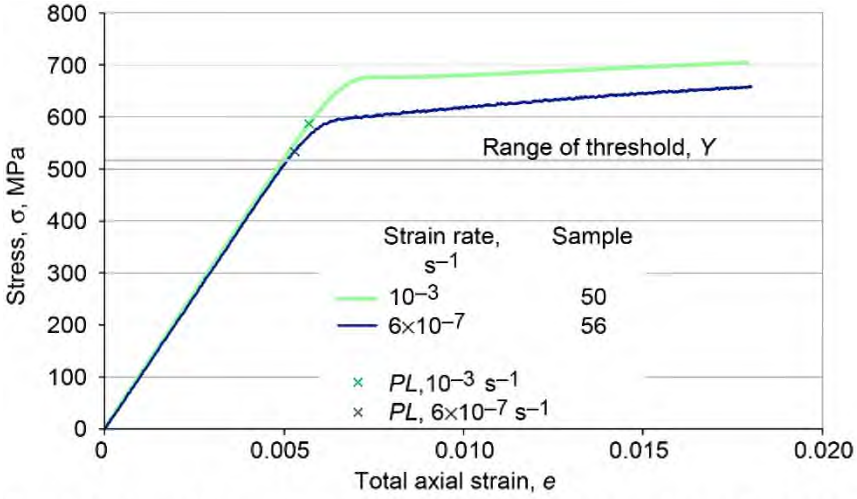

Figure 4.—Tensile behavior of Ti-6-4 at 200 °C at slow and fast strain rates, showing proportional limits *PL* and threshold stress *Y*.

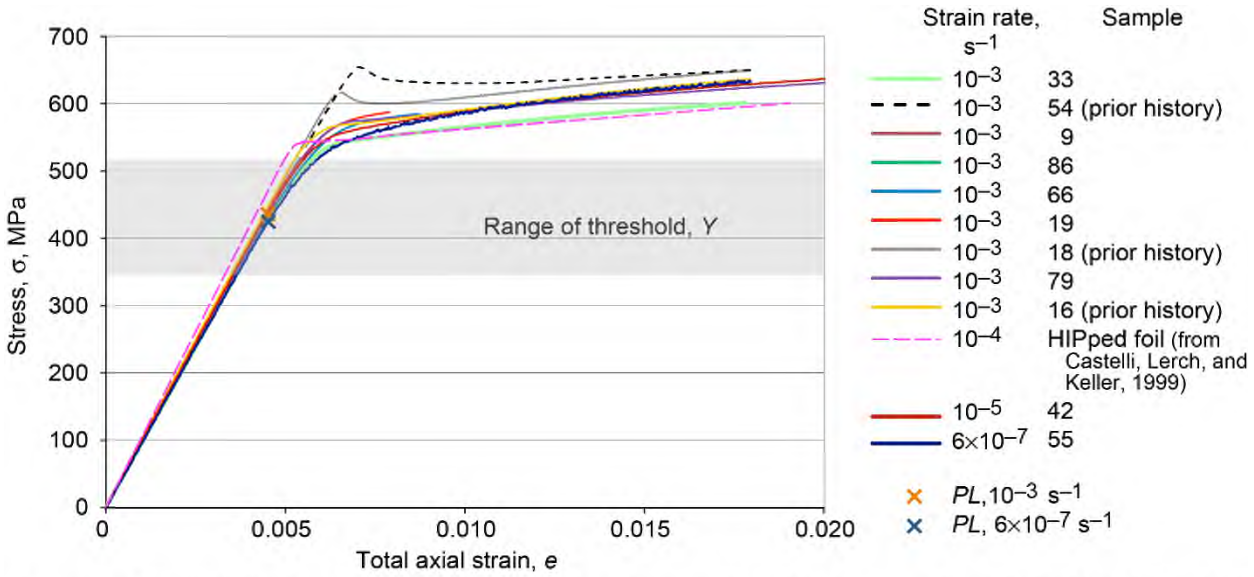

Figure 5.—Tensile behavior of Ti-6-4 at 316 °C at different strain rates, showing proportional limits *PL* and threshold stress *Y*.

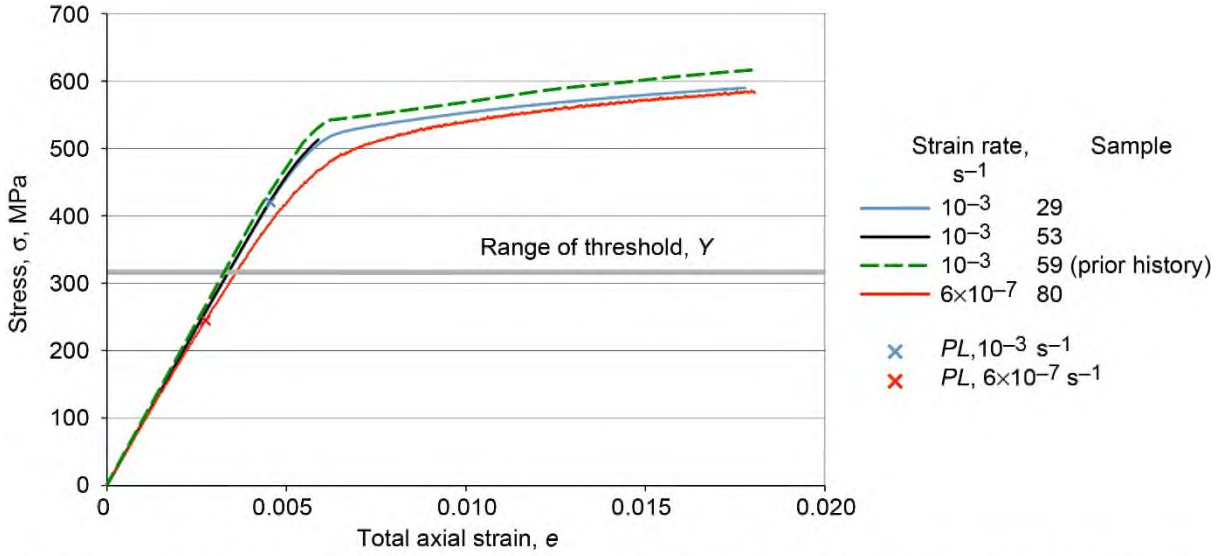

Figure 6.—Tensile behavior of Ti-6-4 at 371 °C at slow and fast strain rates, showing proportional limits *PL* and threshold stress *Y*.

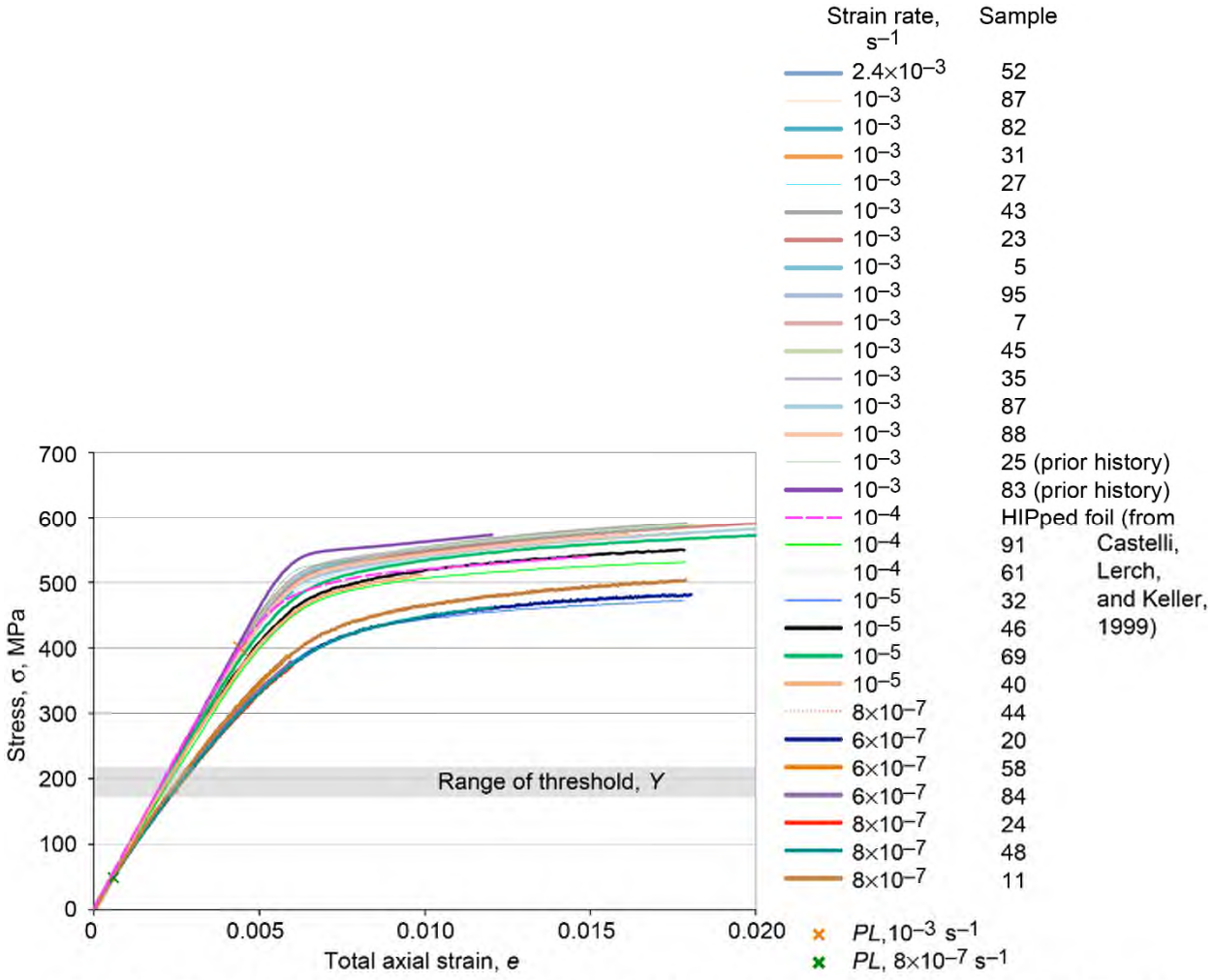

Figure 7.—Tensile behavior of Ti-6-4 at 427 °C and various strain rates, showing proportional limits *PL* and threshold stress *Y*.

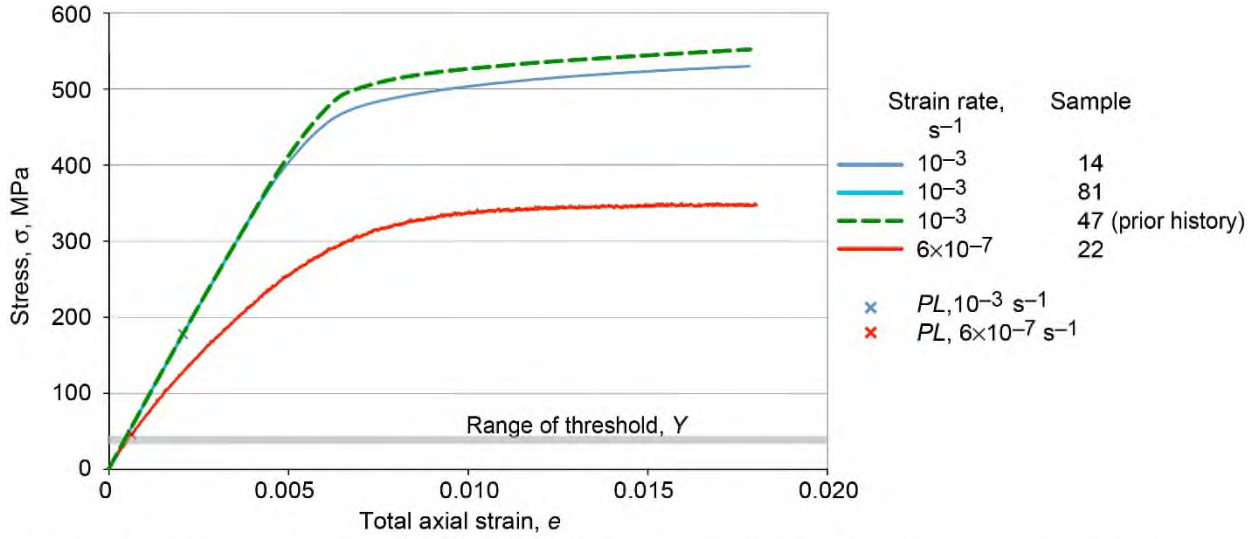

Figure 8.—Tensile behavior of Ti-6-4 at 482 °C at slow and fast strain rates, showing proportional limits *PL* and threshold stress *Y*.

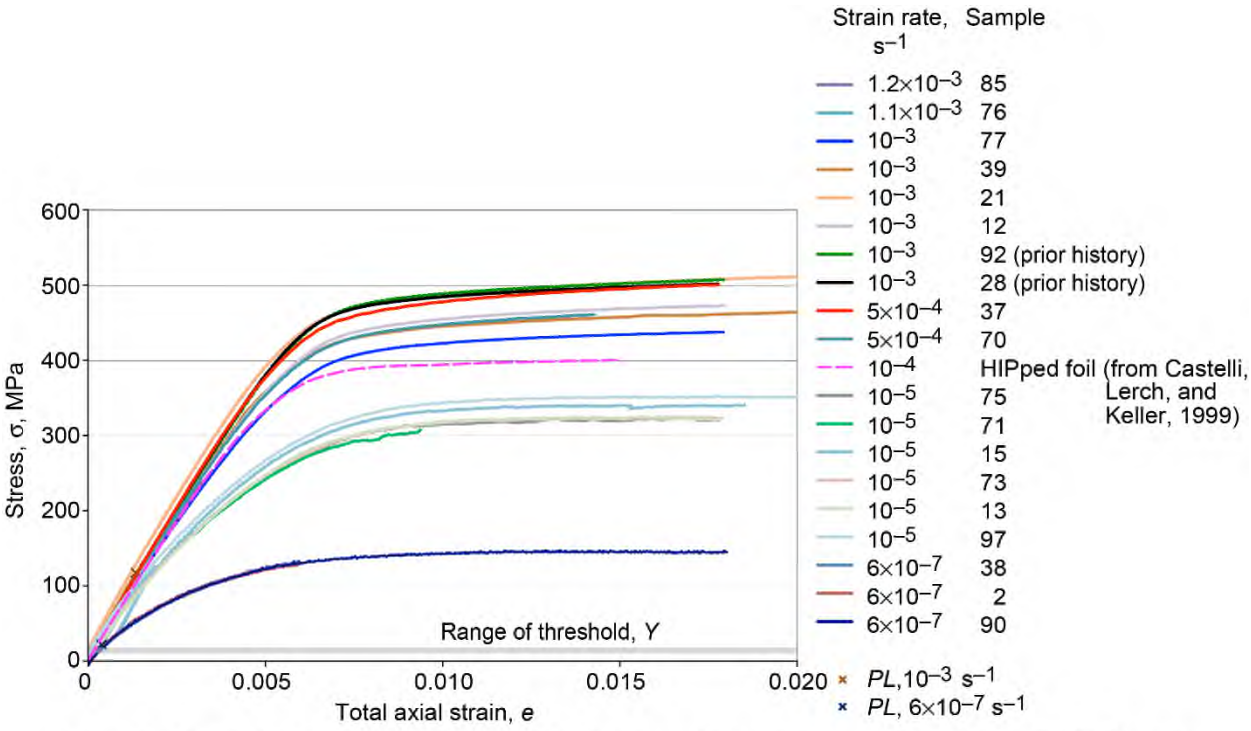

Figure 9.—Tensile behavior of Ti-6-4 at 538 °C and various strain rates, showing proportional limits *PL* and threshold stress *Y*.

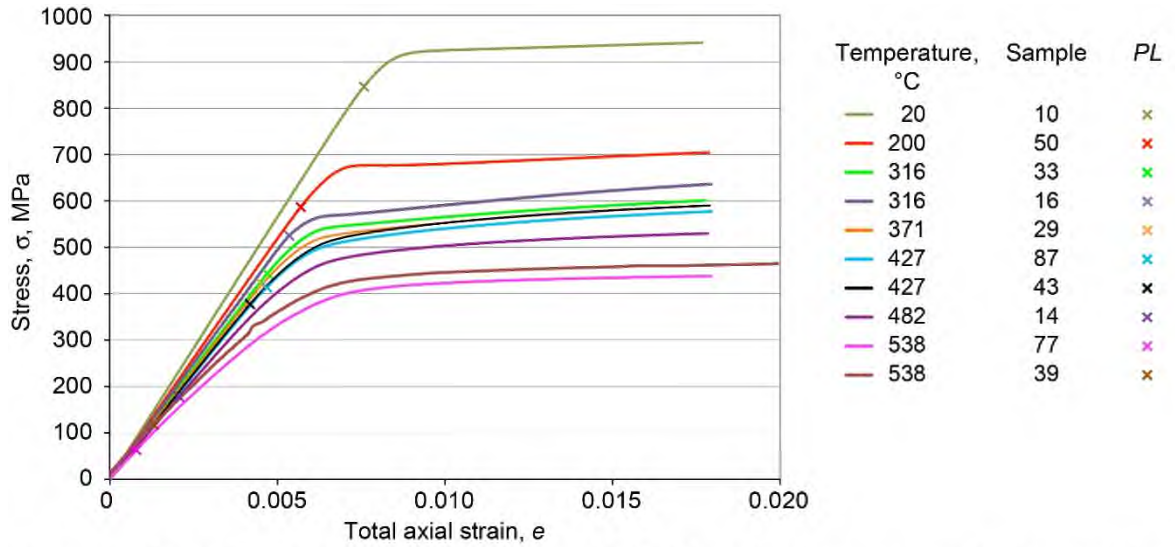

Figure 10.—Tensile behavior of Ti-6-4 at strain rate of 10^{-3} s^{-1} for various temperatures, showing proportional limits *PL*.

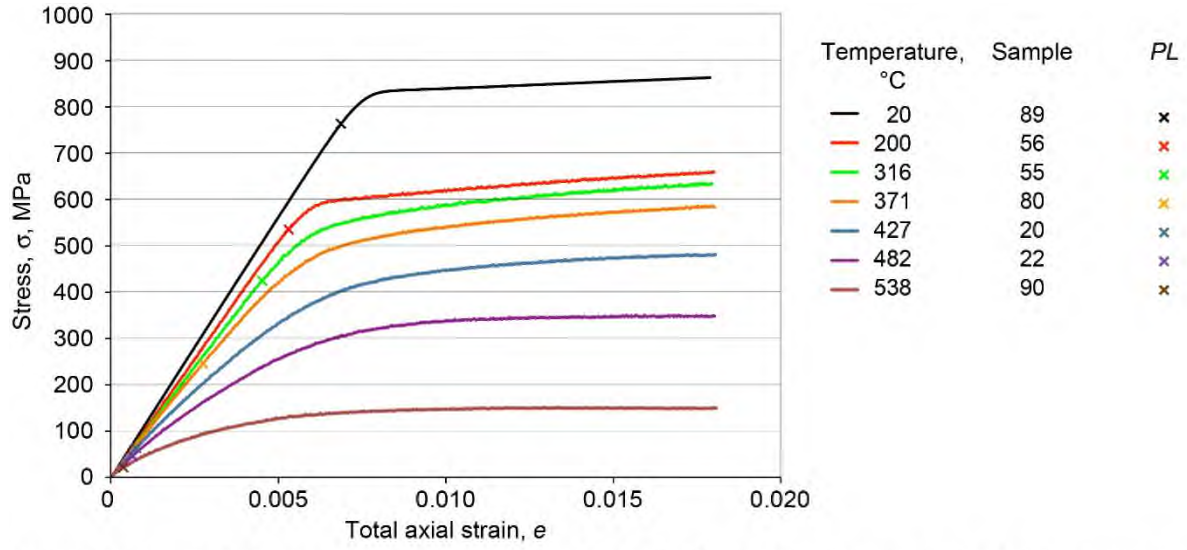

Figure 11.—Tensile behavior of Ti-6-4 at strain rate of 6×10^{-7} s^{-1} for various temperatures, showing proportional limits *PL*.

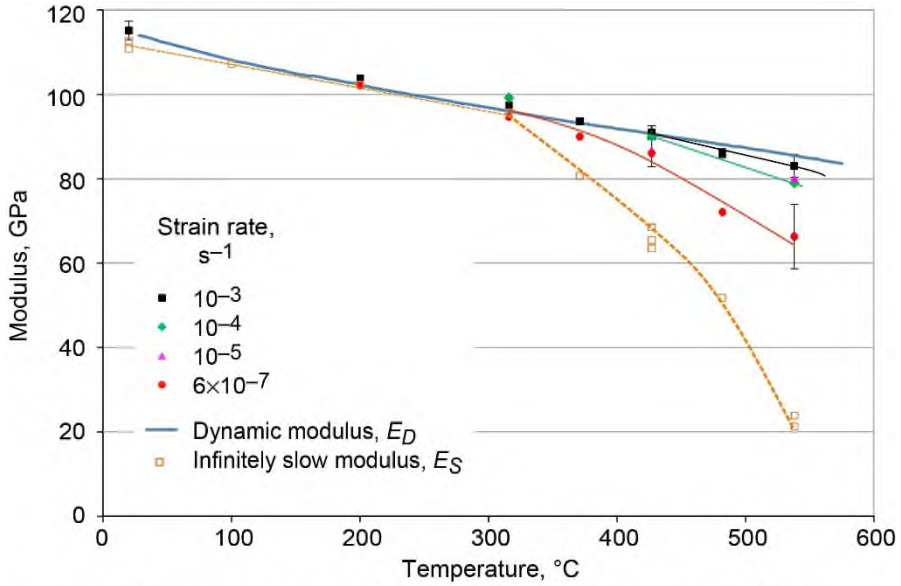

Figure 12.—Young's modulus *E* of Ti-6-4 as function of temperature and strain rate.

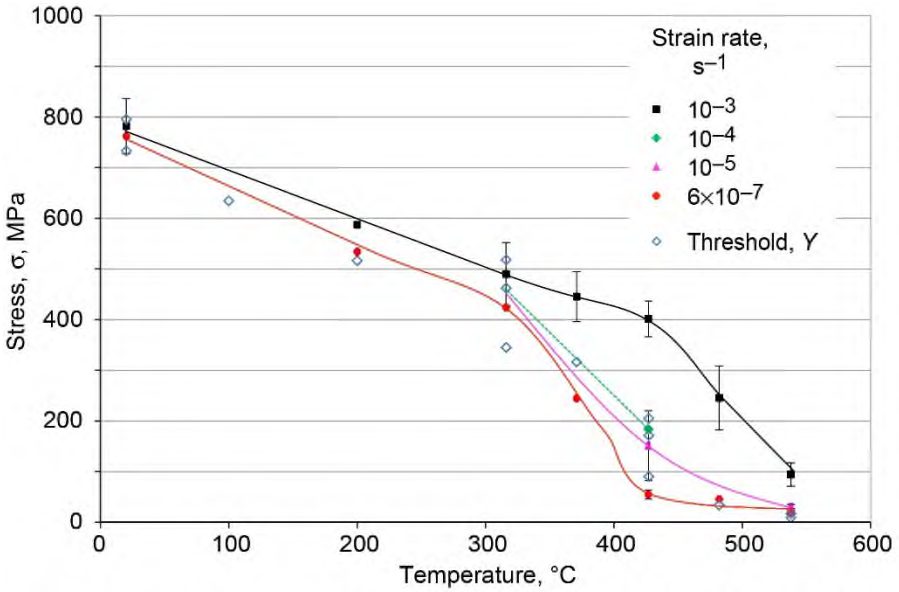

Figure 13.—Proportional limit *PL* as function of temperature and strain rate for Ti-6-4.

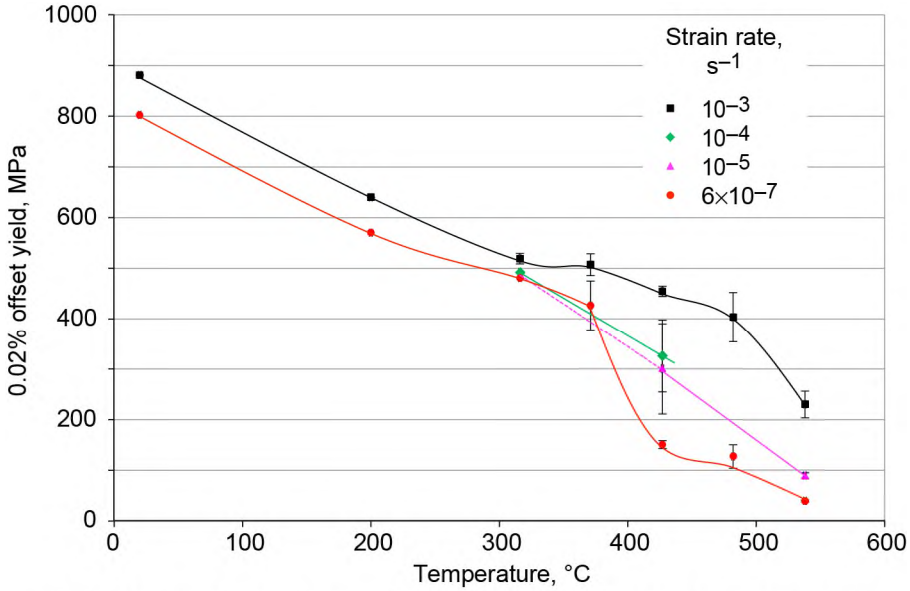

Figure 14.—Classic yield strength $\sigma_{0.02}$ of Ti-6-4 as function of temperature and strain rate.

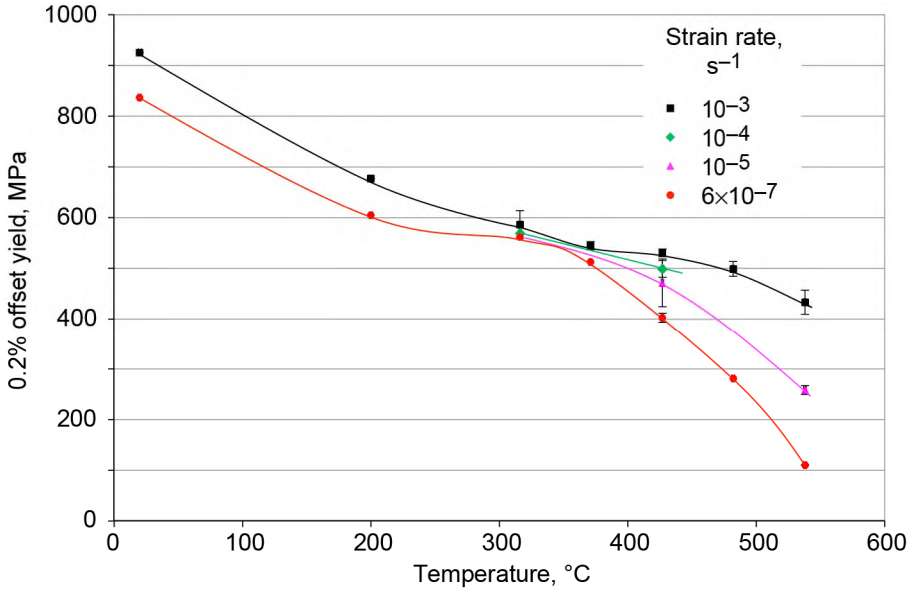

Figure 15.—Classic yield strength $\sigma_{0.2}$ of Ti-6-4 as function of temperature and strain rate.

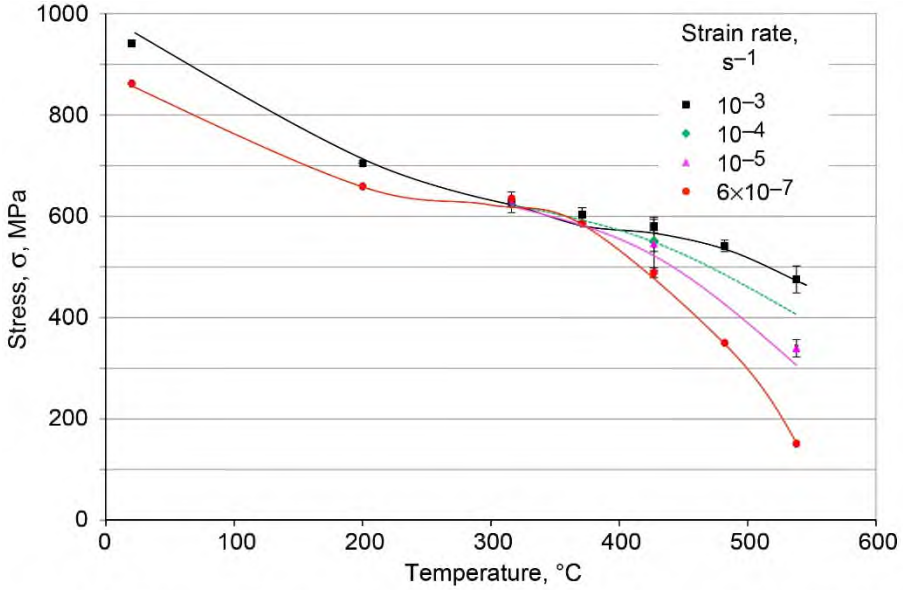

Figure 16.—Maximum stress at 0.018 strain $\sigma_{1.8}$ forTi-6-4 as function of temperature and strain rate.

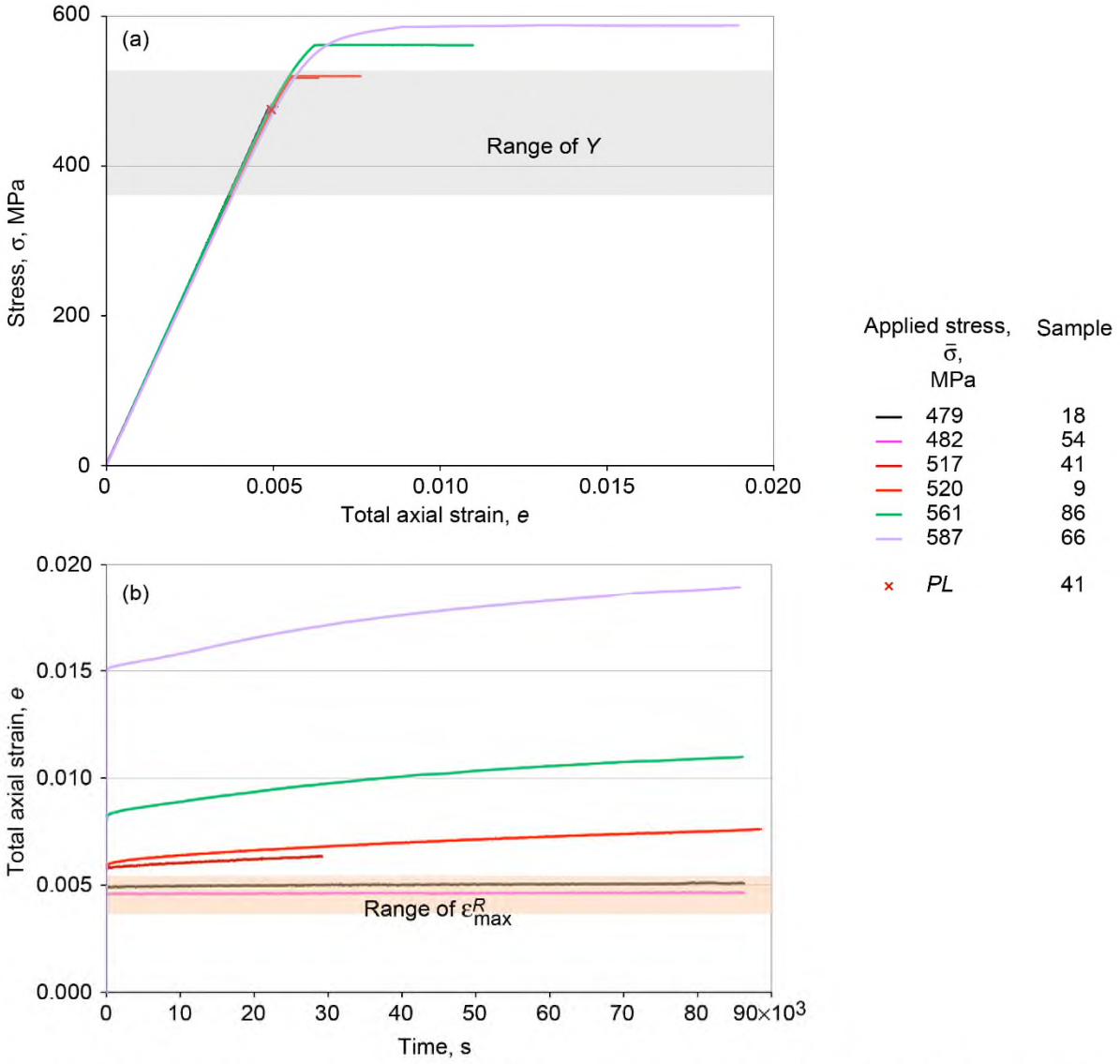

Figure 17.—Creep response of Ti-6-4 at 316 °C and equivalent strain rate of 10^{-3} s^{-1} for various stress levels. (a) Stress as function of total axial strain, showing proportional limit *PL* and threshold stress *Y*. (b) Total axial strain as function of time, showing maximum reversible strain ε^R_{max} (=Y/E_S, where E_S is infinitely slow modulus).

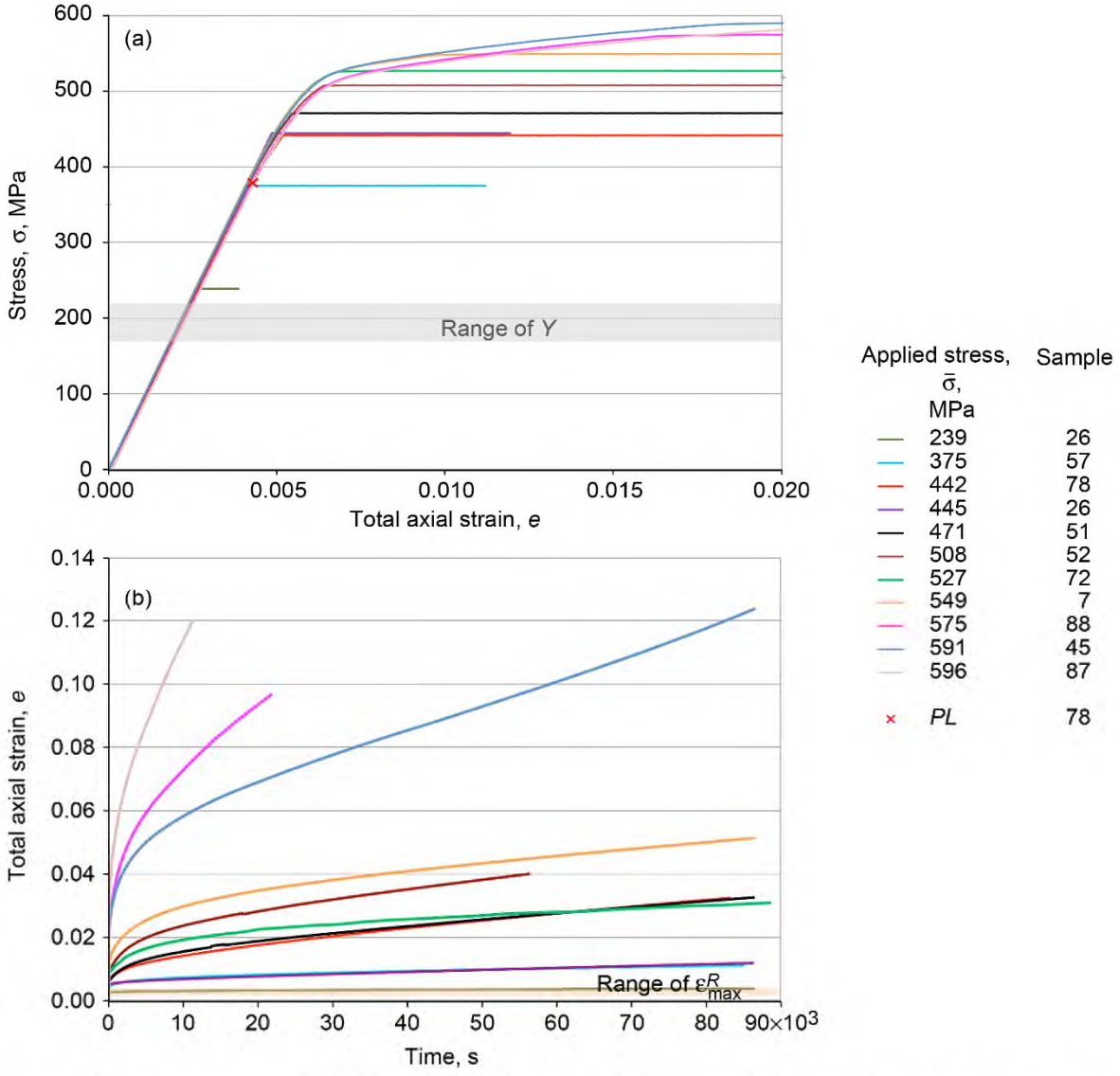

Figure 18.—Creep response of Ti-6-4 at 427 °C and equivalent strain rate of 10^{-3} s^{-1} for various stress levels. (a) Stress as function of total axial strain, showing proportional limit *PL* and threshold stress *Y*. (b) Total axial strain as function of time, showing maximum reversible strain ε^{R}_{max} (=Y/E_S, where E_S is infinitely slow modulus).

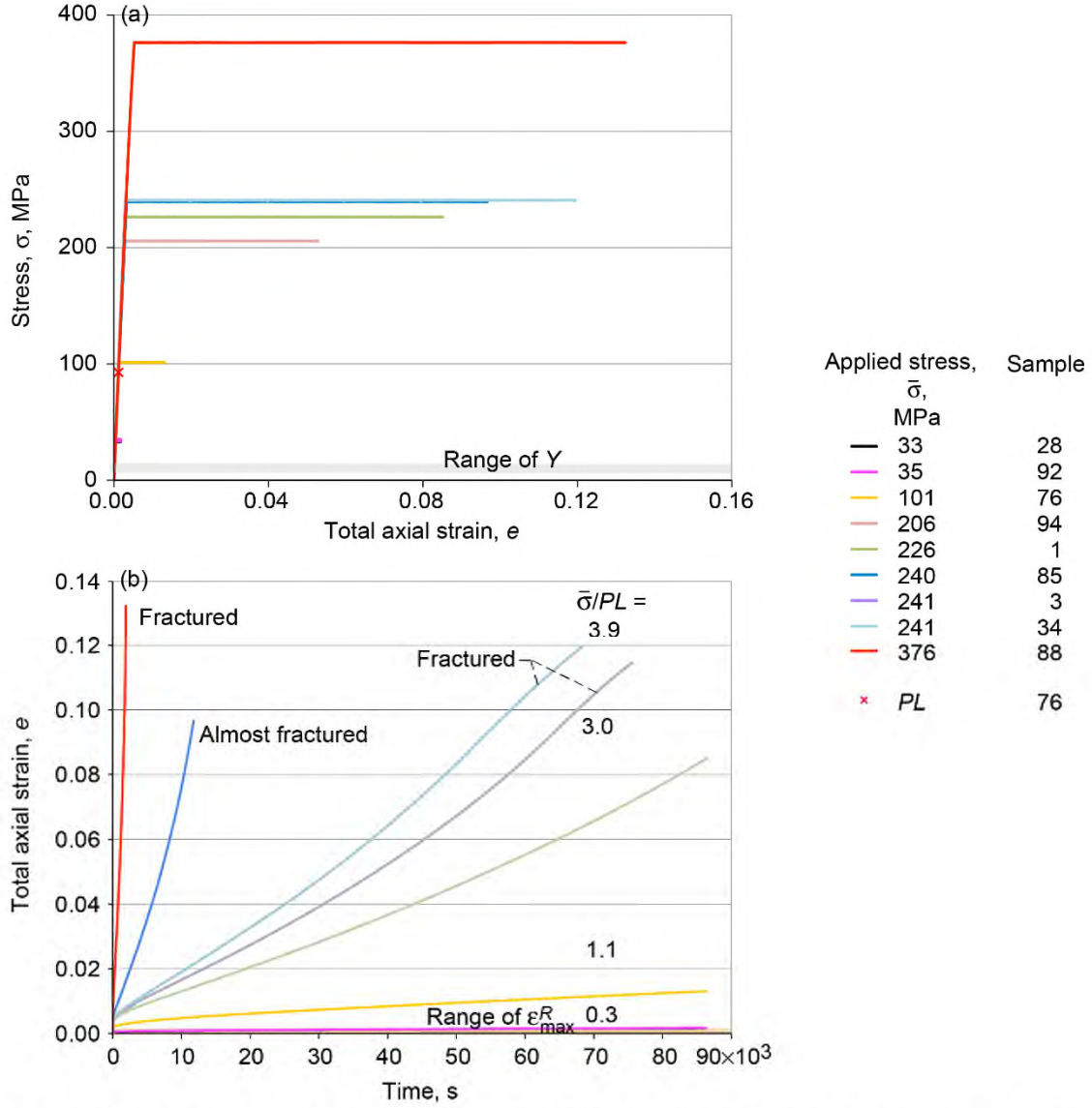

Figure 19.—Creep response of Ti-6-4 at 538 °C and equivalent strain rate of 10^{-3} s^{-1} for various stress levels. (a) Stress as function of total axial strain, showing proportional limit *PL* and threshold stress *Y*. (b) Total axial strain as function of time, showing maximum reversible strain ε^{R}_{max} (=Y/E_s, where E_s is infinitely slow modulus) and ratio between creep stress $\bar{\sigma}$ and proportional limit *PL*. (c) Total axial strain as function of time, enlarged.

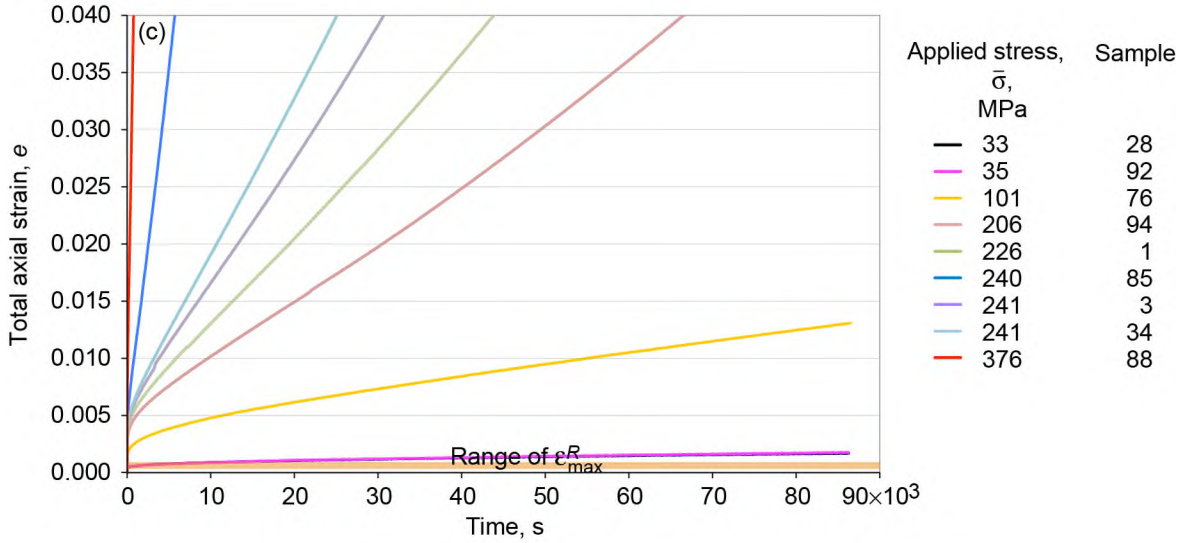

Figure 19.—Concluded. (c) Total axial strain as function of time, enlarged.

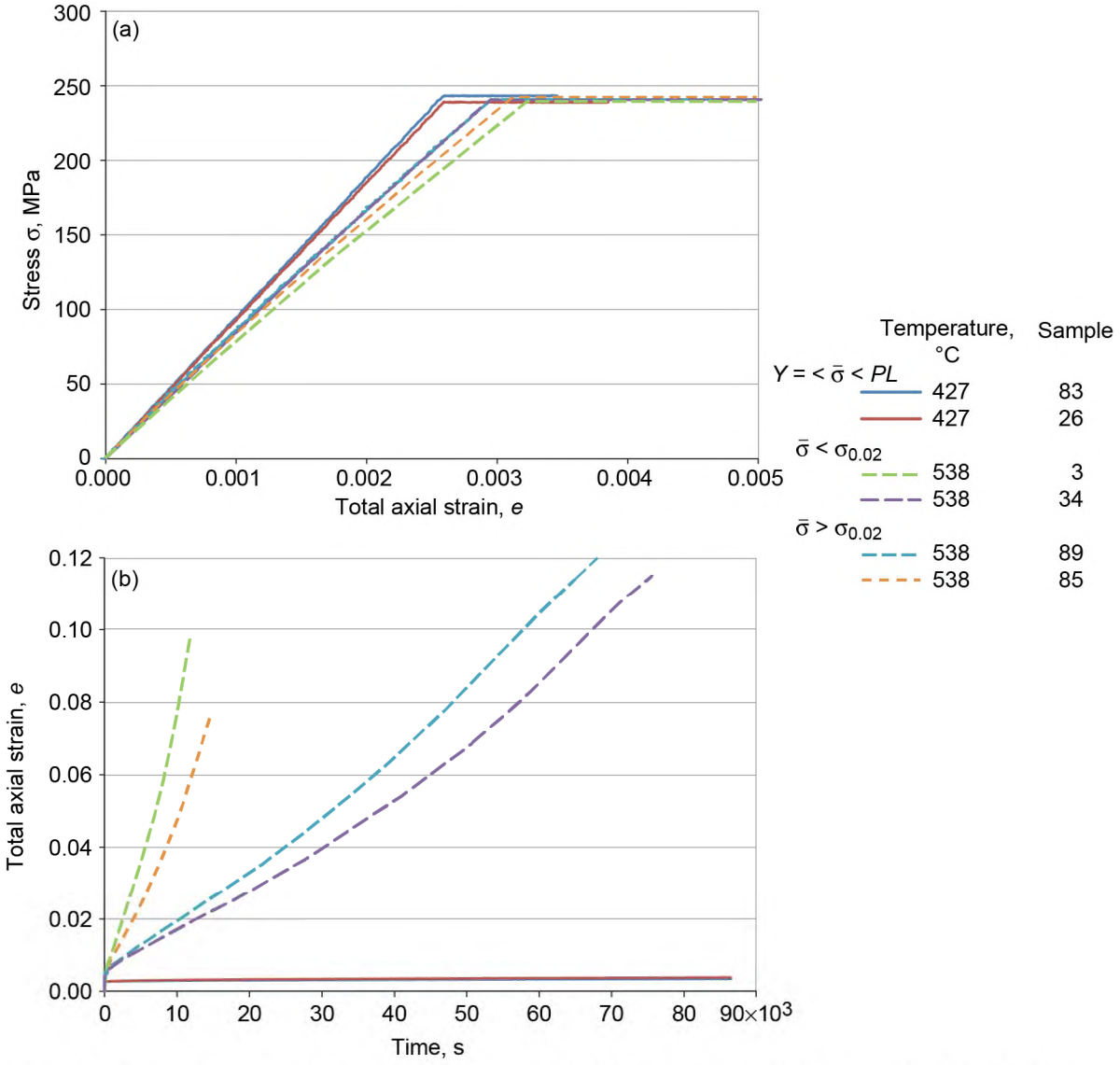

Figure 20.—Creep response of Ti-6-4 at creep stress $\bar{\sigma}$ = 241 MPa and equivalent strain rate of 10^{-3} s^{-1} for various temperatures, giving relationship of $\bar{\sigma}$ to 0.02% yield point $\sigma_{0.02}$, proportional limit *PL*, and threshold stress *Y*. (a) Stress as function of total axial strain. (b) Total axial strain as function of time.

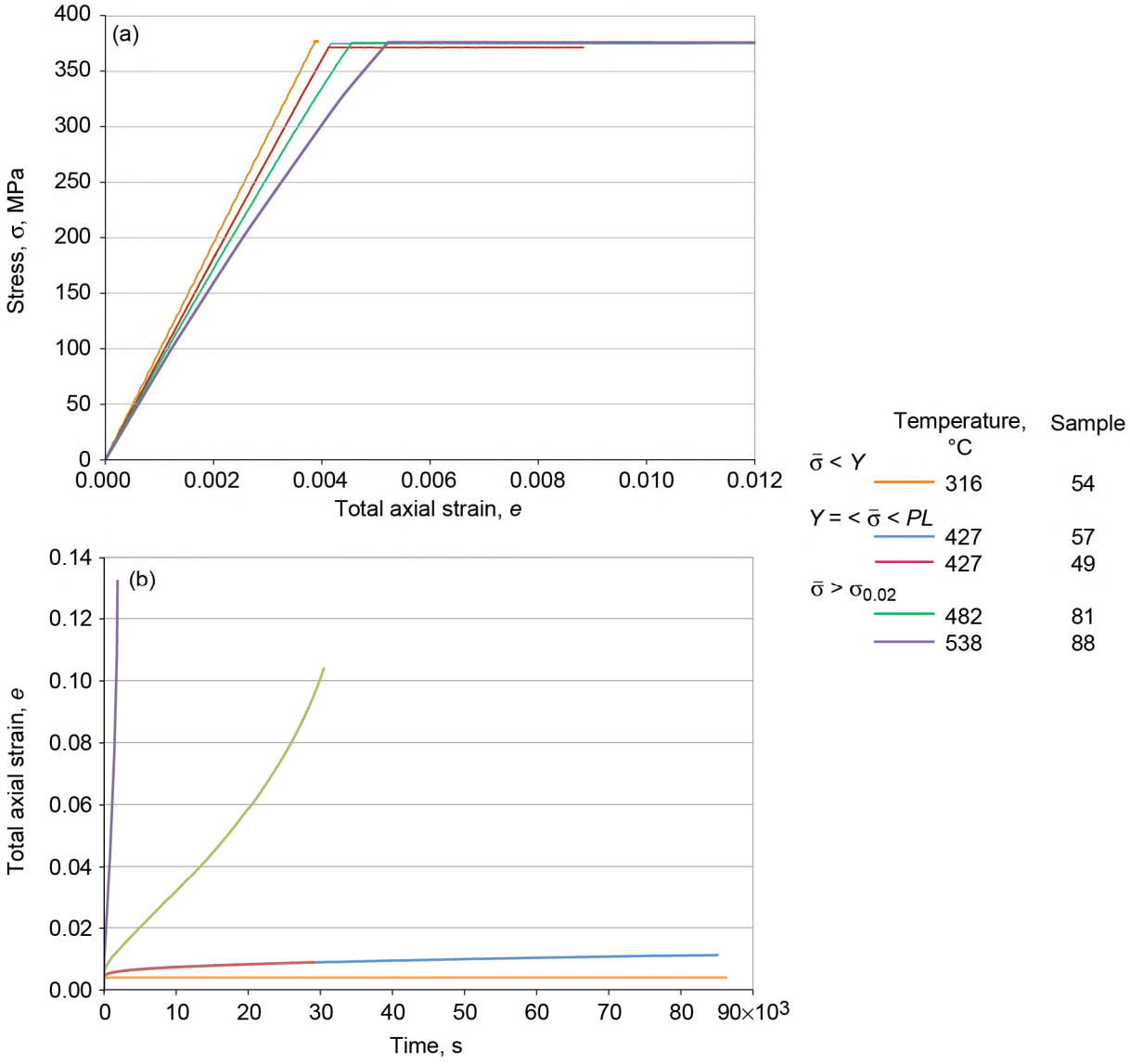

Figure 21.—Creep response of Ti-6-4 at creep stress $\bar{\sigma}$ = 379 MPa and equivalent strain rate of 10^{-3} s^{-1} for various temperatures, giving relationship of $\bar{\sigma}$ to 0.02% yield point $\sigma_{0.02}$, proportional limit *PL*, and threshold stress *Y*. (a) Stress as function of total axial strain. (b) Total axial strain as function of time.

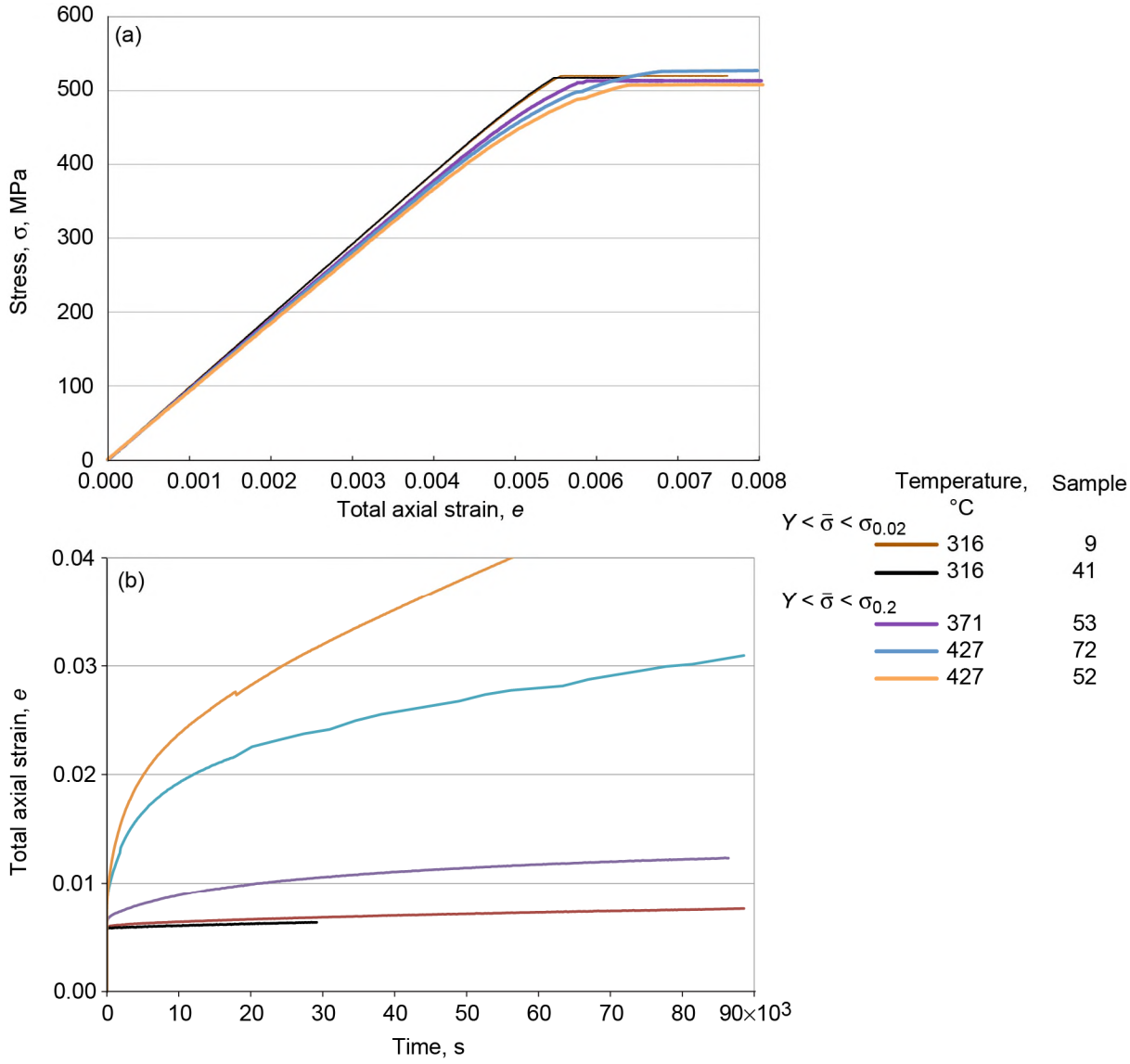

Figure 22.—Creep response of Ti-6-4 at creep stress $\bar{\sigma}$ = 517 MPa and equivalent strain rate of 10^{-3} s^{-1} for various temperatures, giving relationship of $\bar{\sigma}$ to 0.02% and 0.2% yield points $\sigma_{0.02}$ and $\sigma_{0.2}$, respectively, and threshold stress *Y*. (a) Stress as function of total axial strain. (b) Total axial strain as function of time.

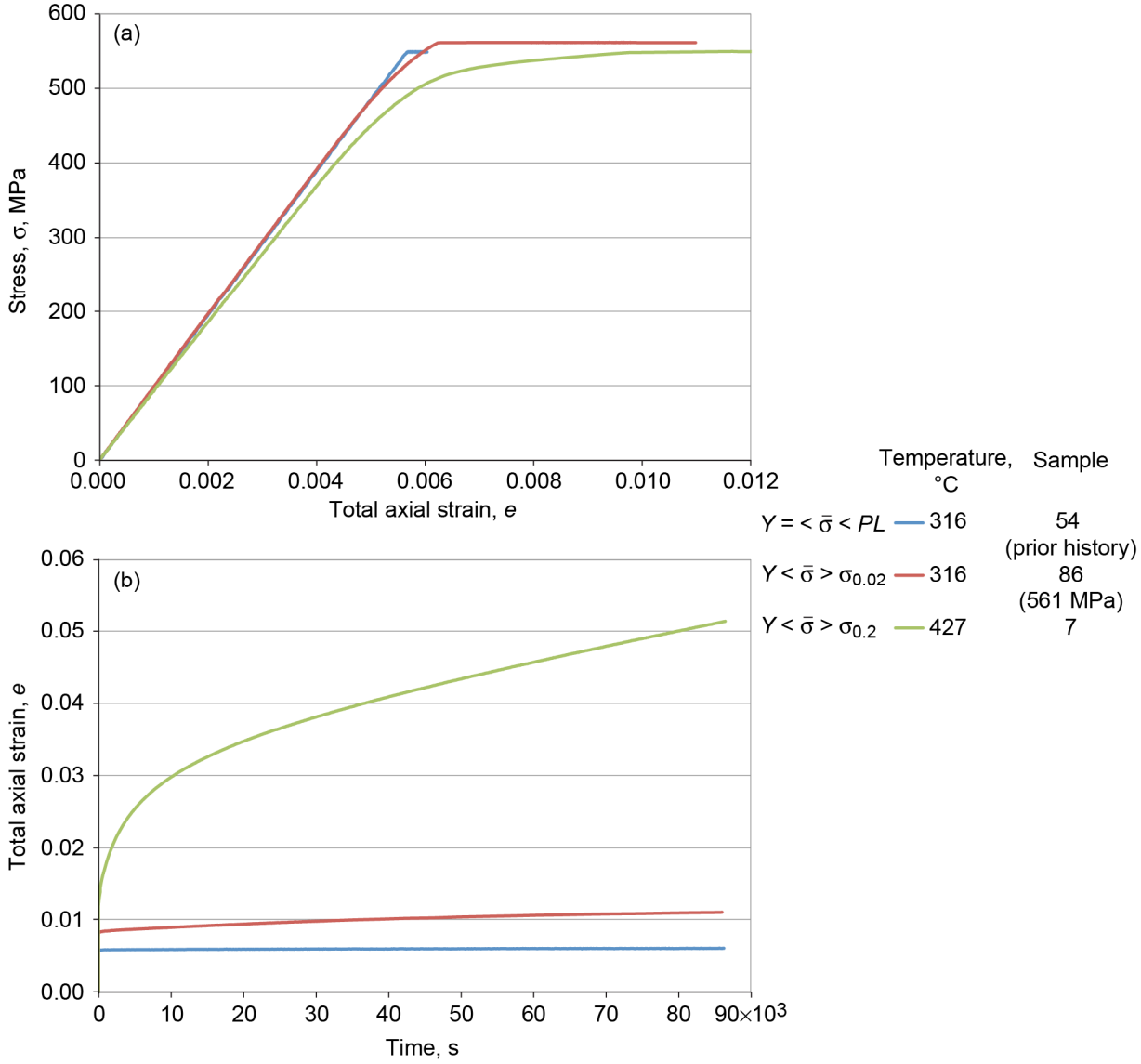

Figure 23.—Creep response of Ti-6-4 at creep stress $\bar{\sigma}$ = ~550 MPa and equivalent strain rate of 10^{-3} s^{-1} for various temperatures, giving relationship of $\bar{\sigma}$ to 0.02% and 0.2% yield points $\sigma_{0.02}$ and $\sigma_{0.2}$, respectively, and threshold stress *Y*. (a) Stress as function of total axial strain. (b) Total axial strain as function of time.

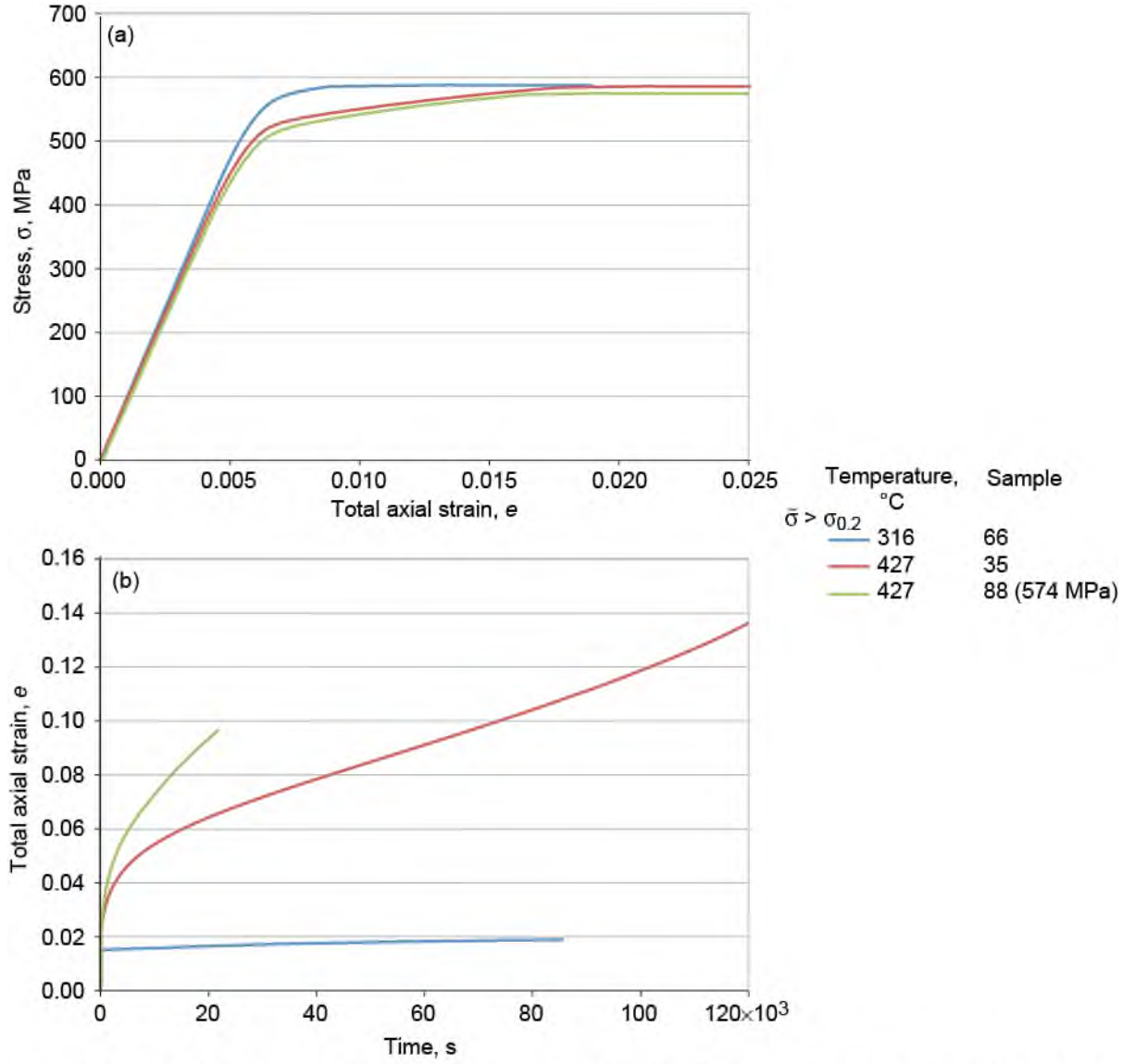

Figure 24.—Creep response of Ti-6-4 at creep stress $\bar{\sigma}$ = 586 MPa and equivalent strain rate of 10^{-3} s^{-1} for two temperatures, giving relationship of $\bar{\sigma}$ to 0.2% yield point 0.2. (a) Stress as function of total axial strain. (b) Total axial strain as function of time.

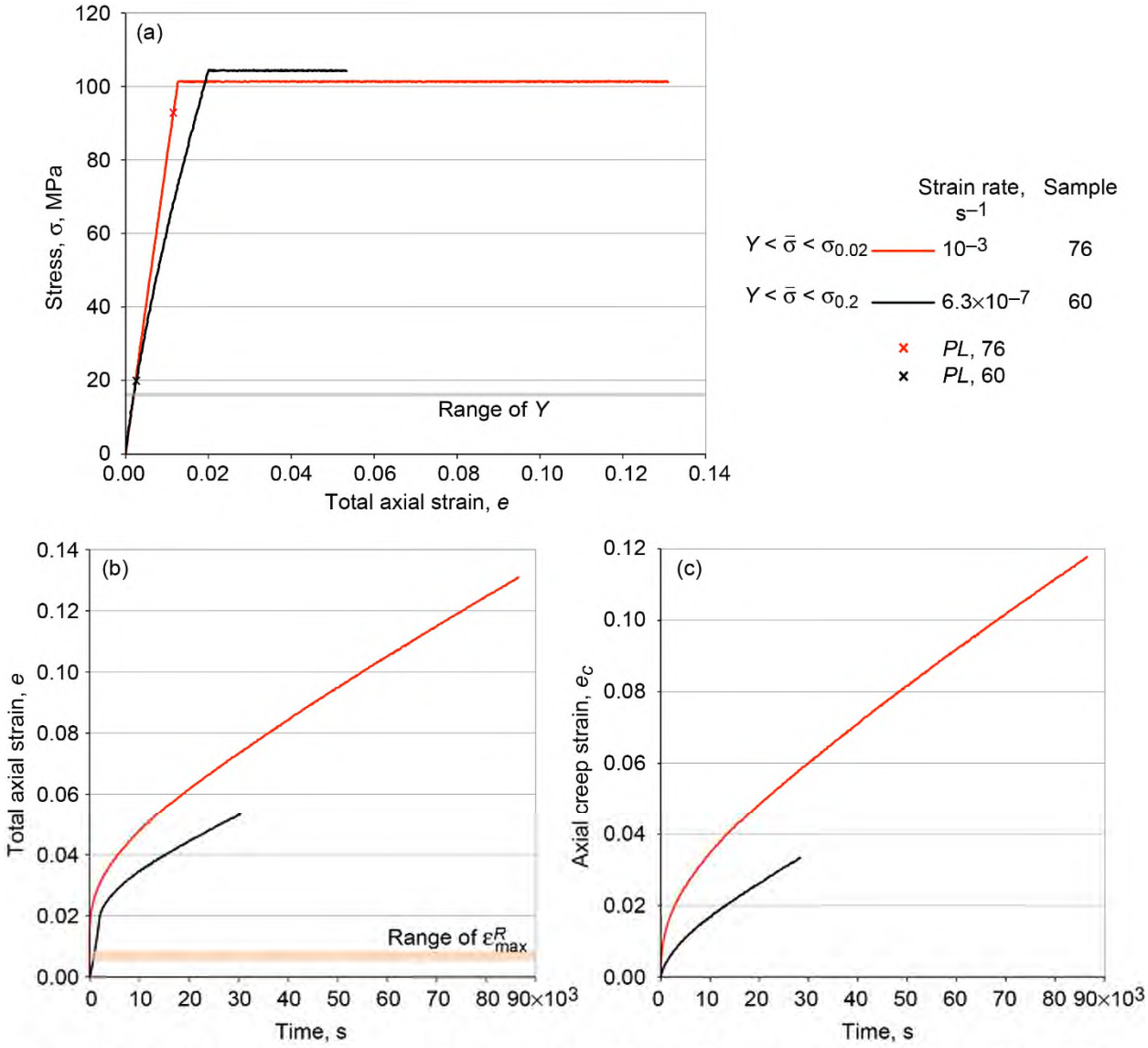

Figure 25.—Effect of loading rate on creep response of Ti-6-4 at 538 °C and 103 MPa. (a) Stress as function of total axial strain, showing proportional limit *PL* and threshold stress *Y*. (b) Total axial strain as function of time, showing relationship of creep stress $\bar{\sigma}$ to 0.02% and 0.2% yield points $\sigma_{0.02}$ and $\sigma_{0.2}$, respectively, and *Y* and showing maximum reversible strain ε^R_{max} (=Y/E_S, where E_S is infinitely slow modulus). (c) Axial creep strain as function of time, showing relationship σ to $\sigma_{0.02}$, $\sigma_{0.2}$, and *Y*.

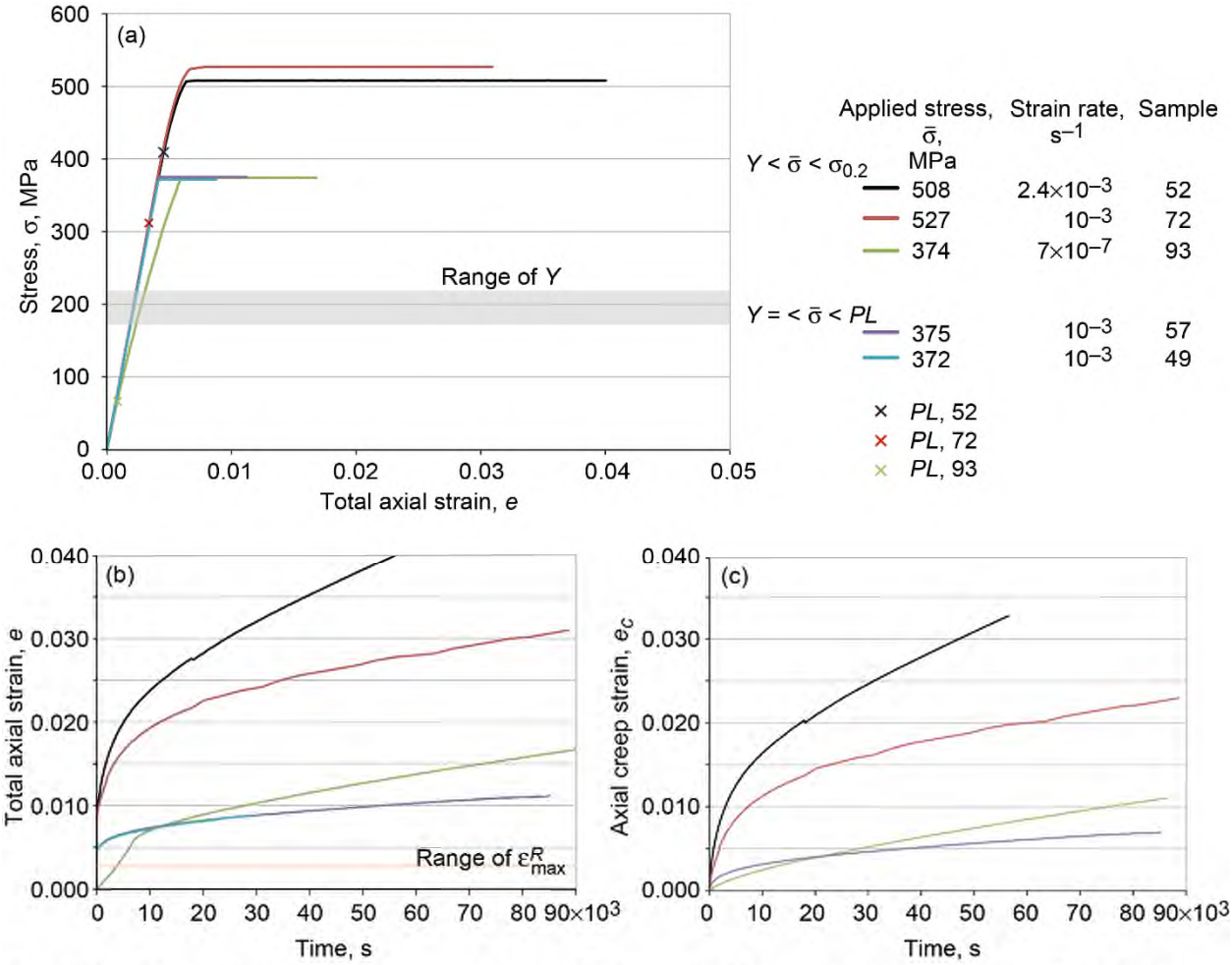

Figure 26.—Effect of loading rate on creep response of Ti-6-4 at 427 °C and two creep stress levels $\bar{\sigma}$. (a) Stress as function of total axial strain, showing proportional limit *PL* and threshold stress *Y*. (b) Total axial strain as function of time, showing relationship of *Y*, $\bar{\sigma}$, and 0.2% yield point $\sigma_{0.2}$; proportional limit *PL*; and maximum reversible strain ε^{R}_{max} (=Y/E_S, where E_S is infinitely slow modulus). (c) Axial creep strain as function of time, showing relationship of $\bar{\sigma}$ and 0.2% yield points $\sigma_{0.2}$, proportional limit *PL*, and threshold stress *Y*.

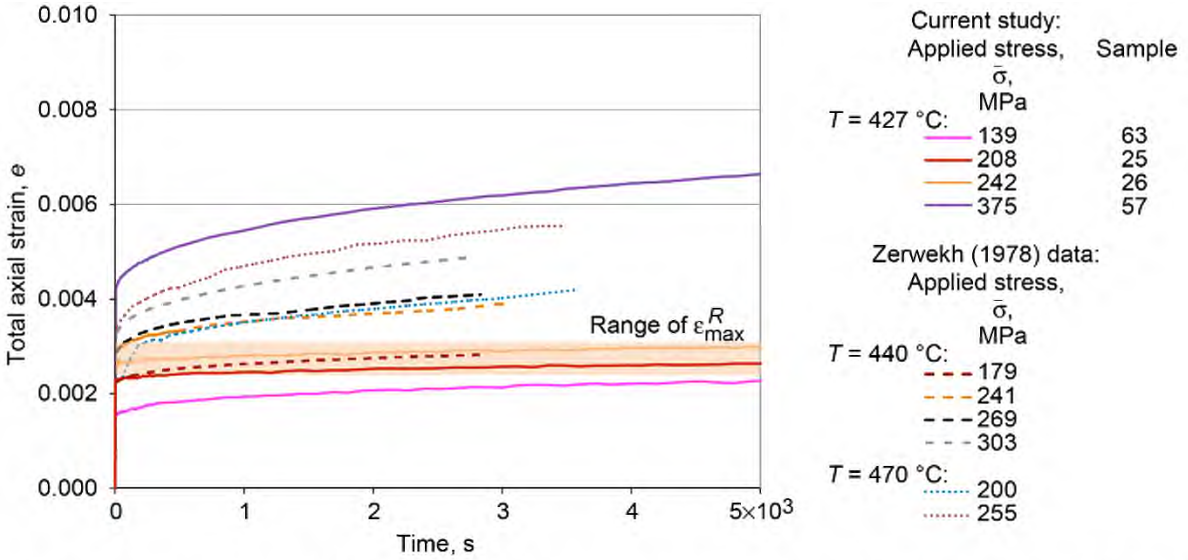

Figure 27.—Creep response of Ti-6-4 at 427 °C and equivalent strain rate of 10^{-3} s^{-1} for various stress levels $\bar{\sigma}$. Comparison to Zerwekh's (1978) data, showing maximum reversible strain ε^R_{max} (=Y/E_S, where Y is threshold stress and E_S is infinitely slow modulus).

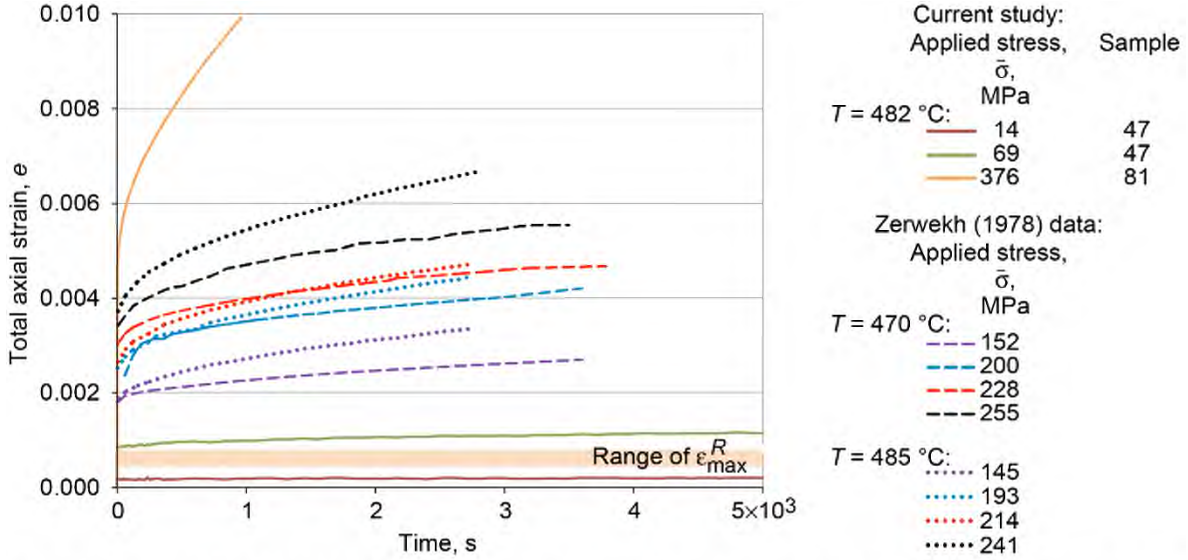

Figure 28.—Creep response of Ti-6-4 at 482 °C and equivalent strain rate of 10^{-3} s^{-1} for various stress levels, showing maximum reversible strain ε^R_{max} (=Y/E_S, where E_S is infinitely slow modulus). Comparison to Zerwekh's (1978) data.

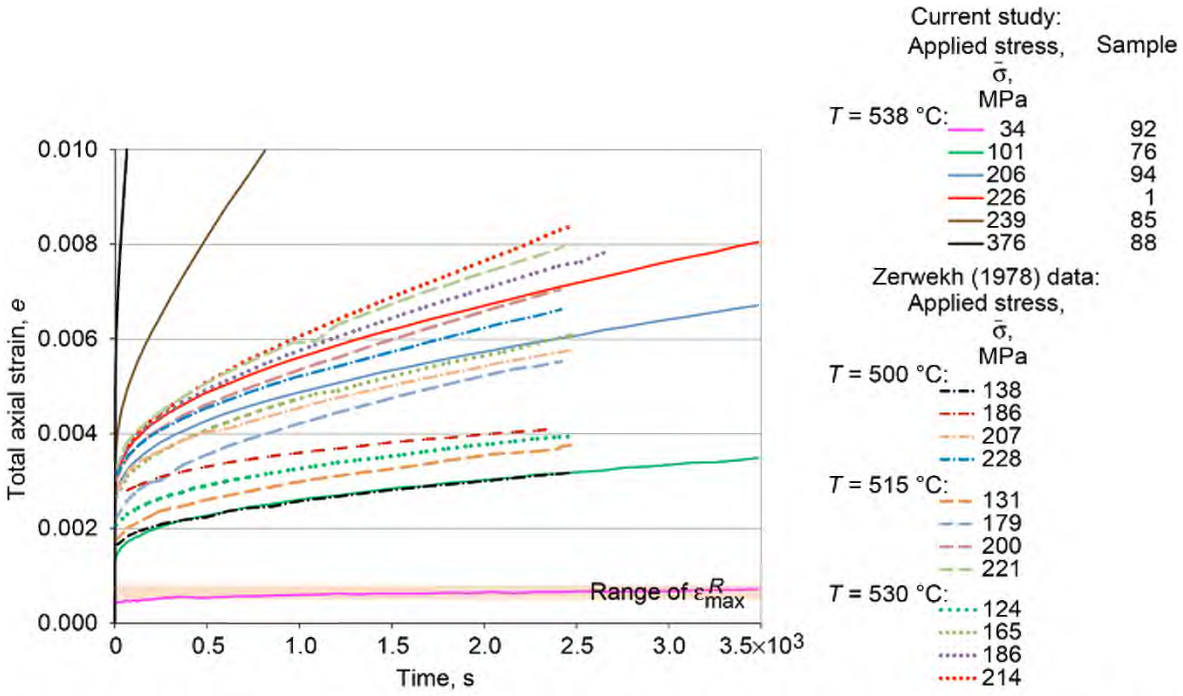

Figure 29.—Creep response of Ti-6-4 at 538 °C and equivalent strain rate of 10^{-3} s^{-1} for various stress levels, showing maximum reversible strain ε^R_{max} (=Y/E_S, where E_S is infinitely slow modulus). Comparison to Zerwekh's (1978) data.

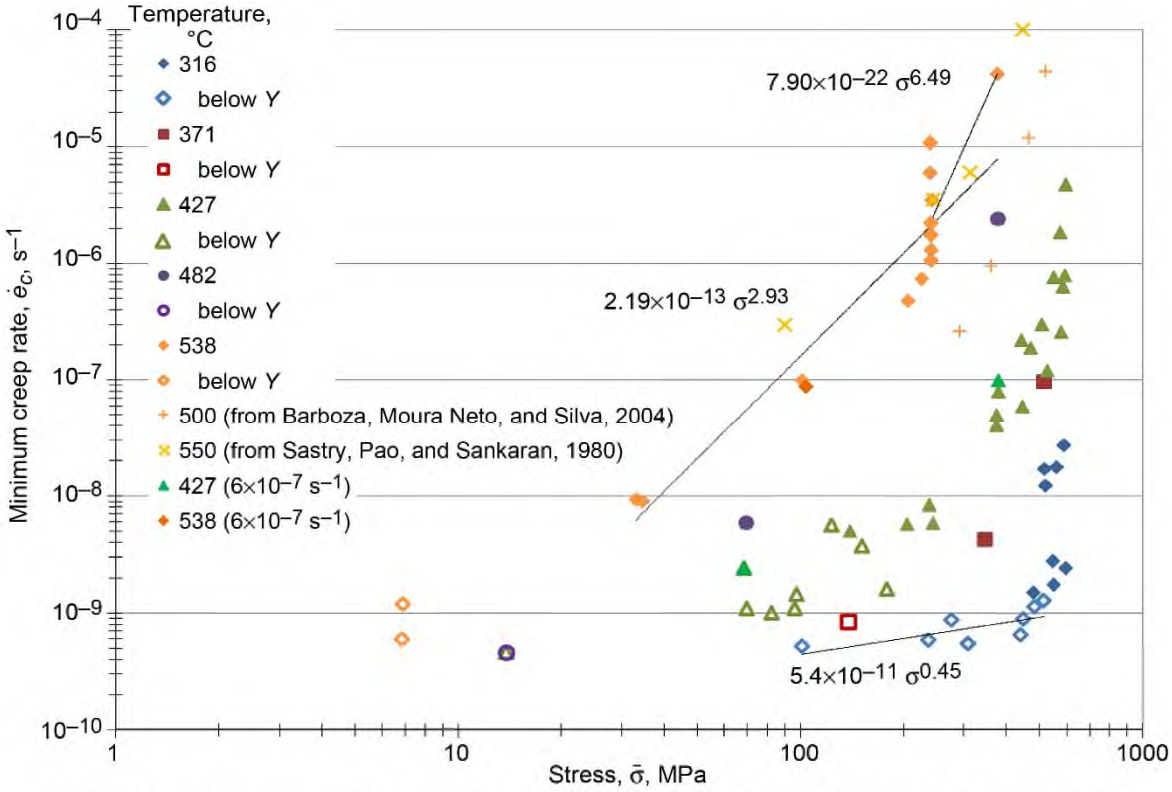

Figure 30.—Minimum creep rate $\dot{e}_c$ of Ti-6-4 at strain rate of 10^{-3} s^{-1} as function of applied stress $\bar{\sigma}$.

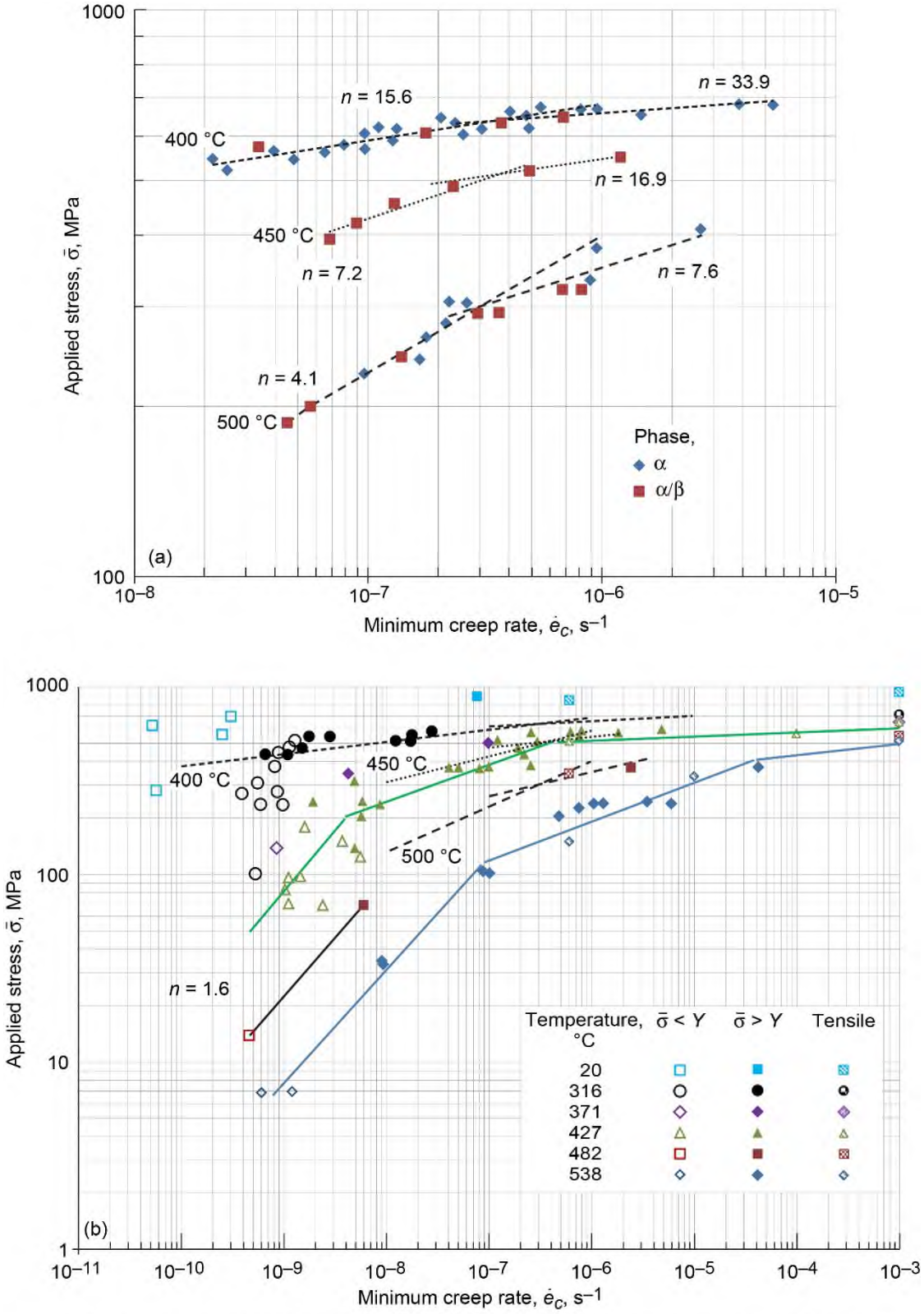

Figure 31.—Stress dependence on minimum creep rate $\dot{e}_C$ of Ti-6-4 (from Evans and Harrison, 1983). (a) Creep data from Evans and Harrison, showing creep power law exponent n. (b) Comparison with data from current study (superimposed onto lines from part (a)).

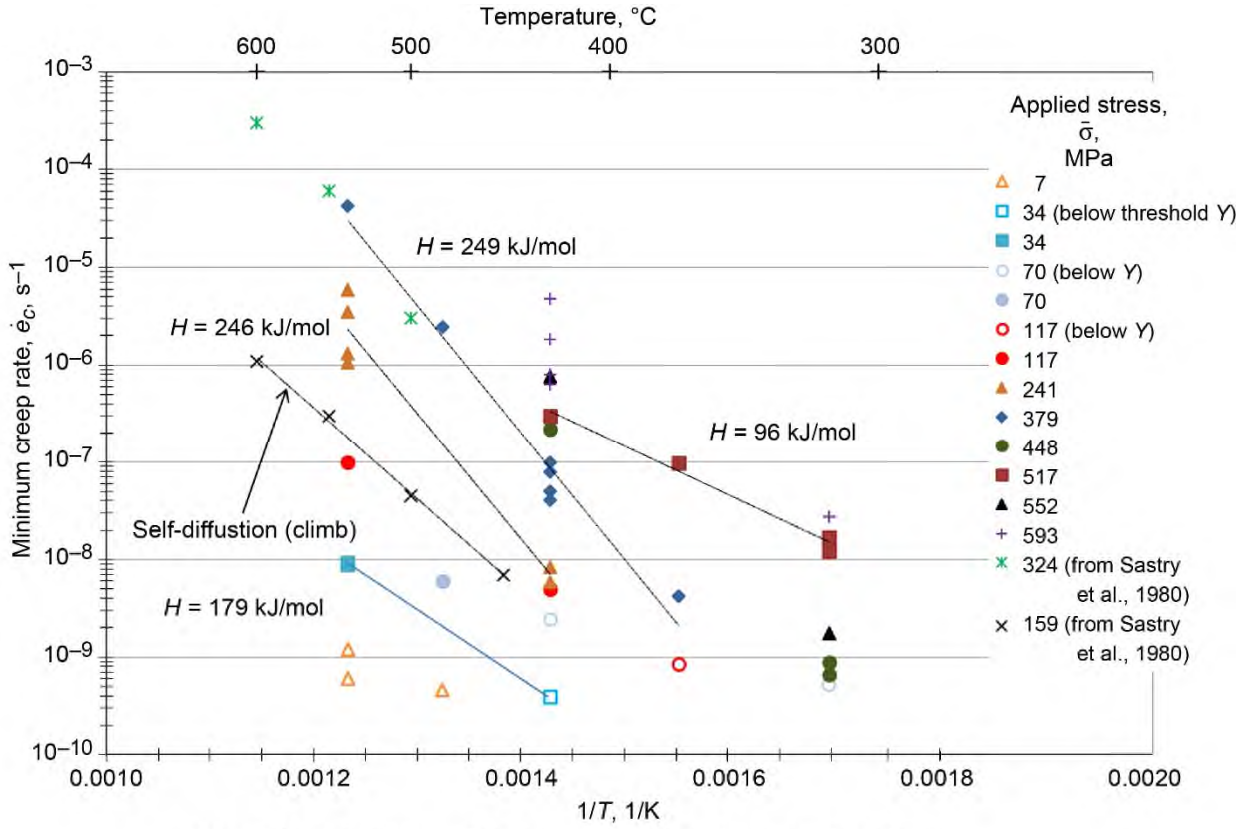

Figure 32.—Creep activation energy H of Ti-6-4 at various stress levels.

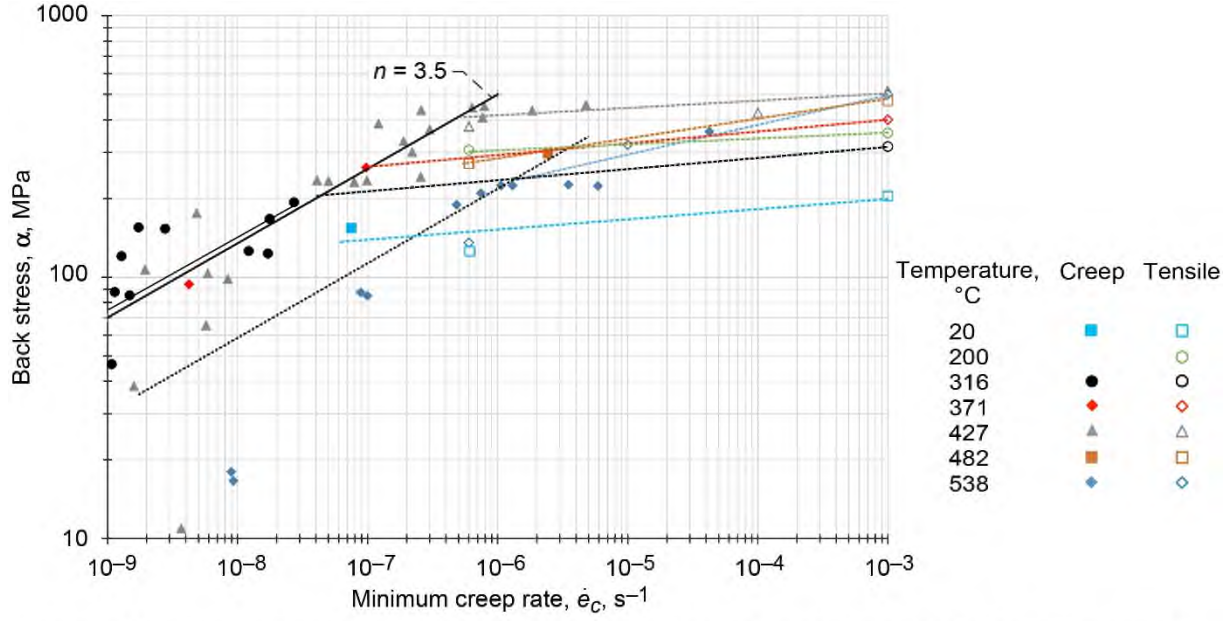

Figure 33.—Minimum creep rate of Ti-6-4 as function of back stress α, showing creep power law exponent n.

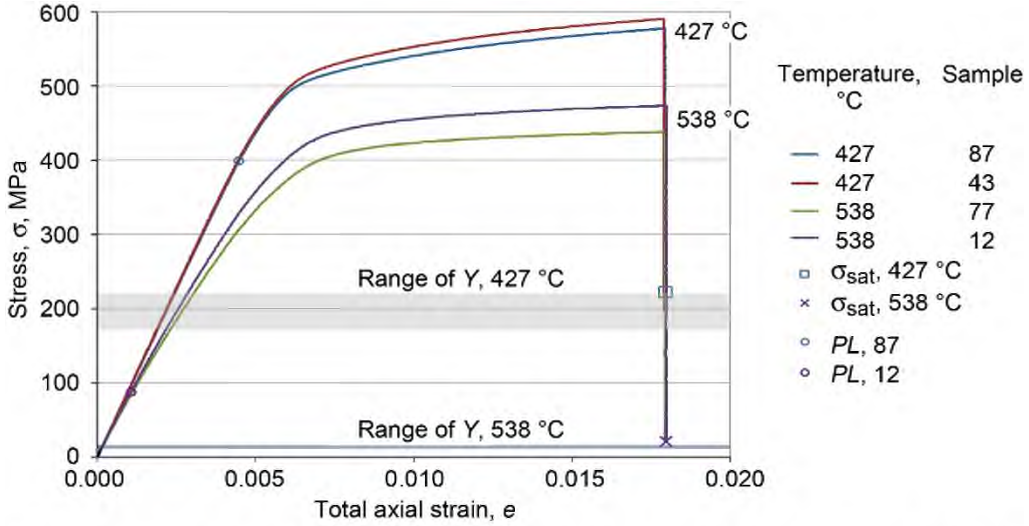

Figure 34.—Stress relaxation of Ti-6-4 at 0.018 strain for two temperatures at applied strain rate of 10^{-3} s^{-1}, showing saturation stress σ_{sat}, proportional limit *PL*, and threshold stress *Y*.

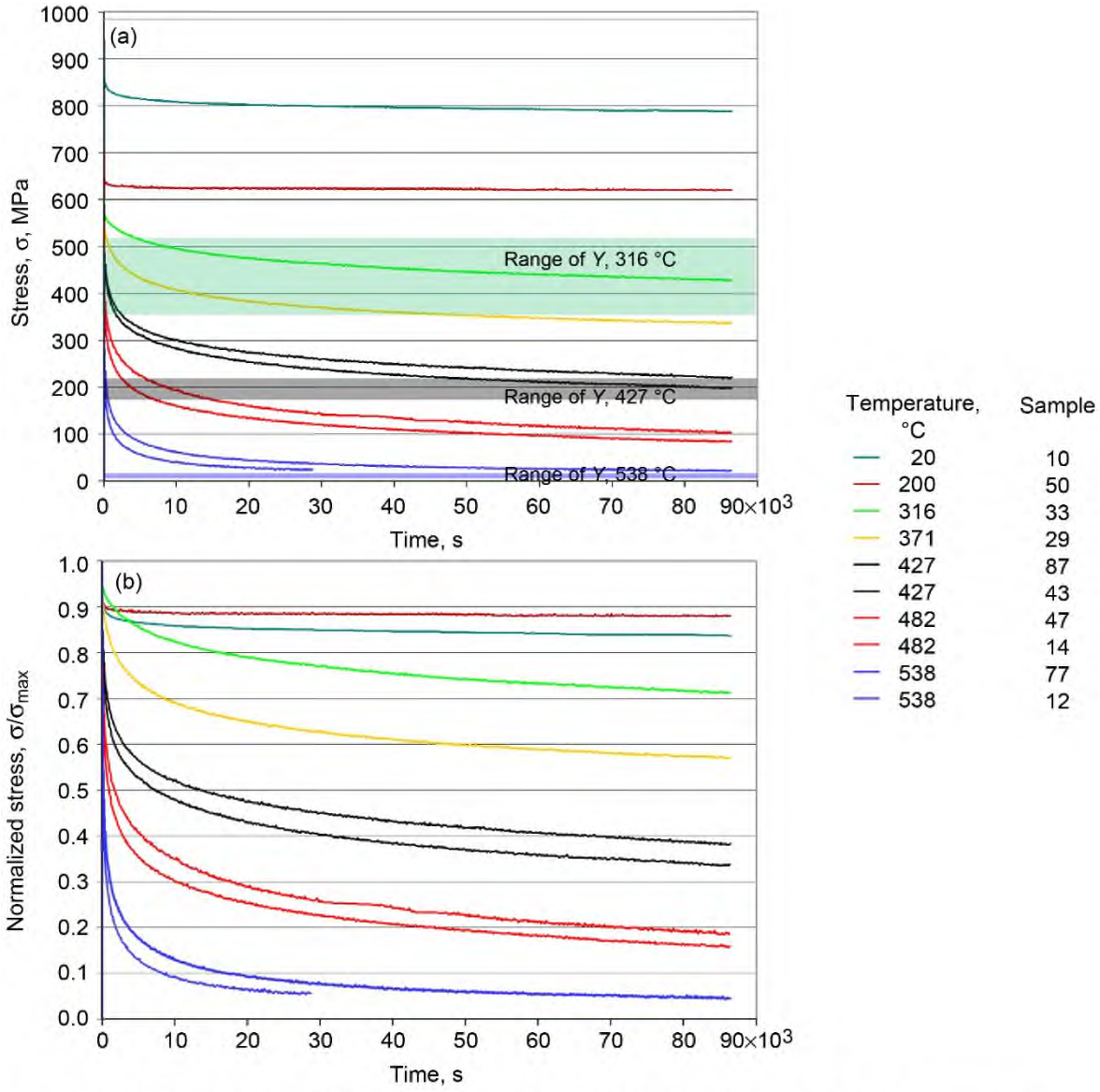

Figure 35.—Stress relaxation of Ti-6-4 at 0.018 strain (applied strain rate of 10^{-3} s^{-1}). (a) Temperature dependence, showing threshold *Y* for selected temperatures. (b) Normalized against maximum stress σ_{max}.

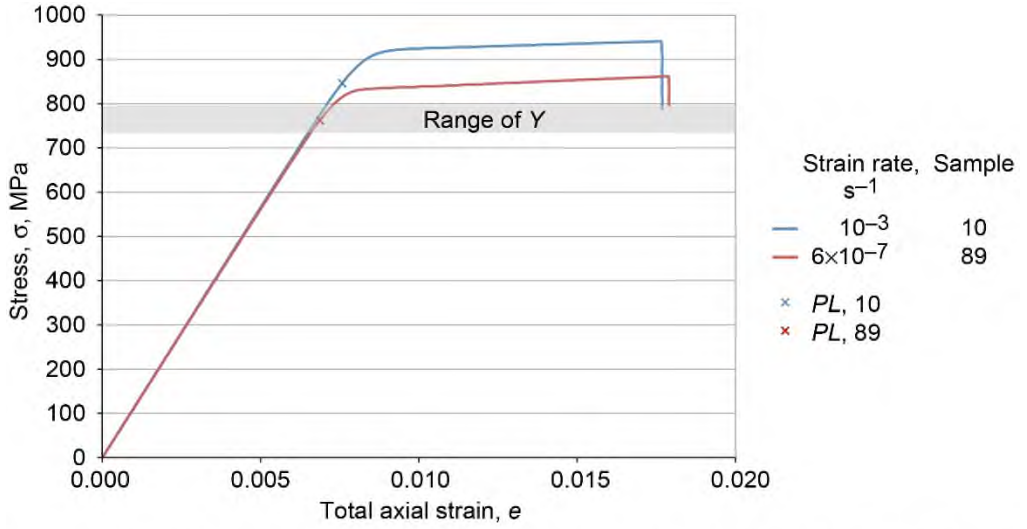

Figure 36.—Stress relaxation of Ti-6-4 at 20 °C and 0.018 strain for slow and fast applied strain rates, showing proportional limit *PL* and threshold stress *Y*.

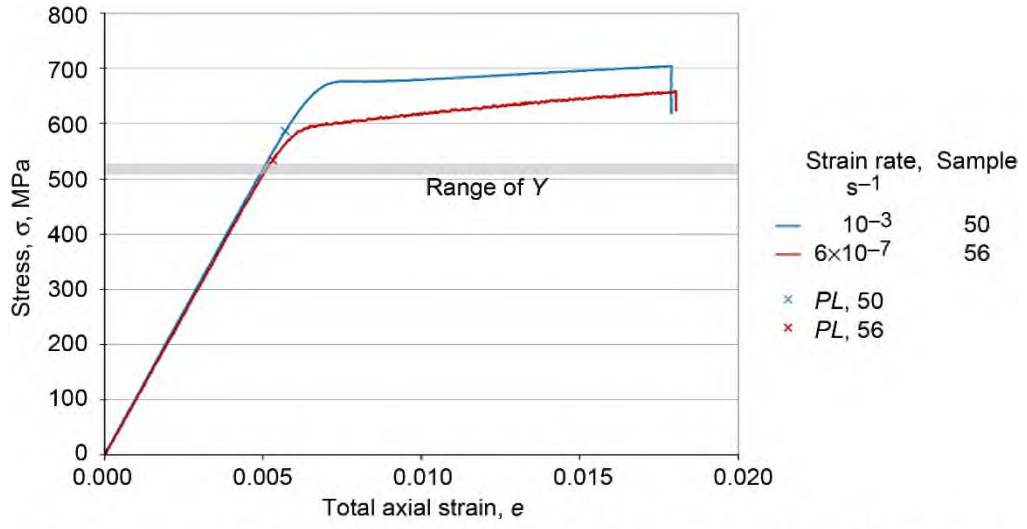

Figure 37.—Stress relaxation of Ti-6-4 at 200 °C and 0.018 strain for slow and fast applied strain rates, showing proportional limit *PL* and threshold stress *Y*.

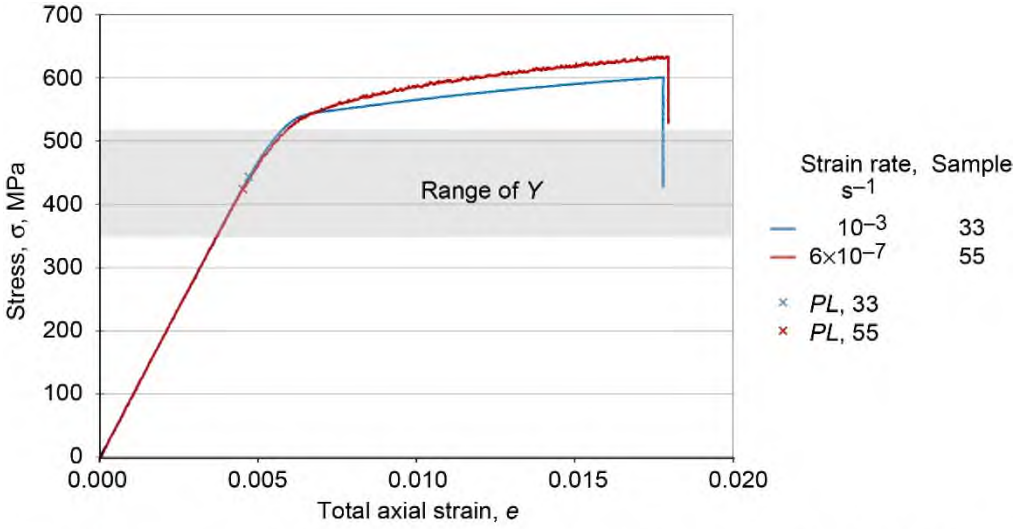

Figure 38.—Stress relaxation of Ti-6-4 at 316 °C and 0.018 strain for slow and fast applied strain rates, showing proportional limit *PL* and threshold stress *Y*.

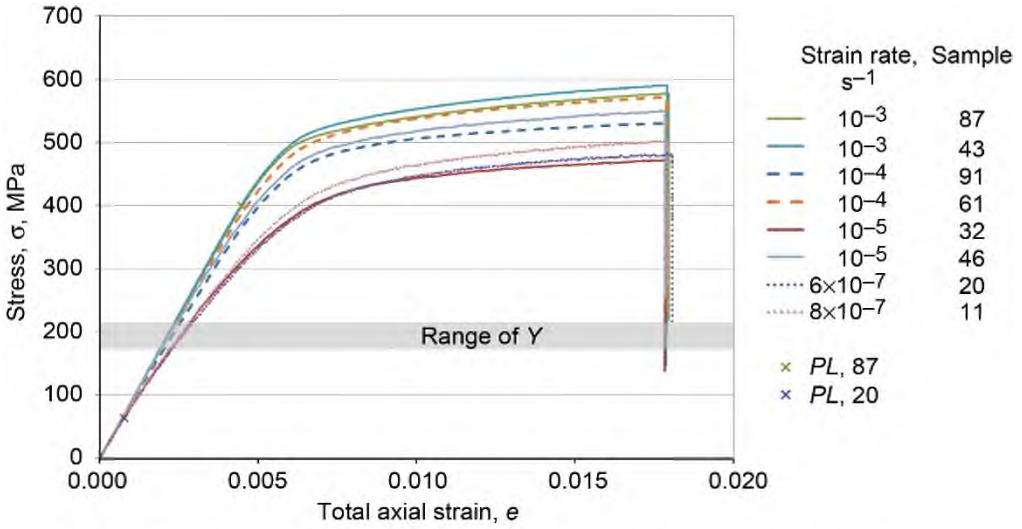

Figure 39.—Stress relaxation of Ti-6-4 at 427 °C and 0.018 strain as function of applied strain rates, showing proportional limit *PL* and threshold stress *Y*.

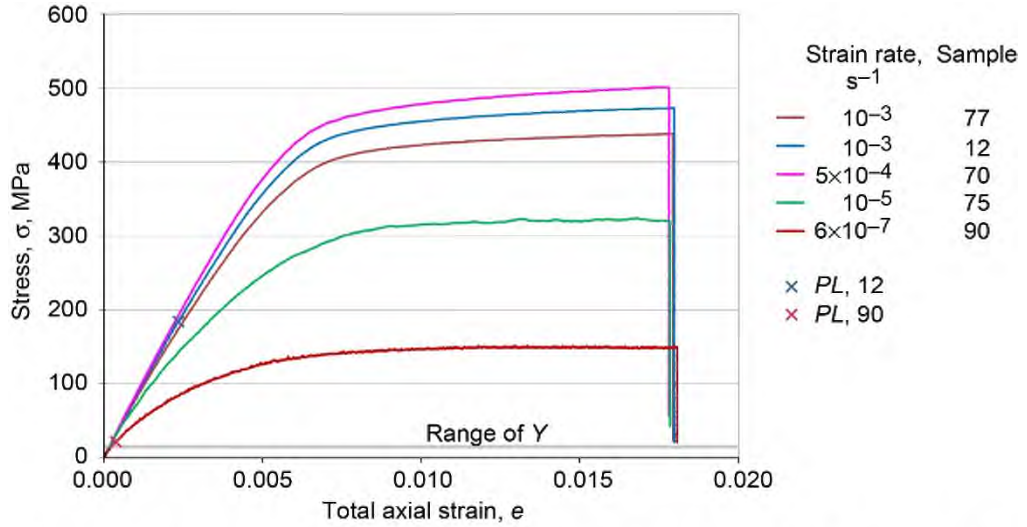

Figure 40.—Stress relaxation of Ti-6-4 at 538 °C and 0.018 strain as function of applied strain rates, showing proportional limit *PL* and threshold stress *Y*.

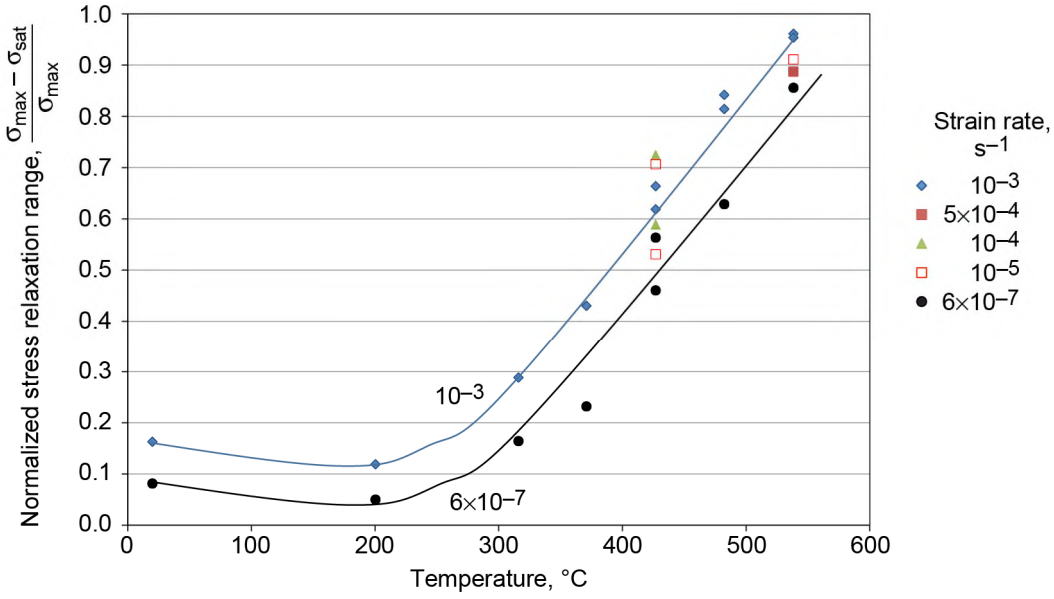

Figure 41.—Stress relaxation range of Ti-6-4, normalized against maximum stress σ_{max} at 0.018 strain as function of temperature at various applied strain rates, where σ_{sat} is saturation stress.

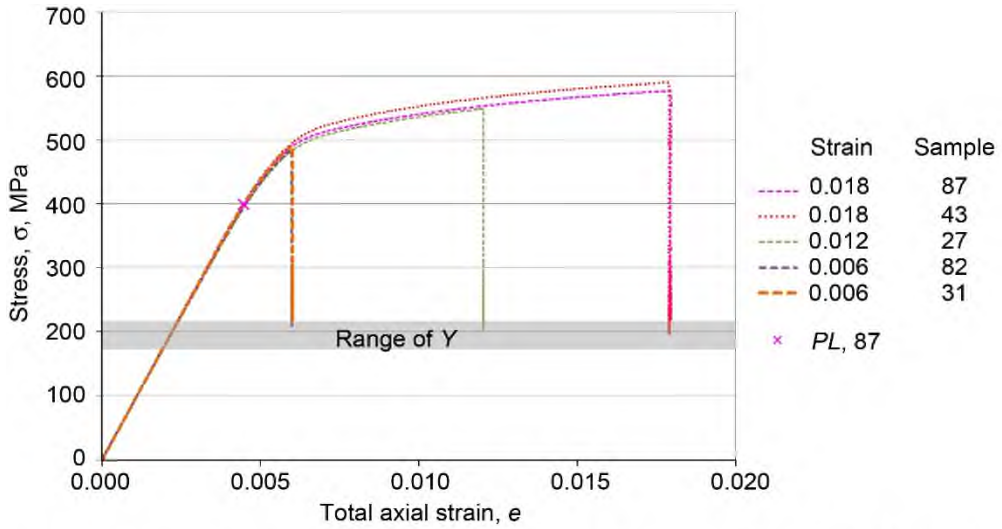

Figure 42.—Stress relaxation of Ti-6-4 at 427 °C and applied strain rate of 10^{-3} s^{-1} for various strain levels, showing proportional limit *PL* and threshold stress *Y*.

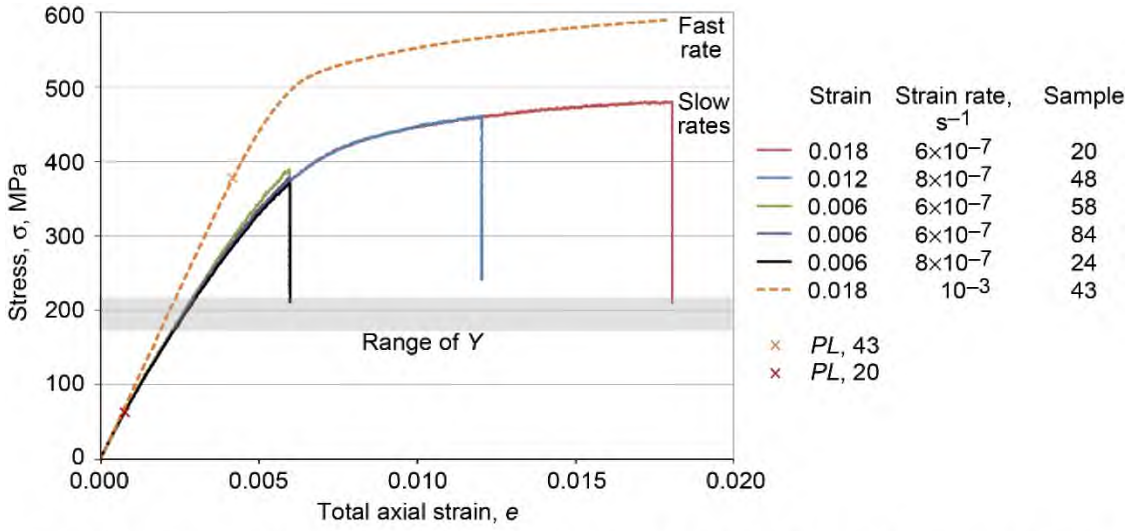

Figure 43.—Stress relaxation of Ti-6-4 at 427 °C for various strain levels and slow applied strain rates, showing proportional limit *PL* and threshold stress *Y*.

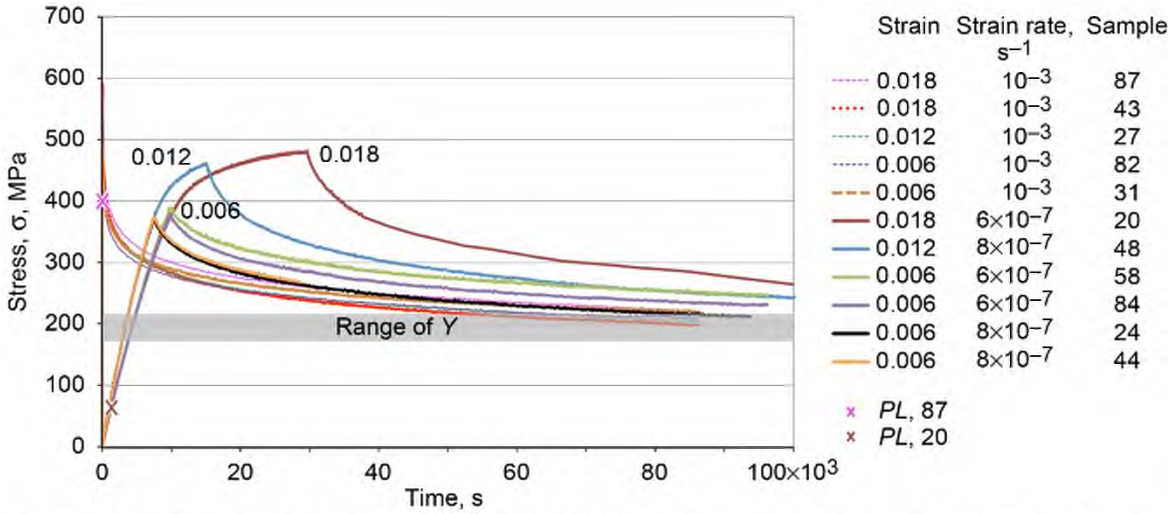

Figure 44.—Comparison of fast- and slow-rate-loaded stress relaxation at 427 °C and various strain levels for Ti-6-4, showing proportional limit *PL* and threshold stress *Y*.

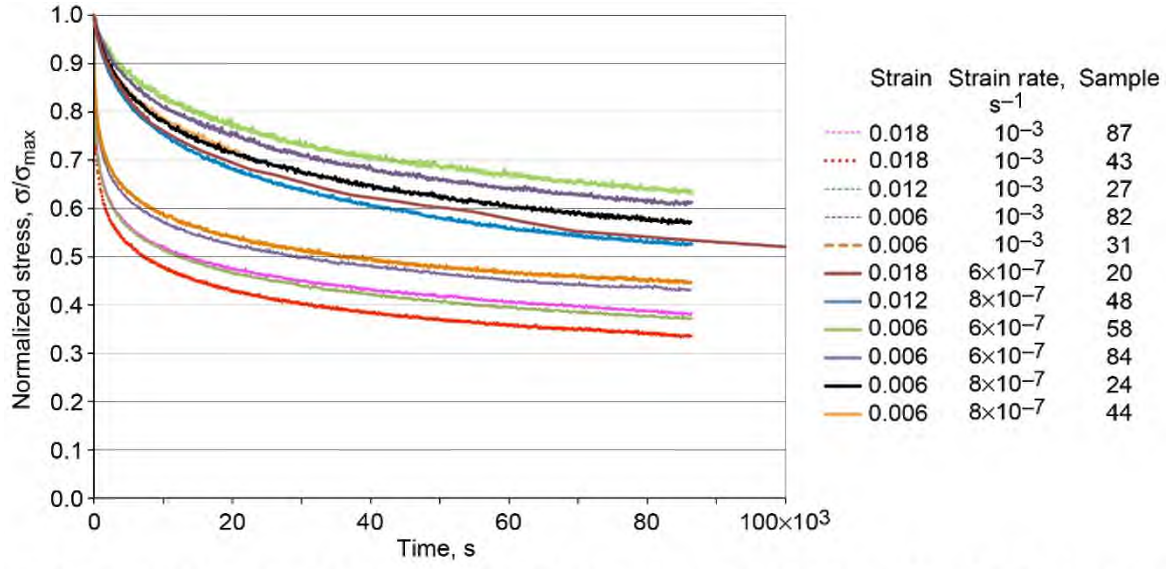

Figure 45.—Stress relaxation of Ti-6-4 at 427 °C for different strain levels and applied strain rates, normalized against maximum stress.

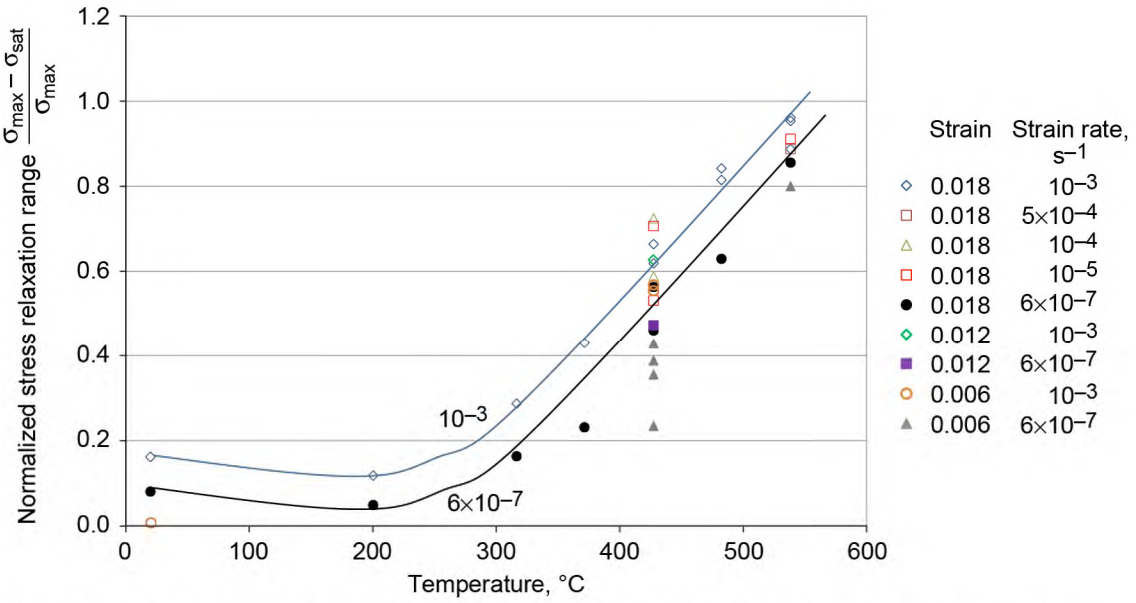

Figure 46.—Stress relaxation range of Ti-6-4 at three strain levels, normalized against maximum stress σ_{max}, as function of temperature for various applied strain rates, where σ_{sat} is saturation stress.

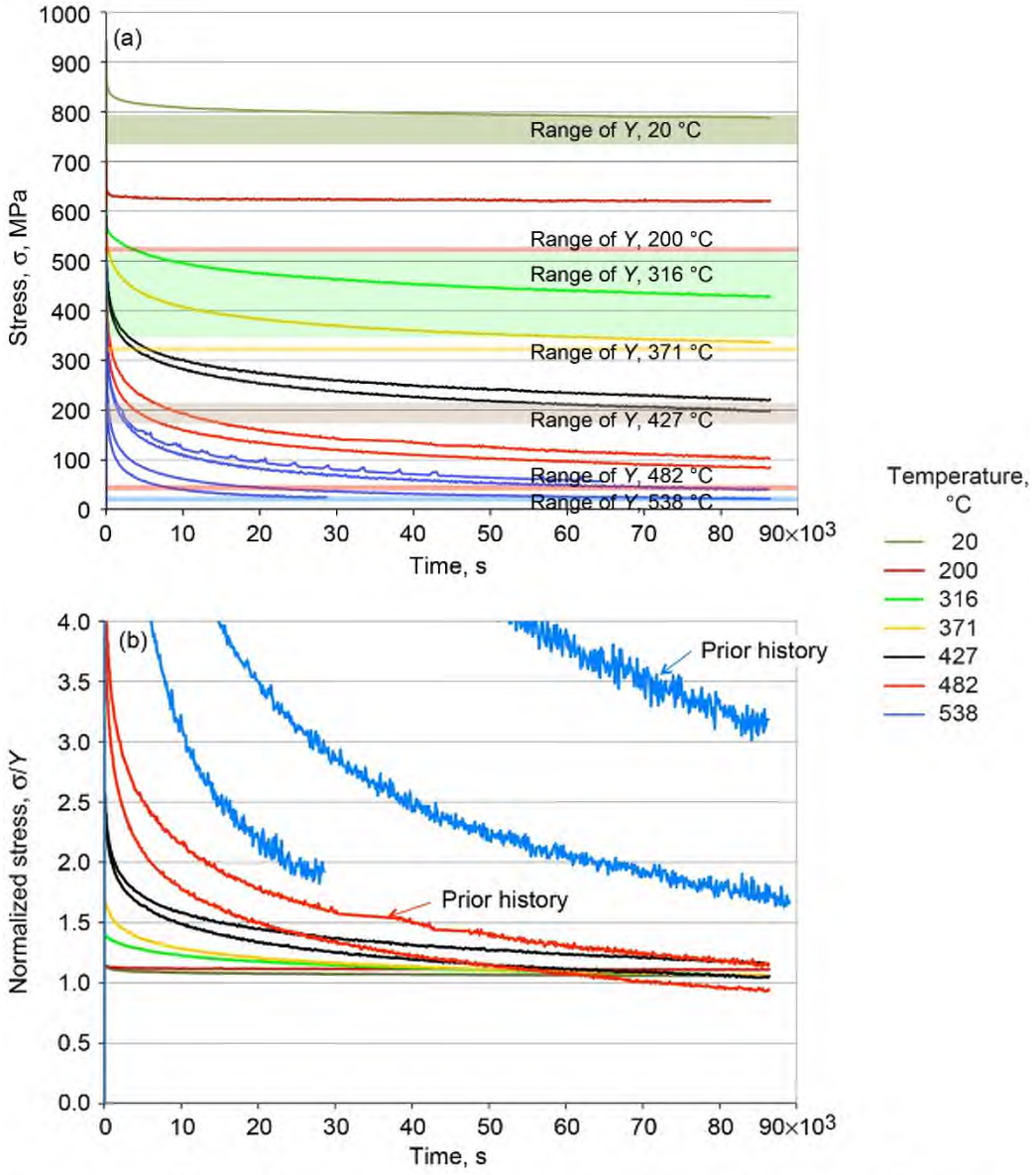

Figure 47.—Stress relaxation of Ti-6-4 at 0.018 strain and strain rate of 10^{-3}. (a) Stress at various temperatures, indicating ranges of threshold stress *Y*. (b) Normalized against *Y* as function of time for various temperatures.

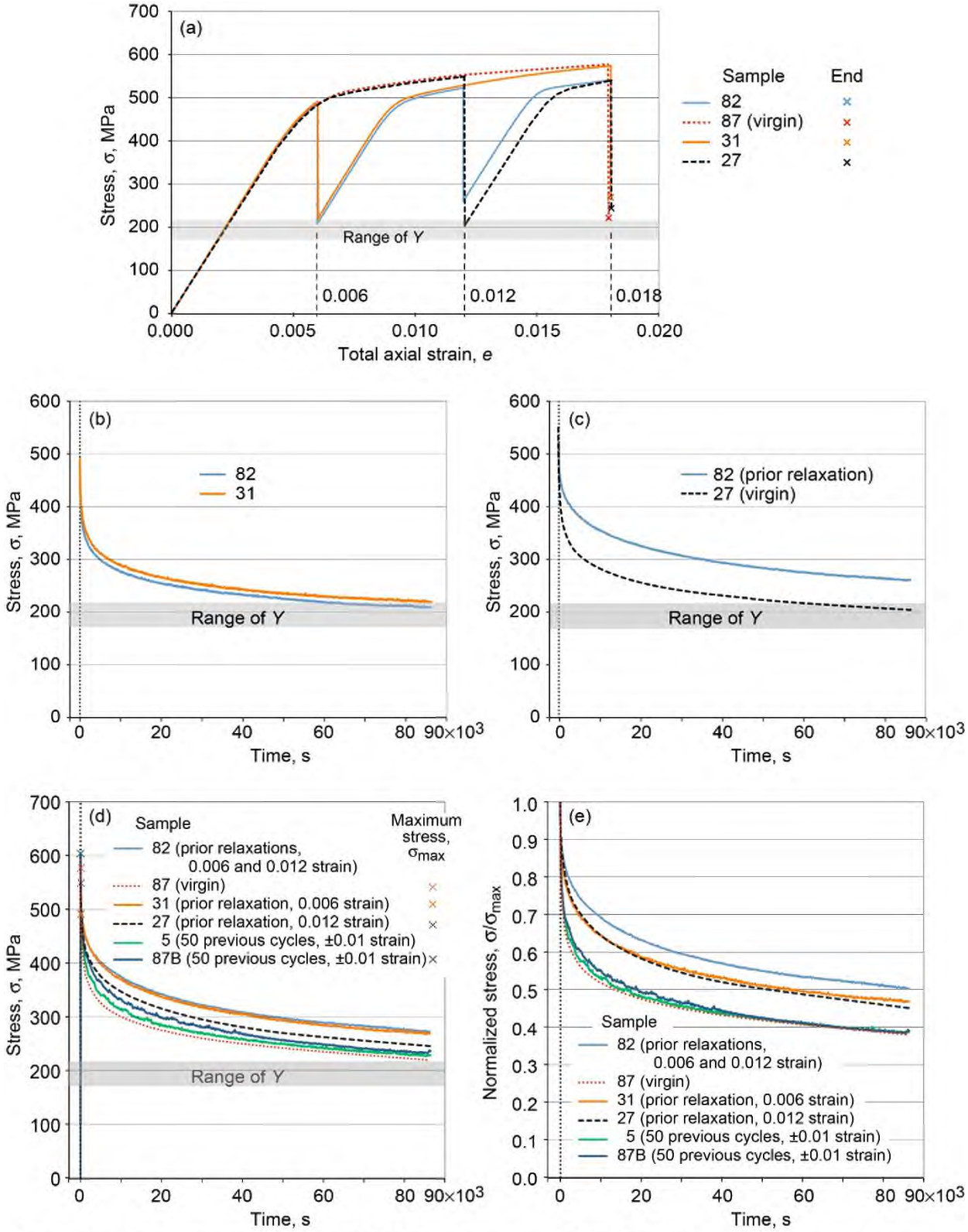

Figure 48.—Stress relaxation of Ti-6-4 at 427 °C and strain rate of 10^{-3} s^{-1} for different hold strains, showing effect of prior relaxation. (a) Step relaxation at 0.006, 0.012, and 0.018 strain, showing threshold stress *Y*. (b) Virgin samples at 0.006 strain, showing *Y*. (c) At 0.012 strain, showing *Y*. (d) At 0.018 strain, showing *Y*. (e) Normalized against maximum stress.

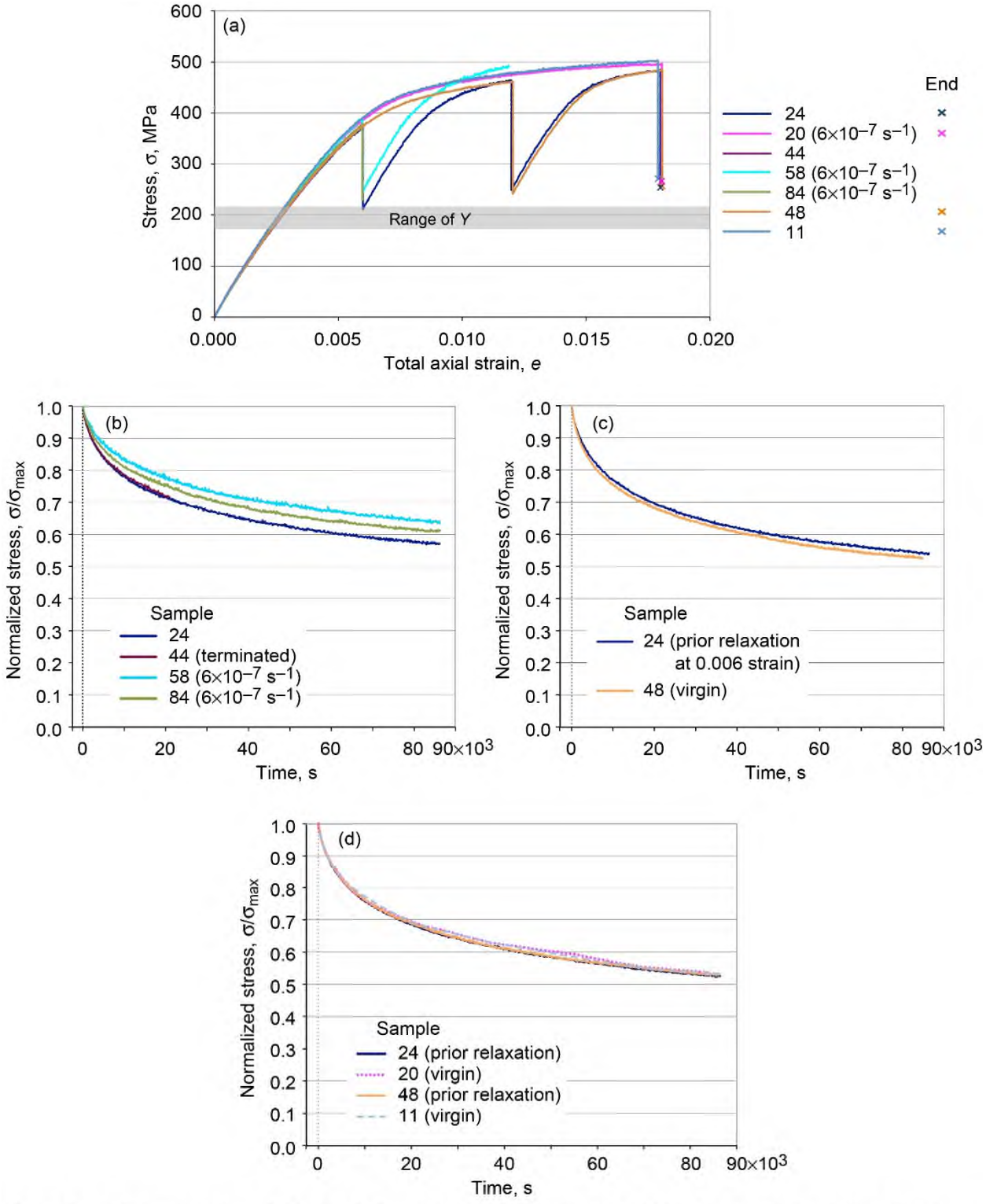

Figure 49.—Stress relaxation of Ti-6-4 at 427 °C and slow strain rates. (a) At 8×10^{-7} strain rate, including relaxations at 0.006, 0.012, and 0.018 strain, showing threshold stress *Y*. (b) Normalized against maximum stress; relaxation at 0.006 strain. (c) Normalized against maximum stress; relaxation at 0.012 strain. (d) Normalized against maximum stress; relaxation at 0.018 strain.

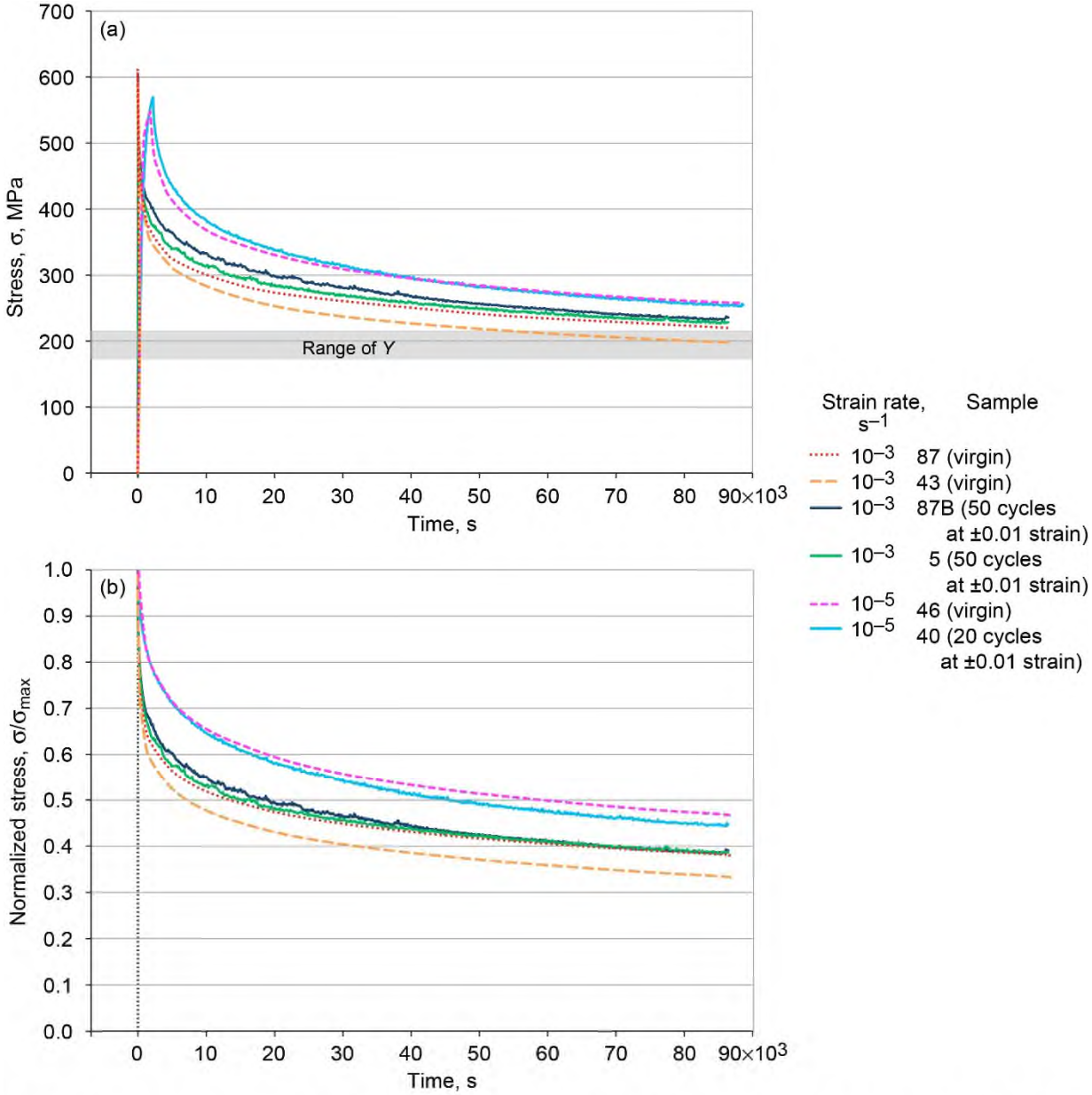

Figure 50.—Stress relaxation of Ti-6-4 at 427 °C and strain of 0.018 at different strain rates, showing effect of prior load cycles. (a) Relaxation curves showing threshold stress *Y*. (b) Normalized against maximum stress.

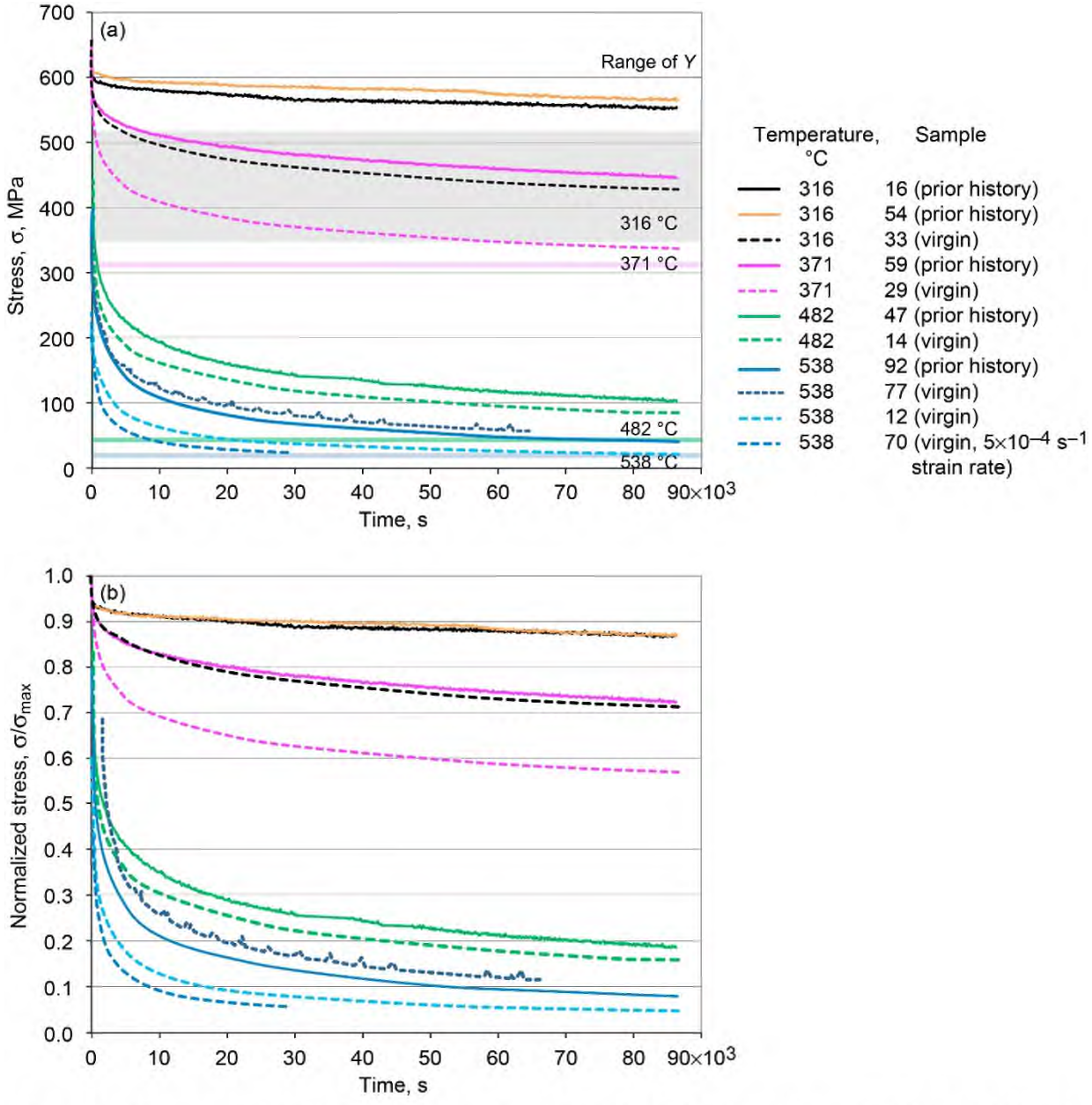

Figure 51.—Stress relaxation of Ti-6-4 at 0.018 strain, strain rate of 10^{-3} s^{-1}, and various temperatures, showing effect of prior relaxation steps. (a) Showing threshold stress *Y*. (b) Normalized against maximum stress.

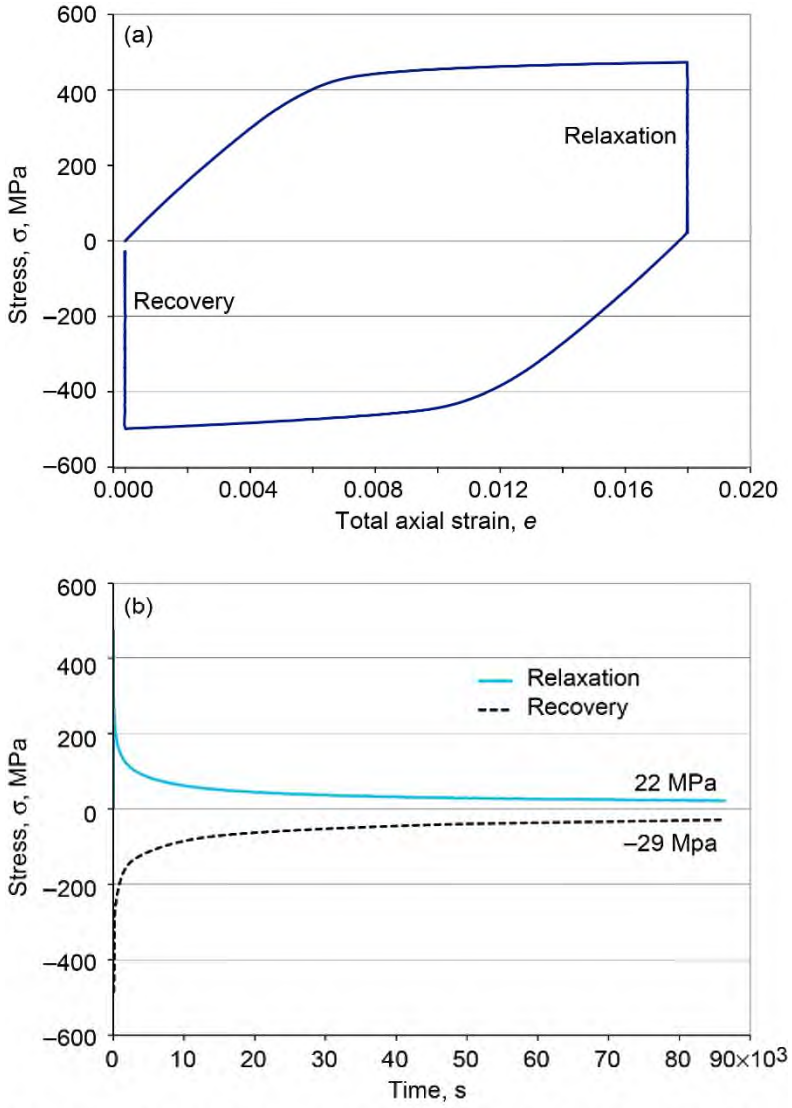

Figure 52.—Stress relaxation of Ti-6-4 (sample 12) for 24 h at 538 °C and strain rate of 10^{-3} s^{-1}; recovery at 0 strain for 24 h. (a) As function of total axial strain. (b) At 0.018 strain and recovery at 0 strain.

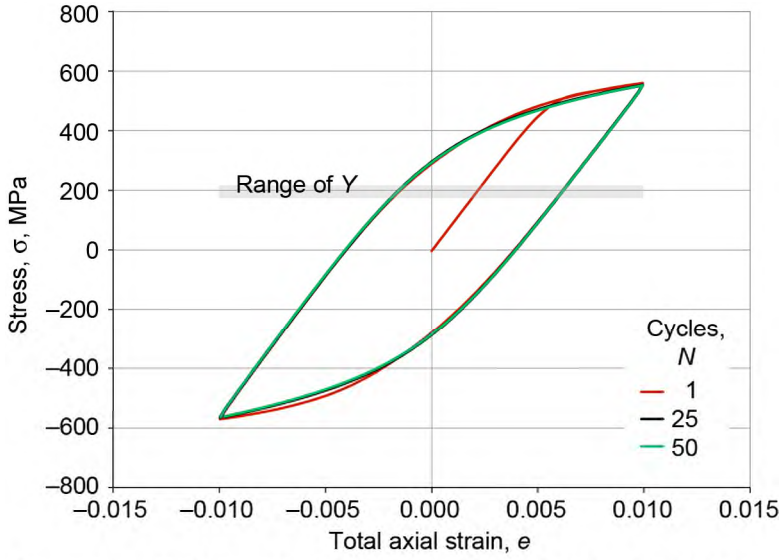

Figure 53.—Hysteresis loops for Ti-6-4 (sample 5) fatigued at 427 °C, ±0.01 strain, and 10^{-3} s^{-1} strain rate for selected cycles, showing threshold stress *Y*.

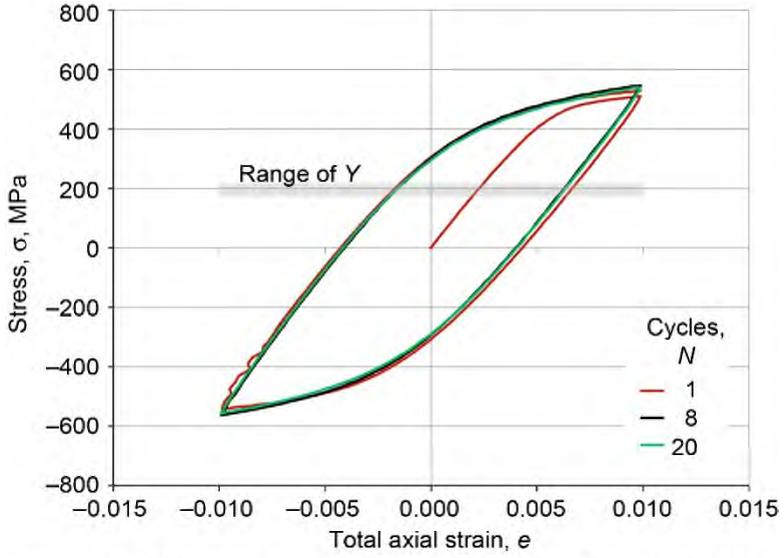

Figure 54.—Hysteresis loops for Ti-6-4 (sample 40) fatigued at 427 °C, ±0.01 strain, and 10^{-5} s^{-1} strain rate for selected cycles, showing threshold stress *Y*.

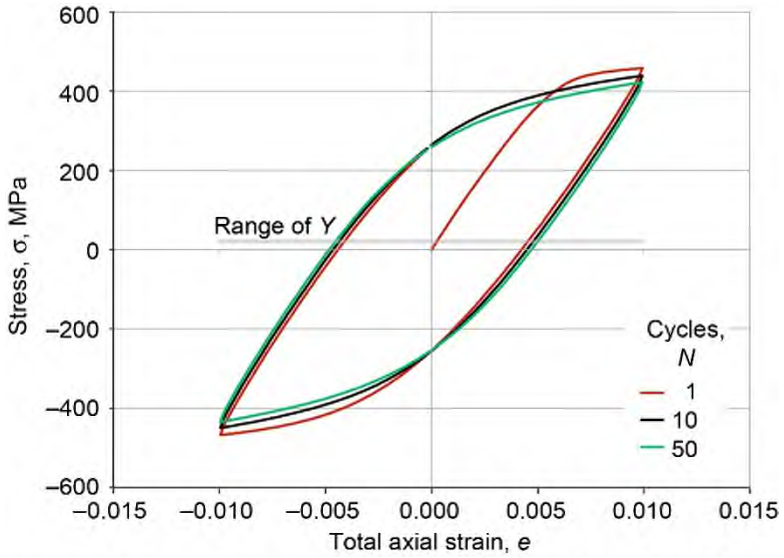

Figure 55.—Hysteresis loops for Ti-6-4 (sample 74) fatigued at 538 °C, ±0.01 strain, and 10^{-3} s^{-1} strain rate for selected cycles, showing threshold stress *Y*.

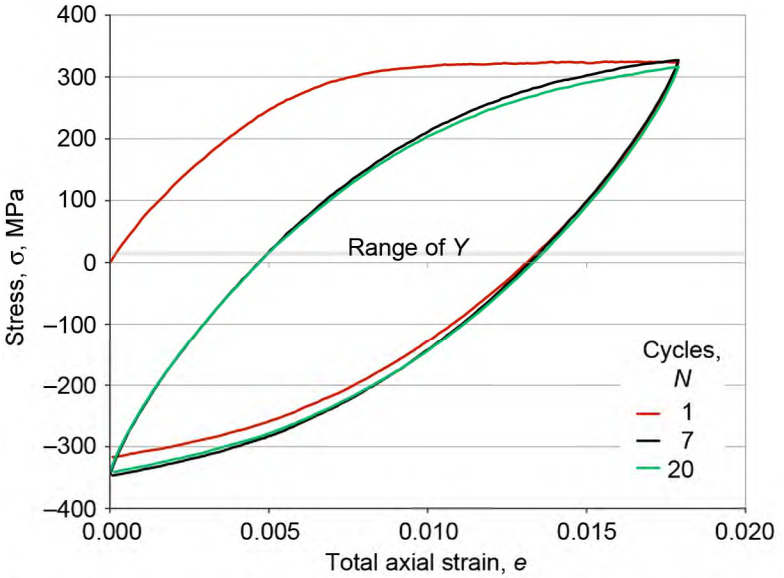

Figure 56.—Hysteresis loops for Ti-6-4 (sample 73) fatigued at 538 °C and 10^{-5} s^{-1} strain rate between 0 and 0.018 strain for selected cycles, showing range of threshold stress *Y*.

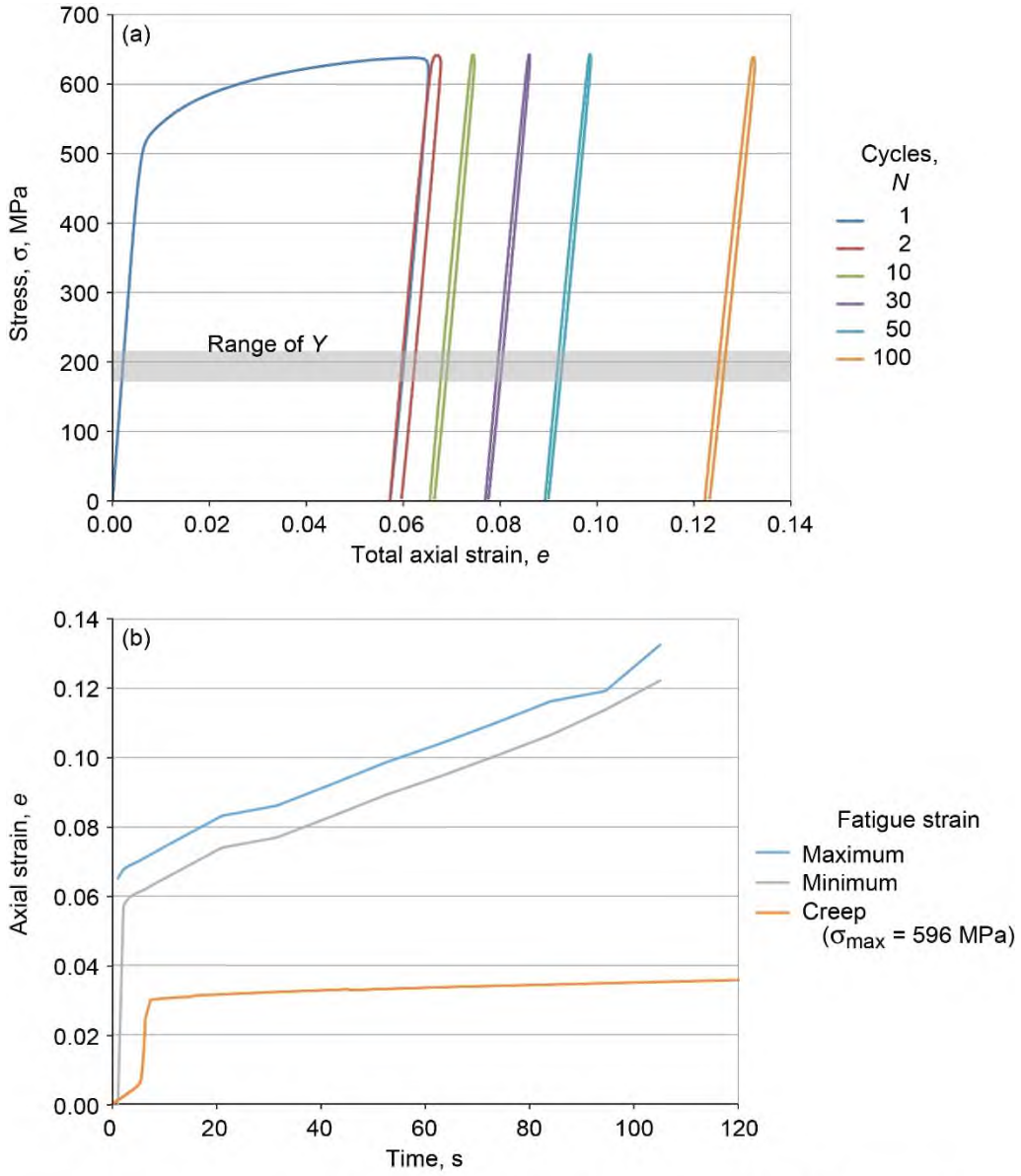

Figure 57.—Fatigue of Ti-6-4 (sample 58) in load control at 427 °C and 10^{-3} s^{-1} strain rate between 0 and 640 MPa for selected cycles; failure at N_f = 115 cycles. (a) Stress as function of total axial strain, showing threshold stress *Y*. (b) Axial strain versus time. Creep (sample 87) at similar maximum stress σ_{max} is shown for comparison.

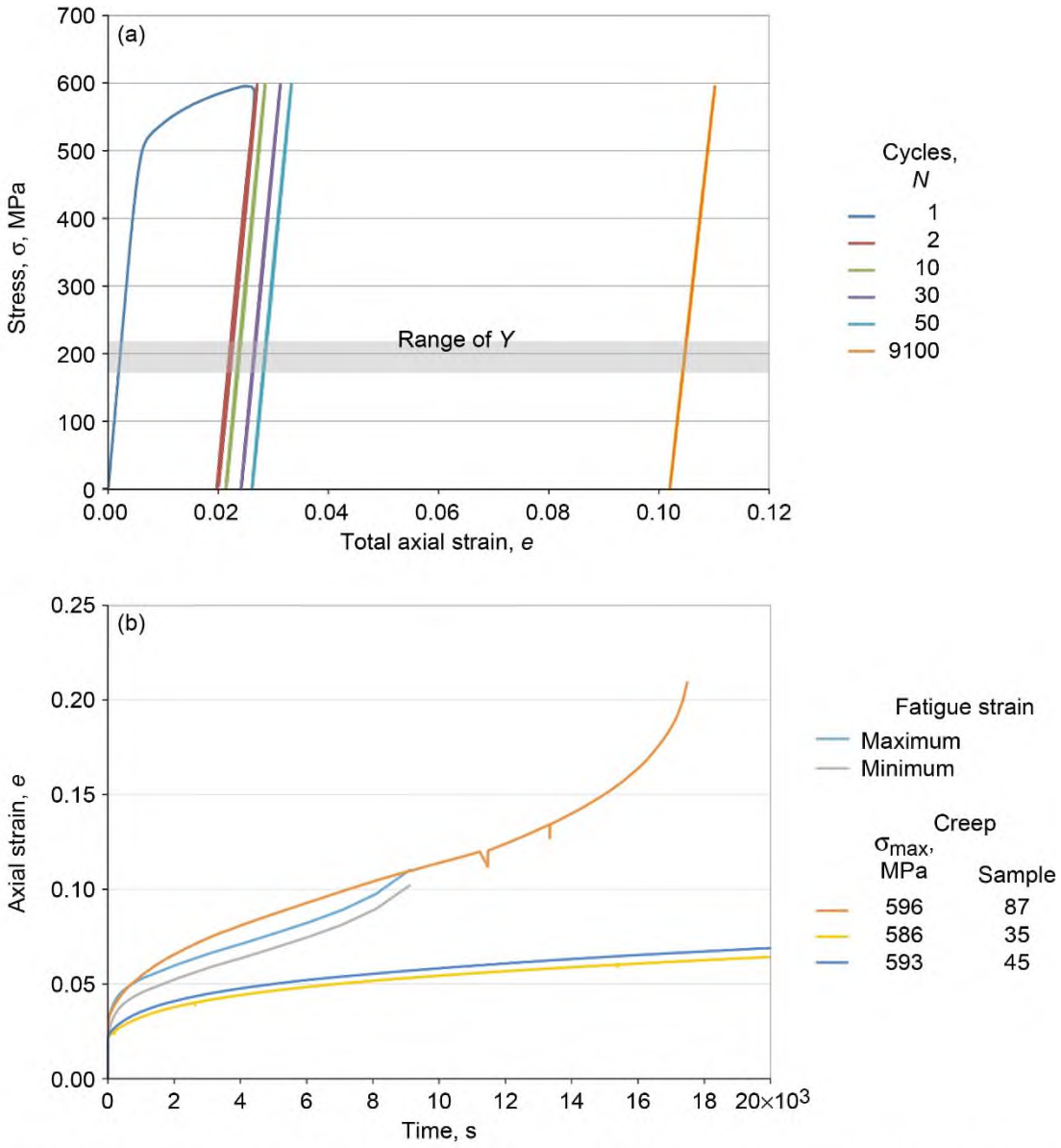

Figure 58.—Fatigue of Ti-6-4 (sample 59) at 427 °C and 10^{-3} s^{-1} strain rate between 0 and 600 MPa for selected cycles; failure at N_f = 9735 cycles. (a) Stress as function of total axial strain, showing threshold stress *Y*. (b) Axial strain versus time during fatigue compared to creep at similar maximum stress.

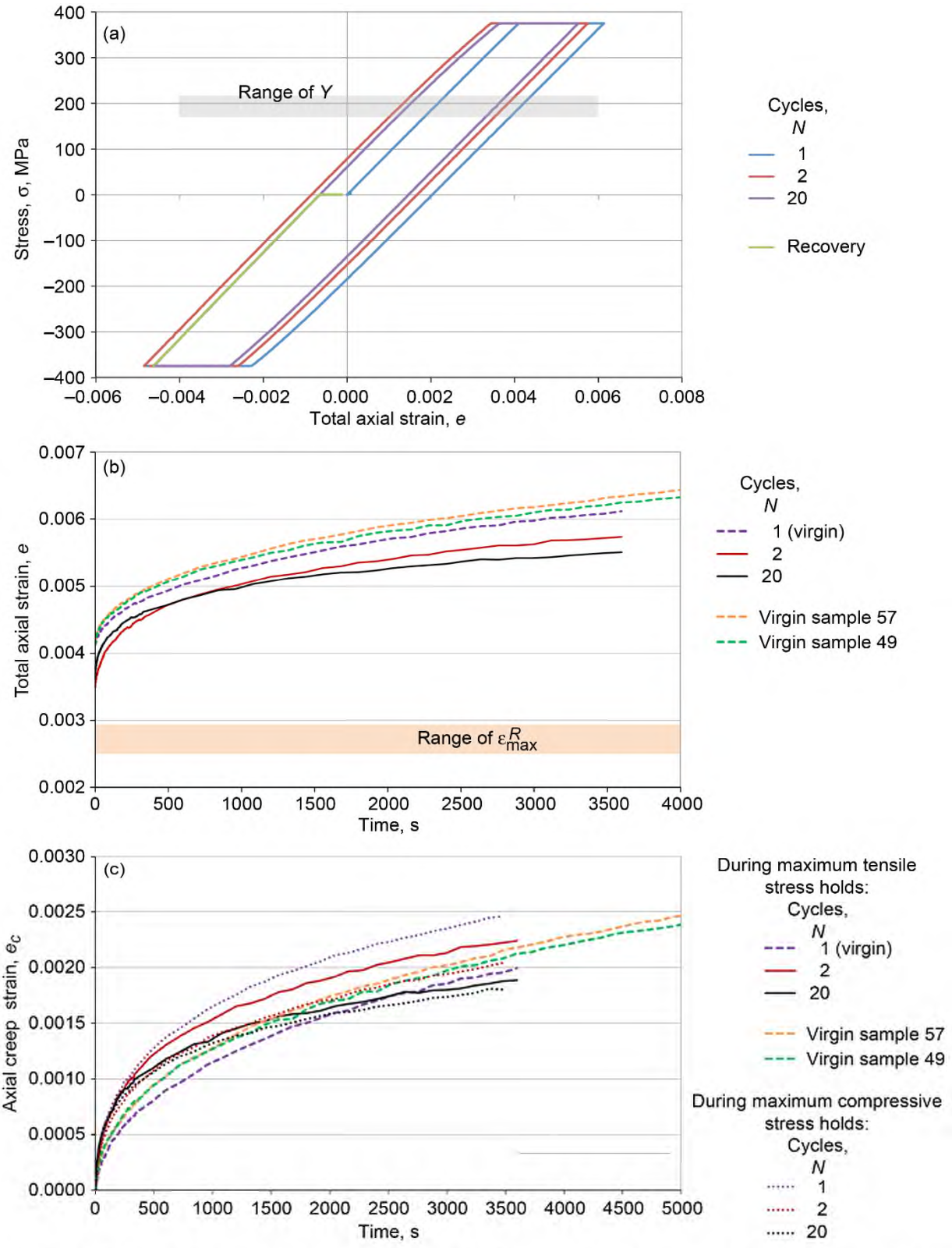

Figure 59.—Fatigue of Ti-6-4 (sample 96) at 427 °C, 10^{-3} s^{-1} strain rate, and ±375 MPa for selected cycles. (a) With stress holds at the maximum and minimum stresses, showing threshold stress *Y*. (b) Creep during the maximum stress holds compared to that of virgin samples, showing maximum reversible strain ε^R_{max} (=Y/E_S, where E_S is infinitely slow modulus). (c) Creep during maximum stress holds compared to that of virgin samples.

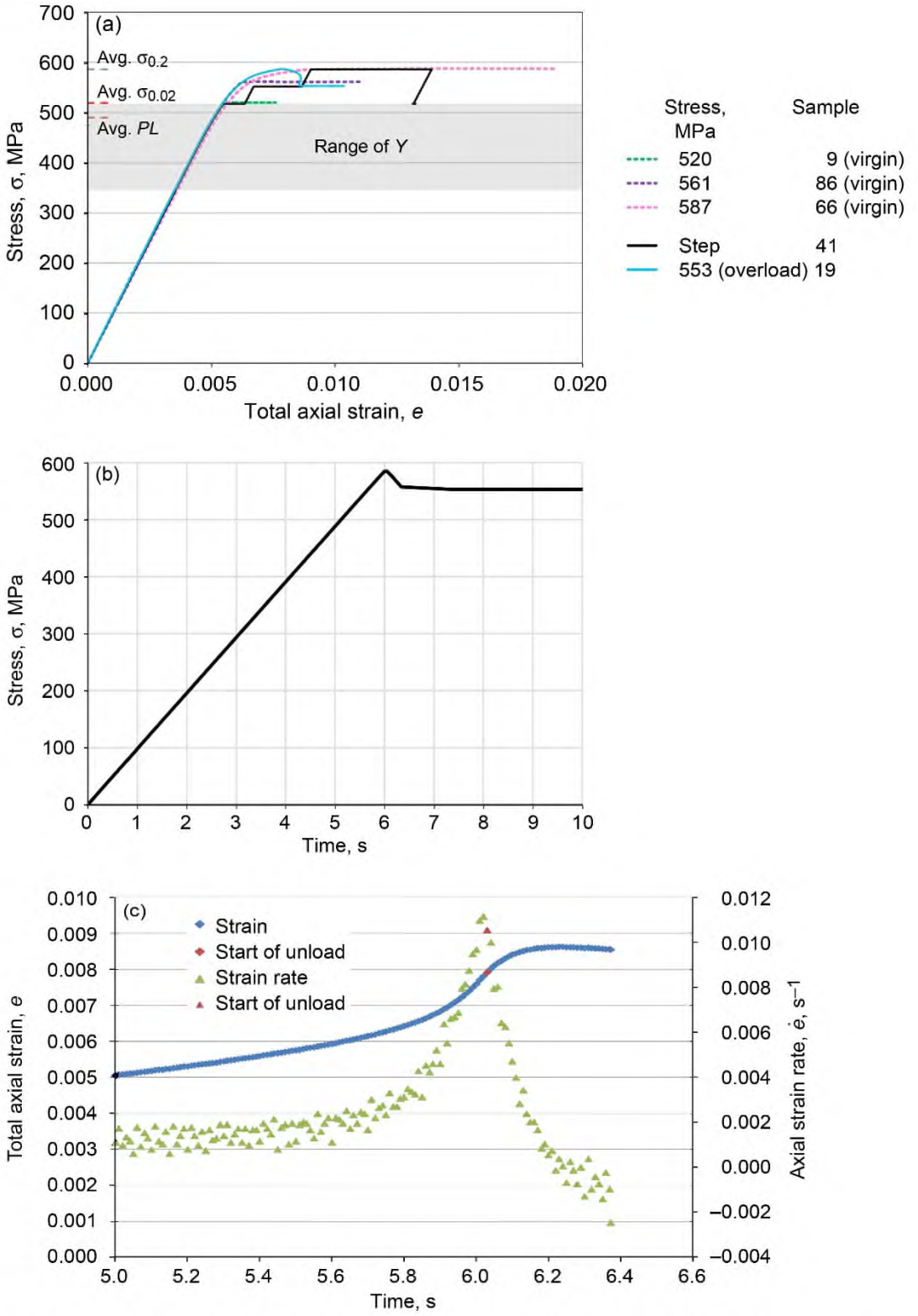

Figure 60.—Creep tests of Ti-6-4 at 316 °C. (a) Stress as function of total axial strain, showing 0.2% yield point $\sigma_{0.2}$, 0.02% yield point $\sigma_{0.02}$, proportional limit *PL*, and threshold stress *Y*. (b) Stress response of sample 19, showing stress overload followed by creep at 553 MPa. (c) Axial strain and strain rate during overload for sample 19. (d) Creep behavior, indicating creep rate $\dot{e}_c$ at end of time creep stage. (e) Creep behavior with zero reset at each step. (f) Creep behavior with zero reset and accumulated strains.

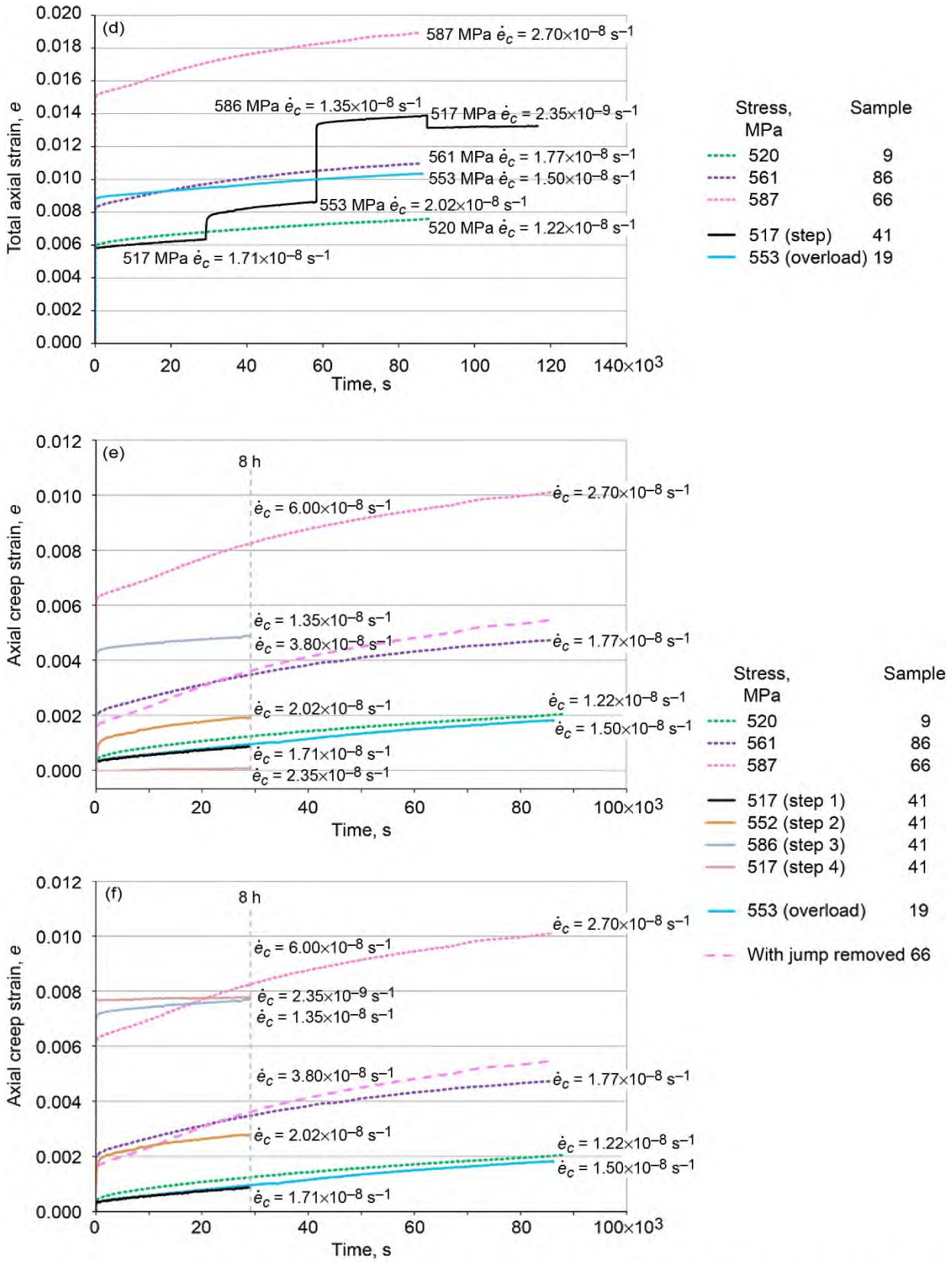

Figure 60.—Concluded. (d) Creep behavior, indicating creep rate $\dot{e}_c$ at end creep stage. (e) Creep behavior with zero reset at each step. (f) Creep behavior with zero reset and accumulated strains.

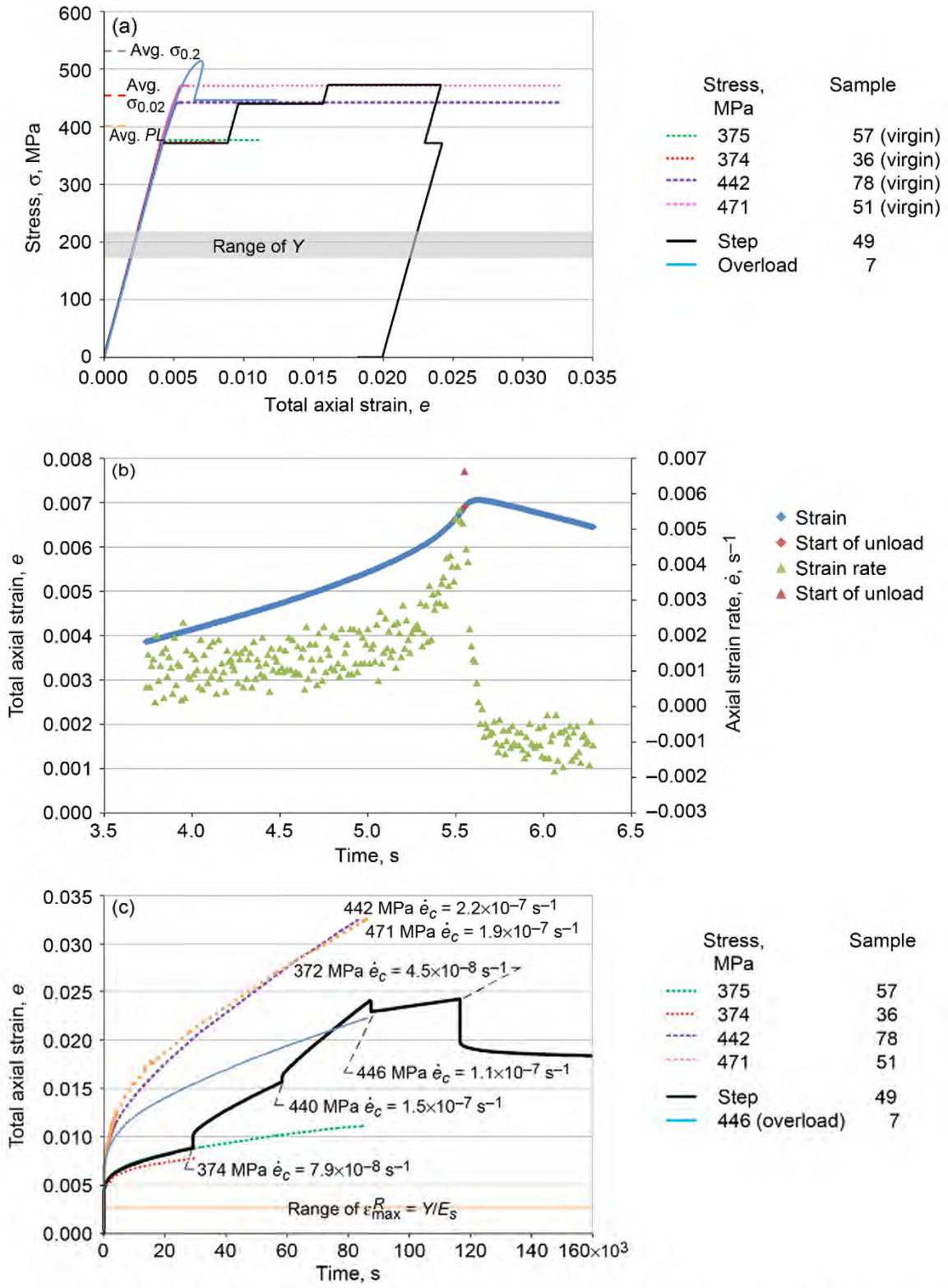

Figure 61.—Creep tests of Ti-6-4 at 427 °C. (a) Stress as function of total axial strain, showing 0.2% yield point $\sigma_{0.2}$, 0.02% yield point $\sigma_{0.02}$, proportional limit *PL*, and threshold stress *Y*. (b) Axial strain and strain rate during overload for sample 7. (c) Creep behavior, indicating creep rate $\dot{e}_c$ at end of creep stage and showing maximum reversible strain ε^R_{max} (=Y/E_S, where Y is threshold stress and E_S is infinitely slow modulus). (d) Creep behavior with zero reset. (e) Creep behavior with zero reset and accumulated strains.

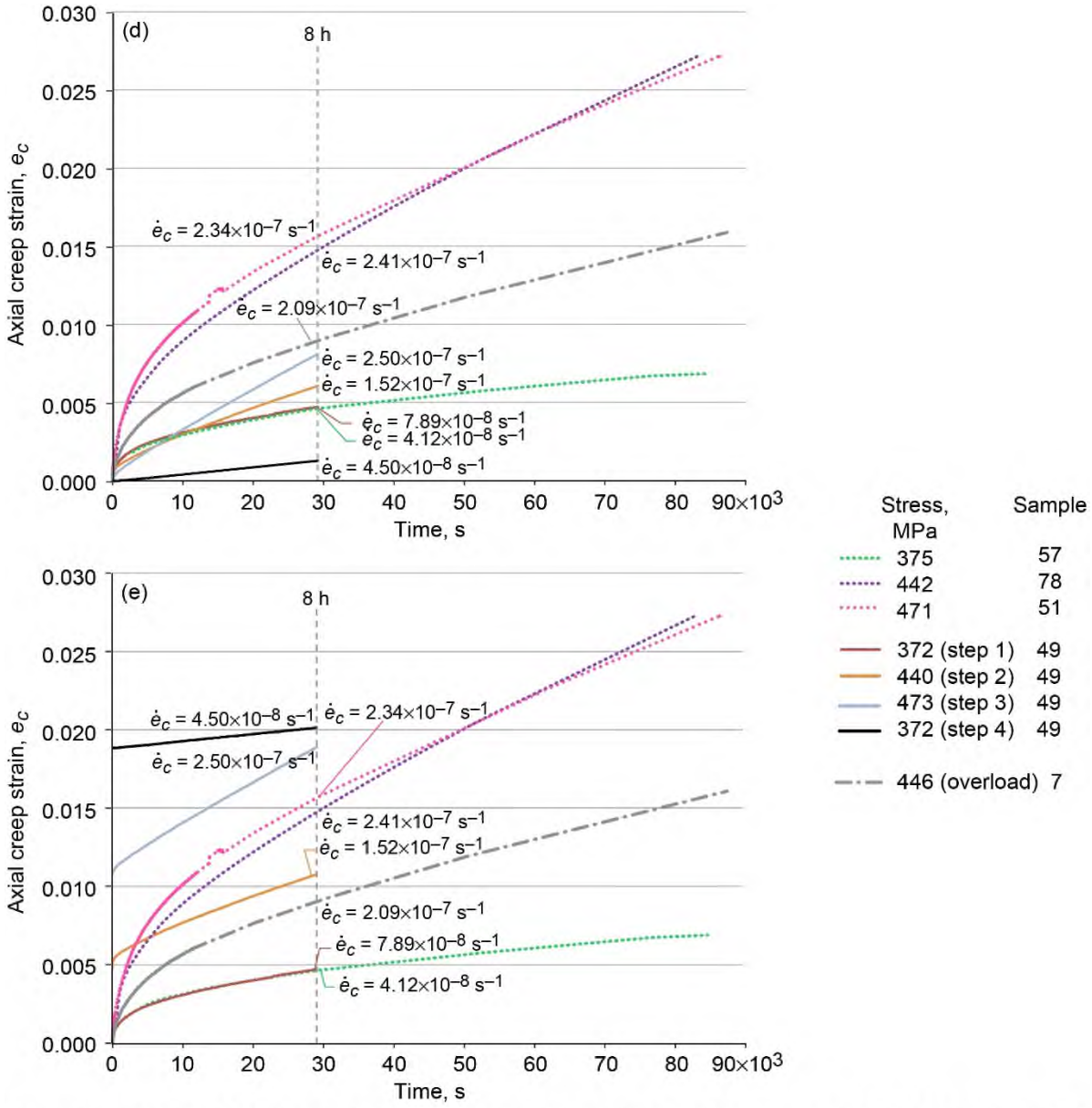

Figure 61.—Concluded. (d) Creep behavior with zero reset. (e) Creep behavior with zero reset and accumulated strains.

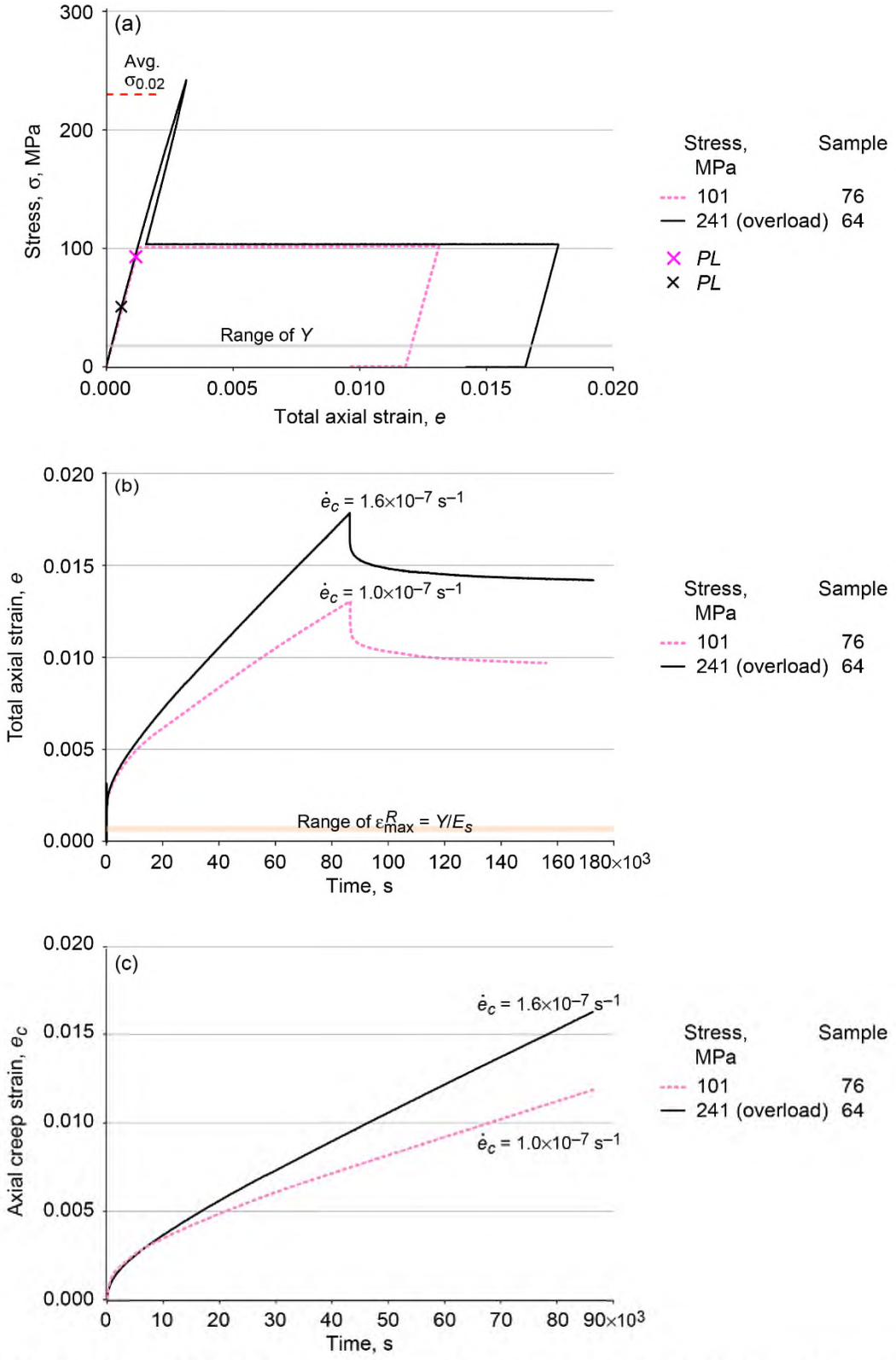

Figure 62.—Comparison of Ti-6-4 overload-creep sample 64 and virgin sample 76 at 538 °C and strain rate of 10^{-3} s^{-1}. (a) Stress as function of total axial strain, showing proportional limit *PL*, 0.02% yield point $\sigma_{0.02}$, and threshold stress *Y*. (b) Creep behavior, showing maximum reversible stress ε^{R}_{max} (=Y/E_S, where E_S is infinitely slow modulus). (c) Creep strain, showing creep rate $\dot{e}_C$.

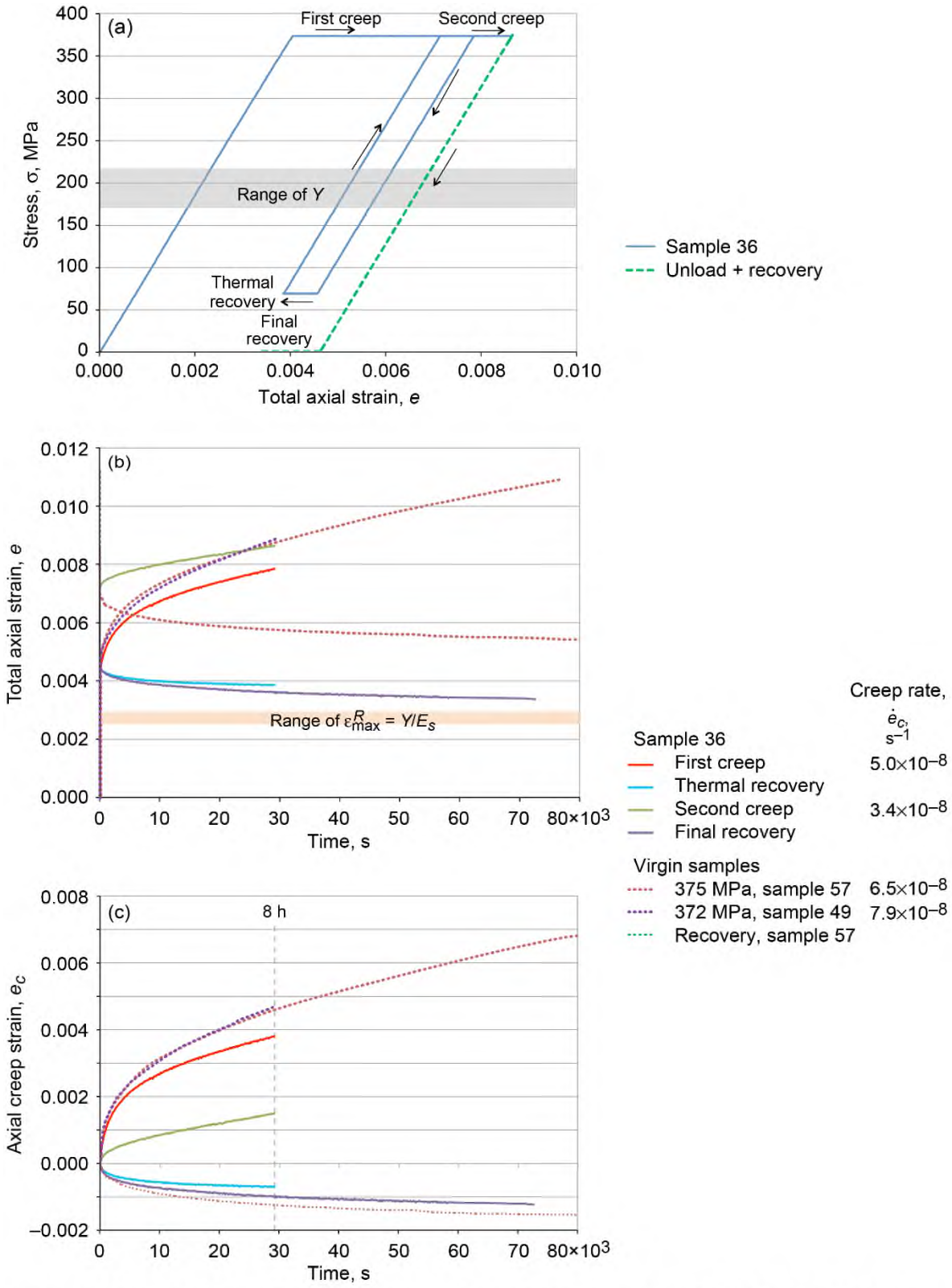

Figure 63.—Thermal recovery of Ti-6-4 at 427 °C, 375 MPa, and strain rate of 10^{-3} s^{-1}. (a) Stress as function of total axial strain, showing threshold stress Y and thermal recovery at 69 MPa. (b) Total axial strain, showing range of maximum reversible stress ε^R_{max} (=Y/E_S, where E_S is infinitely slow modulus). (c) Creep strain, showing creep rate $\dot{e}_c$ after 8 h.

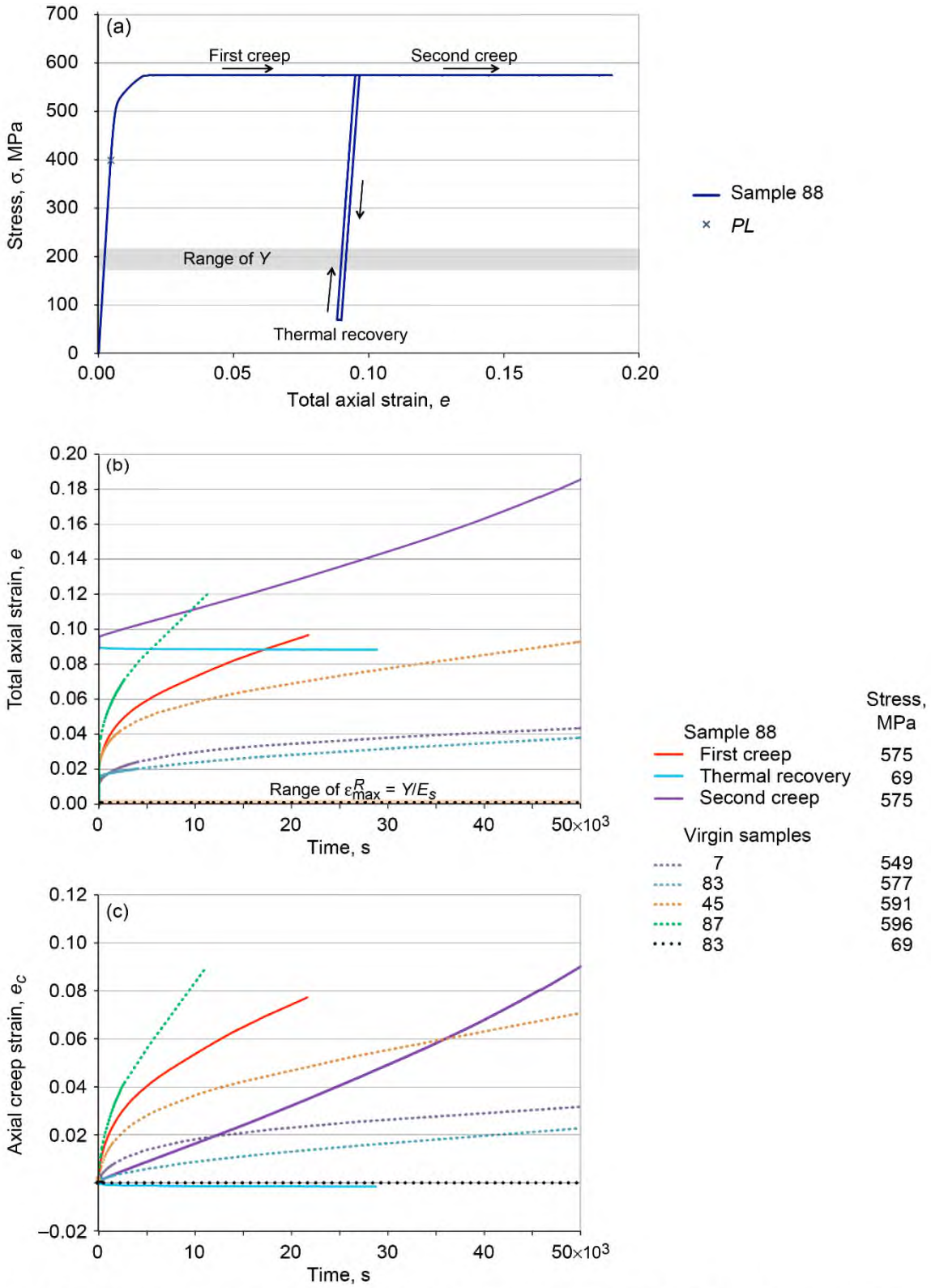

Figure 64.—Thermal recovery of Ti-6-4 at 427 °C, 575 MPa, and strain rate of 10^{-3} s^{-1}. (a) Stress as function of total axial strain, showing threshold stress Y and thermal recovery at 69 MPa. (b) Total axial strain, showing range of maximum reversible stress ε^R_{max} (=Y/E_S, where E_S is infinitely slow modulus). (c) Creep strain, showing creep rate $\dot{e}_c$ after 8 h.

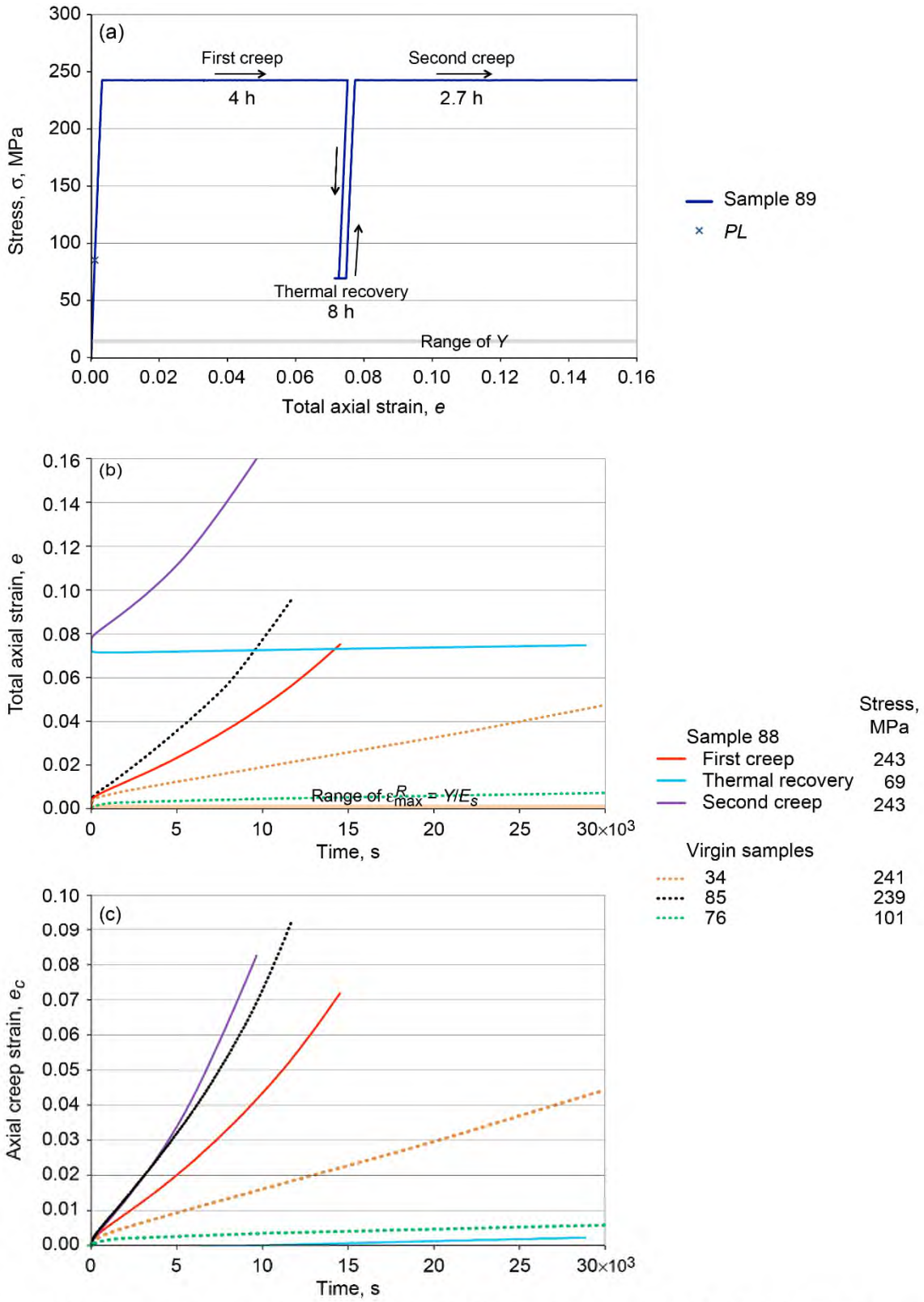

Figure 65.—Thermal recovery of Ti-6-4 at 538 °C, 243 MPa, and strain rate of 10^{-3} s^{-1}. (a) Stress as function of total axial strain, showing proportional limit *PL* and threshold stress *Y*. (b) Creep behavior, showing range of maximum reversible stress ε^R_{max} (=Y/E_s, where E_s is infinitely slow modulus). (c) Creep strain.

Appendix A.—Symbols

a	major axis of ellipse
b	minor axis of ellipse
d	sample diameter
E	static modulus
E_D	dynamic modulus
E_S	infinitely slow modulus
e	axial strain
$\mathbf{e}$	eccentricity
e_c	axial creep strain
$e_{c,t}$	transverse creep strain
e_{sat}	saturation strain
e_t	transverse strain
$\overline{e}$	relaxation strain
$\dot{e}$	loading strain rate
$\dot{e}_c$	creep rate
H	activation energy
LCF	low-cycle fatigue
N	number of load cycles
N_f	fatigue life, failure
n	power law creep exponent
PL	proportional limit
R_ε	strain ratio
R_σ	load ratio
RD	rolling (axial) direction
T	temperature
T_m	melting point
TD	transverse direction, perpendicular to RD
UTS	ultimate tensile stress
Y	uniaxial threshold stress
α	hexagonal close packed (hcp) phase in titanium
$\boldsymbol{\alpha}$	back stress
β	body-centered cubic (bcc) phase in titanium
γ	face-centered-cubic (fcc) phase in nickel-base superalloys
γ'	ordered fcc phase in nickel-base superalloys
ε^{IR}	irreversible strain after achieving full recovery
ε^{R}	reversible strain
$\varepsilon^{R}_{\text{max}}$	maximum reversible strain
ε_{max}	maximum strain

ε_{min}	minimum strain
κ	threshold stress in shear
ν	Poisson's ratio
ν^I	inelastic Poisson's ratio
σ	stress
σ_{max}	maximum stress
σ_{min}	minimum stress
σ_o	creep friction stress
σ_{sat}	saturation stress
$\sigma_{0.02}$	0.02 percent yield point
$\sigma_{0.2}$	0.2 percent yield point
$\sigma_{1.8}$	maximum stress achieved at 1.8 percent strain
$\overline{\sigma}$	applied stress level
$\dot{\sigma}$	loading stress rate

Appendix B.—Definitions

Anisotropic—Material properties are dependent on material direction.

Associative model—Flow and/or evolution equations are normal to a potential function derived from the yield surface. Fully associative is when both the flow and evolution laws are normal to the same, rather than two separate, potential functions.

Back stress—Internal state variable that measures the resistance to slip acting in the reverse direction of the applied shear.

Dynamic (instantaneous) modulus (E_D)—Material stiffness associated with the fastest loading rate possible. This is the stiffness produced when all time dependency of the material is retained. An upper bound on the modulus at a given temperature.

Inelastic strain—Portion of the strain that is not reversible (i.e., elastic). Permanent deformation.

Infinitely slow modulus (E_S)—Material stiffness when loaded at an extremely slow rate (all time dependency of the material has been dissipated). The lowest possible modulus at a given temperature. Any static hold test conducted within the viscoelastic regime should dissipate to a stress-strain point on this modulus line.

Irreversible deformation—Deformation that remains in the material after load removal, usually associated with the creation of dislocations and their tangles. Permanent deformation.

Isotropic—Material has the same properties in all directions.

Nonunified model—Model that separates (partitions) time-dependent (i.e., creep) and time-independent (i.e., plastic) strains.

Orthotropic—Material exhibits different properties in three mutually perpendicular directions.

Permanent deformation—Remaining (i.e., irreversible) deformation after the load has been removed. Non-zero stress (strain) after returning to zero strain (stress).

Plastic strain—Time-independent, permanent deformation.

Prior history—Complete path of deformation that created the current material state.

Proportional limit (PL)—Deviation from linear elastic behavior (elastic limit). It is the first point at which a sufficient quantity of material starts to flow and incurs measureable permanent deformation. At elevated temperature this value is rate dependent.

Rate dependence—Properties are a function of loading velocity (strain rate), generally being larger with higher rates.

Recovery—Process in which dislocations rearrange to lower the strain energy in the crystal. Mechanism can be deformation- or thermal-driven processes.

Reversible deformation—Deformation that can be eliminated (recovered) through either time-independent (elastic) or time-dependent (viscoelastic) mechanisms.

Saturation stress—Equilibrium stress that remains after dissipation of all rheological mechanisms. Often refers to the asymptotic stress after relaxation.

Threshold stress—Series of points in multiaxial space that define the boundary between fully reversible (viscoelastic) and irreversible (viscoplastic) deformation. The analog of yield surface for time-independent processes. The threshold associated with shear, κ, or its uniaxial equivalent, Y, is a function of temperature and is rate independent.

Time dependence—Properties change with time. Normally refers to hold (dwell) times during creep and relaxation where either the stress or strain are held fixed and the other varies with time.

Unified model—Model that treats both time-independent and time-dependent irreversible strains as a single quantity.

Viscoelastic—Material behavior that contains both elastic and viscous components, where the viscous component is time dependent due to the dissipation of rheological mechanisms. Viscoelasticity is fully reversible. Often referred to in the literature as “anelastic” or “delayed elastic” response.

Viscoelastoplastic—Containing elements of both viscoelastic and viscoplastic deformation.

Viscoplastic—Material behavior consisting of inelastic flow. The deformation is rate and time dependent (involving higher magnitudes as temperatures increase) and results in permanent, irreversible deformation.

Yield points—Engineering definitions usually defined as the stress at a percent offset from the elastic line. The most common offsets are 0.02 and 0.2 percent strain.

Appendix C.—Transverse Strain Behavior

Throughout this experimental program transverse strains were measured in the hopes of providing additional data to verify the multiaxial capability of the viscoelastoplastic model put forth by Arnold and Saleeb (see Arnold et al., 2009). Unfortunately, Ti-6-4 ended up exhibiting more anisotropic behavior than initially anticipated, thus making the verification of the isotropic formulation of the present GVIPS model problematic. However, the transverse strain measurements are still informative and are worthwhile discussing. Herein, only a selected sample of the full test matrix strain behavior in the transverse direction is provided, which best illustrates the wide range of transverse behavior encountered. A summary of the specific tests selected from the full test matrix is given in Table IV.

Because the degree of anisotropy observed was not initially anticipated, the specimen orientation with respect to the plate from which these were machined was not maintained. Although the longitudinal axis of the samples was aligned with the final rolling direction, the orientation of the other two plate directions was not controlled. Hence, transverse measurements were not conducted in a way that was optimal for complete interpretation of the results. Yet important and interesting information regarding the transverse behavior of Ti-6-4 was observed and is provided to assist anyone wanting to design and conduct a series of specific experiments to better understand the anisotropic irreversible behavior of alloys in future experimental studies.

Most of the tests were conducted with an optical micrometer to measure transverse strain. This device measured a single diameter at one plane along the gage length. Details of the micrometer (Fig. 66) can be found in the report on the viscoelastic results (Lerch and Arnold, 2014). The rig setup had the micrometer head on the left and right side of the test frame. This would then measure the sample diameter, which ran front to back in relationship to the load frame. The axial extensometer was placed on the front of the sample such that the extensometer probes would be pointing in the direction of the measured diameter, or 90° to the micrometer. Most of the diameter measurements were taken just above the top extensometer probe since the micrometer required line-of-sight to the sample and both the extensometer probes and the induction heating coil interfered with measurements. Near the end of the test program the micrometer heads were lowered such that the sample diameter was measured closer to the midgage between the extensometer probes. For corroboration of both transverse strain and Poisson's ratio, posttest diameter measurements were taken at several locations on the sample using an optical comparator.

Given measurement of both the axial and transverse strain, Poisson's ratio can be theoretically calculated, assuming isotropy, as

$$\nu = -\frac{e_t}{e} \tag{1}$$

where e_t is transverse strain and e is axial strain. As pointed out in the previous publication (Lerch and Arnold, 2014) the Ti-6Al-4V material used in this study had a moderate rolling texture resulting in directional properties as evidenced by the dynamic modulus shown in Figure 67. The modulus in the transverse direction is 12 percent larger than in the rolling direction and this difference is maintained over the 700 °C temperature range of measurement. As the amount of deformation increases the anisotropy becomes more prominent as indicated by the change in cross section from circular to elliptical shown in Figure 68(a). A change in cross-section geometry in anisotropic Ti-6-4 has been documented in the literature (Yang, Su, and Bai, 2000). Neither can we handle anisotropy in the current model nor did we keep track of the transverse material directions of each sample with respect to the parent plate of Ti-6-4. All we know is the rolling direction corresponds to the axial (longitudinal) direction of the sample. Thus, the assumption of isotropy and Equation (1) does not strictly hold in this case. However, given no other

choice and since the amount of eccentricity in the cross section is minimal at small levels of deformation, we will continue to treat the material as isotropic throughout this paper as was done in the prior publication (Lerch and Arnold, 2014). The anisotropy is important in describing the behavior, and so the final cross section of the sample has been plotted for each test in this appendix and oriented with respect to the test rig and both extensometers. An example of this can be observed in Figure 68(b) where a highly eccentric ellipse is shown representing the posttest sample cross section and its orientation with respect to the test rig. In this plot the major axis[2] of the ellipse coincidently coincides with the diameter being measured by the transverse micrometer and is indicated by the two-headed arrow. The length of this diameter is

$$d = 2a = 5.54\,\text{mm} \tag{2}$$

where d is the measured final diameter after the test and a is the length of the major axis of the fitted ellipse. The diameter at 90° to this is only 3.92 mm, yielding an eccentricity, e, of 0.71. Note in this experimental setup the axial extensometer fits on the front of the sample (270° from the x-axis) with its probes pointing toward the back of the test rig parallel to the major axis. Figure 68(a) also shows a photo of the broken sample depicting the localized neck. Since the neck is close to the upper radius of the sample (top-right corner of the photo), it is likely that most of the deformation in this neck was captured by the transverse micrometer for this sample. Flow lines can also be observed on the surface of the specimen running parallel to the sample's axis.

The stress-strain curves for a simple tensile test conducted at 427 °C and at a strain rate of 0.001 s^{-1} is shown in Figure 69(b). The engineering stress is plotted as a function of both the axial and transverse strain. Note that the transverse strain will normally be represented as an absolute value for ease of display. This specimen failed at an axial strain of approximately 20 percent and a transverse strain of 0.06. The cross section is shown in Figure 69(a) and depicts a strongly eccentric ($e = 0.86$) cross section with its major axis rotated 125° from the x-axis. Thus, the diameter being measured for transverse strain calculations by the micrometer is fairly representative of the major axis. Based on this specimen orientation, the transverse strain will show less change (less of a reduction in diameter) over the test compared to what the minor axis would exhibit if the sample were rotated 55° more and the minor axis diameter had been measured.

Figure 69(b) also shows the change in Poisson's ratio with axial strain (Poisson's ratio will always be plotted as a function of total axial rather than transverse strain in this appendix). Poisson's ratio begins in the elastic regime at a constant value of 0.34 and increases to a value of 0.44 at an axial strain of 0.048. Poisson's ratio then decreases to a value of 0.32 at failure. A similar change in Poisson's ratio during tensile testing has been shown by Stang, Greenspan, and Newman (1946) for both aluminum and steel alloys. Note again that this is the Poisson's value associated predominately with the major axis. If the diameter for the minor axis had instead been measured, the value of Poisson's ratio at failure would have been 1.13 as calculated from the posttest diameter measurements. This indicates the influence of anisotropy on the deformation and the care needed to interpret the transverse strain data. It is important to point out that the value for axial strain used to calculate Poisson's ratio was always taken as the value measured by the axial extensometer at midgage. Therefore, it represents the strain average over a 13-mm gage length and does not include potentially higher strains in any localized neck (although the midgage strains may be affected by the localized neck through shielding of the strains).

[2]It is assumed that the major and minor axis correspond to the transverse planes of the original plate. Regardless, this assumption does not influence the results discussed herein.

The value for the maximum stress (UTS) occurs at an axial strain value of 0.105 and a transverse strain of 0.044. However, the maximum Poisson's ratio occurs at a value of 0.048 axial strain as depicted in the figure. This suggests that Poisson's ratio may be a more sensitive indicator of damage during the test than the maximum stress (the point at which localized necking occurs). Another representation of this is shown in Figure 70, where strain and Poisson's ratio are plotted as a function of test time. Note that the maximum stress occurs at a time of 106 s into the test, whereas the Poisson's ratio peaks at a test time of 48 s.

Deformation behavior for a creep test performed at 427 °C, a loading rate of 0.001 s^{-1}, and a stress level of 591 MPa (the creep tests are always conducted under constant load), is shown in Figure 71. This sample was loaded to the desired creep stress, held for 24 h, unloaded to zero load, and maintained at zero load in load control for 4.5 h to recover. Since this sample was loaded past the $\sigma_{0.2}$, it exhibited a large amount of time-dependent creep strain during the creep period with the initiation of tertiary creep at a total axial strain of 0.10. This axial strain is identical to the strain coinciding with the UTS in Figure 69 for the sample tensile tested at the same temperature and strain rate. This would suggest that the tertiary creep coincides in this sample with the beginning of a localized neck. Any indication of tertiary creep in the transverse strain response is difficult to observe. There is still a good amount of transverse strain (0.08) accumulated during the total creep period, which corresponds to a Poisson's ratio at the end of the 24-h creep period of 0.62. The cross-sectional area (Fig. 71(a)) shows a lower eccentricity (0.32) than for the previous tensile test, which may be expected since the final creep strain attained was only half the value of the final tensile strain. The orientation of this sample had its major axis parallel to the x-axis. Hence the diameter being measured for transverse strain was that of the smaller or minor axis. This was also one of the samples where the diameter was measured near midgage and remote from a barely visible localized neck near the top radius. The difference in diameter posttest at these two locations was 5.86 mm at midgage compared to 5.72 mm at the localized neck. This equates to transverse strains at the midgage and neck of 0.075 and 0.097, respectively, and Poisson's ratios of 0.66 and 0.86, respectively. Note that the value of Poisson's ratio at the end of recovery is 0.64 as shown by the midgage optical micrometer value depicted in Figure 71(b) and confirms the posttest reading.

Figure 71(c) shows the strain behavior for the first 20 s of this test. Both strains increase linearly during the elastic region. At the yield point (~6 s) the strains increase at a more rapid rate. The Poisson's ratio follows a similar pattern. In this figure the Poisson's ratio was represented in the elastic region by a constant value of 0.41 (calculated by fitting the linear stress-strain curves and dividing the moduli) to eliminate the large variability of Poisson's ratio in this regime. Starting at yield Poisson's ratio increases to 0.56 by the end of loading. It then jumps to 0.60 during the first second of creep. This jump can also be observed in both of the strain values. Poisson's ratio continues to increase to a maximum of 0.64 (Fig. 71(b)) after approximately 18×10^3 s, which corresponds with the change from primary to secondary creep depicted by the axial strain behavior. Thereafter, Poisson's ratio decreases slightly during continued creep to a final value of 0.62. The creep portion of the strains during the creep period is shown in Figure 71(d), where the strains due to loading have been removed. The curves have a similar shape to the total strains shown in Figure 71(b). Work on concrete by Mazzotti and Savoia (2002) has shown an increase in Poisson's ratio during compressive creep to values over 0.5. However they did not show any decrease in Poisson's ratio with continued creep.

During the sample unload, both strains decrease (Fig. 71(b)), where the decrease in transverse strain corresponds with an increase in the sample diameter. The transverse strain decreases less than the axial strain, resulting in a concomitant increase in the Poisson's ratio. During recovery at zero load, both strains exhibit a small, gradual decrease in value with a corresponding slight increase in Poisson's ratio.

To explore the effects of plasticity on creep, the sample shown in Figure 72 was loaded to a value of 514 MPa and unloaded to a stress value of 446 MPa (overload creep), followed by a 24-h creep period.

Thereafter the sample was unloaded to zero load and held for 24 h to recover. This sample was oriented such that the major axis of the cross section was 143° from the x-axis (Fig. 72(a)), which implies that the diameter measured for transverse strain is an average between the major and minor diameters. The eccentricity for this sample was only 0.18, consistent with the fact that the axial strain incurred in this sample was low, only on the order of 0.02, and much less than the deformation exhibited by the previous two samples. This deformation was sufficient to project the sample into the secondary creep regime, but not large enough to result in tertiary creep during the 24-h period. The behavior of the strains and Poisson's ratio shown in Figure 72(b) is similar to that shown in Figure 71(b) for the higher stress creep test. An enlargement of the first 20 s of the test shown in Figure 72(c) also depicts a similar behavior to that shown in Figure 71(c). There are, however, two features that are different from that of the previous creep sample. The first is obviously the stress overload portion of the test. This resulted in a decrease in the axial and transverse strain upon unloading as well as a slight increase in Poisson's ratio. It is interesting to note that the value for Poisson's ratio in the beginning of this test did not deviate much from the elastic value of 0.36. This is inconsistent with the results from the prior creep test (Fig. 71(c)) which yielded Poisson's values up to 0.55 during loading. One contributing factor for this is that the current sample was loaded to much lower strains. Equivalent strains in the previous test also failed to alter the Poisson's ratio (see Fig. 71(c)). Another contribution could be specimen orientation. The previous sample was coincidentally oriented to measure the minor axis (i.e., the one that would show the most decrease in diameter) for the transverse strain. The current sample is oriented such that an average of the major and minor diameters is measured, resulting in less diametric change for the same axial strain.

The second feature that is absent in this test is the sudden jump in strains and Poisson's ratio during the first second of creep. This is probably due to the reduction in deformation (lower strains) during loadup in this sample and maybe a corresponding reduction in forward-going momentum of both the test rig and the sample deformation. However, it could also be a consequence of the overload portion of this test, which would tend to harden the sample and reverse the direction of deformation going into the creep period.

The behavior of the creep strains for this test is shown in Figure 72(d) and is consistent with the total strains shown in Figure 72(b). The amount of creep strain observed in this sample is an order of magnitude less than what was observed for the higher stress creep test shown in Figure 71(d). However, the creep strains from both tests were a significant portion of the total strain for the axial, and particularly for the transverse, strains.

It is significant to note that the value of Poisson's ratio during creep in this sample continually increases with time, albeit at a continually decreasing rate. This is in stark contrast to the values for the previous sample in which Poisson's ratio reached a maximum after 14 000 s and then slowly decreased until the end of the creep dwell. Moreover, the attainment of the Poisson's maximum in the previous test (Fig. 71(b)) did not coincide with the beginning of the tertiary creep regime, but significantly earlier at the transition from primary to secondary creep. That would suggest that creep in the overload sample (Fig. 72(b)) did not quite reach the secondary regime during the 24-h creep period since its Poisson's value is still increasing although approaching a maximum. Note that the final Poisson's ratio after creep is 0.61, almost as high as for the maximum occurrence during creep of the previous sample. This may imply that the transition from primary to secondary creep may be defined by a specific value of Poisson's ratio.

The next test investigates the creep behavior at multiple stress levels. The creep stresses are applied in a stepwise fashion, and each are maintained for an 8-h (28 800-s) period. Three successively increasing stresses (372, 441, 476 MPa) were applied followed by a fourth step that decreased the value to 372 MPa, the same as the first stress level. After the last creep period, the sample was unloaded to zero load and held for 24 h to recover. The strains and Poisson's ratio results are shown in Figure 73. For this test the

orientation of the sample consisted of the major axis being rotated 11° from the x-axis. The eccentricity for this sample was 0.14 (Fig. 73(a)), which is even smaller than the previous sample and is a bit surprising since the total axial strain observed in Figure 73(b) is larger (albeit minimally) than the previous sample. The diameter measured for the transverse strain represents predominantly the minor axis, or the dimension that would deform the most in the cross-sectional plane.

Both axial and transverse strains exhibit a linear increase during the first loadup (Fig. 73(c)), indicating that the first creep level is below the proportional limit. Both strains increase gradually during the loadups and the subsequent creep periods. The creep during the first period is primary creep. For the second and third periods, there is a primary region transitioning to secondary creep. For the fourth (unload) period, the creep behavior is secondary with no primary region observed. With each change in the creep load the sample displays less primary creep and a more defined secondary section. During load increases, both strains increase as expected and decrease during the unloading section.

Poisson's ratio exhibits a slight increase with time once creep at the first stress level commences. The value starts from an elastic value of 0.33 and reaches 0.61 at the end of this first creep period. During the load increase to the next stress level, Poisson's ratio decreases in contrast to the increasing strain behavior. The opposite behavior occurs during unloading, as has been shown, immediately before the recovery period at the end of the tests. This behavior is consistent with the previous tests. During the creep portion of this test Poisson's ratio increased overall from 0.33 to 0.89 and further increased during unloading and recovery to a final value of 1.04. This is the highest value of Poisson's ratio observed thus far in this study, which is unexpected since the total axial strains observed in this test are substantially lower than both the tensile tests in Figure 69 and the creep test in Figure 71, neither of which had a Poisson's value higher than 0.64. However, the posttest diameter measurements on this sample indicate that the value for Poisson's ratio for the major axis diameter was 0.33 and more in agreement with those from the other tests. This again indicates the influence of the material anisotropy, necessitating careful monitoring of the transverse planes.

The creep strains at each creep stress level for each step are plotted in Figure 73(d). It is significant to note that the axial and transverse creep strains are nearly identical. This result goes against the classic assumption of deviatoric creep strain for metals, assuming isotropic material, which implies Poisson's ratio is 0.5. The value for the inelastic Poisson's ratio, ν^I is shown in the figure, where

$$\nu^I = \frac{e_{c,t}}{e_c} \tag{3}$$

Here, $e_{c,t}$ is the creep transverse strain, and e_c is the creep axial strain. The inelastic Poisson's ratio begins at 0.86 for the first creep stress level and increases at each stress level thereafter, with its highest value being 1.44 during the final stress of 372 MPa.

Figure 74 depicts the behavior of a step relaxation test in which the sample was loaded to 0.012 axial strain, relaxed for 24 h, reloaded to 0.018 strain, relaxed for another 24 h, and finally unloaded to zero load and recovered at zero load in load control for 24 h. This sample was eventually stepped further to failure. However only the first two steps will be shown here. The cross-sectional ellipse (Fig. 74(a)), however, represents the large deformation of the sample taken to failure. The cross-sectional orientation shows the major diameter being aligned at 90° to the x-axis. This orientation allows the transverse strain to be measured as the full major axis. Hence the measured diameter shows the least reduction during the test.

The stress-strain curves are shown in Figure 74(b) for both the axial and transverse total strains. Although the stress-axial strain response appears as a normal relaxation curve, the transverse strain curve displays an unexpected behavior. During the relaxation behavior, the transverse strain is shown to

increase slightly (diameter decreases) over the relaxation period. Since the axial strain is controlled and being held constant, it does not vary during relaxation. The transverse strain however, is not controlled and does not remain constant. Since this curve represents the strain along the major axis, we would expect the minor axis to show even more change during the relaxation periods. Unfortunately only the one axis was measured during any given test.

Poisson's ratio is also shown in Figure 74(b) versus the total axial strain. Its value begins at a constant of 0.26 in the elastic region and remains the same up to the first relaxation strain of 0.012 as expected based on prior results (Fig. 72). At this point Poisson's ratio slowly increases as the stress relaxes. It is during this time that the transverse strain is also slightly increasing. This can be better observed in Figures 74(c) and (d) in which the values are plotted versus time. Furthermore, in Figure 74(d) the axial strain has been removed and the y-axis expanded for easier depiction of the transverse strain. The transverse strain does increase during relaxation, although by a very slight amount. Nonetheless, it is large enough to increase the value of Poisson's ratio from 0.25 to 0.33 during the first relaxation period. During the subsequent loadup to a relaxation strain of 0.018, both the axial and transverse strains increase leading to a slight decrease in the value of Poisson's ratio, as has been pointed out for prior tests. During the second relaxation at 0.018 strain, Poisson's ratio again increases from a value of 0.29 to 0.34 at the end of the 24-h hold. Subsequent unloading to zero load results in the usual increase in Poisson's ratio until it reached 0.36, and it appears to remain constant throughout the recovery period. Note that the value of Poisson's ratio are small within this test sequence and only changes by $\Delta\nu = 0.1$ throughout the test. This is not unexpected since the total axial strain is no larger than 0.018, and given the sample orientation we would expect the transverse strain that was measured (i.e., major axis) to give the smallest change around the circumference of the specimen.

The next two test examples describe the development of transverse strain under cyclic loading. Figure 75 represents a fatigue test with a positive mean stress. This test was conducted under load control between stress values of 0 and 640 MPa. Because of its high maximum stress value (the maximum strain in the first cycle was 0.065), the life was very low and the sample fractured at 115 cycles. Figure 75(a) shows the sample's cross section at two different locations. One is at the top radius where the transverse strain was measured. It had a small eccentricity of 0.23. The other cross section was measured posttest at midgage, where the sample had a localized neck resulting in fracture. Here the eccentricity is larger at a value of 0.52. Surprisingly, the major axes in both locations are different. There is a 48° rotation between the two major axes. Figure 75(b) shows the strain responses for two cycles, $N = 1$ and $N = 100$. During the first cycle both the axial and transverse strains increase to larger values (0.02 for the transverse strain) and then decrease slightly upon unloading to zero load. Because of the tensile mean stress and the elevated test temperature of 427 °C the sample experienced strain ratcheting up to failure (see Fig. 57 in the main text). Hence the strains slowly increased over each cycle until failure. It can be observed in Figure 75(b) that the strain values for $N = 100$ are larger than for $N = 1$. The transverse strain at $N = 100$ (and all cycles after $N = 1$) shows very little change over the cycle varying from strains of 0.034 to 0.037.

Poisson's ratio is plotted for six noncontiguous cycles (Fig. 75(c) and (d)) throughout the test. Poisson's ratio is highest ($\nu = 0.30$) for cycle 1 and decreases very slightly and consistently for each cycle thereafter until it reaches 0.28 at cycle 100. It appears that Poisson's ratio remains constant during any given cycle. Note the significant noise in Poisson's ratio at the beginning of the first cycle. This is typical for all tests and is the reason why the individual data points for Poisson's ratio were replaced in the elastic regime with a constant value calculated from the stiffness of both the axial and transverse stress-strain curves.

Figure 75(d) displays Poisson's ratio as a function of cycles over the life of the test. In this figure Poisson's ratio $\left(-e_t/e\right)$ was calculated at the maximum strain value of each cycle. This plot shows that its

value remains approximately constant throughout the life of the sample. This is similar to what is shown in the previous figure considering that the values in Figure 75(d) seem to contain more variation. Nonetheless, both plots suggest that Poisson's ratio would not be a good indicator of impending damage during fatigue since there is minimal change over the samples' lifetimes. It is possible that during the last 15 cycles (101 to $N_f = 115$) that there is a sudden and dramatic change in Poisson's ratio. However, this test was not designed to pick up on such a response. The consistency of Poisson's ratio over the 100 test cycles was not expected since the specimen incurred a total axial strain of 0.13 during this time due to ratcheting. That is a large amount of deformation and large enough to expect a significant change in Poisson's ratio. For comparison, the tensile test in Figure 69 had a large change in Poisson's ratio up to 0.13 strain as did the creep test in Figure 71.

The second fatigue test was cycled for only 20 cycles between stresses of ±375 MPa (Fig. 76). At both extremes a 1-h dwell time was inserted, allowing the sample to creep in either tension or compression (see Fig. 59 in main text). The cross section is not plotted for this test because the amount of permanent deformation was too small to cause much of an elliptical shape. The values for both major and minor axes (3.16 mm) are nearly identical, resulting in an eccentricity of only 0.04. Total strains are plotted over a cycle for both $N = 1$ and $N = 20$ in Figure 76(a). What is actually visible in this figure are the strains developing during creep. The load reversals (load and unloads) occur quickly and appear as vertical lines in this figure. The transverse strains are a bit higher (absolute value) under tension loading compared to the compression portion of the cycle, resulting in values of .0026 and .0014 at the end of the $N = 1$ and $N = 20$ creep periods, respectively. There is no distinguishable change in the transverse strain behavior between the first and the last fatigue cycle for either portion of the cycle. At the end of the last cycle, the specimen was unloaded to zero load and held for 24 h to recover. Both the transverse and axial strain returned close to zero (104 and –140 microstrain, respectively).

Poisson's ratio is calculated over the cycle for $N = 1$ and $N = 20$ and shown in Figure 76(b). As in the last figure, vertical segments in this figure represent the change in direction of load, whereas the data in between the vertical lines depict the change in Poisson's ratio during the creep portion of the cycles. Two methods were used to calculate Poisson's ratio in the figure: (1) calculations using Equation (1) at each data point and (2) calculations by fitting the axial and transverse strain curves and then taking the ratios of these equations at each point. The fits result in less noise; however, they tend to exhibit more irregularity as a result of unsatisfactory curve fits. Nonetheless, both methods give similar trends. Poisson's ratio appears to remain constant during the tensile-creep portion of the cycle and is equal to the value in the elastic regime (0.39) during the first loadup. This is expected since the maximum stress is just barely out of the linear regime (see Fig. 59(a) in main text). Under compressive creep the value for Poisson's ratio is much lower (0.3). This could be due to the fact that these tests were conducted under constant load and not constant stress. Hence stresses in compression are slightly smaller because of the small increase in the cross-sectional area from Poisson's expansion. It can also be observed in this figure that the values for Poisson's ratio for cycles $N = 1$ and $N = 20$ are largely unchanged. Considering the low load levels and the few cycles in this test, much damage would not be expected to occur over a mere 20 cycles and hence any change in Poisson's ratio would not either, as was indeed experienced.

The remaining figures show test results from a tensile sample tested at a higher temperature of 538 °C. At this temperature rate effects and time dependency are much greater and could cause a different deformation and damage behavior to occur than at the 427 °C. The specimen was oriented (Fig. 77(a)) such that the major axis was at a 170° angle to the x-axis. Thus, the measured diameter was almost entirely due to contributions from the minor axis and would depict the largest change during the test. The eccentricity of this sample was rather large at 0.65. Figure 77(b) displays stress-strain curves for both the axial and transverse directions as well as the Poisson's ratio response. This sample failed in tension at an

axial strain of 0.075. Note, however, that the transverse strain reached a value of 0.21, nearly three times higher than the axial strain. An enlargement of the strain axis is given in Figure 77(c) and indicates that Poisson's ratio increases from the elastic value of 0.3 fairly rapidly until most of the work hardening had exhausted itself at an axial strain of approximately 0.015. From that point until an axial strain of 0.05, Poisson's ratio increased at a much slower rate. At an axial strain of 0.05, which is the point at which the UTS occurs, the value for Poisson's ratio increases dramatically, reaching values of over 3.0 at the end of the test. The reason for these high Poisson's values are as follows.

Figure 77(d) shows a photograph of the sample during the test and immediately before failure. The photo has been rotated 90° for ease of viewing and thus the load is applied in the photo in the horizontal direction. In this photo the induction heating coils can be observed at the far right and far left of the picture. In between the two groups of coils are the alumina extensometer probes which measure the axial strain.[3] This sample has been painted to apply a speckle pattern, which was measured using an optical photogrammetry system capable of showing full field strains. The results from such a system will be discussed shortly and compared to the results from other measurements systems. It is observed that a localized neck has formed in the sample near the right induction coils. This neck is obviously outside of the gage length measured by the extensometer probes. Within the gage length, the diameter in the plane of the photo is constant, indicating that the deformation is uniform and no localized neck exists between the probes. However as one moves further to the right and outside of the gage, the localized neck begins to result in a smaller diameter. In this particular test, the diameter for the transverse strain was measured at the location of the neck and therefore measures nearly the largest reduction in diameter. This is why the transverse strain in Figure 77(b) is so much larger than the axial strain. After-test measurements of the diameter at this neck resulted in a calculated transverse strain of 0.284. While this is slightly larger it is not far from the transverse strain shown in Figure 77(b) as measured by the optical micrometer. This indicates that the micrometer was not quite measuring at the minimal diameter, but slightly to the left of this location where the diameter is a bit larger. Posttest readings using an optical comparator of two other locations on the specimen are indicated in Figure 77(e). The calculated transverse strains at these two locations, termed "near-neck" and "midgage," are 0.084 and 0.046, respectively, significantly less than what was measured with the optical micrometer.

In Figure 77(e) the transverse strains are plotted versus time over the life of the test. Note that the strains are plotted in this figure with their correct sign (negative). Measurements taken from the optical micrometer are from the localized neck and very close to the minimal cross section. As indicated previously, the final strain from this measurement is very close to the posttest reading taken at the minimum cross section (see "neck reading"). The posttest readings at the "near-neck" and "midgage" locations are also given. Also in this figure is a straight line representing the transverse strain measured with the photogrammetry system. This strain was calculated from a virtual 5-mm strain gage placed midgage. Note that the final value of transverse strain in the midgage area is only 0.03, significantly lower than at the localized neck. This generally agrees with the posttest measurement in this area of 0.046. The stress-transverse strain curve using the photogrammetry values are also plotted in Figures 77(b) and (c) and show a more expected relationship (smaller strains) with respect to the axial strain curve.

Since the transverse strain values are dependent on the location of measurement along the sample (as well as around the circumference), the value of Poisson's ratio will also be location dependent. The values of Poisson's ratio are plotted in Figure 77(f). The values calculated from the optical micrometer (which were shown earlier in Figures 77(b) and (c)) are represented. The final value at fracture for Poisson's ratio of 3.4 is given by this measurement method and basically agrees with the value of 4.15 calculated from

[3]Note that the apparent notches in the sample as if due to probe indentation are only shadows. No divots were observed as a result of the attached extensometer.

the posttest reading at the minimum cross section (neck reading). Furthermore, Poisson's ratio measured posttest at midgage yielded a value of 0.67, which is more realistic for a fully plasticized, isotropic material where we would expect a value of 0.5.

Poisson's data are also plotted in Figure 77(f) that were measured using photogrammetry during the test. These values were calculated using virtual strain gages located in the gage section. Both virtual axial and transverse gages were used. The value of Poisson's ratio by this method yielded values of 0.5 within the elastic region. These values are larger than what was measured (0.29) by a simple ratio of the stiffnesses from the stress-axial strain and stress-transverse strain curves (also shown) and measured using the extensometers. At a test time of 10 s the sample begins to yield and the transverse strain (Fig. 77(e)) and Poisson's ratio (Fig. 77(f)) for the two different measurement systems started to deviate from one another. This is due to the measurement location for each diameter. As shown in the ellipse plot (Fig. 77(a)), the optical micrometer measures the smaller diameter approximately equal to the minor axis, whereas the photogrammetry measures the diameter represented by the red arrow inside of the ellipse, which is closer to the major axis. Because of the anisotropy of the sample, the two systems measure different values: the optical micrometer measures a larger change than that of the photogrammetry.

As shown in Figure 77(e), the transverse strain measured by photogrammetry shows a linear decrease over the life of the test. A decrease in Poisson's ratio as calculated by this measurement system also shows a linear, continual decrease (Fig. 77(f)). Poisson's ratio at midgage (photogrammetry) decreases from 0.40 at the inception of yielding to 0.35 at failure. In contrast, both the transverse strain and corresponding Poisson's ratio as measured by the optical micrometer increase throughout the test with a significant increase occurring just prior to failure.

This behavior is further substantiated by the photogrammetry results shown in Figure 77(g) where the sample diameters are shown as a function of axial strain. The full-field images indicate that the initial diameter of the sample is 6.35 mm and is relatively constant around the circumference of the sample. These full-field images document the diameter values over a 90° section of the circumference, where the left side of the image represents the left side of the sample (minus x-axis) and the right side depicts the front of the sample. As the sample continues to deform, the left side of the sample maintains a larger diameter (major axis) than the right side (minor axis). Immediately before failure, the left side has a diameter of 6.27 mm, whereas the front of the sample (right side) has a diameter of 6.12 mm. These convert to transverse strains (absolute) of 0.013 and 0.036 and Poisson's ratios of 0.17 and 0.48, respectively. The plot in Figure 77(h) shows the radius as a function of axial strain at three locations along the measured circumference of the sample, where the locations of these measurements are shown with dots on the full-field images. The plot shows that the diameter on the right side (front of the sample) decreases at a faster rate than the diameter on the left side (left side of the test rig). The diameter in the center (at a 45° angle in quadrant III of the ellipse plot, Fig. 77(a)) is intermediate to the other two locations. These results are consistent with the ellipse shown in Figure 77(a). Furthermore, the plot suggests that the radii deform more uniformly up to axial strains of approximately 0.02, which is also shown in Figure 77(e) by the overlay of the transverse strain taken from both photogrammetry and the optical micrometer up to the time of 20 s.

The full-field photogrammetry images in Figure 77(f) also indicate that the location of the localized neck at the top of the sample contains the smallest diameters. As this neck becomes more pronounced (i.e., more deformation), the photogrammetry fails to register these readings as indicated by the shorter full-field view (Fig. 77(g)) at the higher axial strains. This is because the speckle pattern applied to the sample becomes too distorted and tends to peel off the sample, preventing proper tracking of these points. This can be observed to some extent in Figure 77(d) where the pattern is distorted in the region of the localized neck (between the right most extensometer probe and the right set of induction coils).

Although isotropic metals are assumed to have values of Poisson's ratio that reach 0.5 for constant-volume deformation (Koester and Franz, 1961), many of the values in the previous graphs exceeded this value. To verify that these large values were correct, two additional checks were employed. The first was to examine the residual transverse strain at room temperature after the test. These values were then used for comparison against the values measured at the end of the test. An optical comparator was used to map the cross-sectional area of the posttest samples at three points along the gage length and calculate a corresponding permanent transverse strain through the diameter change, $\Delta d/d_0$. The second method employed a photogrammetry system, in which a full-field strain image of the sample gage was captured at various strains throughout the test. Axial and transverse strains could be measured for numerous virtual strain gages, and Poisson's ratio calculated from these values. A summary of all of these measurements is given in Table V, where each of the values under the header, "Test values," represents the last data point taken during the test, and those under "Posttest Values" are from the measurements of the permanent sample dimensions taken at room temperature after the test. The final column in this table, "Gage information," gives observations regarding the status of the sample gage, which has been shown to influence the strain readings. Note that all of these samples deformed to elliptical cross sections similar to that shown in Figure 68.

All of the methods showed consistency of measured values. However, because of sample anisotropy and the location of the measurement of transverse strain on the sample, various values of both strain and Poisson's ratio could be obtained. First, due to the texture observed in this material, the sample cross section did not remain circular, but changed into an ellipse. Hence the transverse strain (calculated from the change in sample diameter) became a function of the location of measurement around the circumference of the sample. When the transverse strain was taken from the major axis of the elliptical cross section, the magnitudes of transverse strain were lower than if the minor axis had been measured. In cases where there was a high value of eccentricity to the cross section, which occurs at large levels of deformation, this difference was more extreme. Since Poisson's ratio is calculated from the transverse strain, Poisson's ratio also varied around the sample circumference. Technically an anisotropic calculation to Poisson's ratio should have been used, but this would have required tracking of the major and minor axes during the test, and this was far beyond the scope of this work. Only the isotropic calculation as given in Equation (1) was used. Note that in this calculation the axial strain is also required, and the value used for this was always measured using the axial extensometer. This gave an average value for axial strain measured over the 12.7-mm gage length centered along the specimen's length. Local values for axial strain as would be measured using photogrammetry could be much different and greatly affect Poisson's ratio.

Anisotropy has been shown in other investigations to both alter the cross-sectional shape during deformation (Yang et al., 2000) and to yield Poisson's values larger than 0.5 (Ozyhar, Hering, and Niemz, 2013; Taniguchi and Ando, 2010; Povolo and Bolmaro, 1985). In two studies of time-dependent effects in wood, highly orthotropic deformation was observed with Poisson's ratio ranging from –1.0 to 0.94 in creep of beech wood (Ozyhar, Hering, and Niemz, 2013). Creep in Japanese cypress (Taniguchi and Ando, 2009) yielded values of up to 0.8. Both works indicated that Poisson's ratio increased during creep, similar to what was observed in this study. Moreover, both of these investigations showed viscoelastic behavior of wood, which was reported to fully recover after unloading the sample to zero load.

Povolo and Bolmaro (1985) investigated the elastic Poisson's ratio for both cubic and hexagonal metal single crystals and showed that it was very dependent on the crystal orientation. Values as high as 0.95 were found in sodium whereas in another crystallographic direction the value was –0.73.

This leads to the second reason for apparent anisotropy in the sample, and this was reflected by the location of strain measurements along the length of the gage. At high values of deformation, a localized neck formed. This resulted in more eccentricity in the cross section as a consequence of nonhomogeneous

deformation. The amount of transverse strain was highly dependent on where it was measured with respect to the nadir of the localized neck. Technically speaking, Poisson's ratio should have been calculated based also on the local values of axial strain rather than an average measured by the extensometer, and this may have yielded more realistic numbers closer to the 0.5 value expected for uniform and fully plastic deformation. Furthermore, once a localized neck forms, deformation becomes nonuniform, the strain is no longer accurately controlled in the neck, and the condition is no longer a plane strain case. Therefore these discussions on strain and Poisson's ratio have been greatly simplified.

These results show that the transverse strain and Poisson's ratio are very sensitive to the local conditions. Unfortunately, the location of the neck and subsequent failure are unknown prior to testing, and therefore measuring the minimal diameter during the test is fortuitous. In theory photogrammetry could do this, but the large degrees of deformation cause the dot pattern to either distort or fall off of the sample, rendering these areas unmeasurable. This could possibly be fixed by developing a more coherent dot pattern. Clearly more work has to be done up front to develop tests to investigate these issues. Part of the problem is the small size of the sample. While typical for most material tests on metals, the 152-mm length greatly restricts the amount of gage available for measurement. Once a heating system is added, there is very little direct line of sight to the sample for use with photogrammetry. Furthermore, the larger the field of view, the poorer the resolution of the system.

It was observed that Poisson's ratio increased during unloading of the specimen and decreased during loading of the specimen as shown in the step creep test in Figure 73(b). This was independent of the location of strain measurement. This was not expected since both the axial and transverse strain are either increasing or decreasing simultaneously. An increase in Poisson's ratio was always observed during unloading to zero load prior to recovery, and it continued to increase very slightly during recovery.

It has been suggested that Poisson's ratio is more sensitive to damage in the sample than stress or strain (Wang, Laird, and Rahka, 1988; Mazzotti, and Savoia, 2002; Zhaoxia, 1994]. Although damage is the topic of a future paper, some comments can be gleaned from the current work. First, the tensile test shown in Figure 69 implies that Poisson's ratio peaks long before the maximum stress (UTS) can be observed in the stress-strain curves. Also, Poisson's ratio peaked during the transition from secondary to tertiary creep as shown in Figure 71(b); this transition is commonly associated with either the formation of a localized neck (Barboza, Moura Neto, and Silva, 2004) or the formation and coalescence of internal creep voids (Sasikala, Ray, and Mannan, 2004; and Levy, 1986). Works on concrete (Mazzotti and Savoia, 2002; and Zhaoxia, 1994) indicate that damage due to cracking results in Poisson's values above 0.5 and leads to an increasing larger value of Poisson's ratio with continued axial strain similar to that shown in Figure 77(b).

During the two fatigue tests shown here, no change was observed in Poisson's ratio during the test. It is believed that insufficient data collection for the test shown in Figure 75 prevented capturing of any change that may have occurred nearer to the point of failure. For the second cyclic test, the amount of deformation was too small (only a few cycles and at very low cyclic strains) to cause any damage in the sample and induce any change in Poisson's ratio. The relationship between Poisson's ratio and damage in Ti-6Al-4V will be further investigated and reported at a later time.

TABLE IV.—SELECTED TESTS TO BEST ILLUSTRATE TRANSVERSE STRAIN BEHAVIOR OF Ti-6-4

Test type	Associated transverse strain	Associated axial strain	Test conditions[a]
Tensile	Figures 69 and 70	Figure 7	$\dot{e} = 10^{-03}\ s^{-1}$; $T = 427$ °C
Creep	Figure 71	Figure 18	$\sigma = 591$ MPa; $T = 427$ °C
Overload creep test	Figure 72	Figure 61	$\sigma = 446$ MPa; $T = 427$ °C
Step creep test	Figure 73	Figure 61	$\sigma = 372, 441, 476, 372$ MPa; $T = 427$ °C
Step relaxation	Figure 74	Figure 48	$\bar{e} = 0.012$ and 0.018; $T = 427$ °C
Cyclic test	Figure 75	Figure 57	$\Delta\sigma = 0$ to 640 MPa; $T = 427$ °C
Dwell fatigue	Figure 76	Figure 59	$\Delta\sigma = \pm 375$ MPa; $T = 427$ °C
Tensile (necking)	Figure 77	Figure 9	$\dot{e} = 10^{-3}\ s^{-1}$; $T = 538$ °C

[a] $\dot{e}$ is strain rate, T is temperature, σ is stress, and $\bar{e}$ is relaxation strain.

TABLE V.—FINAL STRAIN AND POISSON'S RATIO VALUES

Sample	Test values				Posttest values				Gage information
	Axial	Transverse	Poisson's ratio	Location	Axial	Transverse	Poisson's ratio	Location	
427 °C									
23 (tensile)	0.196	–0.063	0.28	Top radius	---	–0.056	0.29	Bottom radius	Not broken Necked below top extensometer probe Sample out-of-round
						–0.119	0.61	At neck	
58 (LCF, $R_\sigma = 0$)[a]	0.123	–0.034	0.28	Top radius	---	–0.042	0.34	Bottom radius	Broke midgage, 15 cycles after last data reading
45 (creep, 591 MPa)	0.113	–0.073	0.64	Top radius	---	–0.034	0.30	At neck	Not broken Very slight neck at top radius Sample out-of-round
49 (step creep)	0.018	–0.019	1.03	Top radius	0.019	–0.009	0.49	Top radius	Not broken No visible neck Sample out-of-round
7 (overload creep)	0.015	–0.010	0.69	Top radius	0.013	–0.010	0.66	Bottom radius	Not broken No visible neck Sample out-of-round
538 °C									
37B (tensile)	0.103	–0.100	0.97	Near neck	---	–0.220	2.15	At neck	Broke at top radius
	0.108	–0.006	0.05	(a)	---	–0.024	0.23	Midgage	Strong neck
39 (tensile)	0.068	–0.236	3.40	At neck	---	–0.086	1.26	Near neck	Broke at top radius
	0.075	–0.026	0.34	(a)	---	–0.036	0.53	Midgage	Strong neck
70 (tensile)	0.177	–0.122	0.69	Near neck	---	–0.343	1.94	At neck	Broke at top radius
	0.177	–0.072	0.44	(a)	---	–0.082	0.47	Midgage	Strong neck

[a]Strain also measured by photogrammetry.

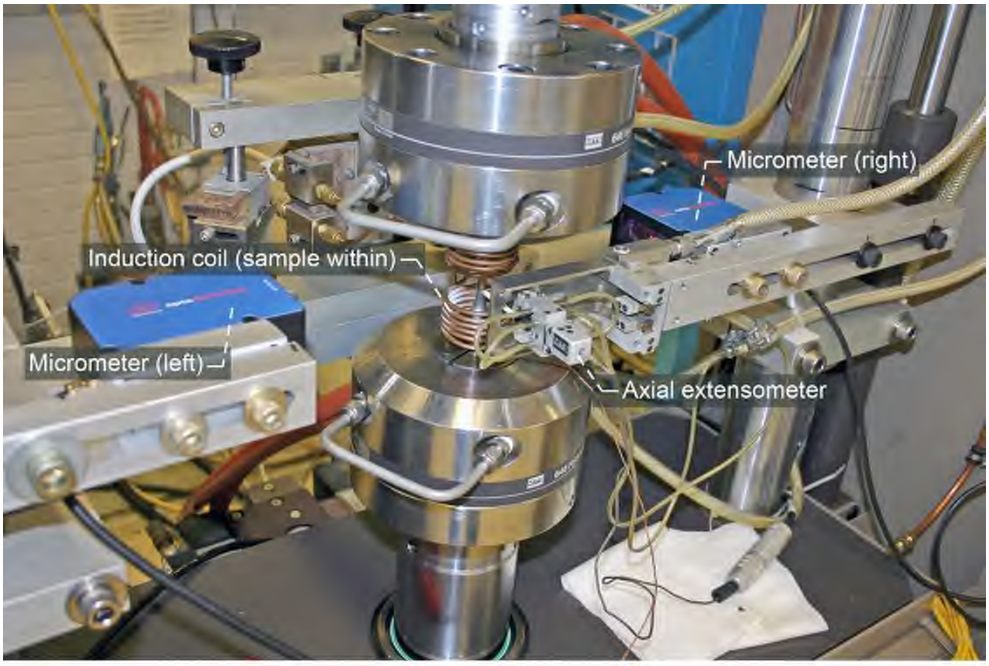

Figure 66.—Test rig setup.

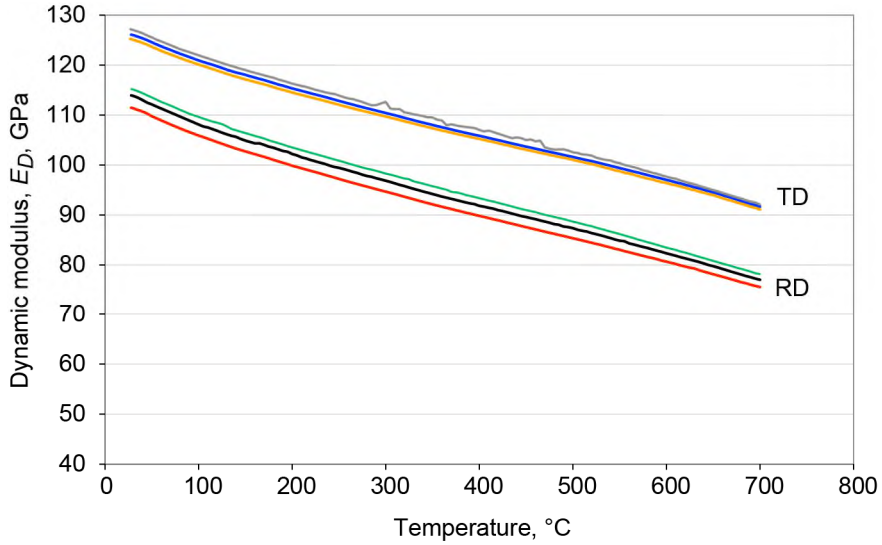

Figure 67.—Dynamic modulus E_D for Ti-6-4 samples in short transverse (TD) and rolling (RD) directions, indicating elastic anisotropy.

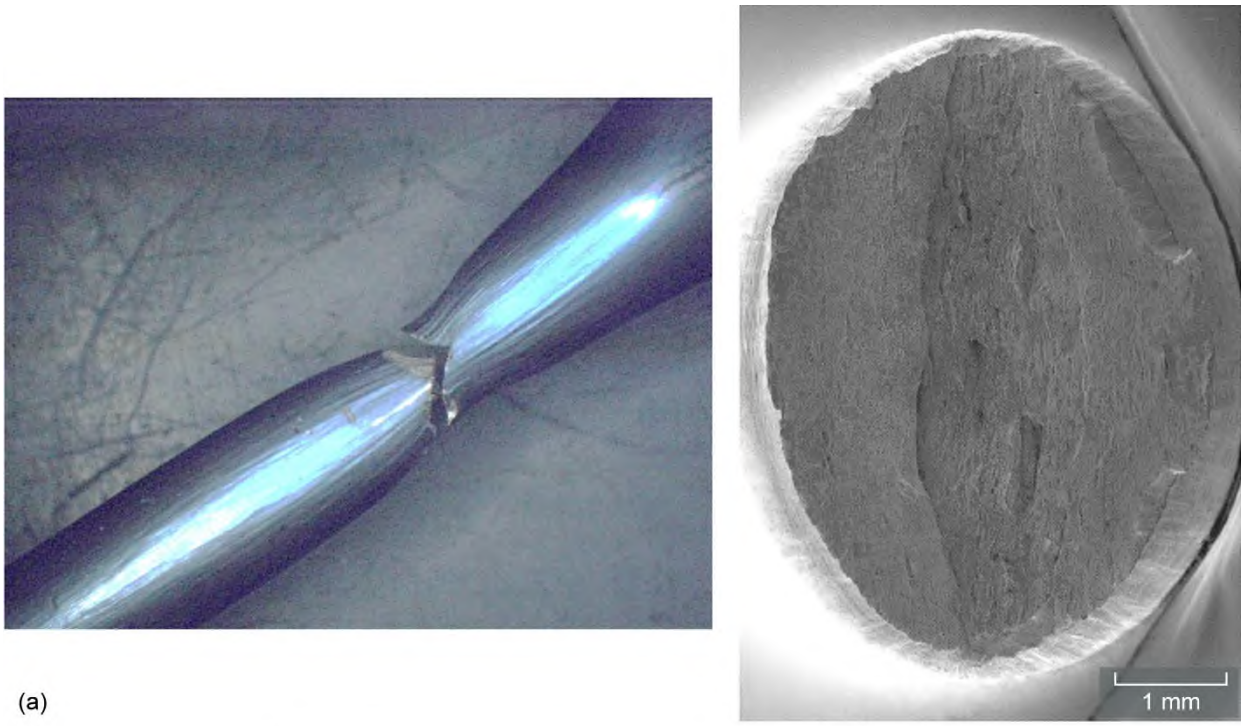

(a)

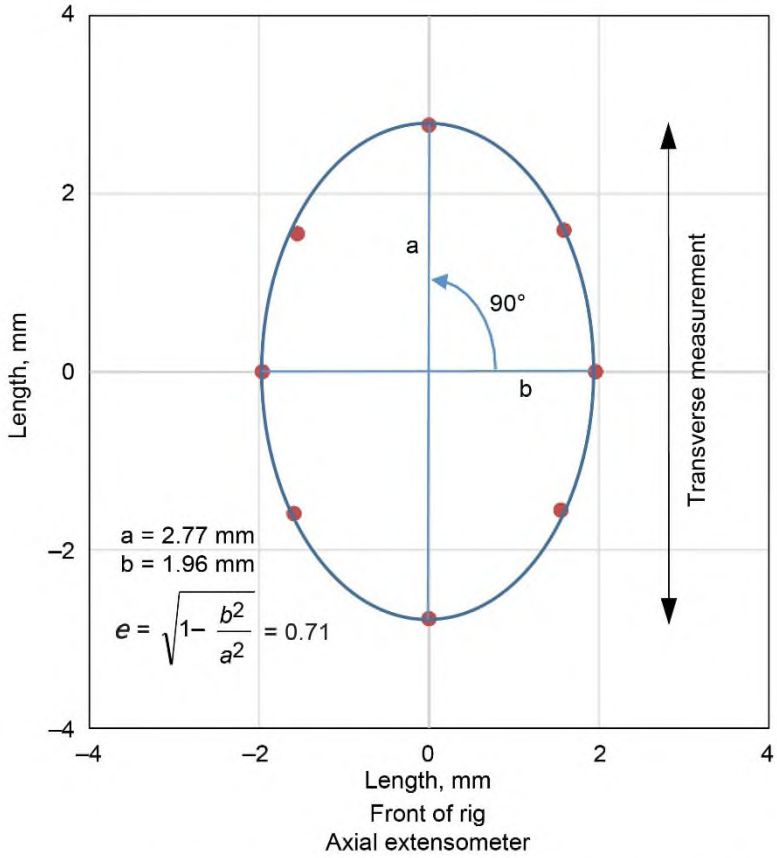

(b)

Figure 68.—Cross section of Ti-6-4 tensile sample at 427 °C, failed under loading. (a) Showing elliptical shape. (b) Elliptical shape of sample, indicating orientation of major (a) and minor (b) axes with respect to right side of test frame and giving eccentricity e.

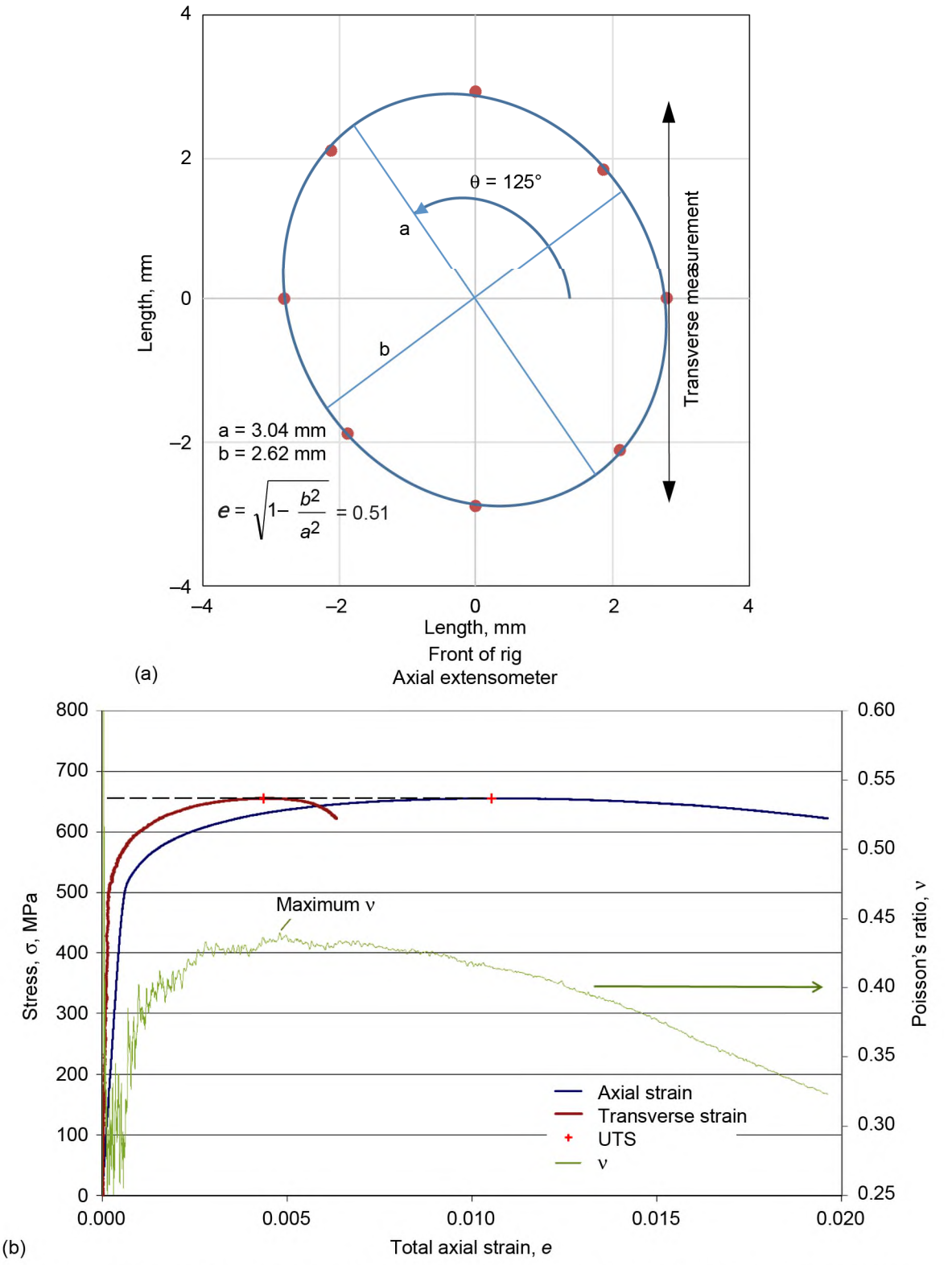

Figure 69.—Tensile test of Ti-6-4 sample 23 at 427 °C and strain rate of 10^{-3} s^{-1}. (a) Sample cross section and rotation, indicating orientation of major (a) and minor (b) axes with respect to right side of test frame and giving eccentricity *e*. (b) Loading curves showing ultimate tensile stress (UTS) and maximum Poisson's ratio ν.

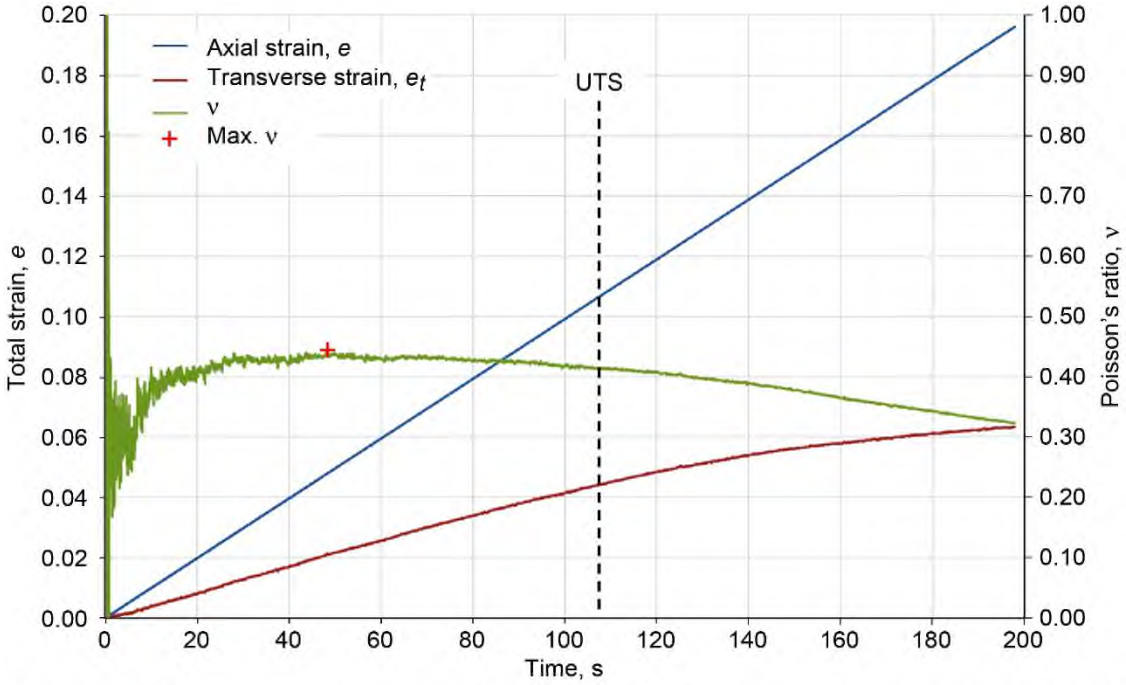

Figure 70.—Strain-time plot for tensile test of Ti-6-4 at 427 °C, showing ultimate tensile stress (UTS) and attainment of maximum Poisson's ratio ν.

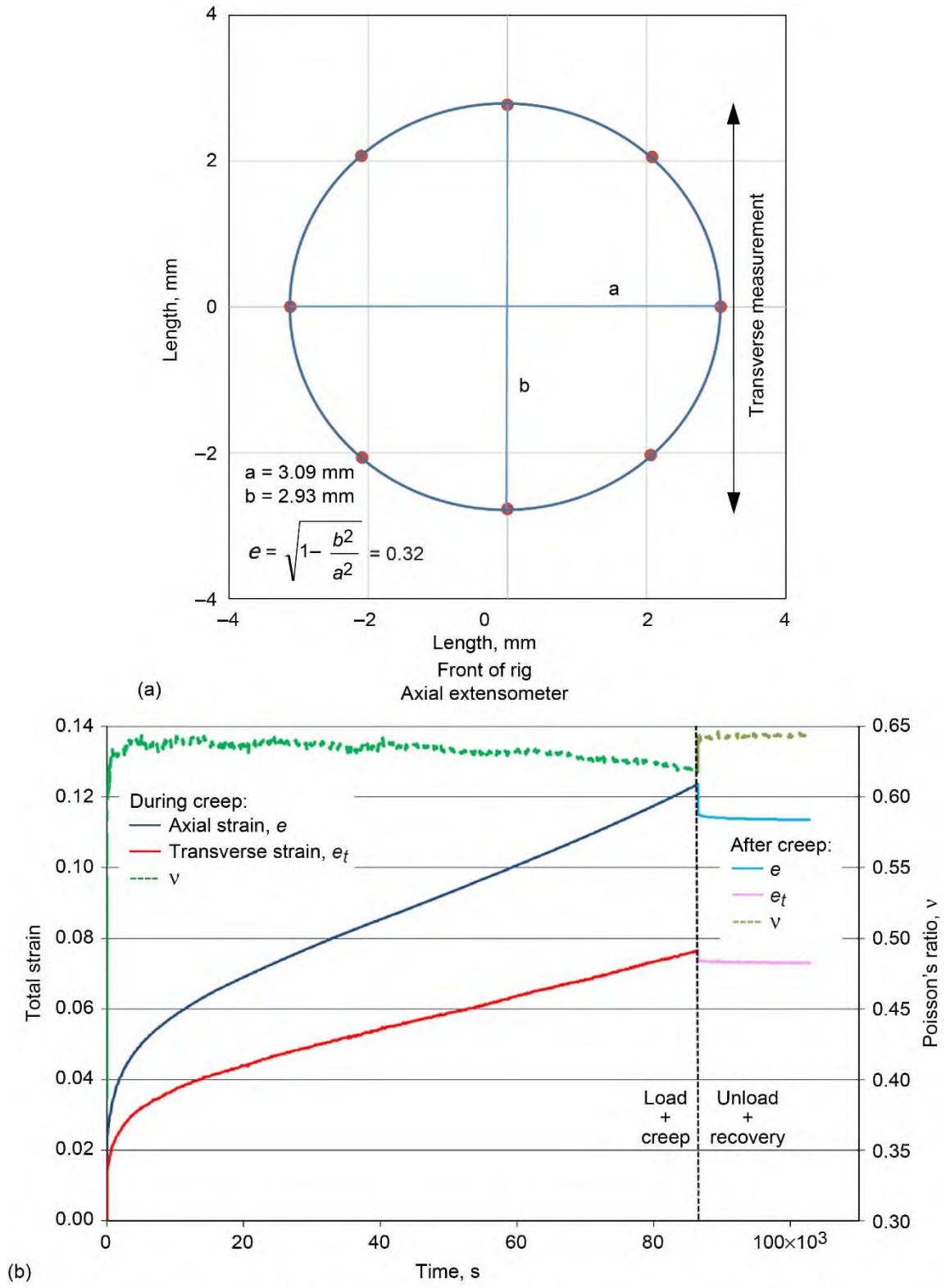

Figure 71.—Creep test of Ti-6-4 sample 45 at 427 °C, 591 MPa, and strain rate of 10^{-3} s^{-1}. (a) Sample cross section and rotation, indicating orientation of major (a) and minor (b) axes with respect to right side of test frame and giving eccentricity *e*. (b) Axial and transverse strain and Poisson's ratio ν. (c) Enlargement of loadup from part (b). (d) Creep strain for both axial and transverse directions.

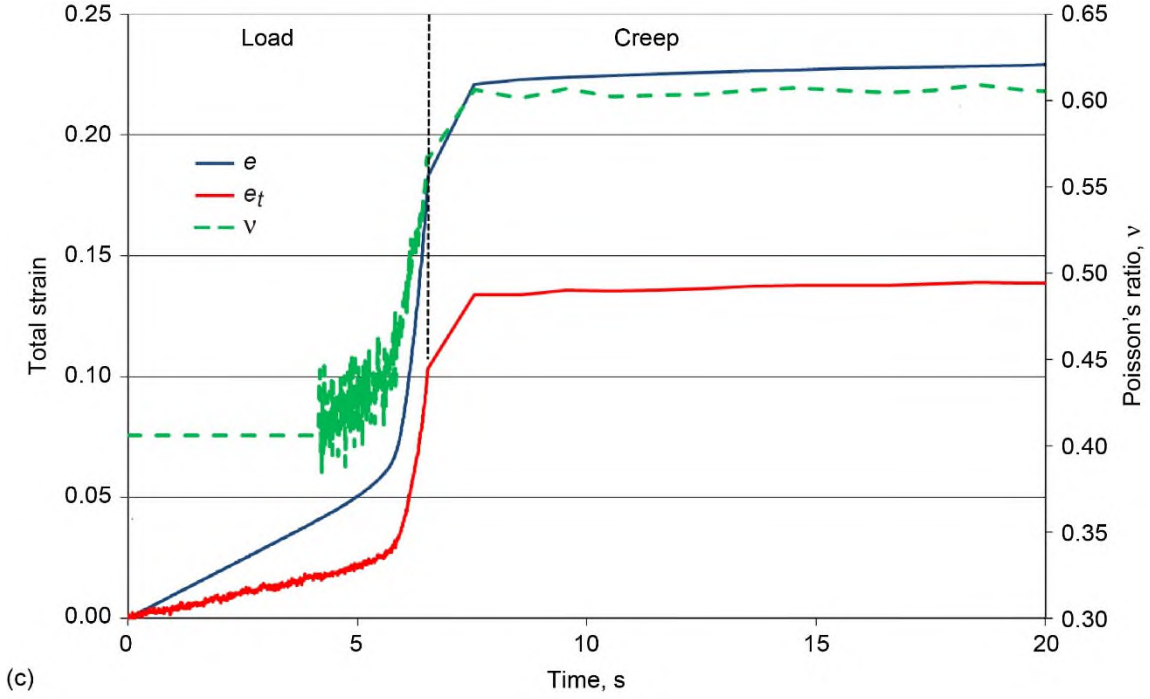

(c)

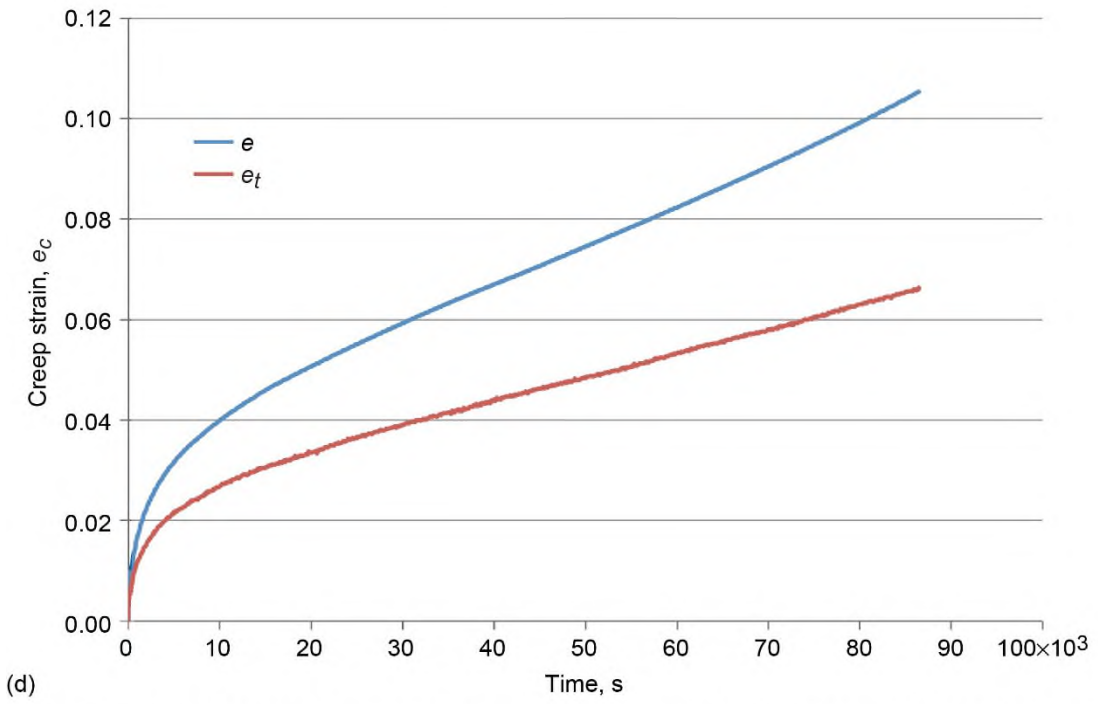

(d)

Figure 71.—Concluded. (c) Enlargement of loadup from part (b). (d) Creep strain for both axial and transverse directions.

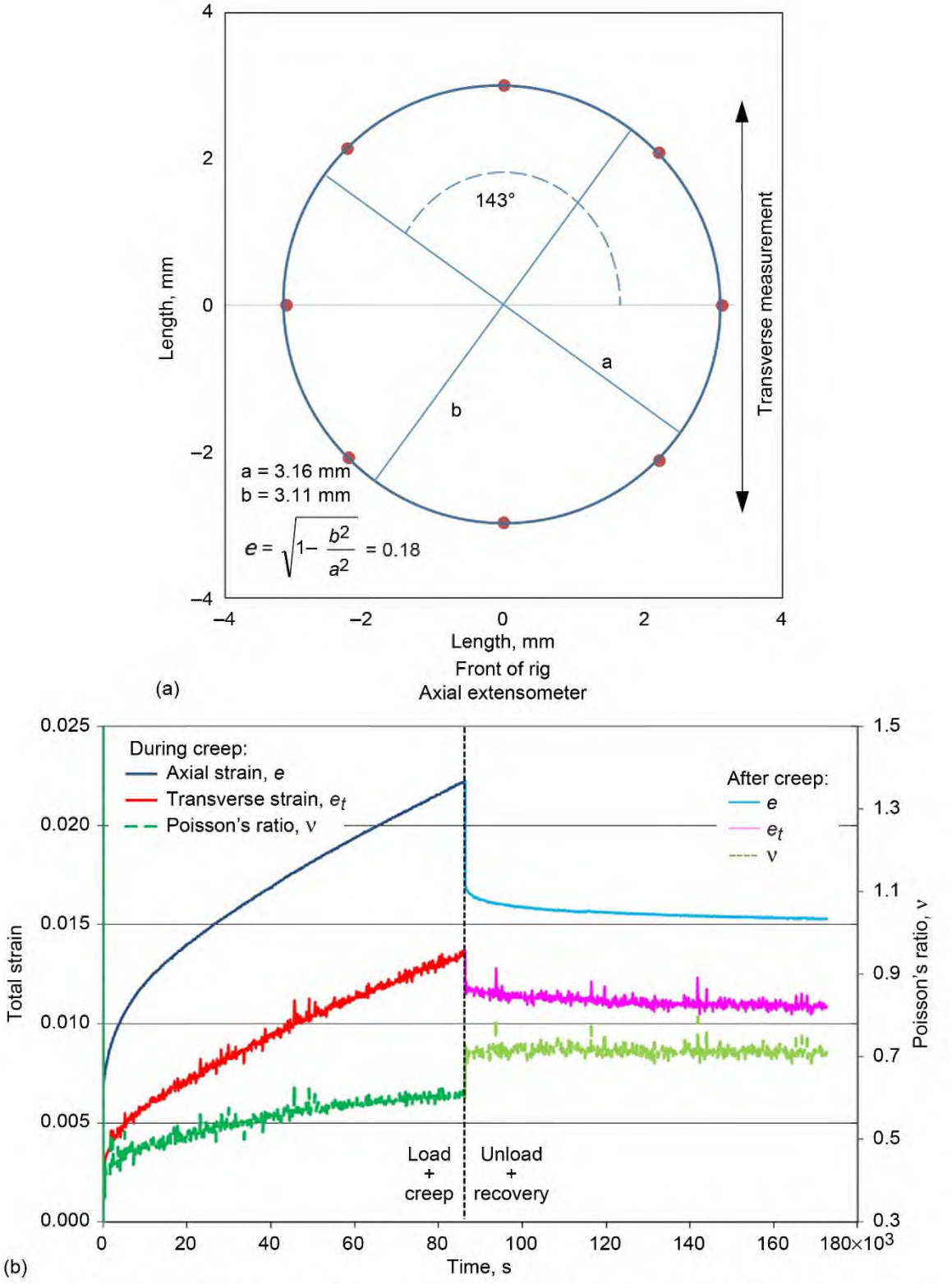

Figure 72.—Overload (514 MPa) and creep (446 MPa) test of Ti-6-4 sample 7 at 427 °C and strain rate of 10^{-3} s^{-1}. (a) Sample cross section and rotation, indicating orientation of major (a) and minor (b) axes with respect to right side of test frame and giving eccentricity *e*. (b) Axial and transverse strain and Poisson's ratio. (c) Enlargement of loadup from part (b). (d) Creep strain after 514 MPa overload for both axial and transverse directions.

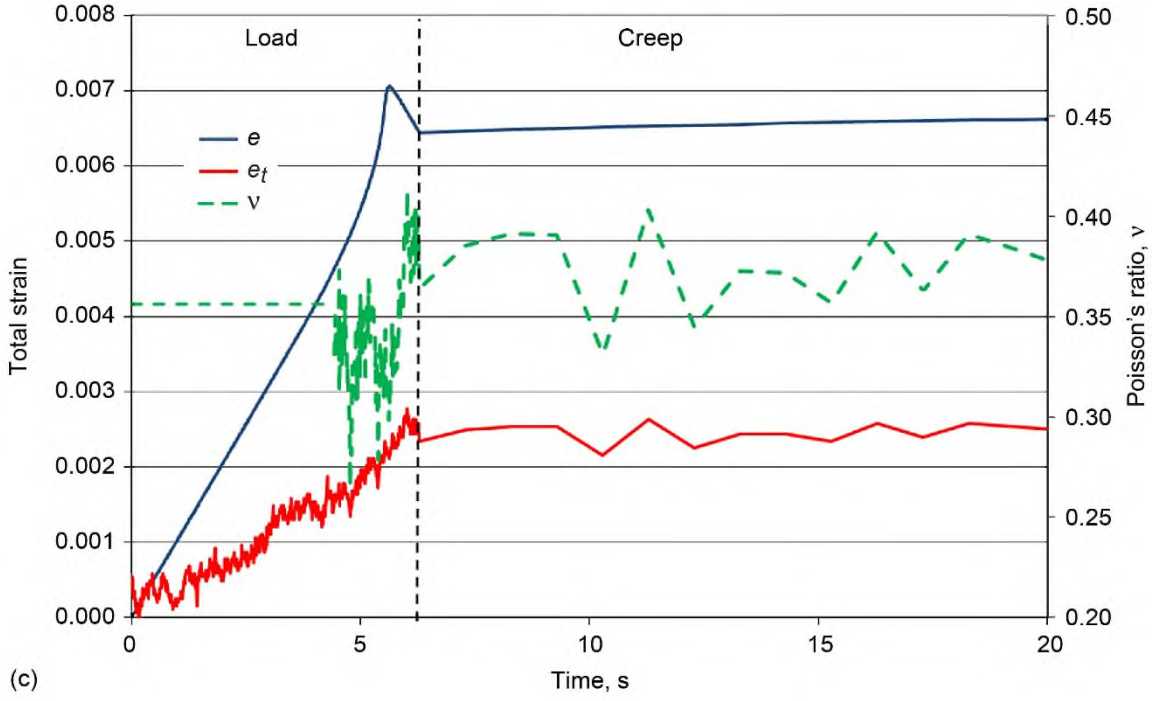

(c)

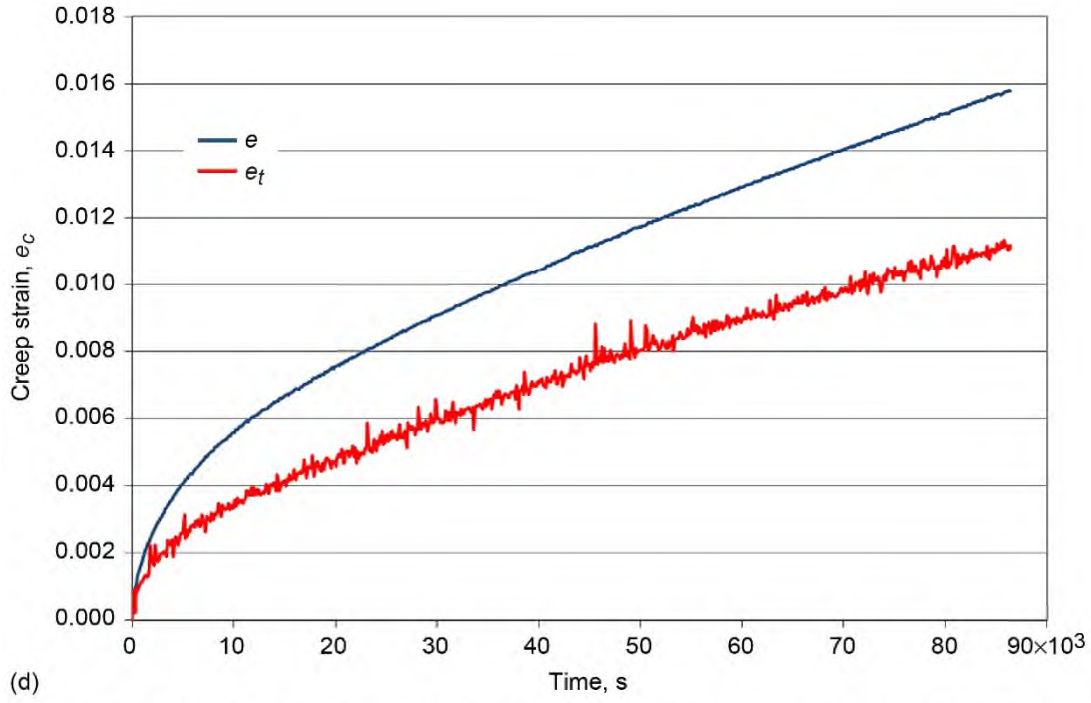

(d)

Figure 72.—Concluded. (c) Enlargement of loadup from part (b). (d) Creep strain after 514 MPa overload for both axial and transverse directions.

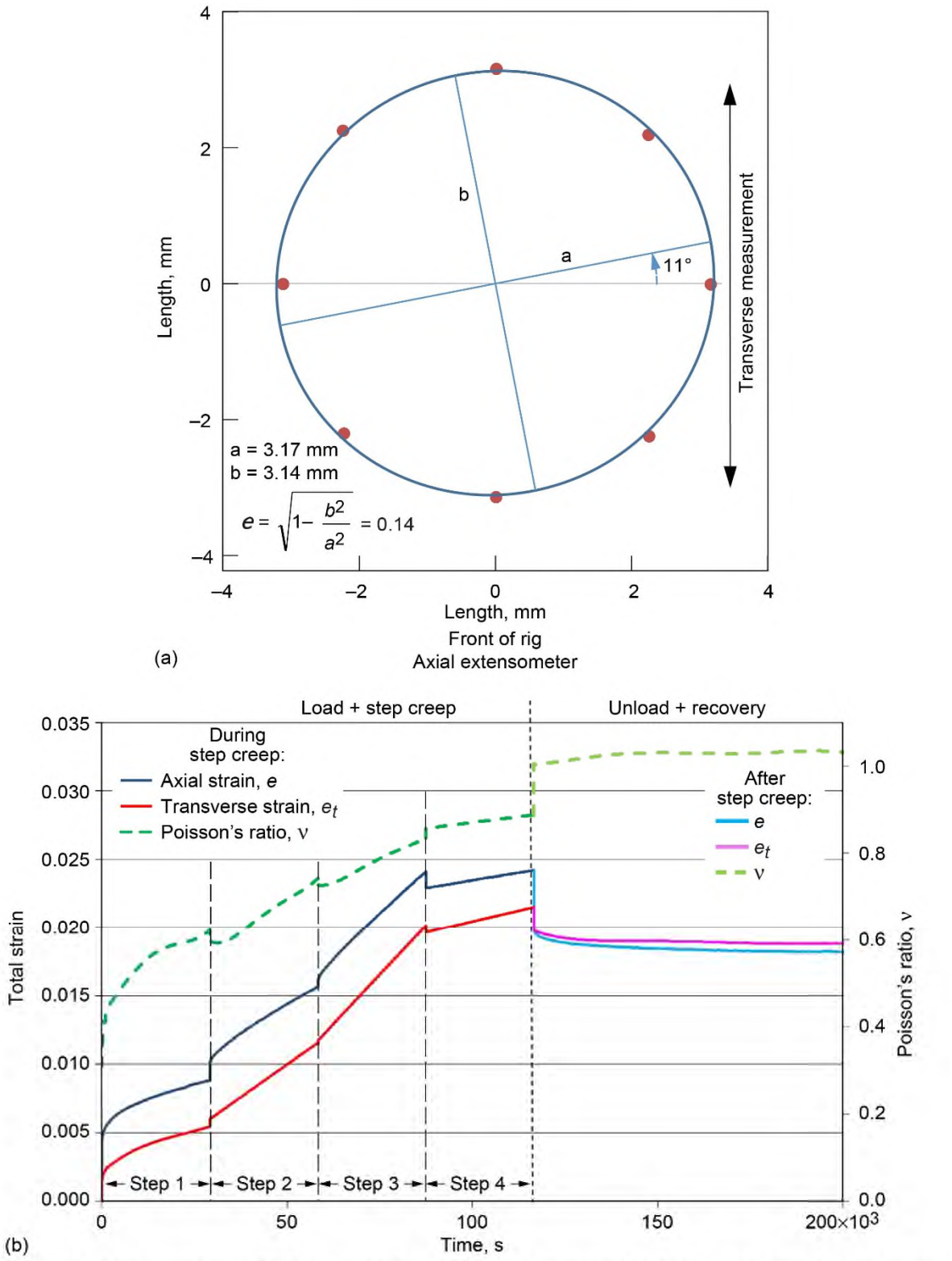

Figure 73.—Step creep test of Ti-6-4 sample 49 at 427 °C and strain rate of 10^{-3} s^{-1}. (a) Sample cross section and rotation, indicating orientation of major (a) and minor (b) axes with respect to right side of test frame and giving eccentricity *e*. (b) Axial and transverse strain and Poisson's ratio. (c) Enlargement of loadup from part (b). (d) Creep strain for both axial and transverse directions, listing inelastic Poisson's ratio ν^I (= $-\varepsilon_C^T/\varepsilon_C$, where ε_C^T is inelastic transverse strain and ε_C is inelastic axial strain) for each step.

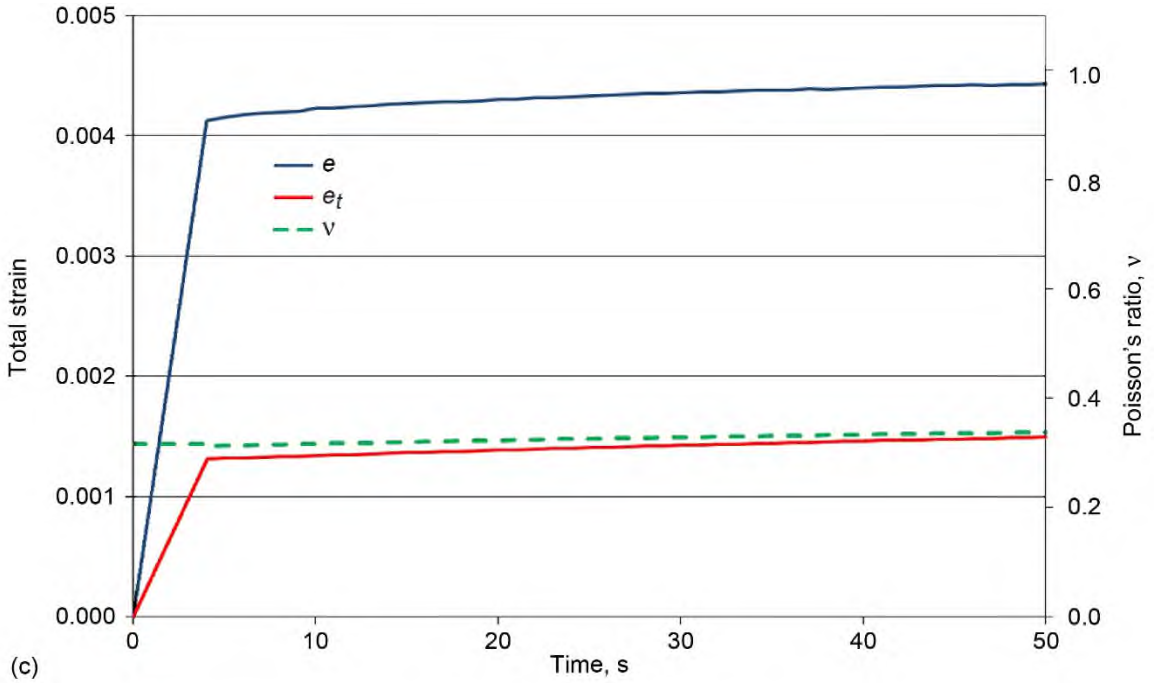

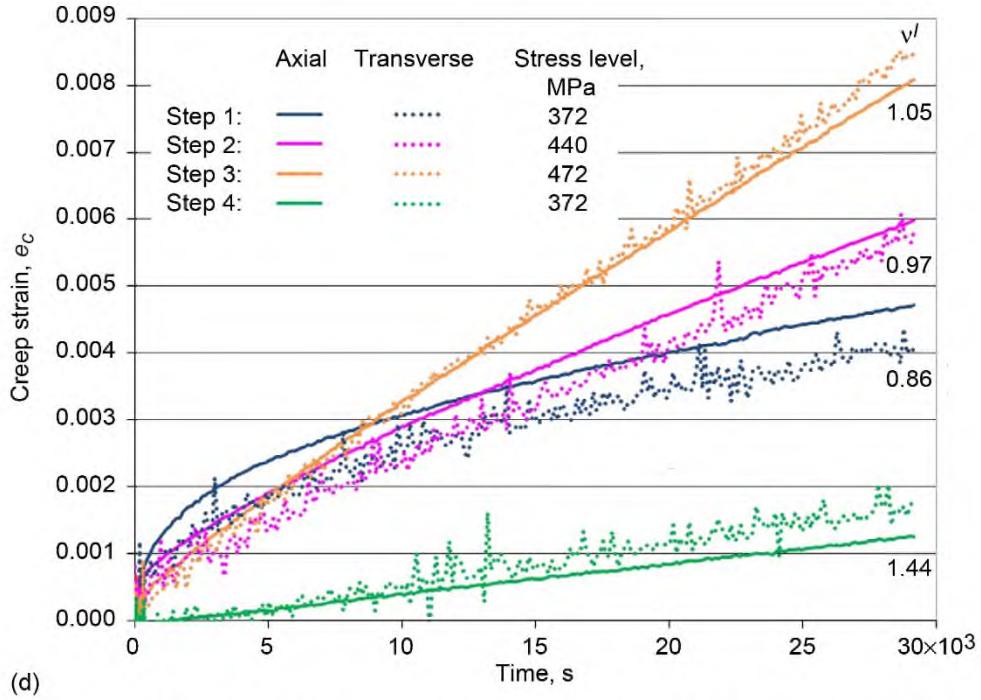

Figure 73.—Concluded. (c) Enlargement of loadup from part (b). (d) Creep strain for both axial and transverse directions, listing inelastic Poisson's ratio ν^I (= $-\varepsilon_c^T/\varepsilon_c$, where ε_c^T is inelastic transverse strain and ε_c is inelastic axial strain) for each step.

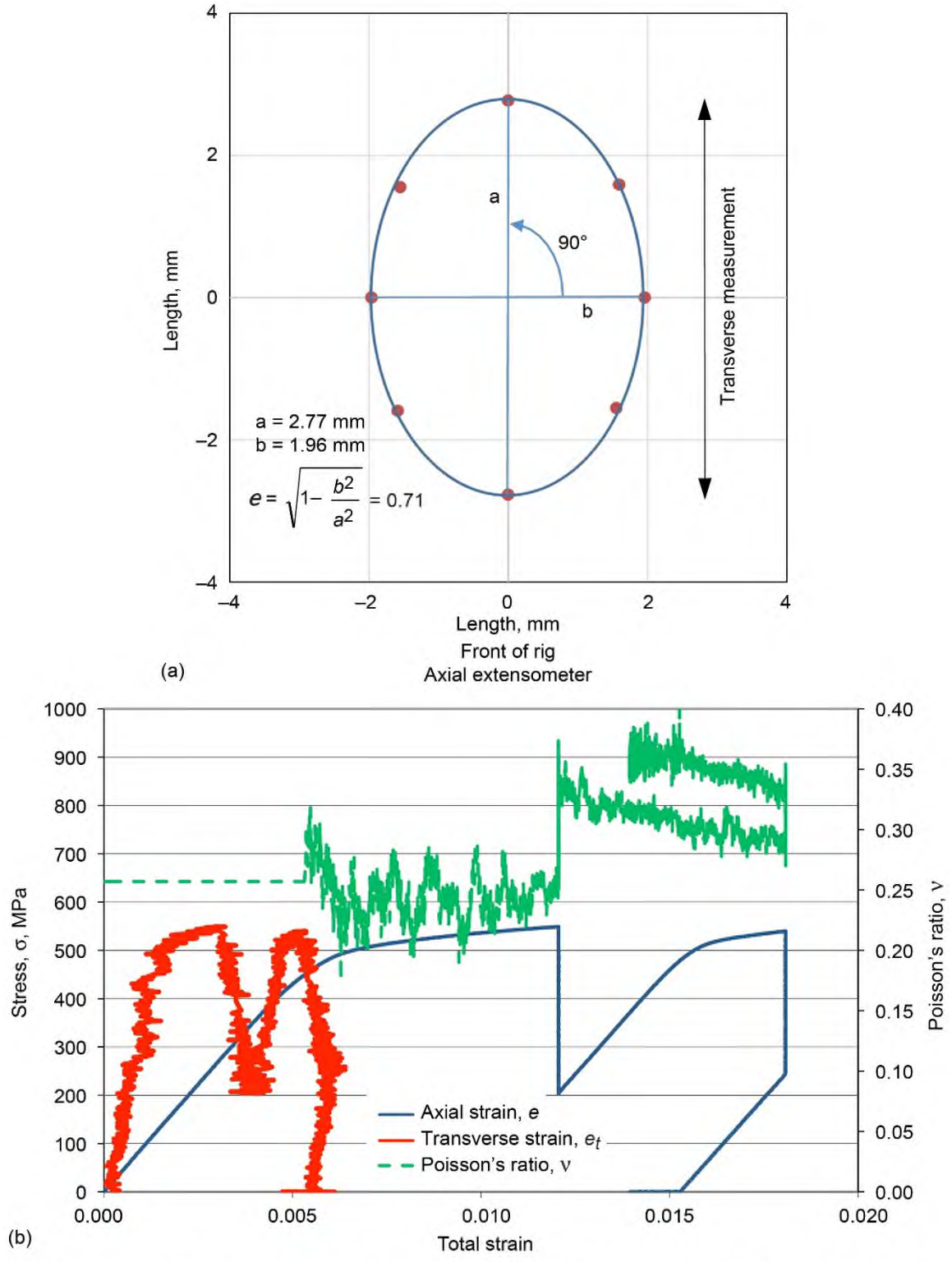

Figure 74.—Step relaxation test of Ti-6-4 sample 27 at 427 °C and strain rate of 10^{-3} s^{-1}. (a) Sample cross section and rotation, indicating orientation of major (a) and minor (b) axes with respect to right side of test frame and giving eccentricity *e*. (b) Stress-strain curves (axial and transverse) and Poisson's ratio. (c) Axial and transverse strain and Poisson's ratio. (d) Enlargement of transverse strain from part (c).

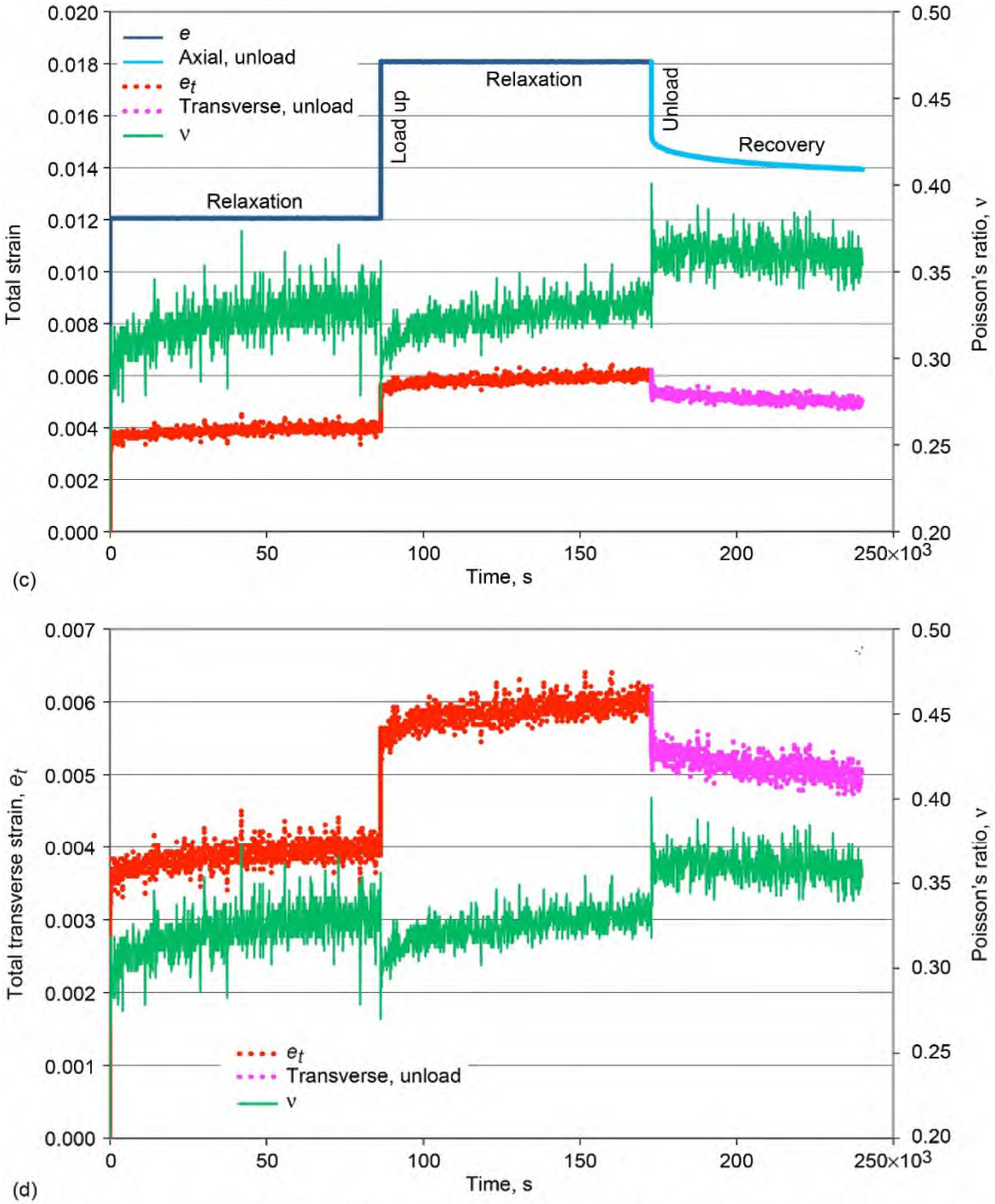

Figure 74.—Concluded. (c) Axial and transverse strain and Poisson's ratio. (d) Enlargement of transverse strain from part (c).

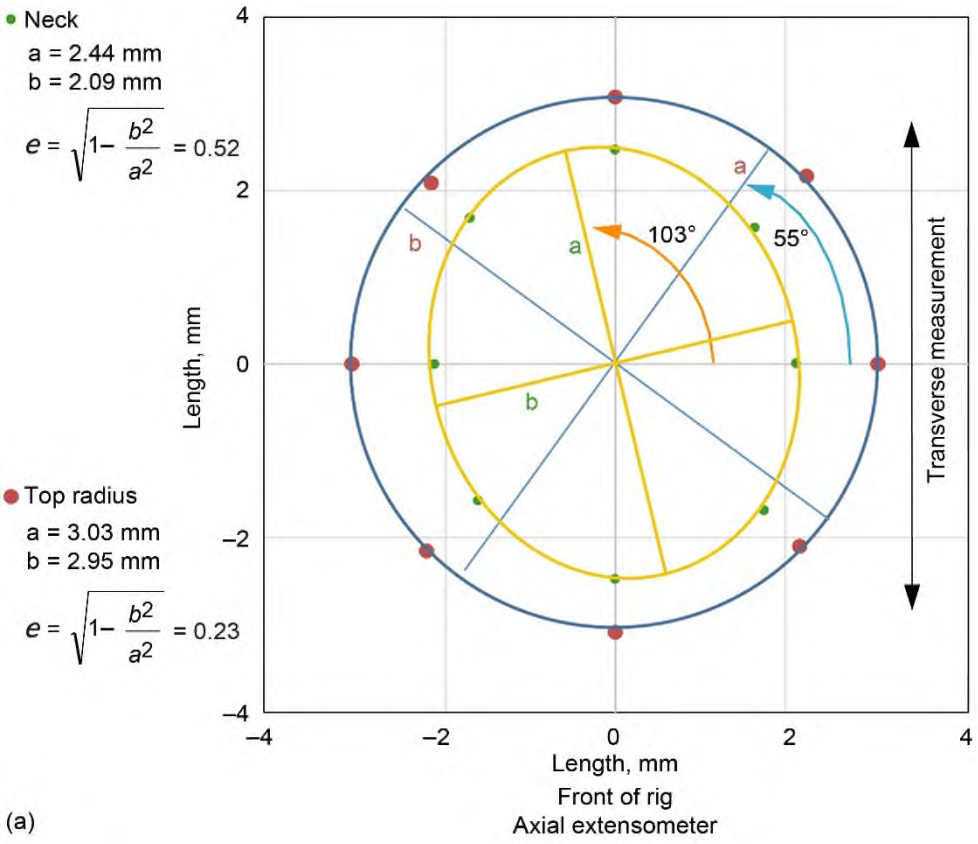

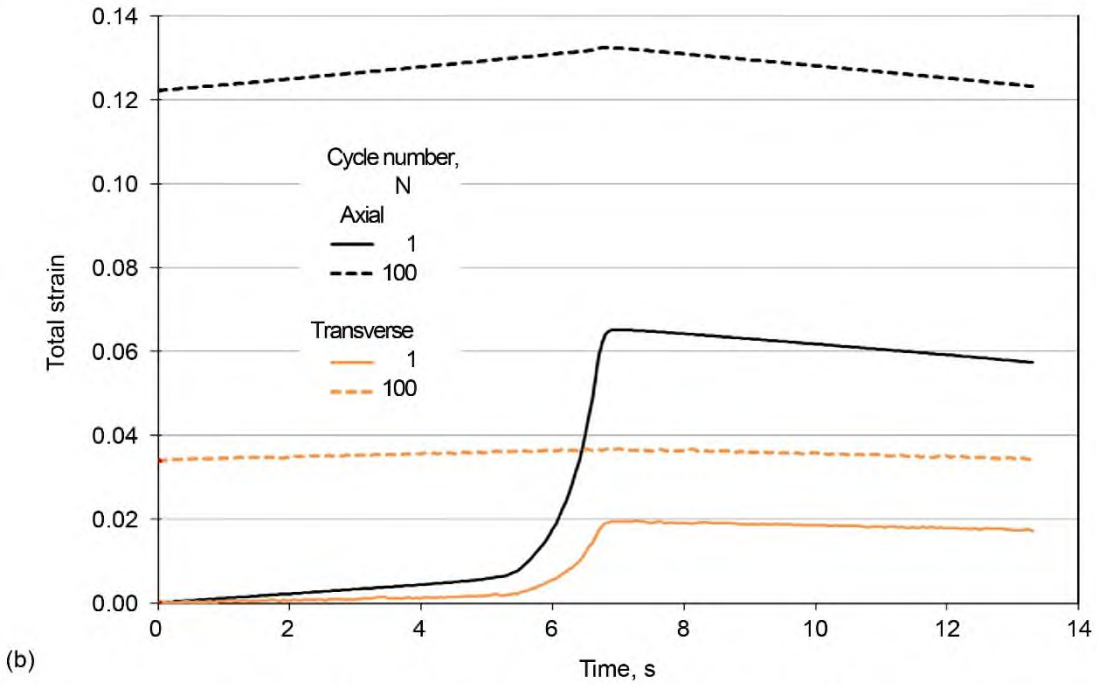

Figure 75.—Transverse strain of Ti-6-4 sample 58 under cyclic loading at 427 °C and stress between 0 and 640 MPa; sample failed at 115 cycles. (a) Sample cross section and rotation, indicating orientation of major (a) and minor (b) axes with respect to right side of test frame and giving eccentricity *e*. (b) Axial and transverse strain response for two cycles. (c) Poisson's ratio for multiple cycles as function of time. (d) Poisson's ratio at maximum stress for multiple cycles.

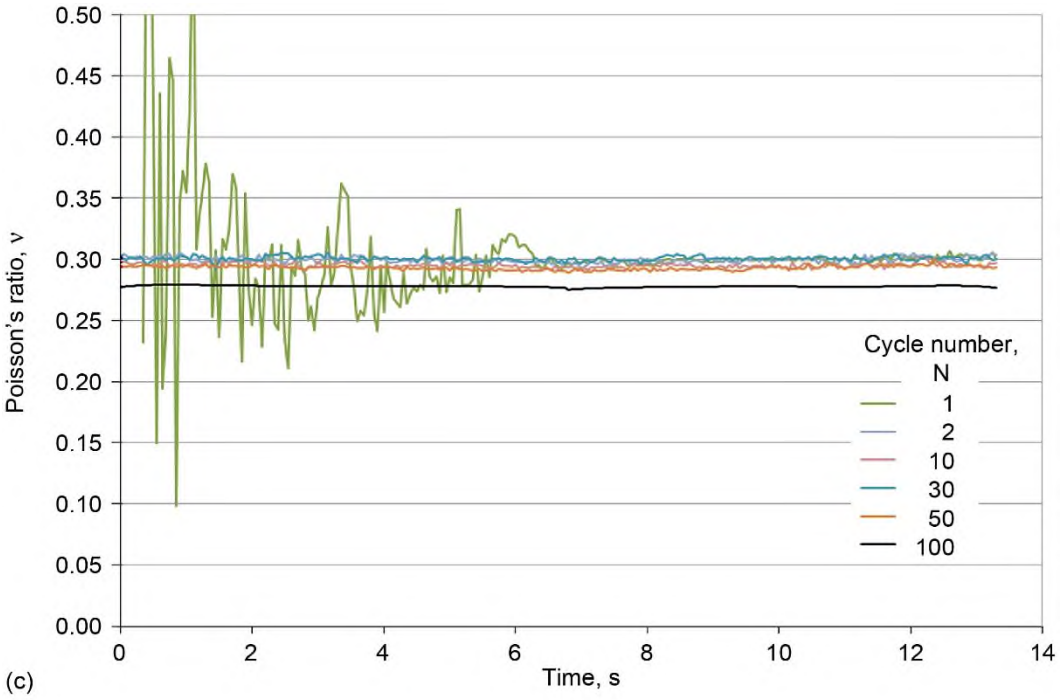

(c)

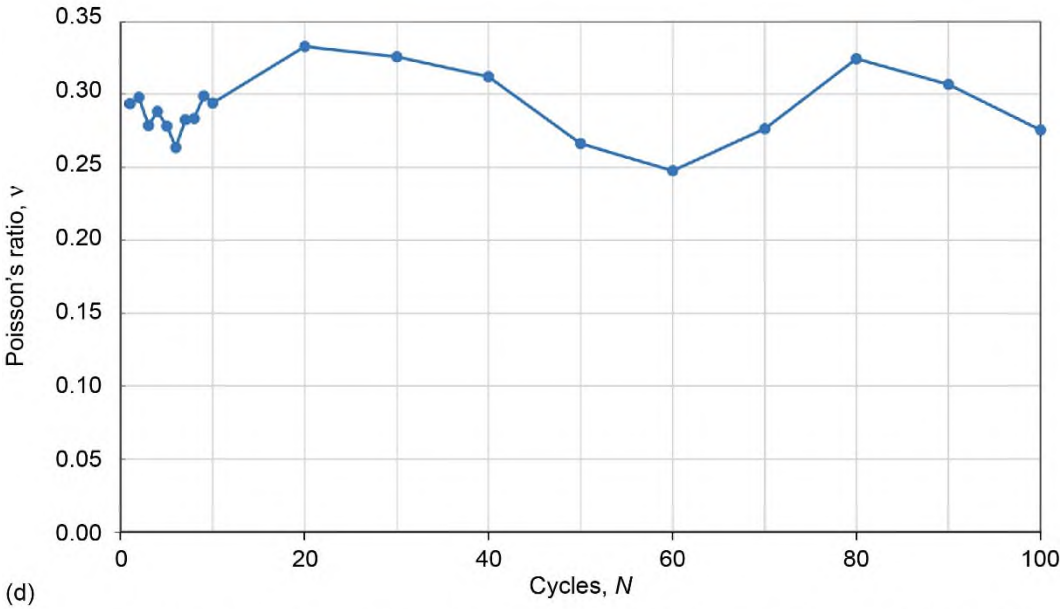

(d)

Figure 75.—Concluded. (c) Poisson's ratio for multiple cycles as function of time. (d) Poisson's ratio at maximum stress for multiple cycles.

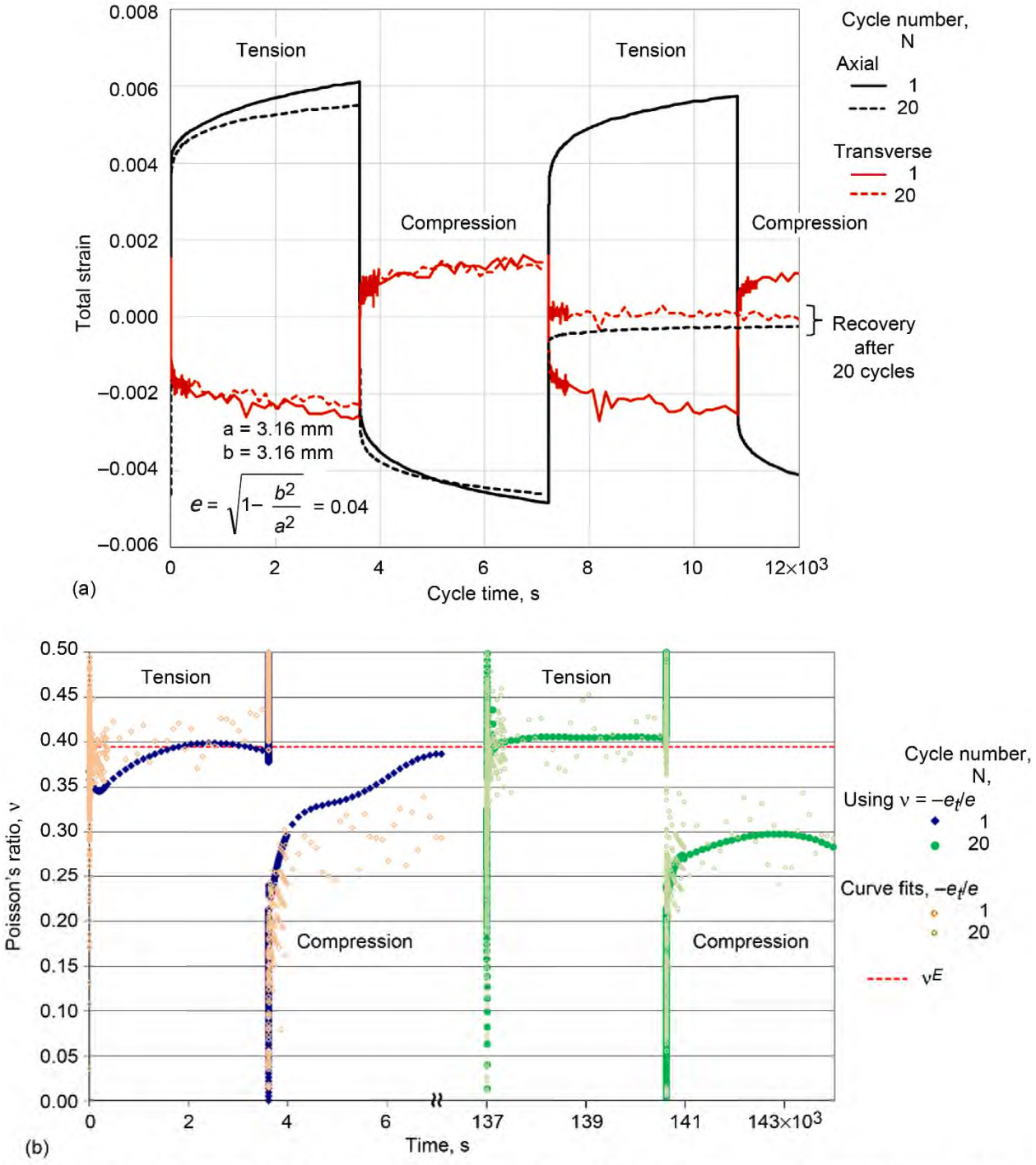

Figure 76.—A 20-cycle test of Ti-6-4 sample 96 at 427 °C with creep holds at maximum and minimum stress. (a) Axial and transverse strain response for first and last cycle, showing length of major (a) and minor (b) axes of cross section and giving eccentricity *e*. (b) Poisson's ratio calculated by two methods for first and last cycle: (1) with $\nu = -e_t/e$ where e_t is transverse strain and *e* is axial strain and (2) with e_t/e determined from curve fit. Also shown is elastic Poisson's ratio ν^E ($=E_a/E_t$, where E_a and E_t are elastic moduli from axial and transverse stress-strain measurements, respectively).

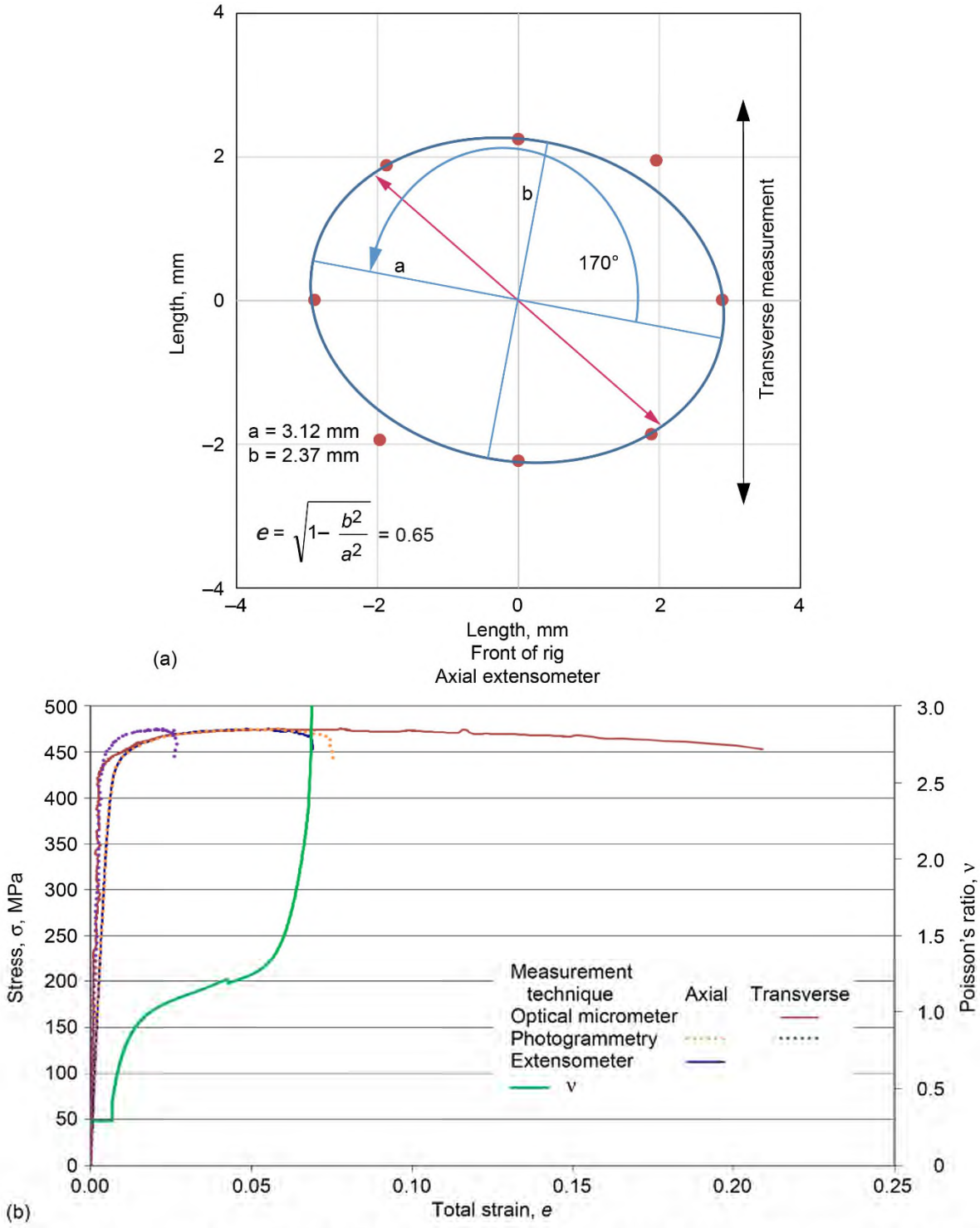

Figure 77.—Tensile test of Ti-6-4 sample 39 at 538 °C. (a) Sample cross section and rotation, indicating orientation of major (a) and minor (b) axes with respect to right side of test frame and giving eccentricity *e*. (b) Stress versus axial and transverse strain determined by two techniques, and Poisson's ratio ν. (c) Enlargement of loadup from part (b). (d) Speckled sample prior to failure at 7.5 percent axial strain. (e) Transverse strain determined by two techniques and measured in three locations. (f) Poisson's ratio determined by two techniques. Also shown is elastic Poisson's ratio ν^E (=E_a/E_t, where E_a and E_t are elastic moduli from axial and transverse stress-strain curves, respectively). (g) Contour plots of sample gage section as function of axial strain. (h) Local sample radius as function of axial strain.

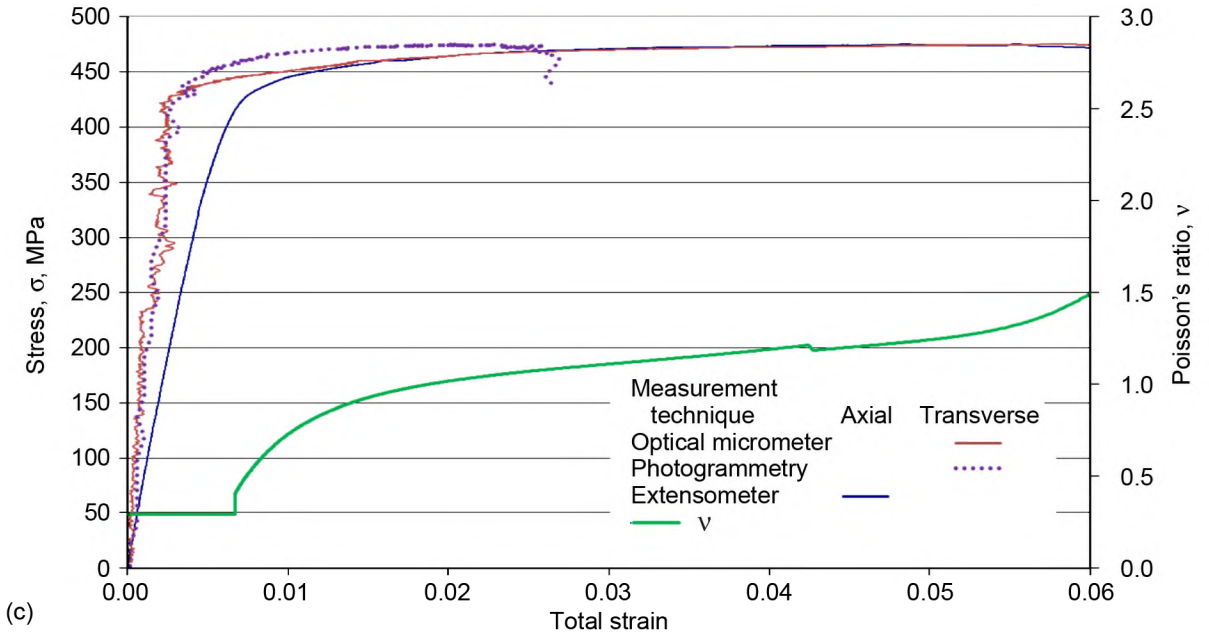

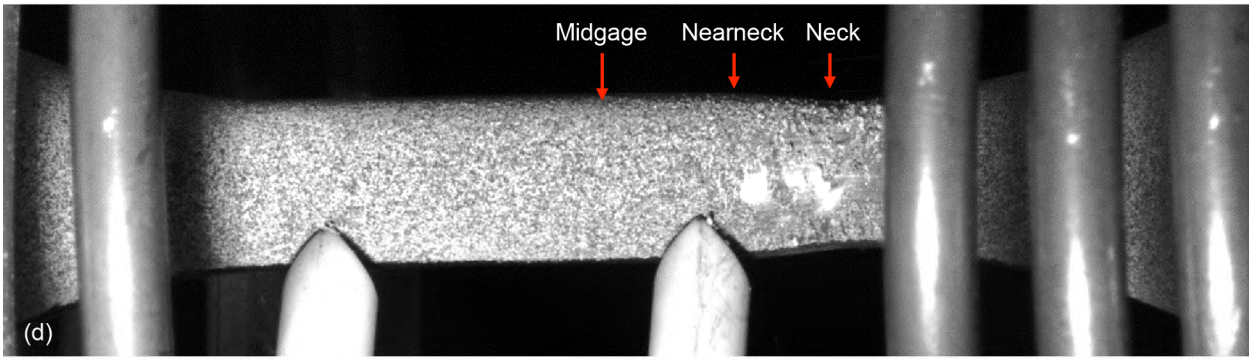

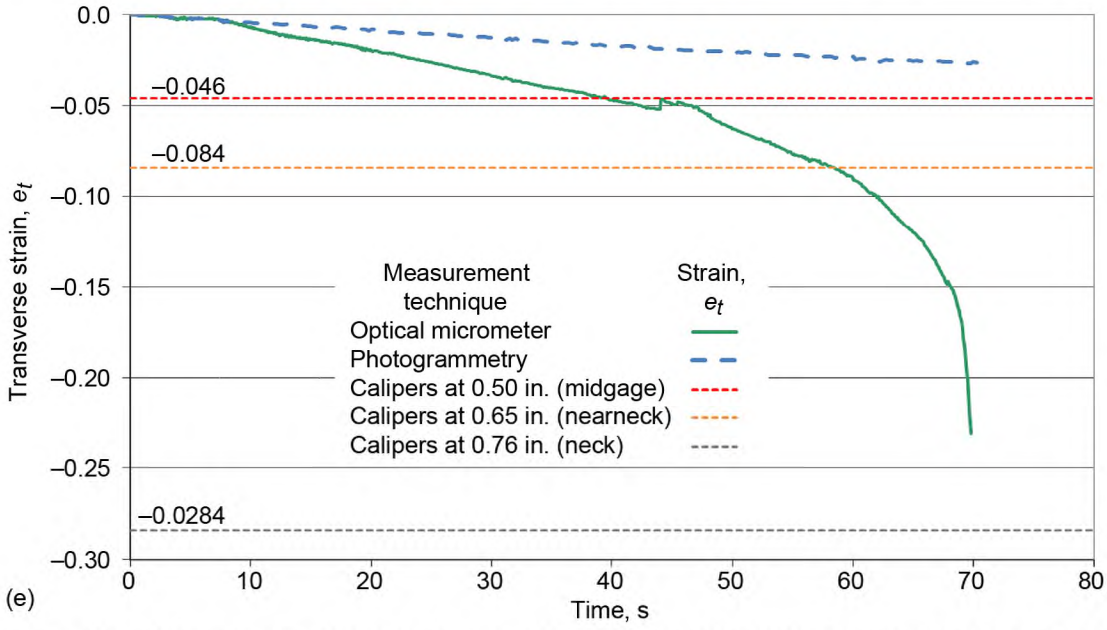

Figure 77.—Continued. (c) Enlargement of loadup from part (b). (d) Speckled sample prior to failure at 7.5 percent axial strain. (e) Transverse strain determined by two techniques and measured in three locations.

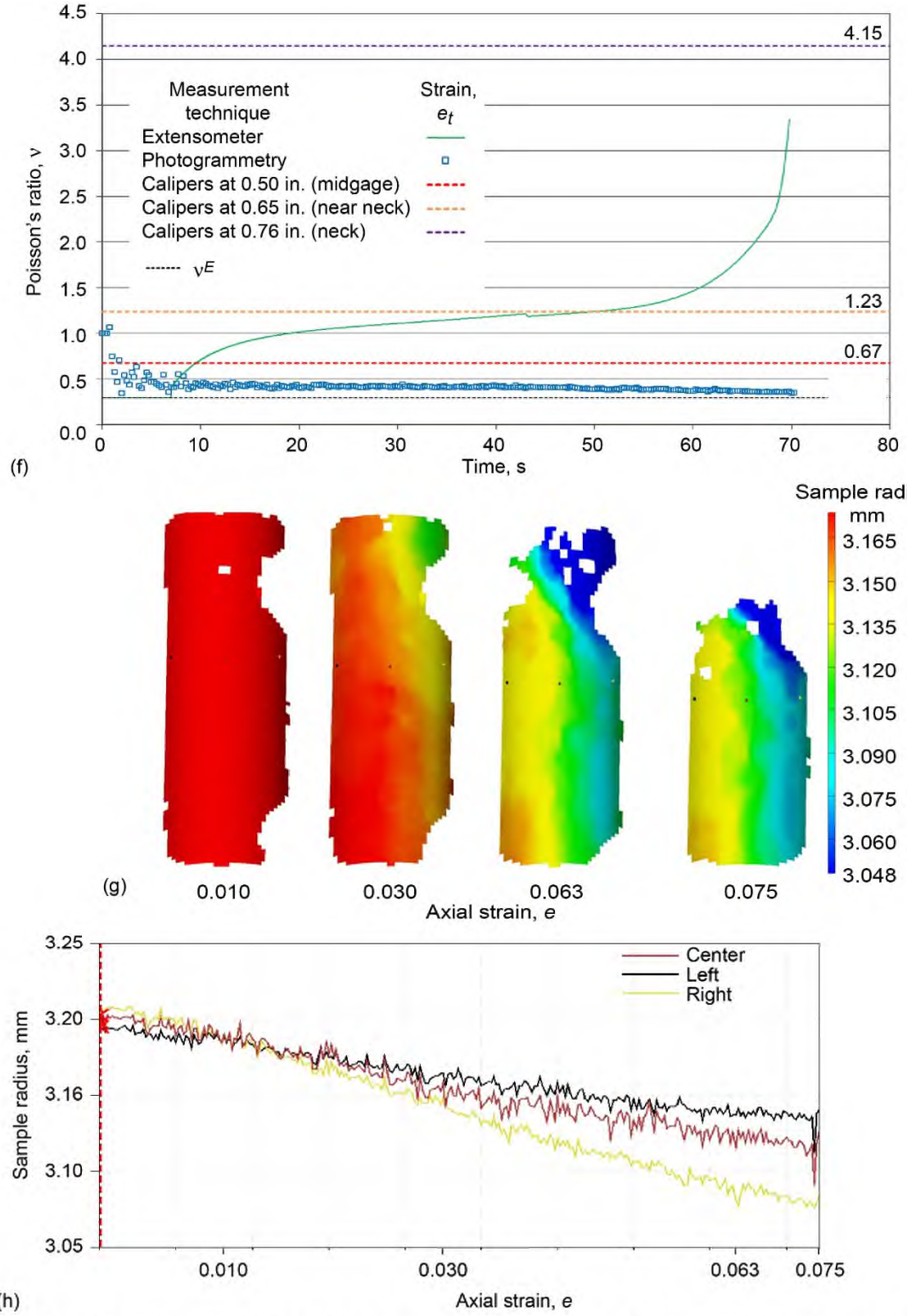

Figure 77.—Concluded. (f) Poisson's ratio determined by two techniques. Also shown is elastic Poisson's ratio ν^E (=E_a/E_t, where E_a and E_t are elastic moduli from axial and transverse stress-strain curves, respectively). (g) Contour plots of sample gage section as function of axial strain. (h) Local sample radius as function of axial strain.

References

Aerospace Structural Metals Handbook, 1997: CINDAS/USAF CRDA Handbook Operations. Section 3707, Purdue University, West Lafayette, IN.

Arnold, Steven M., et al. 2014: Viscoelastoplastic Deformation and Damage Response of a Titanium (Ti-6-4) and Nickel-based Superalloy (ME3) at Elevated Temperatures. Presented at the 2014 SEM Annual Conference and Exposition on Experimental and Applied Mechanics, Greenville, SC.

Arnold, Steven M., et al., 2009: An Overview of Structural Prognosis Health Management Research at Glenn Research Center for Gas Turbine Engine Structures With Special Emphasis on Deformation and Damage Modeling. NASA/TM—2009-215827.

Arnold, S.M.; Saleeb, A.F.; and Castelli, M.G., 2001: A General Time Dependent Constitutive Model: Part II—Application to a Titanium Alloy. J. Eng. Mater. Technol., vol. 123, no. 1, pp. 65–73.

ASTM Standard E1876–09, 2009: Standard Test Method for Dynamic Young's Modulus, Shear Modulus, and Poisson's Ratio by Impulse Excitation of Vibration. ASTM International, West Conshocken, PA.

Barboza, M.J.R.; Moura Neto, C.; and Silva, C.R.M., 2004: Creep Mechanisms and Physical Modeling for Ti-6Al-4V. Mater. Sci. Eng. A, vol. A369, pp. 201−209.

Castelli, Michael G.; Lerch, Bradley A.; and Keller, Dennis J., 1999: A Comparison of Deformation Behaviors of HIPed Foil and Sheet Titanium Alloys. HiTEMP Review 1999, Paper 27, NASA/CP—1999-208915/VOL2. Available from the NASA STI Program.

Chakrabarti, A.K; and Nichols, E.S., 1980: Creep Behavior of Cast Ti-6Al-4V Alloy. Titanium '80, Science and Technology, Proceedings of the Fourth International Conference on Titanium, Kyoto, Japan, pp. 1081−1096.

Cheng, Jingyi; and Nemat-Nasser, Sia, 2000: A Model for Experimentally-Observed High-Strain-Rate Dynamic Strain Aging in Titanium. Acta Mater., vol. 48, pp. 3131−3144.

Chiu, S.S.; Eftis, J.; and Jones, D.L., 1990: Prediction of Fatigue Life With and Without Hold Times Using the Chaboche Viscoplastic Constitutive Theory. J. Eng. Mater-T ASME, vol. 112, pp. 188−197.

Doner, M.; and Conrad, H., 1973: Deformation Mechanisms in Commercial Ti-50A (0.5 at. pct O_{eq}) at Intermediate and High Temperatures (0.3 - 0.6 T_m). Metall. Trans., vol. 4, pp. 2809−2817.

Dunn, DeRome Osmond, 1991: Modeling Cycle and Time-Dependent Creep/Relaxation Effects on Fatigue Lives of Notched Members. Ph.D. Thesis, Virginia Polytechnical Institute, Blacksburg, VA.

Evans, W.J., 1987: Stress Relaxation and Notch Fatigue in Ti-6Al-4V. Scripta Metall., vol. 21, pp. 1223−1227.

Evans, W.J.; and Harrison, G.F., 1976: The Development of a Universal Equation for Secondary Creep Rates in Pure Metals and Engineering Alloys. Met. Sci., pp. 307−313.

Evans, W.J.; and Harrison, G.F., 1979: Friction Stress σ_0 and Relationship Between Initial and Secondary Creep Rates in Precipitation-Hardened Nickel-Base Alloy. Met. Sci., pp. 641−649.

Evans, W.J.; and Harrison, G.F., 1983: Power Law Steady State Creep in α/β Titanium Alloys. J. Mater. Sci., vol. 18, no. 11, pp. 3449−3455.

Hatch, A.J.; Partridge, J.M.; and Broadwell, R.G., 1967: Room-Temperature Creep and Fatigue Properties of Titanium Alloys. J. Mater., vol. 2, no. 1, pp. 111−119.

Imam, M.A.; and Gilmore, C.M., 1979: Room Temperature Creep of Ti-6Al-4V. Metall. Trans. A, vol. 10, no. 4, pp. 419−425.

Katcher, M., 1968: Creep of Titanium Alloys. Metals Engineering Quarterly, pp. 19−27.

Koester, Werner; and Franz, H., 1961: Poisson's Ratio for Metals and Alloys. Metallurgical Review, vol. 6, no. 21, pp. 1−56.

Krempl, Erhard, 1979: Viscoplasticity Based on Total Strain. The Modelling of Creep With Special Considerations of Initial Strain and Aging. J. Eng. Mater. Technol., vol. 101, no. 4, pp. 380−386.
Lerch, Bradley A.; and Arnold, Steven M., 2014: Viscoelastic Response of the Titanium Alloy Ti-6-4: Experimental Identification of Time- and Rate-Dependent Reversible and Irreversible Deformation Regions. NASA/TM—2014-216584.
Levy, A.J., 1986: The Tertiary Creep and Necking of Creep Damaging Solids. Acta Metall., vol. 34, no. 10, pp. 1991−1997.
Lin, Yi-Hsiang, et al., 2011: Dynamic Strain Aging in Low Cycle Fatigue of Duplex Titanium Alloys. Mater. Sci. Eng. A, vol. 528, pp. 4381−4389.
Manson, S.S.; and Halford, G.R., 2006: Fatigue and Durability of Structural Materials. ASM International, Materials Park, OH, pp. 76−77.
Mazzotti, Claudio; and Savoia, Marco, 2002: Nonlinear Creep, Poisson's Ratio, and Creep-Damage Interaction of Concrete in Compression. ACI Mater. J., vol. 99, no. 5, pp. 450−457.
Metallic Materials Properties Development and Standardization (MMPDS) Handbook−07, 2012: Ch. 5, Federal Aviation Administration, Washington, DC.
Morishita, M., et al., 1988: Application of the Overstress Concept for Creep-Fatigue Evaluation. Low Cycle Fatigue, ASTM STP942, H.D. Solomon, et al., eds., ASTM, Philadelphia, PA, pp. 487−499.
Morrissey, R.J.; McDowell, D.L.; and Nicholas, T., 1999: Frequency and Stress Ratio Effects in High Cycle Fatigue of Ti–6Al–4V. Int. J. Fatigue, vol. 21, pp. 679−685.
Nemat-Nasser, Sia, et al., 2001: Dynamic Response of Conventional and Hot Isostatically Pressed Ti-6Al-4V Alloys: Experiments and Modeling. Mech. Mater., vol. 33, pp. 425−439.
Odegard, Ben C.; and Thompson, Anthony W., 1974: Low Temperature Creep of Ti-6Al-4 V. Metall. Trans., vol. 5, no. 5, pp. 1207−1213.
Ozyhar, Tomasz; Hering, Stefan; and Niemz, Peter, 2013: Viscoelastic Characterization of Wood: Time Dependence of the Orthotropic Compliance in Tension and Compression. J. Rheol., vol. 57, pp. 699−717.
Palchan, I.; and Rosen, A., 1978: History Dependent Creep of Ti-6Al-4V Alloy. Metal Science, pp. 163–165.
Povolo, P.; and Bolmaro, R.E., 1985: Poisson's Ratio of Metals and Alloys. International Series on the Strength and Fracture of Materials and Structures, Vol. 1, Pergamon Press, Oxford, pp. 287−292.
Saleeb, A.F.; and Arnold, S.M., 2001: A General Time Dependent Constitutive Model: Part I—Theoretical Developments. J. Eng. Mater. Technol., vol. 123, no. 1, pp. 51−64.
Saleeb, A.F.; and Arnold, S.M., 2004: Specific Hardening Function Definition and Characterization of a Multimechanism Generalized Potential-Based Viscoelastoplasticity Model. Int. J. Plasticity, vol. 20, no. 12, pp. 2111−2142.
Saleeb, A.F., et al., 2001: A General Hereditary Multimechanism-Based Deformation Model With Application to the Viscoelastoplastic Response of Titanium Alloys. Int. J. Plasticity, vol. 17, no. 10, pp. 1305−1350.
Sargent, P.M.; and Ashby, M.F., 1982: Deformation Maps for Titanium and Zirconium. Scripta Metall., vol. 16, pp. 1415−1422.
Sastry, S.M.L.; Pao, P.S.; and Sankaran, K.K., 1980: High Temperature Deformation of Ti-6Al-4V. Titanium '80, Science and Technology, Proceedings of the Fourth International Conference on Titanium, Kyoto, Japan, pp. 873−886.
Sasikala, G.; Ray, S.K.; and Mannan, S.L., 2004: Evolution of Damage in Tertiary Creep of Type 316(N) SS Weld Metal. Acta Mater., vol. 52, pp. 5677–5686.

Savage, M.F.; Neeraj, T.; and Mills, M.J., 2002: Observations of Room-Temperature Creep Recovery in Titanium Alloys. Metall Trans., vol. 33A, pp. 891–898.
Sellers, Cory A., 2009: Characterizing a Constitutive Model for the Viscoelastic Response of a Titanium Alloy. NASA USRP—Internship Final Report.
Sinha, N.K., 2001: Short Strain Relaxation/Recovery Tests for Evaluating Creep Response of Nickel-Base Superalloys Like IN-738LC. J. Mater. Sci. Lett., vol. 20, pp. 951–953.
Sinha, Nirmal K., 2003: Limitations of Stress Relaxation Tests for Determining Stress Dependence of Strain Rate at High Temperatures. Scripta Mater., vol. 48, pp. 731–736.
Sinha, N.K., 2005a: In Search of Delayed Elasticity Prior to Fracture in a Nickel-Base Single-Crystal, CMSX–10. ECCC Creep Conference, London, pp. 244–255.
Sinha, N.K., 2005b: Short-Term Rheology of a Polycrystalline Nickel-Base Superalloy Involving Delayed Elasticity. ECCC Creep Conference, London, pp. 256–267.
Sinha, N.K., et al., 1979: Grain Boundary Sliding in Polycrystalline Materials. Philos. Mag. A, vol. 40, no. 6, pp. 825–842.
Solimine, P.A.; and Lissenden, C.J., 2004: Fatigue of Beta Titanium Alloy at 20, 482 and 648 °C. Fatigue Fract. Eng. Mater. Struct., vol. 27, pp. 943–955.
Srinivasan, K.; and Venugopal, P., 2008: Compression Testing of Ti-6Al-4V in the Temperature Range of 303–873 K. Mater. Manuf. Processes, vol. 23, no. 4, pp. 342–346.
Stang, Ambrose H.; Greenspan, Martin; and Newman, Sanford B., 1946: Poisson's Ratio of Some Structural Alloys for Large Strains. Journal of Research of the National Bureau of Standards, Research Paper RP1742, vol. 37, pp. 211–221.
Stephens, J.J.; and Munford, J.W., 1988: Stress Relaxation of a Titanium (Ti-6Al-4V) Threaded Joint. Sandia National Labs Report SAND–87–1818, pp. 1–24.
Taniguchi, Yusuke; and Ando, Kosei, 2010: Time Dependence of Poisson's Effect in Wood I: The Lateral Strain Behavior. J. Wood Sci., vol. 56, no. 2, pp. 100–106.
Thompson, Anthony W.; and Odegard, Ben C., 1973: The Influence of Microstructure on Low Temperature Creep of Ti-5Al-2.5Sn. Metall. Trans., vol. 4, no. 4, pp. 899–908.
Wang, Z-G; Laird, C.; and Rahka, K.A., 1988: Cycle Stress-Diametral Strain Response and Microstructural Evolution During Low-Cycle Fatigue of a Bainitic Steel. Basic Questions in Fatigue Vol 2, ASTM STP 924, eds. R.P. Wei and R.P. Gangloff, ASTM, Philadelphia, PA, 1988, pp. 60–88.
Wapniarsky, S.; Rotem, A.I.; and Rosen, A., 1991: Creep of Ti-6Al-4V Titanium Alloy at Room Temperature. Strength of Metals and Alloys, Vol. I, Freund Publishing House, Ltd., pp. 437–442.
Williams, K.R.; and Wilshire, B., 1973: On the Stress- and Temperature-Dependence of Creep of Nimonic 80A. Met. Sci., vol. 7, pp. 176–179.
Yang, Henry S.; Su, Xiao-Ping S.; and Bai, Bingzhe, 2000: Analysis of Diametral Strain in Uniaxial Tensile and Compression Testing of Round Specimens of Anisotropic Materials. Int. J. Mech. Sci., vol. 42, pp. 2395–2415.
Zerwekh, Robert P., 1978: The Development of Methods for the Prediction of Primary Creep Behavior in Metals. NASA–CR–158123.
Zhaoxia, Li, 1994: Effective Creep Poisson's Ratio for Damaged Concrete. Int. J. Fracture, vol. 66, pp. 189–196.